DEVELOPING AN EYE-SAFE RAMAN SPECTROSCOPY AND FUNDUS IMAGING DEVICE FOR POINT-OF-CARE NEURODIAGNOSTICS

by

GEORGIA HARRIS

A thesis submitted to
the University of Birmingham
for the degree of
DOCTOR OF PHILOSOPHY

School of Chemical Engineering
College of Engineering and Physical Sciences
University of Birmingham
March 2024

Abstract

Traumatic Brain Injury (TBI) is a prevalent issue for healthcare providers and presents challenges in terms of diagnostics. Current statistics state that approximately 70 million people suffer from a TBI worldwide each year, with a mild TBI (e.g. concussion) occurring every 15 seconds. It is estimated that half of the world's population will have a TBI in their lives. Despite this burden, methods for TBI diagnostics are unreliable, slow and costly, and an alternative is necessary to make triaging decisions at the Point-of-Care (PoC). This thesis explores the use of Raman Spectroscopy to obtain biochemical information from the back of the eye to make non-invasive and neurologically relevant diagnoses. The structure of this thesis is like a sandwich, in which the experimental "filling" involves the experimental steps taken to achieve such a device.

Within Chapters 3, 4 and 5, I combine the necessary challenges to overcome in the designing, building, and testing of a working device that combines Raman spectroscopy and fundus imaging. Including creating a handheld fundus imaging system compatible with near-infrared wavelengths, assembling, and profiling a low-power, portable 830 nm laser diode system and using both to build the final neurodiagnostic system. Due to the experimental nature of this work, the materials and methods utilised are continuously iterated in response to data being collected, therefore the contents of these chapters constantly alternate between methods and results. I think this is a refreshing way to communicate the steps taken in this journey from conception to prototype, a continuous narrative of meeting and overcoming roadblocks as opposed to a highlights reel. This is unlike the "bread" Chapters 2 and 6 that start and finish the thesis.

Chapter 2 extracts the work I completed towards a pre-existing project, which established the idea of eye-based Raman Spectroscopy. I joined this project upon the reopening of the university laboratories and therefore had to restore the system to working condition and finalise the data collection. During this, I learnt many techniques used in developing my own portable device and made design decisions based on the project's limitations. To accompany the experimental development of this work, Chapter 5 presents a reference library of spectral information and assigned peaks is obtained for a cohort of 18 prospective TBI biomarkers, utilised to profile injury of retinal spectra from the portable, eye-safe Raman prototypes.

To support the ongoing development of eye-based Raman spectroscopy for neurodiagnostics, a collaboration has also been established to develop a first of its kind LIVING-EYE system, capable of whole *ex vivo* eye testing with the potential to test tissue damage and simulate a complete pre-TBI to post-trauma model. The continued progress of the steps made in this thesis will aid healthcare providers, increase understanding of TBI pathology and improve neurological outcomes for TBI patients.

Dedication

I dedicate this thesis to the memory of Val Barrett.

I love you all the world.

Acknowledgements

This work was made possible because of the guidance and opportunities provided by my supervisor Professor Pola Goldberg Oppenheimer, who I see as a great friend and inspiration, alongside the invaluable support and kindness from all the members of the ANMSA group, including honorary member Alex Brean.

I am thankful to Matthew Dalby, Michelle Carmicheal, Aimee Soare and Emma Lardner. The LifETIME CDT made my PhD more than just a research project but an environment in which I have gained confidence, transferable skills, and lifelong friends. Thank you for recognising potential in me; the CDT allowed me to enter a world of interdisciplinary research that I am privileged to be a part of.

The CDT also brought me the friendship of three strong and inspiring women, Paige Walczak, Hannah Lamont and Megan Boseley; I am so proud of what we have achieved. I acknowledge Dstl for funding my PhD and I am particularly grateful to Abi Spear and Kelly Curtis who provided me with expertise, wisdom and mentorship that has been more valuable to me than I think you know.

This thesis would not have been completed without the people in my life who have influenced me outside of my academic circle. There is not enough that can be said about the hours shared with my family and friends who supported me during this huge challenge. Melissa Oliver, Gemma Krishnan, Alice Mair, Alice Gough, Ethan Flanagan, and Harry Gardner; you are the compasses who help me navigate when feeling lost and I always find myself in your presence.

I am also grateful for the friends I met during my PhD journey, namely Anna Johnston and Lauren Shute, who have contributed to the fond memories I will cherish of Birmingham. A special mention must be made to Emma Buchan, my PhD partner, I don’t think I could ever describe how important your friendship has been during these years and I am so fortunate that we have crossed paths.

To my mum and dad, Patricia and Vincent Harris, all of my achievements so far are a tribute to the unconditional love and support you have provided me. Whether it was by my side or through the phone, your advice and encouragement has been essential over the past 4 years.

To Holly Harris, my sister and role model, you inspire me to be kind, brave and unashamedly myself, the traits I believe have allowed me to persevere with the difficult days during this PhD, along with appreciating the best ones. Your friendship, alongside Daniel Cooper’s, has been a huge source of comfort and joy, especially when my PhD world felt all-consuming.

Finally, I want to thank Dilshad Ali, my Dil, having you by my side makes me feel like I can achieve anything. The evidence of your love can be found on every page of this thesis, and I am, not only a better scientist but, a better person because of you.

Contents

List of Figures

List of Tables

List of Abbreviations

2D 2-Dimensional

3D 3-Dimensional

AD Alzheimer's Disease

AI Artificial Intelligence

AMD Age-Related Macular Degeneration

ANMSA the Advanced Nano-Materials Structures and Applications

ANOVA Analysis of Variance

BBB Blood Brain Barrier

BTI Banyan Trauma Indicator

CAD Computer-Aided Design

CARS Coherent Anti-Stokes Raman Spectroscopy

CNS Central Nervous System

CSF Cerebral Spinal Fluid

CT Computer Tomography

CTE Chronic Traumatic Encephalopathy

DAI Diffuse Axonal Injury

DARC Detection of Apoptosing Retinal Cells

DstI the Defence Science and Technology Laboratory

ED Emergency Department

ELISA(s) Enzyme-Linked Immunosorbent Assay(s)

FDA Food and Drug Administration

FFF Fused Filament Fabrication

FWHM Full Width Half Maximum

GCL Ganglion Cell Layer

GCS Glasgow Coma Scale

GFAP Glial Fibrillary Acidic Protein

GSH Glutathione

HD High Deinition

HSI Hyperspectral Imaging

ICP Intracranial Pressure

IIH Intracranial Hypertension

IL Interleukin

IR Infra-Red

LED Light Emitting Diode

LLLT Low-Level Light Therapy

MPE Maximum Permissible Exposure

MRI Magnetic Resonance Imaging

MRS Magnetic Resonance Spectroscopy

MS Multiple Sclerosis

MSI Multispectral Imaging

mTBI Mild TBI

NAA N-Acetyl-Aspartate

ND Neurogenerative

NFL Neurofilament Light Chain

NICE the National Institute for Health and Care Excellence

NIRS Near-Infrared Spectroscopy

NMR Nuclear Magnetic Resonance

NoIR No Infra-Red filter

NSE Neuron-Specific Enolase

OCT Optical Coherence Tomography

ON Optic Nerve

ONSD Optic Nerve Sheath Diameter

PBL Pebble Biotechnology Laboratory

PBS Phosphate-Buffered Saline

PCA Principal Component Analysis

PD Parkinson's Disease

PLA Polylactic Acid

PoC Point of Care

RBC(s) Red Blood Cell(s)

RGC(s) Retinal Ganglion Cell(s)

RNA Ribonucleic Acid

RNFL Retinal Nerve Fibre Layer

RPE Retinal Pigment Epithelium

RRS Resonance Raman Spectroscopy

RS Raman Spectroscopy

SANS Spaceflight-Associated Neuro-ocular Syndrome

SERS Surfaced-Enhanced Raman Spectroscopy

SKiNET Self Organising Kohonen Index Network

SOM(s) Self-Organised Map(s)

SOMDI Self Organising Map Discriminant Index

TBI Traumatic Brain Injury

THz Terahertz

t-tau total tau

UCHL1 Ubiquitin C-terminal Hydrolase-L1

US United States

Chapter 1 - Introduction

Emerging Eye-Based Diagnostic Technologies for Traumatic Brain Injury

The purpose of this introductory chapter is to combine all of the themes tackled in this thesis to not only aid the reader with understanding all of the avenues explored, but also convince you that the topic of eye-based Traumatic Brain Injury (TBI) diagnostics is essential for the future of detecting neurodegenerative disorders and diseases. This introduction brings together the aspects of TBI, oculomics and biomarker detection to champion the narrative that Raman Spectroscopy is a worthy technique to pursue for the innovative, novel and accessible point-of-care (PoC) technology that is vital to establish for TBI patients.

"*Oculomics* ", the study of ocular manifestations of neurodegenerative disorders, is a growing field of investigation for early diagnostics, enabling structural and chemical biomarkers to be monitored over time to predict prognosis. TBI triggers a cascade of events harmful to the brain, which can lead to neurodegeneration. TBI, termed the "silent epidemic" is becoming a leading cause of death and disability worldwide. There is currently no effective diagnostic tool for TBI, and yet, early-intervention is known to considerably reduce the length of hospital stays, improve outcomes, fasten neurological recovery, and lower mortality rates, highlighting the unmet need for techniques capable of rapid and accurate PoC diagnostics, implemented in the earliest stages.

This review focuses on the latest advances in the main neuropathophysiological responses and the achievements and shortfalls of TBI diagnostic methods. Validated and emerging TBI-indicative biomarkers are outlined and linked to ocular neuro-disorders. Methods detecting structural and chemical ocular responses to TBI are categorised along with prospective chemical and physical sensing techniques. Particular attention is drawn to the potential of Raman spectroscopy as a non-invasive sensing of neurological molecular signatures in the ocular projections of the brain, laying the platform for the first tangible path towards alternative PoC diagnostic technologies for TBI.

Acknowledgement of contributing material and authors

Content within this chapter has been published in the following journal paper:

- G. Harris, J. J. S. Rickard, G. Butt, L. Kelleher, R. J. Blanch, J. Cooper, P. G. Oppenheimer, Review: Emerging Eye-Based Diagnostic Technologies for Traumatic Brain Injury. *IEEE Rev. Biomed. Eng.* **16**, 530–559 (2023).

1.1 Traumatic Brain Injury

Traumatic Brain Injury (TBI) can cause death or lifelong physical and mental disability. TBI occurs when the brain is damaged by rapid acceleration or deceleration with rotational or shear forces or penetration[1]. It is estimated that between 54 - 70 million TBI occur worldwide each year [2]–[5]. In the UK specifically, head injuries are the leading cause of death in the under 40-year-olds with around 1.4 million emergency departments episodes every year[6], [7]. If the patient survives the TBI there can be long term socioeconomic costs related to lost economic output and a requirement for care caused by the permanent brain damage. Not everyone who suffers trauma to the head has significant TBI, but both diagnosis and distinguishing TBI severity can be very challenging. The most global common causes of TBI are car accidents, falls and assaults[8]–[12], and the most frequent victims of TBI are infants (0-4 years), young adults (15- 25 years) and the elderly (65+ years)[13], [14]. This is true in both high and low-to-middle income countries, though the exact numbers and cases are uncertain as data concerning TBI in LMICs are scarce, despite it being a prevalent public health issue[12], [15]–[17]. For instance, a Nigerian study, at the Lagos State University Teaching Hospital in Ikeja, found that 23% of TBI patients were referred to non-trauma centres because of a lack of bed space[12]. Hospital bed spaces are scarce in LMICs, but also in high income countries and may be occupied by patients misdiagnosed with TBI or with severity over-diagnosed, both of which could be avoided by improved triage[18]. Triaging can also prevent unnecessary time and costs spent on healthcare services used for scanning and monitoring.

While there are numerous extensive reviews of ocular manifestations of common neurodegenerative (ND) diseases [19]–[25], changes in the visual system after TBI, a common neurological condition with huge and growing socioeconomic implications is significantly less well reviewed[26]–[29]. TBI increases rates of ND disorders[30], [31], as trauma triggers neurodegeneration accompanied by an increase in ND biomarkers, such as amyloid-Beta and tau protein[26], [32], [33]. This review summarises the strengths and weaknesses of current TBI diagnostic approaches and the need for new developments in biochemical diagnostic techniques, which are non-invasive and can be implemented in the acute phase of brain injury. Building on the similarities in function and responses between the central nervous and the visual systems[34], along with the existing evidence of ocular changes associated with neurodegeneration creates a strong foundation for identifying TBI through its retinal and optic nerve (ON) manifestations.

TBI may occur as a result of closed, open or crush head injuries, disturbing brain function. Most commonly, there is no break to the skin and the brain accelerates and/or decelerates within the closed skull, twisting, stretching and damaging the axons and blood vessels. Less often, the brain is exposed by an open injury whilst the skull base and brain stem may be damaged by crush injury[35]. Initial trauma causes a primary injury where the physical impact damages the cranial structures, then pathophysiological consequences of the trauma lead to secondary injuries and neurodegenerative processes[36], [37]. Acute axonal and nerve soma damage will usually cause concussion or coma, with duration depending on injury severity, and loss of function such as limb movement, speech, and executive and emotional impairments related to the injury location[7], [16], [35], [38]. This is not always clearly stratified, as the magnitude of biochemical reactions taking place following the primary injury, both contributing to and worsening the patient's state, is not known and its role in initiating a cycle of neurodegeneration is unclear (**Fig. 1.1**)[39].

The most common brain areas involved in TBI are frontal and temporal lobes[40]. TBI may be categorised as mild, moderate, or severe, although symptom severity does not always coincide with injury severity, making TBI severity difficult to diagnose and manage. Mild TBI (mTBI) develops after stretching of neuronal plasma membranes and has common symptoms of headaches, dizziness, nausea, confusion and disorientation, which can last over hours, days or weeks[11], [41], [42]. More

specific inclusion criteria for mTBI includes loss of consciousness for 30 minutes or less and/or post-traumatic amnesia for less than 24 hours[43].

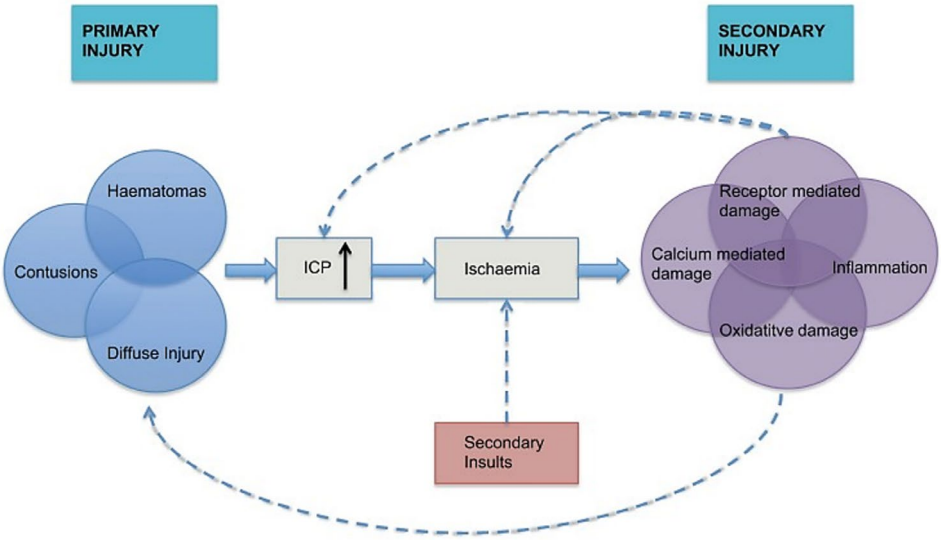

Figure 1.1. Illustration of the inter-relationship between the primary and secondary injuries of TBI. Secondary injuries can contribute to the initial primary ones, creating a cycle causing further damage [39].

Moderate to severe TBI as associated with hematomas (blood leakage) and immediate tissue death, not only losing brain functionality but also releasing toxins[41]. Most of these injuries result in unconsciousness for over 6 hours and long-term effects such as, cognitive and behavioural deficits, often resulting in aggressive behaviour, balance issues, disorientation or memory problems[44], [45]. After TBI, a progressive deterioration of grey and white brain matter can continue for up to a year post-trauma[16]. Sustaining a TBI of any severity can have long-term, detrimental, neurological effects, affecting patient's mobility, cognitive function, social and employable capabilities, economic situation and overall quality of life[7], [16], [46].

TBI has been termed a "silent epidemic", as many incidents go unreported by patients or unrecognised by healthcare professionals[1], [47] thus accurate and reliable reports regarding pathology and costs associated with head injury are limited[48]. Whilst road traffic accidents contribute to 60% of total TBI burden, and make up 2.5% of total deaths worldwide[49], [50]; TBI is also one of the most common injuries sustained by military personnel, with over 400,000 incidents between 2000 and 2018 recorded in the United States (US) Army alone[51]. Most TBI in service personnel are non-battle injuries, sustained during training and motor vehicle accidents[51]. Members of the Armed Forces on deployment are susceptible to enemy action as well as non-battle injury mechanisms and exposure to blast waves[52], [53]. Battle injuries are most commonly blast related TBI and are also frequently sustained by civilians who comprise the most common casualties in modern warfare[53]. TBI is also prevalent in collision sports, American football and football players are at high risk of developing chronic traumatic encephalopathy (CTE) following impact with other players and "heading" balls[54]. In all the aforementioned contexts, TBI sufferers would benefit from PoC diagnostic techniques implemented outside of hospital settings to start the patient journey roadside, pitch-side and in hostile environments.

1.1.1 Current 'State-of-the-Art' Diagnosis of Traumatic Brain Injury

TBI pathophysiology can be split into acute, sub-acute and chronic phases, occurring within 3 – 24 hours, 1 day - 3 weeks and from 3 weeks of the trauma, respectively[36], [55]. Fast, accurate and accessible diagnostics are critical for good TBI patient outcomes as secondary injuries such as

hypoxia and inflammation develop in the acute period (≤ 1hour) after primary injury[56]. These pathologies account for much TBI-related morbidity and mortality (**Fig. 1.2a**)[1], [57], and sorting TBI triage into either mild, moderate or severe categories in the acute phase will ensure the patient receives appropriate initial access to neurosurgical care and later neurorehabilitation[58].

Most established TBI diagnostic techniques can only be implemented in hospital, and a patient would typically undergo multiple examinations before a final diagnosis is made. Out-of-hospital assessment of TBI severity includes the Glasgow Coma Scale (GCS), a neurological scoring system of the patient's conscious state. Whilst neuroimaging is usually only available in a hospital setting, as are surgical interventions such as decompression and insertion of monitoring devices[59]. Many methods take single time-point measurements, such as neuroimaging, which requires intra-hospital transport and is therefore limited in frequency in severe TBI because transporting patients out of ICU increases risk of adverse effects, especially in those requiring continuous sedation in addition to the risks of ionising radiation exposure[60]. Single time-point measurements are unable to capture the dynamically changing state of the patient and can result in misleading diagnoses[61]. An 'ideal' method would monitor continuously or frequently without being laborious or causing harm.

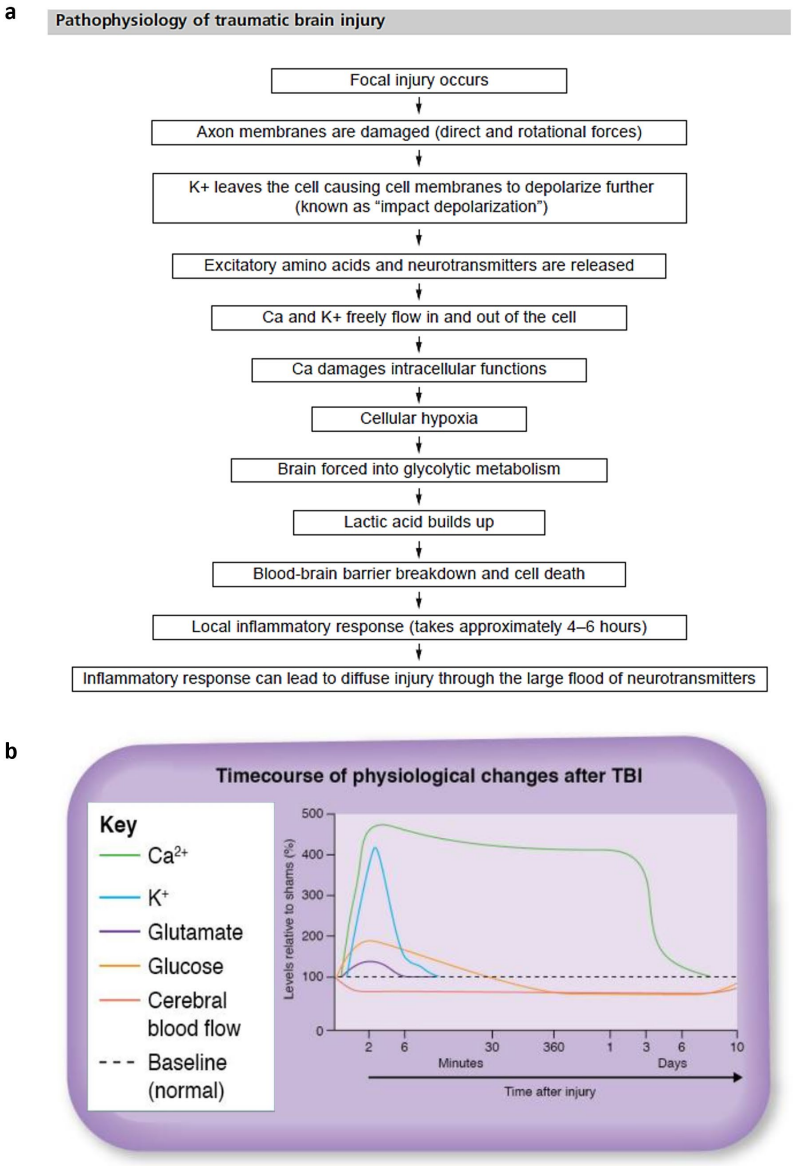

Figure 1.2. ***i*** *Flowchart of the pathophysiological responses to TBI at a cellular level [1]* ***ii*** *Timescale of neurochemical and metabolic changes that take place following moderate to severe TBI [11].*

1.1.1.1 Glasgow Coma Scale

The National Institute for Health and Care Excellence (NICE) highlighted the need for a test to allow paramedics to determine if the patient should be transported from the scene of injury directly to the nearest neurological centre or a hospital with particular resuscitation resources[7]. In current practice, a clinician assesses TBI severity using the GCS, introduced in 1974[62], which evaluates severity and predicts outcome using three main indicators, eye opening, motor response and verbal activity. The visual, verbal and motor responses give an indication as to which regions of the brain are damaged[63]. The GCS was developed as a fast, simple, bedside method to categorise mild to severe TBI by assessing the patient's level of consciousness, with categories being mild (13-15), moderate (9-12) and severe (3-8)[38], [64]. The GCS is widely used in over 80 countries[64], but has a number of limitations. For instance, a study showed that when two physicians independently assessed the same TBI patient using the GCS score within a 5-minute window there was a disagreement in 68% of cases by at least one sub-score[65]. In addition, in the common scenario of TBI sustained under the influence of alcohol or other drugs, intoxication limits the utility of this cognitive assessment especially, during the acute period before the patient is stabilised[38], [66]–[68]. Moreover, the GCS system is not effective for TBI patients who are not capable of completing all three assessment sections[69], which typically occurs in cases of sedation, intubation, intoxication, pre-existing neurological diseases (such as pre-existing dementia[70]), disabilities (such as deafness, blindness, and paralysis), language barriers and infancy[7], [67], [71]. Such incompleteness inevitably skews the final score and predictive value, especially as the GCS relies heavily on the motor response section and makes interventions difficult to implement correctly in short timeframes, which are crucial for survival[66].

Even in the absence of confounding factors, the predictive accuracy of the on-site GCS assessment is lower than GCS on admission to hospital[66], with admission scores, when the patient is more stable, being more accurate predictors of outcome. The acute, pre-hospital, period, however, is a vital time for diagnosis and clinical decisions made here, in the "golden hour", for management and treatment have disproportionate influence on outcomes. Whilst it is the current gold standard, GCS is therefore limited in utility as a predictor of outcome in the pre-hospital space by its subjectivity, low inter-observer agreement and instability-related inaccuracy[72]. However, the GCS is the only non-invasive diagnostic tool that is capable of assessing severity throughout the entire patient journey, and despite negative aspects, the GCS has been shown to correlate with more recent research in TBI diagnostics using biomarkers, neuroimaging and metabolomics[64], and it is commonly used to stratify patients for neuroimaging[73]. The validity of the GCS has been tested during the many years of use against the pathophysiology of TBI, with low scores being associated with lower cerebral metabolic rates, raised intracranial pressure (ICP) and abnormalities detected through neuroimaging[10], [11], [74]. Low GCS scores are also reported alongside increased concentrations of blood biomarkers denoting trauma[64], [75].

1.1.1.2 Neuroimaging and ICP Monitoring

Other current early diagnostic techniques include neuroimaging and ICP monitoring, which are often equivocal on the presence and severity of TBI, particularly in the mild and moderate groups, whilst also being costly, slow, time consuming and requiring highly trained personnel to perform and interpret[1], [76]. Neuroimaging is considered the gold-standard for acute, in-hospital diagnostic techniques and commonplace neuroimaging techniques include computer tomography (CT) imaging or Magnetic Resonance Imaging (MRI)[9]. These are most effective for detecting primary injuries such as skull fracture, contusions, and haemorrhages[71], but cannot identify minor intracranial changes in many mTBI cases[72]. Reliance on in-hospital techniques delays diagnosis and therapeutic intervention, risking the patient's neurological recovery. Whilst CT and MRI scans are

considered fast procedures lasting less than 60 minutes in most cases, transport-time to emergency departments is unpredictable and waiting times for scans may exceed 4 hours[77].

Neuroimaging is not often performed independently as it can provide false-negative results, for example 29% of TBI patients with negative CT scans show positive MRI findings[78], [79], delaying an already lengthy imaging process. Raised ICP is a common TBI indicator triggered by primary injuries such as intracranial haemorrhages and is a cause of morbidity and mortality after TBI[9], [74]. Normal ICP in adults is 10-15 mmHg, whilst TBI patients may experience raised ICP, with prolonged levels above 20 mmHg[1], [80], [81]. Patients with severe TBI require neuroimaging to identify injury and planning therapeutic interventions such as ICP monitor insertion, which is an invasive technique[82]. ICP monitoring is routine after initial CT scanning, and is performed by inserting catheters through a cranial access device, or subarachnoid bolt[1], [39]. ICP monitoring can remain in place throughout hospitalisation for initial diagnosis and monitoring to predict outcomes.

1.1.2 The Unmet Need

Current TBI diagnostic pathways frequently result in over-diagnosis and over-triage of TBI, which creates high healthcare costs from the avoidable tests and treatments[83]. In the longer term, over-diagnosis and over-triage of mild and moderate TBI may lead to unnecessary and ineffective treatment causing avoidable side effects and disability status[84]. There is therefore an urgent and unmet need for PoC TBI diagnostics, allowing for more informed and specialised management closer to the time of injury in a timely and cost-effective manner. Desirable PoC techniques will be non-invasive, avoiding laborious insertion/sample collection and risk of infection commonly associated with ICP monitoring and cerebral spinal fluid (CSF) sampling techniques.

mTBI cases are the most difficult to identify and only 5% of TBI cases in UK emergency departments each year are moderate or severe injuries based on GCS categorisation[7], which highlights the reluctance to rely completely on GCS triage in the pre-hospital space. This creates an immense but avoidable pressure on emergency departments to triage the moderate and severe cases requiring acute treatment from the mTBI ones, to improve neurological outcomes and avoid over-investigation and over-treatment.

TBI severity is often variably defined because of injury heterogeneity. mTBI can accompany one or multiple symptoms of headaches, nausea and disorientation, lasting from days to weeks[41], and is often overlooked in emergency departments, because of a lack of immediately apparent symptoms. Compounding this, over 90% of patients with mTBI are never admitted to hospital[67], [85], despite the significant risk of long-term morbidity and the fact that they encompass 90% of all sustained TBI[1], [36], [56], [86]. Many cases of TBI, particularly mTBI, cause functional and metabolic abnormalities without any detectable structural damage, or damage at a molecular level that is un-detected by neuroimaging[9], [83]. The diagnostic challenges around mTBI, and consequent lack of appropriate engagement with neuro-rehabilitation services leaves many patients with untreated long-term neurological disorders or disabilities[33], [67], [85], [87], [88].

Moderate and severe TBIs, on the other hand, are accompanied by more obvious and immediate symptoms indicating neurological injury. However, in the context of polytrauma and substance abuse, which may also affect conscious level, this does not guarantee correct identification of TBI or categorisation between mild and severe injuries, especially as both severity levels may coincide with initial unconsciousness, eliminating cognitive function assessment. Despite similarities, neurological outcomes after moderate and severe TBI are very different, with in-hospital mortality rates of 10% and 40%[89], [90] respectively. Thus, PoC diagnostics need to be not only early, but capable of obtaining information from unresponsive patients and distinguish between moderate and severe cases to allow for intervention and facilities to be prioritised. Of the 30-40% of patients with severe

TBI who die, approximately 40% do so within 48 hours of the injury[91], [92] whilst survivors experience neurological disfunction[90], thus early triage and management are key to reducing neurological deterioration and saving lives in this cohort and a quick and accurate diagnostic and monitoring tool could greatly contribute to improving outcomes[68], [93].

Variation in presentation generates different drivers for PoC diagnostic techniques. Cognitive techniques fall short for all severities due to mild or delayed effect on mTBI patients, whilst moderate-to-severe patients experience greater time spans of unconsciousness. Mild cases would benefit from techniques that utilise biochemical responses, as structural changes are less common, whilst early structural changes do not effectively differentiate moderate-to-severe cases, and thus sensitive and specific biochemical responses may aid differentiation. Thus, PoC TBI diagnostics would benefit from a sensitive biomarker imaging technique capable of categorising all severity levels. Monitoring the biochemical and metabolic changes over time following initial injury in the acute phase (**Fig. 1.2b**), either individually or simultaneously, is where the potential lies for diagnosing and monitoring the presence and severity of TBI. The limitations of imaging biomarkers in detecting these progressive changes (primary and secondary injuries) both in the acute phase and during follow up limit the ability to intervene to improve outcome. The presentation of acute TBI develops over hours after injury, therefore signs and symptoms may exist at different time-points depending on severity. There is also, therefore, an unmet need for a monitoring tool to detect biochemical deterioration both in the acute phase, throughout treatment and during follow up.

1.2 Ocular Responses to TBI and Neurodegeneration

There is a growing field of research looking at ocular neurodegenerative diseases like age-related macular degeneration and glaucoma[94], as well as how degeneration in the brain can present in the retina and optic nerve[23], [95]–[97]. TBI has been shown to affect the eye[98], [99], either through direct damage to the cranial nerves involved in vision (II) and eye movement, facial muscles and taste (III, IV & VI) (**Fig. 1.3b**), or dysfunction of the control and regulatory centres of the visual function, which was observed even following mTBI cases[29], [100]. Head trauma can often result in neuro-ophthalmic deficits though the symptoms can be masked by other secondary injuries[100]. Visual function may be examined clinically in a number of different ways including visual acuity, colour vision, visual field, pupillary function, eye movements and electro-diagnostic testing[101], [102]. Chen *et* al. and others demonstrated delayed progressive optic neuropathy after TBI[103], [104], suggesting that late secondary injury after TBI causes damage to the visual function. Whilst Faria *et* al. and others explore changes in the optic nerve sheath diameter (ONSD) and pupil diameter as indicators of raised ICP and TBI[82], [105].

1.2.1 The Optic Nerve – “The Window to the Brain”

The eye, and more specifically the retina, is often referred to as ‘the window to the brain’[22], [34], [106]. The visual system is linked to the brain by the ON, which consists of axons whose cell bodies lie in the retina, located in the posterior segment of the eye[34], [107]. The neuroanatomy of the human visual pathway is shown in **Fig. 1.3a**, featuring the retina as well as the ON, optic tract, optic radiation and visual cortex, which are surrounded by CSF[108]. Light enters the eye through the anterior segment and reaches the posterior segment where the retina converts light into electrical signals, which are relayed to the visual cortex through the ON (**Fig. 1.3c**)[34]. The visual pathway is formed of long axons, vulnerable to stress, and the anterior pathway includes 3 main neuronal types: photoreceptors, interneurons, and retinal ganglion cells (RGCs). Thirty percent of cerebral cortical neurons are devoted to the visual pathways and visual processing and share multiple functional components with the rest of the central nervous system (CNS)[109], [110], and thus CNS pathologies are often associated with retinal abnormalities[19]. This has facilitated research surrounding neurodegenerative (ND) disorders and diseases to characterise associated changes in the

morphology, movement and chemistry of the eye and visual tract[111]–[113]. This “window” to neurodegeneration in the brain, provides an opportunity for monitoring, triaging scans and diagnoses even before the first symptoms of ND disorders become detectable[19], [114]. The success in this field suggests the potential for the characterisation of other neurological conditions such as TBI, which has a complexity and heterogeneity that makes it difficult for emergency healthcare workers and clinicians to accurately diagnose in a timely manner and thus allocate the correct tailored treatment.

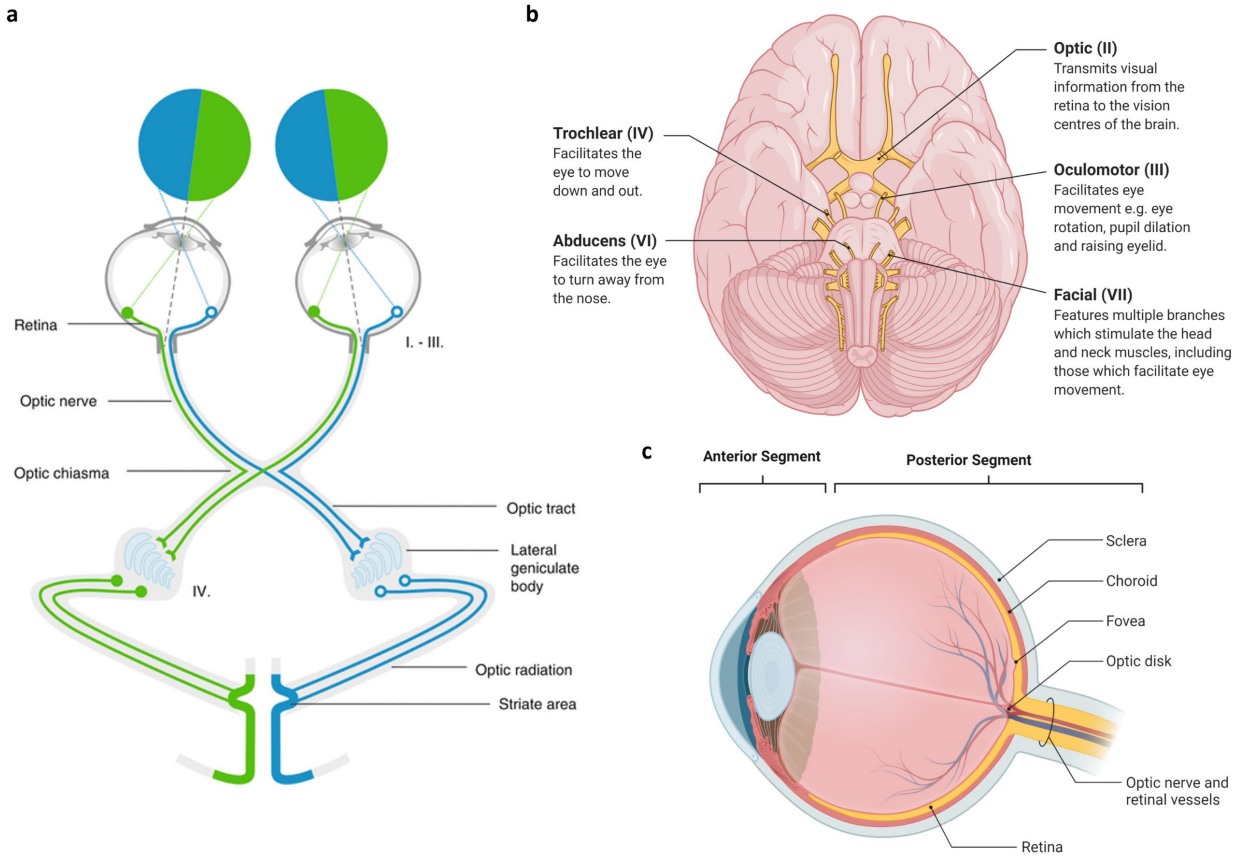

Figure 1.3. The neuroanatomy of the human visual tract ***a*** *Photoreceptors in retina transform incident light into changes in membrane potential. This signal is received by bipolar cells and transmitted to retinal ganglion cells whose axons travel to the lateral geniculate body (LGN) in the optic nerve (surrounded with CSF), the optic chiasma and the optic tract. In the lateral geniculate body, part of the midbrain, RGC axons synapse with cells of the optic radiation that travel to the striate cortex (primary visual cortex) [108].* ***b*** *Cranial nerves II-VII located within the skull base, responsible for vision and eye and facial movement.* ***c*** *The posterior segment of the human eye including the choroid with a dense vascular network to supply the outer retina, and the fovea in the centre of the macula containing only cone receptors to allow for sharp images in photopic conditions. This figure was created using Biorender.com.*

1.2.2 Visual Impairment

Many of the areas of the brain most vulnerable to mTBI are related to vision[52], including the long axonal fibres connecting the retina to the lateral geniculate nucleus (LGN) and the LGN to the visual cortex, that get distorted by trauma causing diffuse axonal injury (DAI)[42]. There is a further potential for TBI indicators to be found in the retina, which is as an extension of brain tissue with biochemical changes in the retina occurring after various neuronal disturbances[115], and there is potential for ocular manifestations of TBI to be detected by ophthalmic imaging techniques[27], despite the lack of prospective data[116], for example, oculomotor deficits may be, demonstrated by eye tracking in paediatric patients[104], [117]. Fifty four percent of blast induced TBI patients had global visual field loss and visual field dysfunctions were present in all TBI severities[118]. TBI patients described symptoms of photosensitivity, blurred and double vision, decreased visual acuity and visual field

defects and patients with depressed visual field sensitivity reported subjectively lower visual quality[118], [119]. In 500 service members with mTBI there was no difference between the visual dysfunctions and symptoms whether sustained through blast or non-blast mechanisms[52].

1.2.3 Axonal Damage, Blood Brain Barrier Damage, Cerebrospinal Fluid Leaks

After TBI, axonal damage in both the ON and retina is indicated by ON oedema caused by stretching and oxidative stress[120], [121]. Axonal damage is detectable in the ON as early as 1-3 hours following trauma, a possible acute TBI marker, and is present as late as 12 weeks post-injury[120], [121]. Myelin injury in the subacute and chronic phase is evidenced by demyelination of the ON detectable up to 13 weeks after mild, repetitive TBI[119], [122], and in the optic tracts within 7 days, although not in the acute phase [123]. A modified impact acceleration (IA) rat model was utilised to demonstrate blood brain barrier (BBB) damage and axonal swelling an ON segments[124]. BBB damage allows CSF proteins to act as TBI biomarkers in the blood stream and also affects ON tract, worsening axonal injuries developed in the ON after mTBI[125].

The CSF is present in the subarachnoid space surrounding the ON and involved in the ocular glymphatic system[108], [126], [127], and may communicate with the eye[128], [129]. Glymphatic dysfunction, characterised by the failure to clear interstitial waste and distribute non-waste compounds in the brain, is linked to neurological pathologies including TBI, mTBI in particular[126], [127], [130], [131]. Interestingly, Plog *et* al. demonstrated in a murine model that TBI biomarkers may be transported from the brain to blood *via* the CSF in the glymphatic system[132]. Christensen *et* al. explored mTBI in rats, observing an increase in glymphatic influx and decrease in glymphatic efflux, resulting in CSF being inadequately cleared, contributing to cerebral edema associated with TBI[126].

There has also been a recent increase in research surrounding Spaceflight-Associated Neuro-ocular Syndrome (SANS), which is a series of ophthalmologic and neurologic findings in astronauts following spaceflight. SANS encompasses ON head swelling, globe flattening, choroidal/retina folds and increased CSF volume in ON sheaths[133], [134]. SANS is believed to be caused by elevated ICP and CSF compartmentalisation to the globe or ON[133]–[135], which has been described earlier as a common secondary injury of TBI, thus suggesting similar CSF pathology following brain trauma. SANS has been measured using optical coherence tomography (OCT), MRI, fundus imaging and ultrasound[134], [135].

Killer *et* al. analysed the potential compartmentalisation of the CSF after ON disorders and found that CSF is biochemically continuous up until the ON, but CSF obtained from the subarachnoid space of the ON differed from that surrounding the brain, with both fluids containing different biomarker concentrations[136]. Unfortunately, there is a high chance of contamination in the CSF, adding complications if measuring the chemical response to TBI. Though, CSF leaks are a common complication following all TBI severities, thus the presence alone could be utilised as a TBI indicator[137], [138], Apkarian *et* al. were able to detect beta-2-transferrin in the subconjunctival fluid with a 25-gauge needle, a marker of CSF leaks[139].

1.2.4 Cell Loss

RGC loss occurs alongside ON degeneration as early as seven days after mTBI and persist at 6 months post-injury, detectable using OCT both in human and animal studies[124], with the extent of RGC loss being proportional to the TBI severity in animal models, showing the potential of OCT as a structural diagnostic approach[119]. Axonal injury within the ON may or may not drive RGC loss, which may also be affected by cerebral primary and secondary injury[140].

Many systemic and cerebral neurodegenerative (ND) diseases manifest in the eye including Alzheimer's disease (AD), a form of dementia most commonly associated with memory disturbance,

motor neuron disease (leading to muscle weakness), Parkinson's disease (PD), another form of dementia presenting as a movement disorder and Multiple Sclerosis (MS), a CNS disorder that causes vision, motor and sensory difficulties[19], [34], [112]. Structural and physical ocular changes may be measured in the "early" phases of neurodegeneration[141]–[143]. For instance, Cheung *et* al. linked clinical retinal diseases with dementia, including macular degeneration, glaucoma, and diabetic retinopathy, which develop from biochemical pathologies that could be identified even before cognitive decline and changes in vision become apparent[20], [107], [109].

Eye movement and afferent visual abnormalities are amongst the earliest clinical manifestations of ND diseases, including PD[34], [141], [144], AD[23], [110], [111], MS[112], [145] and TBI[117], [146]. Eye-tracking techniques are typically used to identify oculomotor impairments[144] [147], with strong evidence that eye movement disorders associated with the neurodegeneration could provide diagnostic information or disease progression evaluation in PD and MS[112], [148]. In addition, eyelid function is also abnormal in some ND disorders, being present in patients with neurodegeneration such as PD, Huntington's Disease, Progressive Supranuclear Palsy and Chronic Progressive External Opthalmopledia identifying disturbances to blinking rates, eyelid retraction and ptosis *(*droopy eyelid)[141].

1.2.5 Change in Retinal and Blood Vessel Morphology

The relationship of changes in ocular structures, such as the retina, ON, choroid, pupil, and lens as well as tears, with neurodegenerative diseases has been extensively reviewed elsewhere[19], [20], [22], [23], [145]. TBI, AD, MS, cerebrovascular disease, and PD patients suffer retinal nerve fibre layer (RNFL) and ganglion cell layer thinning (indicating RGC loss), reduced retinal vasculature, and increased neuronal plaques in the visual pathways[19], [22], [86], [109], [111], [149]. Such changes are typically monitored through OCT, an *in-vivo* ocular imaging technique that utilises laser interferometry[34], [109], [111], [145], [149].

The retina provides a convenient window to assess neuronal and vascular changes in the CNS[20], [23], [107], [109], [114], [149]. Frost *et* al. suggested that retinal amyloid-Beta tests can differentiate between the presence of AD with 100% sensitivity[113], and this association between ND diseases and early biomarkers including the amyloid-Beta, tau proteins and inflammation has been further echoed in more recent reviews[20], [21], [23], [24], [110]. Further cellular changes investigated alongside the ND disorders have been the microglia activation leading to neuroinflammation, which translates into retinal inflammation[107], [114].

The retina and ON (**Fig. 1.3**) can undergo structural changes, unrelated to mechanical shear[150], but correlated with the loss of post-synaptic neurones having detrimental effect on RGC, a process termed trans-synaptic degeneration and resulting in retinal thinning[116], [151]. CT scans and ultrasound have identified ON sheath distention in all TBI severities, related to elevated ICP[152]–[154], which may also be associated with papilloedema (swelling of the optic disc). Even athletes who partake in high-impact sports with no history of even mTBI, show signs of ON damage[155], suggesting that it would be difficult to standardise TBI diagnostics without symptoms to warrant scans. Multiple studies demonstrated either the RNFL thinning or thickening using OCT after TBI[104], [121], [156], with **Fig. 1.4** illustrating significant loss in the peripapillary RNFL thickness[121], as well as reduced sub-foveal choroidal thinning after mTBI, which also associates with disease severity in other ND disorders[111], [156]. However, these structures are also known to be affected by age and therefore age-adjusted normative databases are required. Retinal photography has also detected changes in the morphology of retinal vessels and fractal analysis (markers of cerebral vascular changes post mTBI), with increased arterial and venous tortuosity in the acute period and increases retinal venular calibre[115], [157].

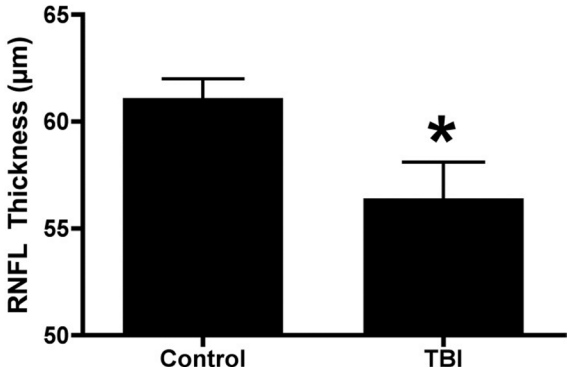

Figure 1.4. OCT measurements of control and indirect, blast mediated TBI, murine eye samples, illustrating significant loss in the peripapillary RNFL thickness [121].

1.2.6 Inflammation - Histology, Computerized Tomography and Magnetic Resonance Imaging

An inflammatory response within the brain can affect the retina *via* the ON[107]. After TBI, microglial activation (indicator of neuron damage and poor CNS health[158]) in both the optic tract and the retina, indicated inflammation, within the subacute period (2-7 day) after TBI and inflammation is detectable up to 2 weeks following trauma[102], [124], [159]. In a histological study of murine eyes and brain subjected to TBI and ocular blast injury, neuron loss biomarkers were not identified, and neuroimaging (CT and MRI) was normal, despite inflammation being present after both eye and brain injury[123], [159]. Thus, neuroinflammation of the retina and ON may evolve as a diagnostic measure of the pathological changes in the brain following TBI as the states of the two are closely related. Whilst most studies focus on structural changes, biochemical responses will develop much more rapidly than structural changes and may be detectable much earlier in the ND disorder pathogenesis[106], suggesting that TBI indicative early-stage biochemical biomarkers being detected, identified and characterised in the ocular tract.

1.3 Biochemical Responses to TBI

Identifying chemical responses to TBI and correlation with injury severity would enable a better mechanistic understanding, development of new diagnostic modalities and opportunities for more effective therapies. Recent publications investigate chemical responses to TBI for early and accurate diagnostics[36], [61], [160], [161], and the capability to detect changes as early as an hour after trauma[162]–[165], in biofluids such as blood, CSF, urine and saliva[166]–[170], using molecular sensing techniques[171]. Changes present in biofluids can be termed as biomarkers and concentrations correspond to changes in metabolism, vascular function, inflammation, extracellular matrix status and damage to axons, neurons and glial cells after injury[76], [172]. TBI is heterogeneous without symptoms that define injury severity levels, however, even mTBI can produce short periods of neurological dysfunction[166], which can be detected using biochemical measurement techniques. Since mTBI is the most frequent injury severity sustained[56], [86], reliable biomarkers at early stages post-trauma are essential, and increasing evidence indicates that the biochemical biomarkers may be both sensitive and correlate well with injury severity[70].

NICE guidelines recommend focussing research on biomarkers for diagnosing, monitoring progression and stratifying patients with TBI for therapies[7]. Acute, mild to moderate TBI biomarkers in blood have been validated with high specificity to negative neuroimaging with the potential to eliminate 39% of unnecessary scans[78], [173], potentially saving 39-71 Euros per patient[77]. Biomarker-based triaging could focus subsequent hospital-based neuroimaging on those patients at greatest need, avoiding unnecessary radiation exposure and facilitating significant savings to the healthcare providers[78], [174], [175]. Implementing accurate diagnoses through TBI biomarkers in

the acute phase and, especially, at the PoC could allow better, faster, and more efficient management through more accurate and appropriate triage, decision-making, and management[167], [176].

1.3.1 Biomarkers for TBI Diagnostics

Many ND diseases and disorders are being detected through biomarker detection[177], [178] [179], and, more specifically, increasing TBI biomarkers are assayed in accessible biofluids [36], [61], [76], [160], [166], [168], [175], [180], Edalatfar *et* al. systematically retrieved 540 TBI-relevant biochemical markers from blood, CSF, saliva and urine, extracting time of detection and types of measurement methods[175]. Pineda *et* al., stated that 'good' biomarkers should be in easily accessible biofluids, with low background levels in healthy control groups, have high sensitivity and specificity to all injury severities and be released in a "time-locked sequence" after the injury[36], [181], [182]. In addition, the response time, clearance, and half-life of a biomarker must be considered, all of which give indication of the timeframe during which it can be detected post injury and the expected final baseline concentration in bodily fluids[168]. The most commonly used biofluids for TBI biomarker detection are blood and CSF, which contain molecular patterns representative of the CNS[183]. Blood samples are most accessible in the acute, PoC settings although CSF samples may better model the brain's response to TBI being on the brain side of the BBB[183], however this becomes permeable almost immediately after even very mild trauma[125]. Nevertheless, biomarker concentrations in CSF show significant interpatient variability[184], making diagnostic procedures difficult to standardise.

Although well recognised and validated, acute TBI biomarkers may overlap with other disease and injury processes, such as extracranial plasma or serum, proteins released from damaged cells, polytraumatic organ and muscle injury[61], [185], lung tumours[186], and subclinical ND conditions[70], [100]. Despite this, in 2007 the Scandinavian healthcare system introduced S100B as the first brain biomarker to be used within clinical practice guidelines to predict negative CT scans, aiming to reduce the number of unnecessary scans on patients without significant TBI[77], [187].

Recognised biomarkers measured in the acute phase after TBI include, S100B, glial fibrillary acidic protein (GFAP), neuron-specific enolase (NSE), Ubiquitin C-terminal hydrolase-L1 (UCHL1), total tau (t-tau) protein and αII-spectrin breakdown products[36], [166], which align with standard TBI diagnostics, for example measuring raised concentrations of GFAP, S100B, UCHL1 NSE and t-tau in blood when abnormalities are present in CT scans[167], [188]. **Fig. 1.5** summarises the biomarkers identified with TBI progression, categorising them into acute, subacute and chronic phases after TBI[36]. **Table 1.1** outlines these biomarkers along with some of which are emerging in the field of TBI, categorising the associated location, biofluid, sensitivity, specificity and injury severity for each.

The most widely investigated acute biomarkers include S100B, a calcium-binding protein expressed in glial cells of the CNS regulating calcium level, and GFAP, a structural, filament protein of astrocytes located in the CNS CSF, associated with astrocyte and BBB injury[56], [166], [168], [175], [177], [182], [184], [189], [190]. Acute phase S100B is a powerful TBI biomarker because its concentrations are elevated in CSF and serum, by astroglial injury[166], and align with CT abnormalities[36], [174], [191], [192], as well as raised ICP and poor outcomes[189], [193], [194]. As S100B is widely researched and documented, the healthy baseline concentration in adult serum is stated and agreed to be approximately 0.11 ug/L[171], [192], [195]. However, the literature surrounding other sample types and TBI severity are varied. Studies tends to focus on elevations and subsequent fluctuations in biomarker concentrations following injury, making each one context specific. Even in the case of three studies, all measuring S100B serum concentrations after mTBI within the acute phase using immunoassays; all conclude mild levels to be 0.31 ug/L, 0.043 ug/L and 0.39 pg/mL [79], [192]. These discrepancies are worsened by different sample types, timeframes, storage methods, patient age and measurement techniques, and in-depth discussions surrounding each TBI biomarker behaviour post-injury are beyond the scope of this review article. These inconsistencies have led to confusion

in characterising the biochemical response, which is detrimental to refinement of new techniques. This highlights the value of a technique that utilises repeated, time-sensitive measurements or of biomarker panels that allow concentrations to be assayed as ratios to one another.

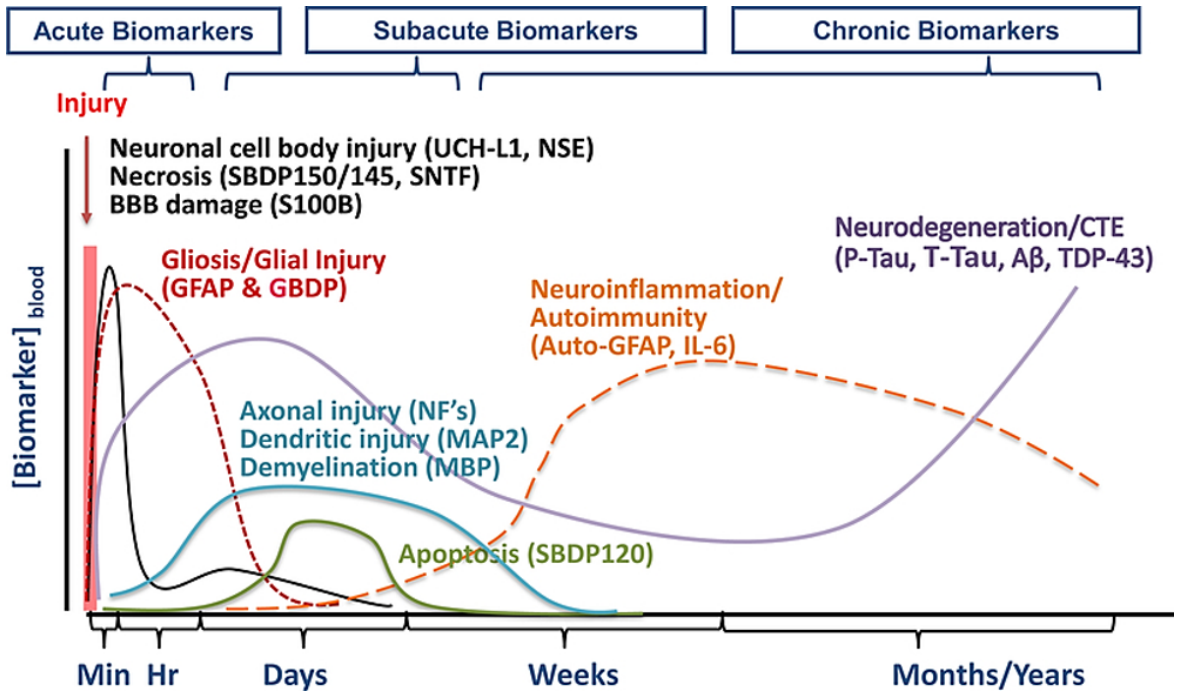

Figure 1.5. Illustration of the concentrations of validated TBI biomarkers in the acute, subacute, and chronic phases following after the primary injury. Early, on-site diagnostics would be completed within minutes to hours following injury and thus, necessitates the need to be sensitive to acute-phase indicative biomarkers [36].

Table 1.1. Outline of the recognised and emerging biomarkers of TBI with their respective locations, sensitivities, specificities and associated injury severities. GFAP = Glial Fibrillary Acidic Protein; UCHL1 = Ubiquitin C-Terminal Hydrolase L1; NSE = Neuron-Specific Enolase; t-tau = Total tau; NAA = N-acetyl-aspartate; GSH = Glutathione; RNA = Ribonucleic Acid. Sensitivity/Specificity: High = ≥85%, Moderate = 50-84%, Low = <50%.

Biomarker	Origin	Biofluid	Timeframe	Sensitivity	Specificity	Severity	Refs
S100B	Calcium-binding protein expressed in glial cells	Blood, CSF	Acute	High	Low	Moderate, Severe	[56], [70], [166], [168], [175], [182], [184], [189], [190], [194], [196]
GFAP	Structural filament protein of astrocytes	Blood, CSF	Acute	High	High	All	[36], [56], [70], [162], [166], [168], [175], [182], [184], [189], [190], [196]–[198]
UCHL1	Cytoplasmic enzyme expressed in neurons	Blood, CSF	Acute	High – less sensitive to mTBI	Moderate – not CNS specific	All	[36], [56], [61], [70], [166], [173], [180], [196], [199]–[203]
NSE	Glycolytic enzyme expressed in red blood cells	Blood, CSF	Acute	Moderate – limited evidence for mTBI	High – to the brain	All	[36], [56], [162], [166], [180], [196], [204], [205]
αII-spectrin	Cytoskeleton protein found in axons and presynaptic terminals	CSF	Acute - Chronic	Moderate – limited evidence for mTBI	Low	All	[36], [166], [181], [206]–[208]
t-tau	Microtubule-associated protein expressed in	CSF	Acute - Chronic	High	High	All	[70], [78], [166], [167], [197], [209]–[211]

	neurons and astrocytes						
NAA	Amino acid derivative located in neurons	Blood, CSF	Acute	High	Moderate	All	[45], [212]–[218]
GSH	Non-enzymatic antioxidant present in cells	Blood, CSF	Acute	High	Moderate	All	[219]–[223]
MicroRNA	Small molecules regulating gene expression	Blood, CSF	Acute - Subacute	High	High	All	[176], [182], [224]–[231]

GFAP is brain-specific and raised concentrations in the CSF[36], [162], [166], [197], appear as early as 1-hour post-injury[162]. GFAP is the most discriminatory acute, TBI biomarker for predicting CT abnormalities[167], [174], [191], and is also associated with inflammation[232], and patients who have sustained blast related TBI[233], having been cleared by the US Food and Drug Administration (FDA) to predict the need for CT scans within 12 hours of mTBI[191]. In mild to moderate TBI cases, elevated GFAP serum levels have been detected within 1 hour of injury, peaking at 20 hours and declining to regular levels by 72 hours[234], [235].

Biomarkers associated with neuronal damage include NSE, a glycolytic enzyme and UCHL1, a protease expressed in red blood cells (RBCs) and CSF, respectively[36], [56], [166]. NSE is correlated to posttraumatic inflammation[180], and raised NSE levels, within 4 hours of moderate-severe TBI may identify patients at higher risk of cognitive dysfunction[205]. The detectability of NSE in RBC makes it readily accessible but introduces a risk of cross-contamination in blood samples in the event of haemolysis (RBC rupture), rendering it less specific[236].

UCHL1 is a cytoplasmic enzyme found in a high abundance in neurons[61], [163], [165]. Studies have identified elevated levels in plasma after mild to moderate injuries (**Fig. 1.6a**), as early as 1-hour post-injury, associated with axonal damage and DAI[163], [165]. UCHL1 is sensitive to patients with positive CT scans and unfavourable outcomes[173], [180], [199], but has low specificity, in the CSF, blood, peripheral nervous system, limiting its utility[61], [203].

αII-spectrin is a cytoskeleton protein in axons and presynaptic terminals[208]. Calcium activated products formed during *αII*-spectrin protein degradation in response to necrosis (uncontrolled cell death) are a potential TBI biomarker for secondary injuries such as, ischaemia[36], [166], [168]. *t-tau* protein is a microtubule-associated protein expressed in neurons and astrocytes[166], and associated with ND disorders including AD[237]. *t-tau* levels are elevated at various injury severities[167], [197], and in association with DAI[78], [211], as early as 1 hour after TBI and correlated with positive findings on CT[180], [210], as well as self-reported symptoms after mild TBI[61]. MicroRNAs are small molecules that contribute to gene expression regulation, blood, CSF and brain tissue levels [176], [182], [224], [225], [227]–[229]. It has been demonstrated that microRNA expression is altered across all TBI severities over time periods ranging from 1 hour to several days post-trauma[176], [230], [231].

Plasma S100B and GFAP have been shown to remain elevated throughout the entire 24-hour period after TBI and were consistently more elevated in TBI patients with unfavourable outcomes (**Fig. 1.6c**)[193]. Both astroglial injury biomarkers combined have the potential to be used as a duo-marker panel for reliable and sensitive TBI diagnostics and outcome predictions, or with other multiple biomarkers such as UCHL1 and GFAP to give high diagnostic accuracy[201], [238], [239]. Nevertheless, using biomarkers in tandem does not always outperform S100B or GFAP alone[167], [193]. On the other hand, UCHL1 may be the dominant blood biomarker, with little additive effect of combining with GFAP and S100B[173]. Ongoing studies towards the clinical application of these biomarkers for TBI diagnostics[240], combined with the advancements in biomarker sensing

techniques and increasing data on the biofluid markers correlating with underpinning pathologies, suggest a great promise for future TBI diagnostics.

1.3.2 Emerging TBI Biomarkers

N-Acetyl-Aspartate (NAA) is a highly abundant amino acid derivative in adult brain neurons[212], [241], produced by neuronal mitochondria and thus, levels reflect mitochondrial oxidative metabolic status and stress[213], [214], [242], and is therefore a biomarker of neuronal and axonal function and loss[45], [214]–[217]. DAI, direct injury and ischemia are a frequent cause of neuronal injury[45]. Shannon *et* al. utilised microdialysis to establish elevated extracellular NAA levels after TBI due to an efflux of NAA due to adverse brain chemistry which then decreases in the 50-96 hour period post-injury[212]. This fluctuation in eNAA levels over the subacute time-course of a TBI was explored by Belli *et* al., and illustrated in **Fig. 1.6b**, reporting low-levels in severe survivors followed by a large peak, whereas non-survivors expressed irregular levels throughout[214]. Fu *et* al. demonstrated decreased NAA concentration in normal-appearing white matter after axonal damage, linking NAA levels with mitochondrial dysfunction and acute inflammatory lesions[242], [243]. Malisza *et* al. found that in ischaemic rat brains, there was a continuous decrease in NAA levels in animals with tissue death[244], replicated in other TBI studies[212], [215], [245], with brief elevation after insertion of a cerebral catheter for microdialysis and polyethylene catheters for blood sampling and pressure monitoring[212], [241], [246]. NAA is also detectable at PoC using a non-labelled lab-on-chip device and Raman spectroscopy to measure an immediate NAA spike in severe TBI patient blood samples up to five control group levels, decreasing over 24 hrs post-injury[213].

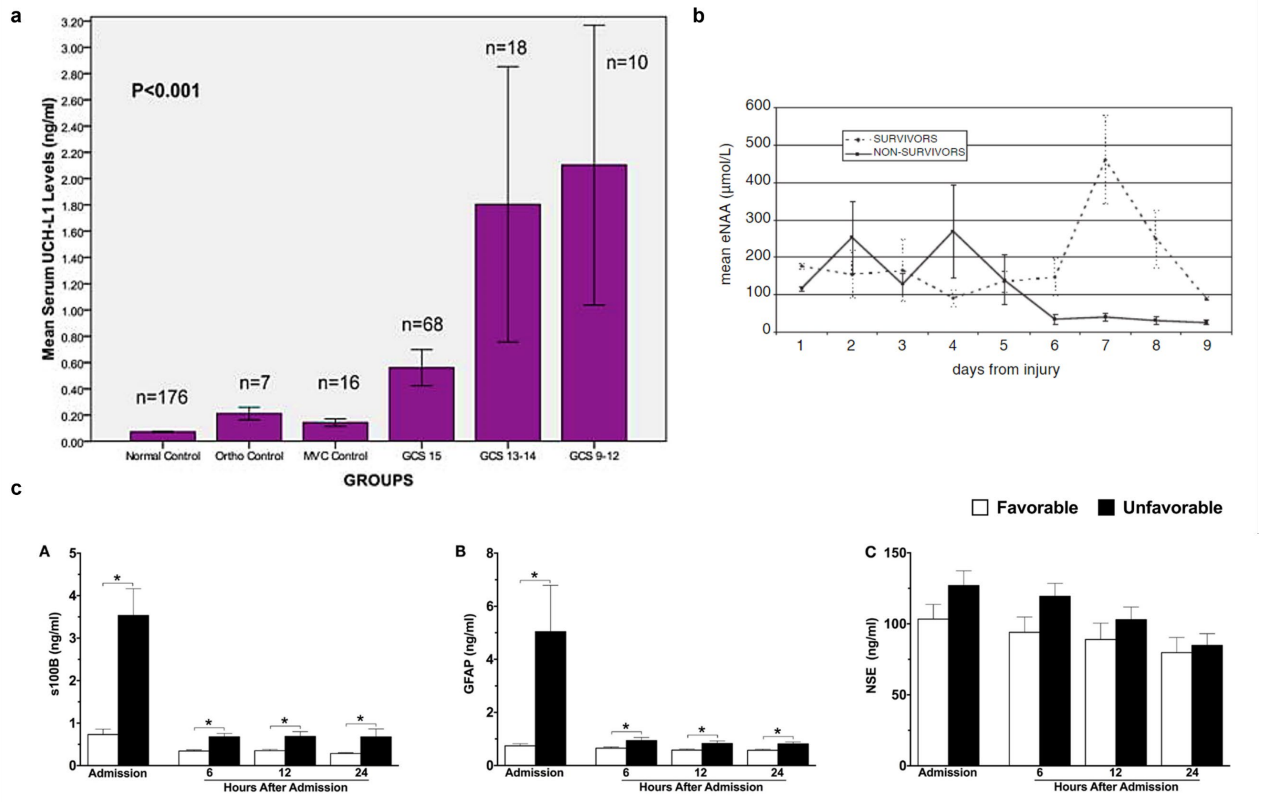

Figure 1.6. Examples from literature of TBI biomarker (UCHL1, NAA, S100B, GFAP and NSE) levels changing following trauma. ***a*** *Mean UCHL1 levels in uninjured and in TBI patient groups, illustrating increased levels after trauma, with measurements taken from serum 4h post trauma. Analysed using an enzyme-linked immunosorbent assay (ELISA) kits[163].* ***b*** *Time-course of eNAA using microdialysis in severe TBI survivors and non-survivors, demonstrating irregular levels in non-survivors and low levels followed by a large spike in survivors [214].* ***c*** *Plasma concentrations of S100B, GFAP & NSE of moderate-severe TBI patients within the first 24 hours of hospital admission [193].*

The BBB is compromised in the acute phase after head injury with increased glutathione (GSH) levels[219]. GSH is a non-enzymatic antioxidant present in cells, that has a role in protecting cell membranes from oxidative damage and maintaining the integrity and function of the BBB[207], [220]–[222]. Low GSH suggests oxidative damage and can initiate oxidative stress-mediated neuronal loss, and associates with neurological disorders including AD, PD, MS and TBI[222], [247], outlining GSH as a potential acute TBI biomarker, although variable GSH levels in healthy control groups and potential of artifacts in detection may limit utility[223].

1.3.3 Potential Eye-Based TBI Biomarkers

Levels of GFAP and UCHL1 increased in plasma after direct trauma in a porcine ON crush model[248]. **Table 1.2** summarises ocular changes associated with TBI and the pathologies that alter indicative biomarkers that may be present in ocular structures, blood, or CSF after trauma.

t-tau and NAA are potential candidates, since *t-tau* has been identified in the retina in AD[20], [21], [23], [24], [110], and NAA is sensitive to ocular pathologies after TBI such as neuronal and axonal damage[215], [216]. *t-tau,* NAA, *αII*-spectrin, GSH and NSE are all expressed in or associated with neurons and axons[78], [166], [208], [247], and their release after TBI therefore suggests neuronal and axonal damage[122], [214], such as retinal ganglion loss and RNFL thinning[120], [124], [156]. NAA, NSE and GFAP are also associated with inflammation[180], [232], [242], which is also an ocular response to TBI, particularly within the ON[102], [124], [159].

Disproving CSF compartmentalisation would suggest the possibility of biomarker detection in the CSF such as, the GFAP[36], [166], [197], UCHL1[36], [56], S100B[56], [190], αII-spectrin[181], and MicroRNAs[182], in the retrolaminar CSF (behind the ON head) and potentially in the eye. This is particularly applicable to the detection of GFAP, since it is a marker of BBB dysfunction[36], [166], [197], which facilitates the CSF leakage[125].

Table 1.2. Potential biochemical eye-based TBI biomarkers and their associated ocular manifestations. The strongest biomarker candidates have been included because of their specificity and sensitivity to TBI severity.

Ocular Manifestations of TBI	**Strongest Biomarker Candidates**	**Refs**	**Associated Biomarkers**	**Refs**
Neuronal and Axonal Damage	t-tau, NAA	[42], [78], [120], [122], [166], [214]	αII-spectrin, GSH, NSE, UCHL1	[36], [42], [56], [61], [120], [122], [164], [208], [247]
Retinal Ganglion Loss and RNFL thinning	t-tau	[124], [249]–[251]	NSE, GSH, NAA	[124], [252]
Neuroinflammation	NAA, S100B	[102], [242], [253]–[255]	NSE, GFAP	[180], [232]
Chemical Response in CSF	t-tau, GFAP, NSE	[36], [166], [190], [197], [249]	UCHL1, S100B, αII-spectrin, microRNAs	[36], [56], [181], [182], [190]

1.4. Biomarker Detection Techniques

Developments in correlating TBI biomarker levels with trauma severities would constitute a major step towards more accurate identification and understanding of head injuries, particularly mild TBI or concussion[181]. This would also enable a better grasp of the underlying molecular mechanisms and signalling pathways, facilitating improvement in management, recovery and potential drug treatments[181], [256]. Biomarker detection methods discussed below have the potential to be

implemented for continuous monitoring throughout the various stages of TBI, unlike the aforementioned common TBI diagnostic methods, many of which are invasive, time-consuming, expensive, or potentially harmful due to the ionising radiation or risk of infection. Though biomarker readings can be seen as single time-point measurements, work is ongoing to develop kinetic models of TBI biomarkers to predict the concentration trajectory up to 12 hours following injury[171].

These molecular sensing techniques all exhibit attributes as potential routes for biomarker detection and TBI diagnostics however currently, no single method has the capacity to measure *in-vivo* biofluids rapidly, effectively, and non-invasively. Urine is a potential *ex-vivo* biofluid for detection of brain biomarkers [169], however, it has low specificity, varying sample volumes and indirect route for sampling, making it often highly diluted once released from the kidney and requiring patient's cooperation[162]. Saliva has also been investigated as a potential biofluid for TBI biomarkers[166], [170], and whilst it is easy to collect non-invasively, only S100B and UCHL1 have been so far successfully measured from it [160], with the analysis typically including an additional step of exosomes isolation thus, introducing additional challenges for real-time measurements and diagnostics [257]. Biomarker sensing techniques which require *ex-vivo* sampling incorporate additional risk of samples being affected by preparation and preservation methods as was illustrated by Abdelhak *et* al. who has freeze- thawed CSF samples over 5 cycles showing a 50% decrease of the GFAP within those[258].

Habli *et* al. summarised all commercially available PoC TBI devices and their respective FDA clearance statuses, listing eight systems, half of which are based on biomarker evaluation and only two have FDA clearance[68]. The FDA approved the Banyan Trauma Indicator (BTI), a novel biomarker screen to aid triaging of mild to moderate TBI patients before undergoing CT scans, with the intent of reducing costs and exposure to radiation, along with increasing availability to other patients. The BTI measures the UCHL1 and GFAP levels in blood samples, indicating the presence of intracranial lesions in the form of positive or negative assay results[259], [260]. A study was carried out to determine the cost-effectiveness of this product, concluding that for moderate injuries, the test would need to considerably cheaper[259], [261]. The test utilises limited biomarkers that have been detected within 12 hours of brain trauma and reportedly it takes 3-4 hours for results to become available[259], [261].

In clinical settings, optical techniques are favoured for being highly sensitive, non-destructive and rapid. Optical brain imaging methods capable of identifying microscopic structure and function have been continuously developed over the past 40 years since Jöbsis first measured brain blood and tissue oxygenation using near-infrared light[262], [263]. We summarise some of these techniques below as they show potential for translation to the ocular system, and **Fig. 1.7** overviews how some of these techniques have been used in literature to detect or monitor TBI biomarkers to date[264].

1.4.1 Mass Spectrometry

Mass spectrometry measures the mass-to-charge ratio of gas-phase ions, which involves ionising the sample to break down molecules into fragments of separate masses and analyse them[183], [265]. However, this method typically requires samples to be analysed under a vacuum and to be ionised, limiting its use in continuous, *in-vivo* measurements due to difficulties in maintaining physiological states of biological samples[265]; as continuous measurements are necessary for determining TBI severity, this limits the potential of mass spectrometry as a TBI monitoring technique.

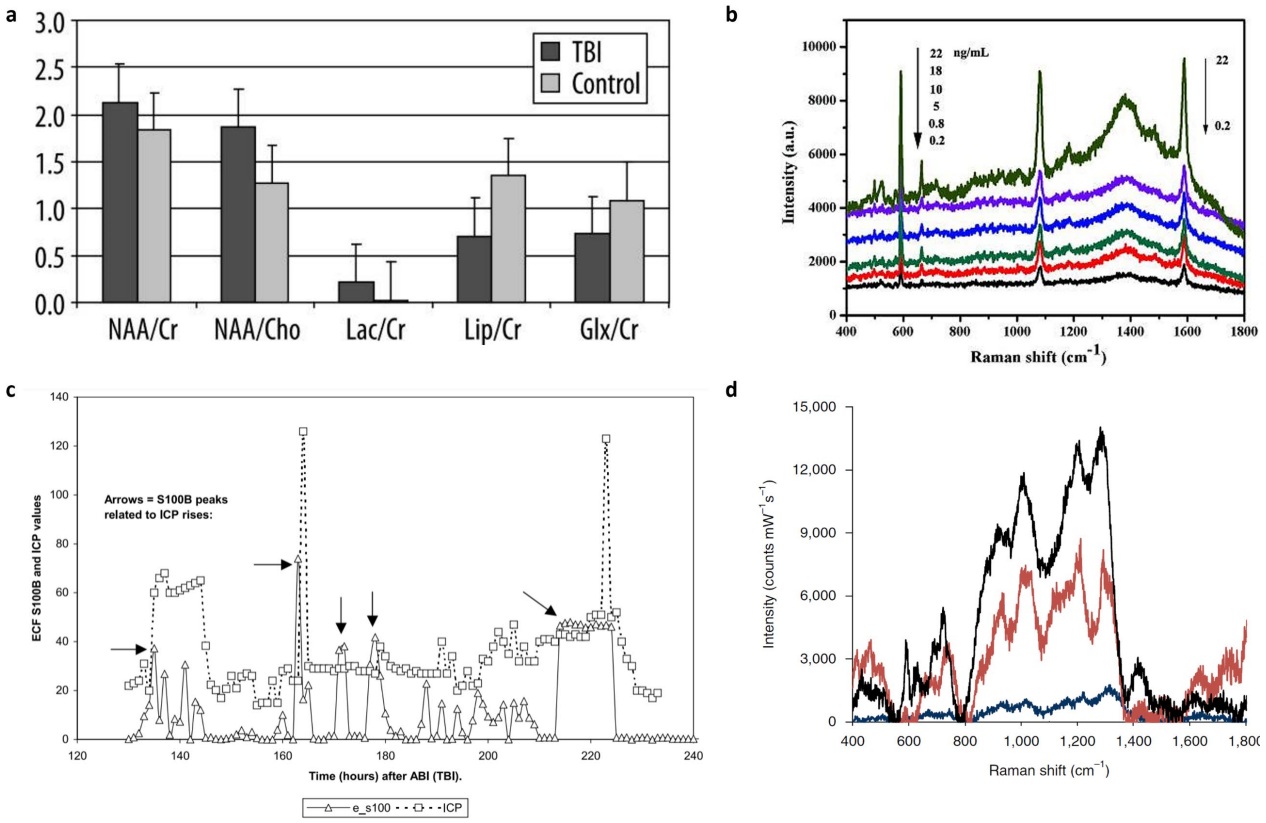

Figure 1.7. Examples of chemical sensing techniques utilised to measure TBI biomarkers ***a*** *NAA levels measured as metabolite ratios in mild TBI patients and healthy volunteers using proton MRS. Measurements were taken 1-20 days following trauma and indicate higher NAA concentrations in mild TBI patients than controls [264].* ***b*** *Surface Enhanced Raman Spectroscopy (SERS) used to measure ex-vivo samples, determined that SERS can detect a clear change in spectra when measuring multiplex immunosensors after incubation with varying concentrations of S100B and NSE [161].* ***c*** *in-vivo measurements of S100B, from brain extracellular fluid, using microdialysis. S100-B levels peak in alignment with periods of raised ICP following TBI. [189].* ***d*** *SERS used to measure NAA concentrations in finger-prick blood plasma samples at t = 0 (black) and t = 8 hrs (red) following TBI, compared to healthy volunteers (navy) [213].*

Mass spectrometry is often compared to another metabolomic technique, nuclear magnetic resonance (NMR), which can be utilised *in-vivo* when combined with magnetic resonance spectroscopy and capable of non-destructive sample analysis, but has a lower sensitivity than mass spectrometry[266]. Such comparisons highlight the strengths of mass spectrometry, including the large number of metabolites its capable of detecting and low skill required to implement it (ideal for PoC settings). However, the requirement for extensive sample preparation and sample destruction prevent *in-vivo* applications and greatly limit use pre-hospital or to obtain real-time monitoring data[267]. Mass spectrometry can be applied to microdialysis samples which is obtained by a catheter inserted through a lumen into the brain, where perfusion fluid is pumped through the catheter[189]. The tip of the catheter allows diffusion of sample fluid along a concentration gradient to equilibrate with the perfusion fluid, mimicking a blood vessel and sampling extracellular fluid without blood withdrawal[268]. The extracted fluid may also undergo high-performance liquid chromatography, resulting in separation of the chemical components[212], [269]. Studies have successfully detected TBI biomarkers using microdialysis including for instance, S100B and NAA[212], [214], [220], [246]. However, artefactual disruption from catheter insertion with increase in injury markers has been observed in many studies[212], [241], [245], [246], pointing towards an inconvenient waiting period after catheter insertion to allow biomarkers to reach a steady state.

1.4.2 Magnetic Resonance Spectroscopy

Magnetic resonance spectroscopy (MRS) is an *in-vivo* analytical technique that non-invasively interrogates brain tissue metabolism. Similar to MRI, radio-frequency electromagnetic radiation is used to excite nuclei into alignment and then stopped to allow nuclei to return to their original state,

creating a fluctuating magnetic field which is detectable as a current induced in the receiver coil[217], [270]. In a complex chemical environment, nuclei are shielded from the main (external) magnetic field by the electrons surrounding the nucleus. This electron shielding results in small changes of the frequency of the MR signal detected and is called the chemical shift and is the basis for metabolite identification using MRS. This creates an output in the form of a spectrum which provides the information on which molecular bonds are present in the sample in the form of spectral bands located at unique wavenumbers, which are split into regions representing vibrational modes and with intensities indicating the relative concentration of each molecule[271].

Proton MRS uses the radio-frequency signal from MRI to obtain a chemical shift from a sample, which indicates its metabolite concentration *via* spectral peaks[71], [217], [272], obtaining the biochemical information of an otherwise morphological scan[215]. Were proton MRS pursued for TBI diagnostics then it could be easily implemented within a pre-existing MRI facility, which are available in most western hospitals. Proton MRS is the most used MRS technique for studying brain metabolism after TBI and measures several metabolites. Several targets of proton MRS may have value as prognostic indicators including NAA, choline, myoinositol and lactate[215], [273], [274]. Of these NAA and choline are decreased and increased in severe injury respectively, and together may be the most reliable indicators of eventual outcome[273].

MRS holds great potential in the post-injury follow up period, when it may be useful for monitoring neurodegeneration, which can complicate the long term follow up of patients with TBI[275]. However, there are drawbacks of MRS that may deter researchers from establishing standardisation. Patients with restlessness preventing them from lying still for a prolonged time are excluded or must undergo anaesthesia to ensure they are stationary, delaying diagnoses and potentially interfering with other assessments[215], [217]. Proton MRS also requires specialised knowledge to align and calibrate each measurement, along with a well-trained, dedicated personnel to regularly service it.

1.4.3 Fluorescence to Detect TBI Biomarkers

Fluorescence occurs when incident light undergoes the Stokes Shift, in which the scattered light has longer wavelengths than that of the source[276]. Whole-body fluorescent imaging has been performed on cryolesioned mouse TBI models to measure apoptosis using near-infrared molecular probes and tracers[277]. Fluorescent microscopy can also be used to monitor apoptosis (cell death) after TBI and has been done so to image Rabbit anti-AIF and anti-EndoG antibodies[278], [279]. Inverted fluorescence microscopy has been used in animal studies to image nitrogen monoxide NO in real-time[280], BBB degradation increases NO levels, an important TBI free radical, however, there are currently few viable techniques for *in-vivo* imaging of NO brain concentrations in humans[281], though there has been success in ophthalmic applications.

Cordiero et al. have utilised fluorescent signals with confocal laser scanning ophthalmoscopy to single retinal nerve cell apoptosis *in-vivo* and termed the technique detection of apoptosing retinal cells (DARC)[282], [283]. DARC was developed to diagnose glaucoma in the early stages before vision loss and has been translated into humans to identify retinal cell apoptosis in retinal images of glaucoma patients, finding DARC counts were significantly higher (correlating to a greater number of apoptosis) in glaucoma patients compared to healthy controls, and even more so for those with increased disease progression, indicated by the optic disc, RNFL and visual parameters[284]. Fluorescent microscopy combined with ophthalmoscopy has the potential for monitoring DARC counts *in-vivo* in the acute phase of TBI to diagnose and characterise injury severity, but require numerous patient preparation steps, firstly being a single injection dose of ANX776 to visualise cells during imaging, followed by pupillary dilation.

Bermond et al. imaged human retinal pigment epithelium (RPE) cells from *ex-vivo* fovea, perifovea and near-periphery, using confocal fluorescence microscopy[285]. Whilst Fundus Autofluorescence

(FAF) is proving a promising tool for monitoring posterior uveitis (inflammation)[286], [287]. FAF utilises blue-light excitation to form a brightness map and it is found commercially in fundus cameras, confocal scanning laser ophthalmoscopes and ultra-widefield imaging devices[288]. FAF falls short due to its low signal strength and the tendency to produce autofluorescence artifacts, all whilst being potentially harmful to the retina and causing patients' discomfort without device-specific mitigations[288]. These challenges have been overcome to achieve FAF systems capable of diagnosing and monitoring age-related macular degeneration, central serous chorioretinopathy, macular dystrophies and more, discussed in Yung *et* al., but it does not so readily detect inner retinal (retinal ganglion cell) damage [288]. Malamos et al. utilised lipofuscin, the main source of autofluorescence in human fundus, in patients diagnosed with uveitis using FAF, demonstrating its potential as a non-invasive, single follow-up tool for progressive inflammatory disorders affecting the outer retina[289].

1.4.4 Hyperspectral Imaging

Hyperspectral imaging (HSI) involves the acquisition of two-dimensional images across a broad range of the electromagnetic spectrum. The precise number of wavelengths varies in the literature and there is some overlap and often arbitrary differentiation from multispectral imaging (MSI). However, HSI is differentiated from MSI by primarily relying on the use of narrow adjacent spectral bands over a continuous range, as opposed to the discrete and spaced wavelength bands in MSI[290]. The number of bands can range from two up to several hundred. Target illumination is delivered by a white broadband light source *e.g.,* a halogen lamp, although supercontinuum lasers may also be used. The specific interactions of the light with the various chromophores in the tissue can result in reflected, emitted or fluorescent light from the sample, which are received by a detector[291], [292].

HSI can provide real-time images of a sample and as such has application in many tissues and biological contexts. Regarding the brain, it has been used to assess cerebral blood flow and tissue oxygenation[293], and unlike Near-infrared spectroscopy (NIRS), HSI is able to provide high resolution images and can potentially target multiple chromophores at a time. One drawback is that it is an invasive procedure requiring access to the target tissue, limiting its potential for *in-vivo* human applications, due to complications introduced by complex imaging equipment and computational issues[294]. However, there are a limited number of HSI applications for *in-vivo* brain metabolism and haemodynamic measurements, reviewed here[294], and it has successfully been used to image retinal vasculature[295], [296]. Due to the close relationship of retinal and cerebral physiological states[296], the investigation of retinal vasculature with HSI in the context of TBI is promising[19].

Multispectral imaging has also been developed towards ophthalmic applications, although again these are focussed on the outer retina. Histological parameters have been extracted from multispectral images of the human ocular fundus to map the concentration and distribution of the retinal haemoglobins, choroidal haemoglobins, choroidal melanin, RPE melanin and macular pigment[297], [298]. Further work has completed in this field to obtain images of the human retina in rapid succession to eliminate discrepancies from saccades (natural eye movements) and reduce exposure times to 0.05s[299]. This exploration of multispectral imaging establishes it as viable as a quantitative analysis technique for the diagnosis of eye diseases like diabetic retinopathy and age-related macular degeneration (AMD)[299], and developments in novel multispectral analysis methods would reduce long computational times to aid the practicality of multispectral imaging being used in clinical settings[300].

1.4.5 Near-Infrared Spectroscopy

NIRS is an *in-vivo* technique that has undergone considerable testing in human subjects[301]–[303]. It utilises wavelengths between 700 nm and 1000 nm, which can penetrate the skull and several

millimetres into brain tissue, to monitor brain cortical perfusion and oxygenation. Attenuation of reflected light by differential chromophore absorption including oxygenated and deoxygenated haemoglobin and cytochrome-c-oxidase[304], enables their quantification in tissues, and determination of cerebral oxygenation changes as a ratio of oxy to deoxyhaemoglobin[305].

NIRS cannot discriminate between arterial, capillaries or venous blood and therefore provides a combined reading of tissue blood oxygenation. As venous blood is most abundant within the cranium, the normal cerebral oxygenation value obtained by NIRS is lower than that obtained by pulse oximetry which assess the pulsatile arterial blood oxygenation signal[306]. NIRS correlates with jugular venous blood oxygenation[307], which is indicative of the relationship between cerebral blood flow and cerebral metabolic and oxygen requirements[308]. Thus, where cerebral perfusion may be decreased by raised intracranial pressure or systemic blood volume loss, or cerebral tissue metabolic changes take place[309], NIRS enables the assessment of brain tissue oxygenation and cerebral perfusion, as well as the inference of changes in cerebral perfusion autoregulation and metabolic state during the early post-traumatic period.

Rodlan *et* al. investigate and review the promising applications of NIRS in TBI monitoring, collating examples of experiments that find good agreement between NIRS and current gold standard techniques, *i.e.,* neuroimaging, ICP monitoring[310]. They highlight that algorithms used within NIRS, wavelengths and source-detector separation differ between commercial systems, complicating direct comparisons and thus hindering the ability to characterise pathologies such as TBI severity. This challenge is exacerbated by extracerebral contamination introduced, the scalp, skull and CSF, and regional differences in pigmentation and pathophysiology[304].

1.4.6 Terahertz Spectroscopy

Terahertz (THz) spectroscopy uses electromagnetic radiation in the wavelength range between microwaves and infrared to detect properties of matter. The vibrational and rotational energy of many biomolecules, such as proteins, are within this range thus making it an effective analytical technique that does not require pre-processing or labelling[311], [312]. The high sensitivity THz spectroscopy with the content and state of water in biological tissues has drawn interest in biophotonics[313], whilst also exhibiting non-invasive and non-ionizing characteristics[314]. Whilst it has been investigated in live animal models of TBI, successfully differentiating between traumatised and normal brain tissue[314], [315], it is used as an *ex-vivo* technique and requires tissue to be sectioned. Wang *et* al. identify THz spectroscopy as an early diagnostic tool for blast-induced TBI and able to differentiate the serum and CSF of mice with differing TBI severities[315]. Therefore, as a future clinical tool, THz spectroscopy would be much better suited for the analysis of liquid samples such as serum and CSF, rather than a PoC diagnostic technique. However, THz spectroscopy is a relatively new biochemical imaging technique, and current limitations may be due to the lack of representation in literature. Further research efforts could identify THz as an ideal tool for rapid, label-free biological imaging.

1.5 Raman Spectroscopy

1.5.1 Raman Spectroscopy Theory

RS is a powerful, sensitive and specific technique capable of measuring the chemical composition of complex samples, which can be accomplished non-invasively in a label-free manner[316], [317]. In this process, illustrated in **Fig. 1.8a,** incident monochromatic coherent light provides identical packets of energy in the form of photons. In Raman scattering or inelastic scattering, incident photons are momentarily absorbed, setting the sample molecule into a bigger vibration, transitioning it to a higher excited, vibrational “virtual” state, resulting in the release of a new photon when the molecule falls from the virtual state back to a lower state[271], [318], [319], the scattered photons have a different energy from the incident ones, with a change equal to the energy required to vibrate the molecule to

the higher excited state[320]. Each type of a molecular bond vibrates at a different frequency, requiring different amounts of energy for photons being scattered and thus, different frequencies hence, constituting of the Raman signal.

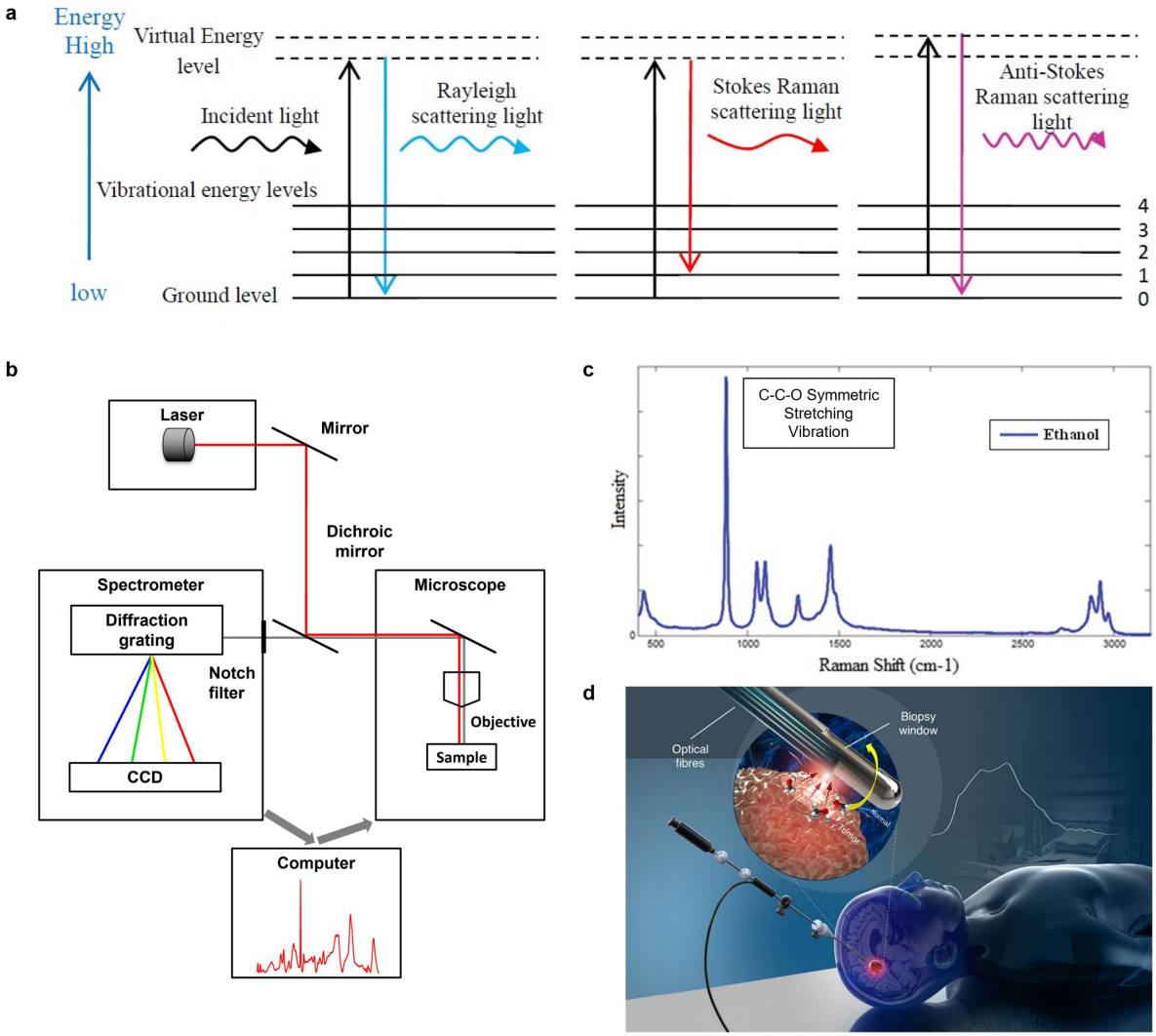

Figure 1.8. ***a*** *Diagram of the energy transitions involved in Raman (inelastic) scattering compared to Rayleigh (elastic) scattering. In Stokes scattering, the incident photon has greater energy than the scattered photon, whereas the incident photon in anti-Stokes scattering has lower energy [124]* ***b*** *Schematic diagram of a generic Raman Spectroscopy system [321]* ***c*** *Representative Raman spectrum of Ethanol with a prominent characteristic peak at 882cm-1 of the C-C-O bond symmetric stretching vibration [322].* ***d*** *Schematic of a Raman fibre optic probe, an example of a popular RS development for clinical applications, used here for a optical core needle biopsy for in-vivo detection of brain cancer tissue [336].*

Given that the intensity of a Raman signal is a millionth of that of the incident light source, due to the low probability of inelastic scattering[318], it is vital for the sufficiently sensitive RS system to be constructed using high-performing components to ensure minimal signal loss. A generic RS set-up is provided in **Fig. 1.8b**[321], the Raman signal is fed into a spectrometer where it can be detected and converted into a visual output as a spectrum of wavenumber (cm^{-1}) against intensity (arbitrary units)[317].

A wavenumber is the spatial unit of frequency, indicating the difference between the energy and thus, wavelengths of the incident and scattered photons[318]. This results in multiple peaks that represent the vibrational modes that are characteristic for each molecule present in a given sample, creating a biochemical molecular fingerprint for a certain excitation wavelength[318]. A representative Raman spectrum of ethanol shows the characteristic peaks at $882cm^{-1}$ due to C-C-O bond symmetric

stretching vibrations along with two peaks at 1050cm^{-1} and 1090cm^{-1}, due to the C-O bond scaling and C-C-O bond stretching vibrations, respectively (**Fig. 1.8c**)[322], [323].

The many attributes of RS have indicated a potential promise for its implementation in clinical settings, including its sensitivity in rapid molecular sensing and the unique capability to be employed outside the laboratory without significant loss of performance[183], [324]. Furthermore, for biological applications, where often a high-water content is present, RS, utilising visible or near-infrared light, enables highly resolvable *in-vivo* measurements with the signal from water being negligible due to the reduced absorption effects[316], [317]. In the past decade RS systems have become more portable, modular and more sensitive by utilising optical fibres, endoscopes, nanostructures and micro-spectroscopy[213], [324]–[326], making them more suitable for clinical and PoC applications[327].

1.5.2 Raman Spectroscopy in Neurodegeneration

Raman spectroscopy (RS) has shown promise in neuro-applications and has been utilised to analyse neurochemistry[328], [329], *in-vitro* neuronal cells[330], cancers[331], [332], and cerebral brain metastases[324], [333]. Fibre optic Raman probes are handheld systems comprising an optical arm to deliver excitation light and a collection arm to detect the Raman signal[317], [325], [334], [335]. There have been numerous fibre optic Raman probes developed for clinical applications, **Fig. 1.8d** features an example, that can diagnose numerous cancers *ex-vivo* using either biopsies or blood samples[336], as well as imaging intact brain tissue during a surgery[324], [336], [337], directly measuring the CSF obtained through existing external ventricular drainage devices[338].

RS also detected neurodegeneration, allowing early and sensitive neurodiagnostics through the rapid, non-invasive spectroscopic assessment of biofluids at the point-of-injury[161], [339]. Most current successful RS systems are geared towards *ex-vivo* characterisation of ND diseases, focussed on the study of blood and tissue in both animal and human models, with only a single human study of MS, in which Bergholt *et* al. investigated the lipid content of post-mortem brain tissue[340]. Further studies employed Coherent Anti-Stokes Raman Spectroscopy (CARS) in murine MS models[341], and on tadpoles using surface enhanced Raman spectroscopy (SERS), showing the *in-vivo* capability for real-time imaging of an MS model[342], highlighting the non-destructive nature of RS for research into neurological diseases.

RS applications in AD diseases are more extensive and the research is majorly split into the characterisation of CSF or blood to identify protein and lipid biomarkers[318], [343]. The tracking of blood biomarkers has been investigated with SERS and CARS to allow for very low concentrations of tau protein and amyloid-beta to be monitored[344]–[346]. RS also allowed sensitive AD detection using SERS, detecting trace level amyloid-beta[334], [347]. Although, most studies concluded that further larger scale clinical validation and optimisation was required for successful transition into a clinic, they highlighted the rapidness, sensitivity, and specificity achievable using the various RS methods, successfully measuring various neurological molecular changes in patients.

1.5.3 Raman Spectroscopy in TBI

RS is a non-invasive technique able to measure biomarkers rapidly and in real-time. As a molecular sensing technique, RS could be a powerful method for detecting TBI indicative biomarkers[183], particularly given the significant cascade of biological and chemical metabolic changes accompanying TBI, which could provide diagnostic information in the acute phase and detect the development of secondary injuries[56], [238]. User-friendly, hand-held PoC devices capable of monitoring a panel of TBI biomarkers, using miniaturised RS hold the biggest promise for TBI diagnosis[168], [271], [319], [332].

The multiplex ability to obtain chemical information and detect low-level biochemical changes in tissue samples makes it a potentially powerful technique in, not only diagnosing TBI but also in, deciphering between mild, moderate, and severe cases. RS applied in animal TBI injury models[348]–[350], and human plasma[213], [351], demonstrates the feasibility of spectroscopically identifying and classifying head injury and its severity, and how RS can monitor changes in tissue biochemistry after trauma[348], [349].

TBI indicative biomarkers from human plasma have been characterised using SERS. One system demonstrates that combining an optofluidic, SERS lab-on-a-chip with a portable RS system presents promise for injury diagnostics and subsequent monitoring by profiling the levels of the NAA, S100B and GFAP[213]. Another system incorporates portable SERS into a disposable paper-based lateral flow strip to detect NSE in blood plasma samples[352]. Both methods provide alternatives to commonplace Enzyme-Linked Immunosorbent Assay (ELISA) approaches that can be deployed rapidly, portably and with small sample sizes, ideal parameters for PoC settings. SERS has also been utilised for *ex-vivo* studies in detecting and monitoring TBI biomarkers in various biofluids[353], [354].

1.5.4 Raman Spectroscopy and the Eye

1.5.4.1 *Ex-Vivo* Studies

RS analysis of tears and tear meibum have shown promise, studying composition[355], [356], eye-related disease[357], [358], non-eye-related disease[359], [360] and contact lens use[361]. RS of tears has also been used for assessments of AD and mild cognitive impairment using principal component analysis (PCA), to detect change in healthy and disease states[356]. RS can monitor changes due to surgery, therapy and age[362]–[365]. In addition, Resonance Raman Spectroscopy (RRS) determined the efficacy of a scleral iontophoresis device (drug delivery through a gradient) by measuring the levels of lutein in the sclera, choroid, retinal periphery and macula following therapy[364], and analysed age-related changes in *ex-vivo* Bruch's membrane samples, the inner-most layer of the choroid, suggesting the potential of doing the same *in-vivo* to determine those at high risk of ocular disease and the success of therapy and also that Bruch's membrane and sclera are composed of similar biomolecules, suggesting the sclera could be used as a viable (and more readily accessible) surrogate marker for changes in the Bruch's membrane[365], [366].

Ex-vivo studies of enucleated human eyes have shown promise for development of ocular RS[364], [367]–[370]. The retina has a dense neuron structure and it is a highly metabolically active tissue[115], [371], which can be accessed externally through the optics system of the eye to perform RS. A method to measure carotenoid levels in flat-mounted retinae, was an initial proof-of-concept for future *in-vivo* studies[372], [373], using carotenoids (a biomarker for macular pigment level), detecting lutein and zeaxanthin resonance enhancement when excited by a 488 nm excitation wavelength, which has been widely replicated[362], [364], [367], [374], [375]. The presence of validated TBI biomarkers in the eye such as elevated concentrations of tau, (detected using immunohistochemistry), in the retina supports the potential of TBI as an ocular diagnostic tool[124].

Stiebing *et* al. continued previous work in mouse retinae, identifying retinal layers using RS and discriminating between healthy and AD subjects[142]. They found that spectra obtained of *en-face* healthy and AD retinae are not distinguishable without statistical analysis to detect underlying changes (**Fig. 1.9a**), which was able to correctly recognise AD retinae with a sensitivity of 86.2%[142]. The inclusion of *en-face* samples, as well as probing the retinal layers, mimics *in-vivo* measurements which makes the study more translatable once an *in-vivo* system has been achieved. Marro et al. studied *in-vitro* murine retinal cultures treated with lipopolysaccharide to create an MS model of the retinal ganglion cell layer (GCL) using an *in-vivo* RS measurements of the tissue, examining

neuroinflammatory molecular changes as a function of time[376]. Subsequently, curve fitting with known retina components was utilised to de-convolve the Raman spectra highlighting bands which undergo changes with increasing treatment time (**Fig. 1.9b**)[376]. The authors identified markers in the molecular components of the RGC layer which indicate changes in inflammatory mediators, components of mitochondria and fatty acids during neuroinflammation.

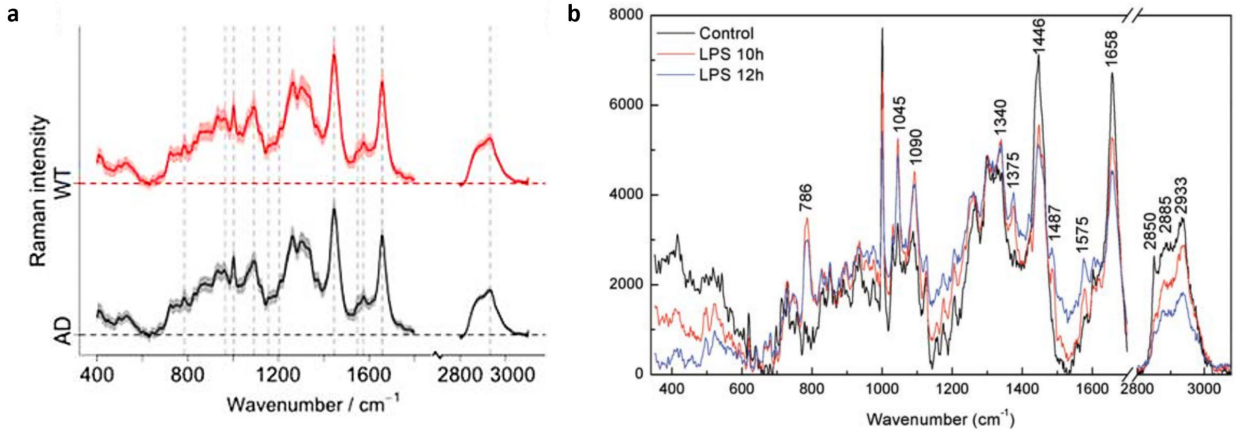

Figure 1.9. Raman spectra of eye tissue undergoing chemical changes indicative of neurodegeneration ***a*** *Raman spectra of en-face murine retina using 785 nm laser, grouped into wild mice and AD model mice. Chemometric analysis revealed biochemical changes indicative of structural and pathological manifestations of AD [142].* ***b*** *Spectra of murine, retinal cultures modelling MS using LPS, measured using a 785 nm Raman system. Increasing incubation with LPS lead to changes in the heights of characteristic peaks in the spectra, indicative of neuroinflammation [376].*

1.5.4.2 *In-Vivo* Studies

In-vivo RS measurements of the lens has also been explored with the aim to identify the presence of artificial intraocular lenses used for the treatment of cataracts and investigated the effect of lens yellowing and transparency loss on *in-vivo* RS measurements[375], [377]. In post-mortem lenses of 7 dementia patients with confirmed diagnoses of AD high lens amyloid-beta levels did not correlate with brain tissue immunostaining, although the research demonstrated that RS could take non-destructive measurements in the eye[378]. Martinez-Lapiscina et al. explored the prospect of monitoring inner nuclear layer thickening within the retina by coupling RS with a confocal scanning laser ophthalmoscope. The study measured key molecules of inflammation and neurodegeneration in human retina, demonstrating the potential of RS non-invasively addressing molecular changes of *in-vivo* CNS *via* the retina[143].

Previously mentioned stimulated Raman techniques, such as SERS and CARS, are of interest to researchers seeking Raman-based solutions in biological samples. In particular, CARS has been successfully implemented for spectroscopic imaging of *in-vivo* retina of nonhuman primates, favoured as sample preparations such as fluorescent dyes are not required[379][380], but requires longer measurement times due to low fluorescence, which is of interest in obtaining spectra from biological tissue [381]. CARS utilises multiple laser beams, commonly a pump beam and Stokes beam which produce four types of simultaneous Raman processes when the frequency difference between the two beams corresponds to a chemical bond vibrational frequency within the target sample[382]. Whilst it is stated that CARS can produce signals orders-of-magnitude stronger than RS[383], the mutli-laser set-up that sometimes requiring an additional probe beam limits its applications in portable devices and complicates meeting eye-safety regulations. Masihzadeh *et* al. provide an example of this applying CARS for imaging mouse tissue, requiring a 1064 nm laser to direct two near-IR beams to the sample. In this process, a 532 nm beam was generated which complicates eye-based systems that aim to be invisible to the human eye to avoid pupil contraction[379]. Petrov *et* al. achieved a one-laser CARS set-up; however, the signal was only ~100 times stronger than RS, and they discuss that

a greater signal using CARS does not necessarily mean better signal-to-noise ratio due to laser fluctuations and strong background signals[384]. Despite limitations, CARS may be a necessary avenue to explore if the final portable eye-based Raman device cannot obtain sufficient signal from *in-vivo* retinae.

In 1998, Gellermann *et* al. provided a proof-of-concept design that used RRS to obtain *in-vivo* macular pigment measurements within the human retina, patented in 1999, limiting the majority of succeeding publications to the same research group and method[385]–[390]. The macular pigment has been investigated this way to monitor macular pigment levels decreasing with decreasing foveal thickness following surgery[362], [391], to identify a 50% decrease in macular carotenoid pigments in patients with Stargardt macular dystrophy compared to healthy controls[392], to examine macular pigment optical density to determine macular pigment level decrease following intraocular lens implant[363], [393], and the intake of lutein supplements[394].

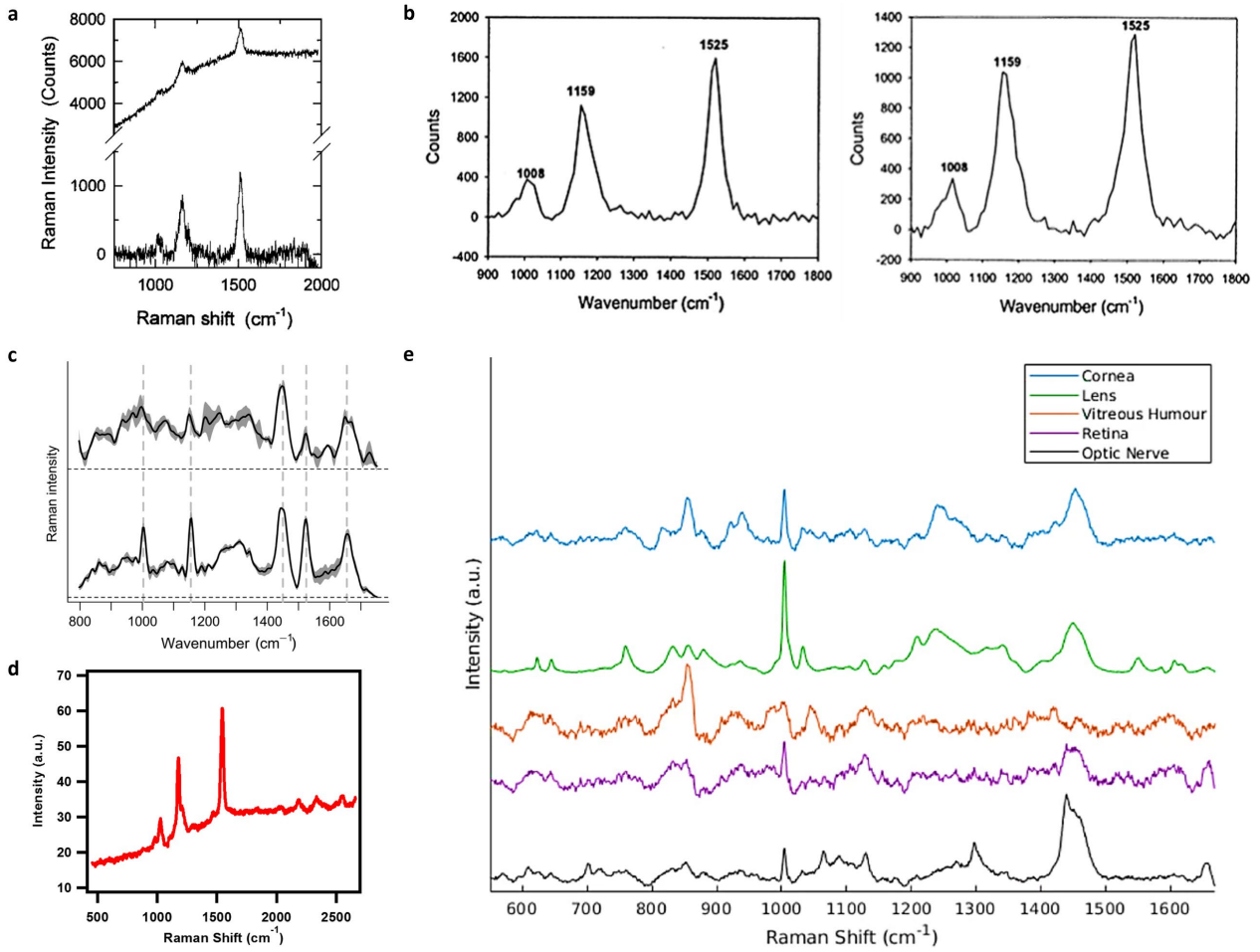

Figure 1.10. Raman spectra of in-vivo samples and models which simulate an in-vivo environment. ***a*** *Raman spectra of healthy, human retina, measured in-vivo with dilated pupil (~8 mm diameter), using a 488 nm laser. The top spectrum is from 3 summed measurements and the bottom spectrum is the same measurements with baseline subtracted. Characteristic carotenoid peaks are present at 1008, 1159 and 1525 cm^{-1}[388].* ***b*** *Comparative study of Raman spectra taken in a human eye in-vivo and macular carotenoids in liquid form within an eye model [386]* ***c)*** *Comparative spectra of flat-mounted, murine retina using 785 nm lasers within a commercial Raman system (bottom) and an in-house built Raman set-up (top) which simulates in-vivo parameters in the eye. Characteristic carotenoid peaks are present in both [400].* ***d*** *Spectra taken of ex-vivo macular pigment tissue samples which were fixed using formalin fixative, using a 488nm excitation wavelength [367].* ***a - d*** *demonstrate that the same characteristic carotenoid peaks are present in in-vivo, fresh ex-vivo and fixed ex-vivo eye samples.* ***e*** *Raman spectra of fresh, ex-vivo, porcine eyes that were dissected into 5 main features. Measurements were taken using a commercial system, 785 nm laser and settings were chosen based on the maximum permissible exposure defined by eye-safe limits [348].*

RRS with a 488nm excitation wavelength to create a strong vibrational response from the carotenoid, permitted a lower laser power and exposure time to be used compared to previous work and

facilitated confocal Raman spectra of an *in-vivo* human retina, measuring the concentration of macular carotenoid pigments lutein and zeaxanthin (**Fig. 1.10a**) and obtaining clear carotenoid peaks[388]. In 2004, the authors provided an update regarding the method obtaining spectra using eye-safe exposure levels in just 0.25 second and its use in clinical trials[389]. That same year, the group corroborated their results by taking spectra of macular carotenoids through a “model eye” to mimic *in-vivo* conditions, obtaining clear results (**Fig. 1.10b**)[395]. More recently, the same research group has investigated the use of photometry[396], which has been explored in other literature to validate the reproducibility of Bernstein’s method[362], [374], and have been able to distinguish lutein and zeaxanthin within *ex-vivo* retina samples, measuring macular pigment distribution using Raman spectroscopy and autofluorescence imaging[397]–[399].

With eye-safe RS laser safety protocols, protein, lipid and nucleic acid were detected on mounted retina tissue samples, *ex-vivo* using the 785nm excitation wavelength predicting the success of the future *in-vivo* RS system to diagnose macular degeneration[400]. The study compares spectra from an in-house built RS set-up to those obtained by an optimal confocal Raman imaging system (**Fig. 1.10c**), finding good agreements and predicting the success of the in-house built system to diagnose macular degeneration *in-vivo*[400]. Banbury et al. have recently detected, distinguished and categorised the response of segments of an *ex-vivo* porcine eye samples using a 785nm excitation wavelength (**Fig. 1.10e**)[348]. If similar results could be achieved using near-IR wavelengths, to reduce tissue auto-fluorescence[317], whilst adhering to eye safety regulations, these studies lay the platform for potential developments of non-invasive, *in-vivo* RS systems for real-time diagnostics and monitoring of TBI.

1.6 Towards Ocular Raman Spectroscopy for TBI Diagnostics

Detection of biochemical ocular TBI biomarkers, requires *in-vivo* and eye-safe molecular sensing techniques that can characterise the chemical constituents of the eye, suggesting RS as a potential solution. RS using an 800nm excitation laser was used to detect glutamate in whole *ex-vivo* porcine eyes as well as to characterise the various eye segments[401]. In ocular diseases such as AMD, glaucoma, diabetic retinopathy and retinal detachment, increased levels of glutamate in the retinal nerve cells diffuse into neighbouring tissue suggesting that detection of glutamate biomarker excitotoxic neuronal death[402], which indicates the potential of spectroscopic integration of TBI indicative biomarkers *via* the eye. Banbury *et* al. have recently demonstrated exploitation of eye-safe RS to measure the biochemical response in the retina of an *ex-vivo* murine TBI tissue, using a 633nm excitation wavelength. The acquired data was subsequently analysed using advanced machine-learning algorithms, successfully classifying injury severity levels of severe, moderate and control cohorts with sensitivities of 82.0%, 75.1% and 69.4%, respectively[403]. Recently, the high wavenumber peaks from fatty tissue samples, similar to that found in the brain were successfully measured using a non-invasive portable Raman spectroscopy device comprised of a fundus camera and an un-dilated eye phantom, laying the platform for the *in-vivo* retinal measurements for TBI diagnostics at the PoC. RS applied to murine retina organotypic cultures undergoing an inflammatory response, creating a spectral library of 5 biomolecules which yielded the strongest peaks in response to neuroinflammation, including NAA and glutamate[404], [405]. Both studies demonstrated the effectiveness of RS with PCA statistical analysis to detect and monitor neuroinflammation in the retina and potentially identifying retinal metabolites present in ocular manifestations of TBI.

In the immediate future, there is a need to validate recent findings through internal and external references. Internal references refer to a method of direct analysis of brain tissue *in-vivo* in humans in the context of TBI. We have recently performed a preliminary work for incorporating Raman spectroscopy into an existing standard of care for invasive monitoring in intensive care following TBI, *via* an external ventricular drainage device[406]. This approach reduces the barrier to entry for ethical approval and allows ground truth assessment with respect to the GCS and ICP. External referencing

refers to validation of the biochemical attributions made by a means other than Raman spectroscopy. Since it is possible to measure the ON sheath diameter using MRI[136], it may also be feasible to measure chemical information from the ON sheath using MRS. Chemical species detected by MRS such as, the S100B, GFAP or the NAA could then be used as reference compounds in a fitting library for complementary Raman spectra. However, this requires further developments of the portable Raman devices and ethical approval for use *in-vivo*.

RS can offer a label free mechanism for measuring changes to biochemistry, which can be applied *in-vivo* in invasive settings such as surgery but has also shown promise for non-invasive measurement, in the field of ophthalmology. Given a rooting in more fundamental chemistry, the analysis of spectra from biological samples, formed of complex permutations of thousands of individual molecules in a single sample remains challenging[324], [407]. Although RS has proven to be employable outside of laboratory settings, Raman signals are intrinsically weak and clinical applications introduce additional factors including the surgical lighting, excess blood, unstable patients and the complexity of living tissue[324]. Historical chemometric analysis tools such as, PCA are commonly used inappropriately in the literature in efforts to overcome the high dimensionality of the data. By aiming to study posterior tissue through a thick heterogeneous sample (the eye) and indirectly detect subtle changes from brain injury, will require improvements to analysis methods. The link between damage to the retina and CNS has been noted in the literature[22], [34], [106], but this has not currently been applied to a specific model of disease or injury. In exploring whether it is fundamentally possible to study biochemical changes resultant from TBI will expand the possibilities of RS as an emerging diagnostic platform.

The intrinsically weak signal (10^8 times lower than elastic scattering) obtained using RS is complicated from noise generated by laser instabilities and dark current produced by thermally activated electrons within the detector (spectrometer), reducing the signal to noise ratio[408]. This exacerbated by the low powers required for biological tissue, which is even more important when considering safety parameters for the eye, which is likely to be overshadowed by autofluorescence. Additive noise from background and the detector can be reduced by increasing the laser power or acquisition time, however, this will increase fluorescence [409], as well as creating a poorer patient experience when scanning the eye *in-vivo.* In an investigation to estimate noise-induced instability, Barman *et* al. quantified the Raman signal from glucose (one of the prospective TBI biomarkers explored in **Chapter 6**) to be less than 1% of the height of the entire spectrum produced from dog skin[410]. On the other hand, Jermyn *et* al. assessed the signal-to-noise ratio of an in-house built RS probe for *in-vivo* cancer detection by altering the integration time. They determined that an RS scan as short as 0.05s was sufficient to discriminate between healthy and cancerous tissue with an accuracy of 92%, and the signal-to-noise ratio was increased by 41% and 73% by extending the acquisition time to 0.1s and 0.2s, respectively[411]. However, the laser power used was utilised between 37 and 64 mW, much higher than eye-safe levels discussed in **Chapter 4**, but providing a hopeful range in which ocular RS could find a compromise.

A remaining factor limiting eye-based RS for TBI diagnostics, in the context of PoC medical devices within a healthcare system, such as the National Health Service (NHS), is in relation to cost. To achieve higher confidence in triaging TBI in the acute phase and increase availability of neuroimaging facilities, the diagnostic technique must be widespread and standardised. This would require the portable diagnostic technique to be available in ambulances or kept in-house at medical centres of high-impact sport venues. Telemedicine medical devices are recognised for making compromises, being more affordable and accessible but losing resolution and robustness [412]. The growing use of miniaturised computers such as Raspberry Pi's allows for electronics to be built smaller and cheaper than previously, with opportunity for continuous modifications [413]. This thesis, particularly **Chapters 3** and **5**, explores these avenues in maximising portability of fundus imaging to combine with Raman spectroscopy, however, the costs and dimensions provided do not factor in the external

components required the to run the system. To achieve Raman spectra for injury profiling, a high-resolution spectrometer is required, and in this work a custom portable spectrometer was purchased at a high cost of ~£11,000. It is argued that the price of medical imaging systems come from extreme mark-ups, and this is the same for spectrometers. In order to fully envision portable RS for eye-based PoC diagnostics, a compatible spectrometer must be built in-house to determine future commercial ability. However, as mentioned previously, the spectrometer detector is a big contributor to thermal noise[414], so a lower quality system will impact the signal-to-noise ratio, which is already poor in a biological, low-power spectroscopy device. Therefore, a machine-learning algorithm to determine differences between spectra, mentioned above**,** may be necessary to create an injury profile of TBI when noisy spectra cannot be visually assessed.

1.7 Summary and Prospects

TBI is a silent, world-wide epidemic, affecting populations of all ages, in civilian and military life, in work, home and sporting activities with significant long-term morbidity and economic impacts. Current PoC triage and diagnostic tools do not reliably allow timely intervention (under-triage) and often waste resource through over-triage. There is therefore a strong need for reliable, early, PoC molecular diagnostics to support triage and clinical decision-making to allow patient treatment to improve outcomes within the golden hour.

This introduction presents an overview of the status, opportunities, and obstacles faced by researchers exploring early diagnostic tests for TBI and other neurodegenerative diseases. The translation of neurological biomarkers from the bench to the secondary care and pre-hospital, PoC arenas is progressing rapidly in a number of areas, showing promise particularly in spectroscopic techniques such as RS. To accelerate the field of biomarker imaging, categorisation is key. Clear standard ranges and concentration thresholds of TBI biomarker(s) in blood and CSF the acute phase after injury would accelerate diagnoses and severity characterisation for all biomarker detection techniques. Not only would this facilitate diagnoses but also aid better understanding of an incredibly heterogeneous pathology, stratifying biochemical responses to differing injury severities and guiding potential therapies. RS therefore has the potential to provide complete non-invasive imaging through the eye. Employing this technique in a portable system would mitigate limitations and ambiguities introduced by the GCS and triage patients during the critical time before transport to emergency departments. In time-sensitive and remote settings such as in military service or at roadside or sport pitch-side settings, this would monitor ongoing health to protect patients from secondary or repeat injury and therefore long-term neurological, cognitive, and psychological morbidity.

TBI diagnostics is a broad field with clear objectives to improve the speed and precision of triaging decisions to maximise patients' neurological recoveries. However, there are few therapies mentioned when discussing medical intervention following diagnoses, another great unmet need. Advances in TBI treatments would develop in tandem with developments in diagnostic techniques to improve the patient journey and reduce deaths from TBI worldwide. All the current technologies discussed have challenges relating to specificity and sensitivity, but the potential of RS as a new addition to the ocular and TBI diagnostics toolbox is significant. The potential of eye based and PoC RS for TBI diagnostics is explored throughout this thesis, facing the aforementioned limitations head-on, in an attempt to fill the gap identified in this introductory chapter.

1.8 References

[1] A. Capizzi, J. Woo, and M. Verduzco-Gutierrez, "Traumatic Brain Injury: An Overview of Epidemiology, Pathophysiology, and Medical Management," *Med. Clin. North Am.*, vol. 104, no. 2, pp. 213–238, Mar. 2020, doi: 10.1016/j.mcna.2019.11.001.

[2] M. C. Dewan *et al.*, "Estimating the global incidence of traumatic brain injury," *J. Neurosurg.*, vol. 130, no. 4, pp. 1080–1097, 2019, doi: 10.3171/2017.10.JNS17352.

[3] V. L. Feigin *et al.*, “Incidence of traumatic brain injury in New Zealand: A population-based study,” *Lancet Neurol.*, vol. 12, no. 1, pp. 53–64, Jan. 2013, doi: 10.1016/S1474-4422(12)70262-4.
[4] M. Parsonage, “An economic analysis Traumatic brain injury and offending,” 2016.
[5] M. D. Wiles, “Management of traumatic brain injury: a narrative review of current evidence,” *Anaesthesia*, vol. 77 Suppl 1, no. S1, pp. 102–112, Jan. 2022, doi: 10.1111/ANAE.15608.
[6] “Head injury: assessment and early management,” *NICE*, 2014. https://www.nice.org.uk/guidance/cg176/resources/head-injury-assessment-and-early-management-pdf-35109755592901 (accessed Aug. 25, 2020).
[7] NICE, “Head injury: triage, assessment, investigation and early management of head injury in children, young people and adults,” 2013.
[8] H. Levin, D. Shum, and R. Chan, *Understanding Traumatic Brain Injury: Current Research and Future Directions*. 2014.
[9] J. J. Kim and A. D. Gean, “Imaging for the Diagnosis and Management of Traumatic Brain Injury,” *Neurotherapeutics*, vol. 8, no. 1, pp. 39–53, Jan. 2011, doi: 10.1007/s13311-010-0003-3.
[10] P. Goetz, A. Blamire, B. Rajagopalan, T. Cadoux-Hudson, D. Young, and P. Styles, “Increase in apparent diffusion coefficient in normal appearing white matter following human traumatic brain injury correlates with injury severity,” *J. Neurotrauma*, vol. 21, no. 6, pp. 645–654, 2004, doi: 10.1089/0897715041269731.
[11] M. Prins, T. Greco, D. Alexander, and C. C. Giza, “The pathophysiology of traumatic brain injury at a glance,” *DMM Dis. Model. Mech.*, vol. 6, no. 6, pp. 1307–1315, Nov. 2013, doi: 10.1242/dmm.011585.
[12] O. E. Idowu and O. Akinbo, “Neurotrauma burden in a tropical urban conurbation level i trauma centre,” *Injury*, vol. 45, no. 11, pp. 1717–1721, Nov. 2014, doi: 10.1016/j.injury.2014.05.028.
[13] M. Galgano, G. Toshkezi, X. Qiu, T. Russell, L. Chin, and L.-R. Zhao, “Traumatic Brain Injury: Current Treatment Strategies and Future Endeavors,” *Cell Transplant.*, vol. 26, no. 7, pp. 1118–1130, 2017, doi: 10.1177/0963689717714102.
[14] Y. Helps, G. Henley, and J. Harrison, “Hospital separations due to traumatic brain injury,” 2008.
[15] A. Mehmood, N. Zia, C. Hoe, O. Kobusingye, H. Ssenyojo, and A. A. Hyder, “Traumatic brain injury in Uganda: exploring the use of a hospital based registry for measuring burden and outcomes,” *BMC Res. Notes*, vol. 11, no. 1, p. 299, Dec. 2018, doi: 10.1186/s13104-018-3419-1.
[16] H. M. Bramlett and W. D. Dietrich, “Progressive damage after brain and spinal cord injury: pathomechanisms and treatment strategies,” *Prog. Brain Res.*, vol. 161, pp. 125–141, 2007, doi: 10.1016/S0079-6123(06)61009-1.
[17] N. Newall *et al.*, “Epidemiology and Pattern of Traumatic Brain Injuries at Annapurna Neurological Institute & Allied Sciences, Kathmandu, Nepal,” *World Neurosurg.*, vol. 141, pp. 413–420, May 2020, doi: 10.1016/j.wneu.2020.04.250.
[18] N. S. Malik *et al.*, “The BCD Triage Sieve outperforms all existing major incident triage tools: Comparative analysis using the UK national trauma registry population,” *EClinicalMedicine*, vol. 36, Jun. 2021, doi: 10.1016/J.ECLINM.2021.100888.
[19] E. Courtie, T. Veenith, A. Logan, A. K. Denniston, and R. J. Blanch, “Retinal blood flow in critical illness and systemic disease: a review,” *Ann. Intensive Care*, vol. 10, no. 1, p. 152, Dec. 2020, doi: 10.1186/s13613-020-00768-3.
[20] P. Colligris, M. Jesus Perez De Lara, B. Colligris, and J. Pintor, “Ocular Manifestations of Alzheimer’s and Other Neurodegenerative Diseases: The Prospect of the Eye as a Tool for the Early Diagnosis of Alzheimer’s Disease,” *J. Ophthalmol.*, vol. 2018, pp. 1–12, 2018, doi: 10.1155/2018/8538573.
[21] P. van Wijngaarden, X. Hadoux, M. Alwan, S. Keel, and M. Dirani, “Emerging ocular biomarkers of Alzheimer disease,” *Clin. Experiment. Ophthalmol.*, vol. 45, no. 1, pp. 54–61, Jan. 2017, doi: 10.1111/ceo.12872.
[22] Y. Kusne, A. B. Wolf, K. Townley, M. Conway, and G. A. Peyman, “Visual system manifestations of Alzheimer’s disease,” *Acta Ophthalmol.*, vol. 95, no. 8, pp. 668–676, Dec. 2017, doi: 10.1111/aos.13319.
[23] F. Z. Javaid, J. Brenton, L. Guo, and M. F. Cordeiro, “Visual and Ocular Manifestations of Alzheimer’s Disease and Their Use as Biomarkers for Diagnosis and Progression,” *Front. Neurol.*, vol. 7, p. 55, 2016, doi: 10.3389/fneur.2016.00055.
[24] D. Mahajan and M. Votruba, “Can the retina be used to diagnose and plot the progression of Alzheimer’s disease?,” *Acta Ophthalmol.*, vol. 95, no. 8, pp. 768–777, Dec. 2017, doi: 10.1111/aos.13472.
[25] E. Nerrant and C. Tilikete, “Ocular Motor Manifestations of Multiple Sclerosis,” *J. Neuro-Ophthalmology*, vol. 37, no. 3, pp. 332–340, Sep. 2017, doi: 10.1097/WNO.0000000000000507.
[26] J. Ramos-Cejudo *et al.*, “Traumatic Brain Injury and Alzheimer’s Disease: The Cerebrovascular Link,” *EBioMedicine*, vol. 28, pp. 21–30, Feb. 2018, doi: 10.1016/j.ebiom.2018.01.021.
[27] N. H. Saliman, A. Belli, and R. Blanch, “Afferent visual manifestations of traumatic brain injury,” *J. Neurotrauma*, vol. 38, no. 20, pp. 2778–2789, Jul. 2021, doi: 10.1089/NEU.2021.0182.
[28] S. Ambika *et al.*, “Visual profile of acquired brain injury in Indian cohort: a retrospective study,” *Brain Inj.*, vol. 34, no. 9, pp. 1168–1174, 2020, doi: 10.1080/02699052.2020.1792985.
[29] R. E. Ventura, L. J. Balcer, and S. L. Galetta, “The neuro-ophthalmology of head trauma,” *Lancet Neurol.*, vol. 13, no. 10, pp. 1006–1016, Oct. 2014, doi: 10.1016/S1474-4422(14)70111-5.
[30] R. Daneman and A. Prat, “The Blood–Brain Barrier,” *Cold Spring Harb. Perspect. Biol.*, vol. 7, no. 1, p. a020412, Jan. 2015, doi: 10.1101/CSHPERSPECT.A020412.
[31] M. L. Werhane *et al.*, “Pathological vascular and inflammatory biomarkers of acute- and chronic-phase traumatic brain injury,” *Concussion*, vol. 2, p. 1, Mar. 2017, doi: 10.2217/cnc-2016-0022.
[32] N. S. N. Graham and D. J. Sharp, “Understanding neurodegeneration after traumatic brain injury: From mechanisms to clinical trials in dementia,” *J. Neurol. Neurosurg. Psychiatry*, vol. 90, no. 11, pp. 1221–1233, Nov. 2019, doi: 10.1136/jnnp-2017-317557.
[33] S. T. Dekosky and B. M. Asken, “Injury Cascades in TBI-Related Neurodegeneration,” *Brain Inj.*, vol. 31, no. 9,

pp. 1177–1182, 2017, doi: 10.1080/02699052.2017.1312528.
[34] L. Guo, E. M. Normando, P. A. Shah, L. De Groef, and M. F. Cordeiro, “Oculo-visual abnormalities in Parkinson’s disease: Possible value as biomarkers,” *Mov. Disord.*, vol. 33, no. 9, pp. 1390–1406, Sep. 2018, doi: 10.1002/mds.27454.
[35] “Traumatic brain injury,” *Headway*. https://www.headway.org.uk/about-brain-injury/individuals/types-of-brain-injury/traumatic-brain-injury/ (accessed Jan. 13, 2020).
[36] K. K. Wang *et al.*, “An update on diagnostic and prognostic biomarkers for traumatic brain injury,” *Expert Rev. Mol. Diagn.*, vol. 18, no. 2, pp. 165–180, Feb. 2018, doi: 10.1080/14737159.2018.1428089.
[37] V. Raymont *et al.*, “Impact of mild head injury on diffusion MRI brain characteristics in midlife: Data from the PREVENT Dementia Study,” *Alzheimer’s Dement.*, vol. 16, no. 5, Dec. 2020, doi: 10.1002/ALZ.044517.
[38] D. Kushner, “Mild traumatic brain injury: Toward understanding manifestations and treatment,” *Arch. Intern. Med.*, vol. 158, no. 15, pp. 1617–1624, Aug. 1998, doi: 10.1001/archinte.158.15.1617.
[39] C. Hawthorne and I. Piper, “Monitoring of intracranial pressure in patients with traumatic brain injury,” *Front. Neurol.*, vol. 5, no. 121, 2014, doi: 10.3389/fneur.2014.00121.
[40] A. Georges and J. Booker, *Traumatic Brain Injury*. 2020.
[41] M. L. Pearn *et al.*, “Pathophysiology Associated with Traumatic Brain Injury: Current Treatments and Potential Novel Therapeutics,” *Cell. Mol. Neurobiol.*, vol. 37, no. 4, pp. 571–585, May 2017, doi: 10.1007/s10571-016-0400-1.
[42] M. P. Alexander, “Mild traumatic brain injury: Pathophysiology, natural history, and clinical management,” *Neurology*, vol. 45, no. 7, pp. 1253–1260, 1995, doi: 10.1212/WNL.45.7.1253.
[43] L. J. Carroll, J. D. Cassidy, L. Holm, J. Kraus, and V. G. Coronado, “Methodological issues and research recommendations for mild traumatic brain injury: The WHO Collaborating Centre Task Force on Mild Traumatic Brain Injury,” *J. Rehabil. Med. Suppl.*, vol. 1, no. 43, pp. 113–125, Feb. 2004, doi: 10.1080/16501960410023877.
[44] “What happens in a TBI? | Headway.” https://www.headway.org.uk/about-brain-injury/individuals/types-of-brain-injury/traumatic-brain-injury/what-happens-in-a-tbi/ (accessed Nov. 06, 2020).
[45] B. Lee and A. Newberg, “Neuroimaging in traumatic brain imaging,” *NeuroRx*, vol. 2, no. 2, pp. 372–383, 2005, doi: 10.1602/neurorx.2.2.372.
[46] M. Königs, E. A. Beurskens, L. Snoep, E. J. Scherder, and J. Oosterlaan, “Effects of Timing and Intensity of Neurorehabilitation on Functional Outcome After Traumatic Brain Injury: A Systematic Review and Meta-Analysis,” *Arch. Phys. Med. Rehabil.*, vol. 99, no. 6, pp. 1149-1159.e1, Jun. 2018, doi: 10.1016/j.apmr.2018.01.013.
[47] D. Pavlovic, S. Pekic, M. Stojanovic, and V. Popovic, “Traumatic brain injury: neuropathological, neurocognitive and neurobehavioral sequelae,” *Pituitary*, vol. 22, no. 3, 2019, doi: 10.1007/S11102-019-00957-9.
[48] I. Humphreys, R. L. Wood, C. J. Phillips, and S. Macey, “ClinicoEconomics and Outcomes Research The costs of traumatic brain injury: a literature review,” *Clin. Outcomes Res.*, vol. 5, pp. 5–281, 2013, doi: 10.2147/CEOR.S44625.
[49] A. A. Hyder, C. A. Wunderlich, P. Puvanachandra, G. Gururaj, and O. C. Kobusingye, “The impact of traumatic brain injuries: A global perspective,” *NeuroRehabilitation*, vol. 22, no. 5, pp. 341–353, Jan. 2007, doi: 10.3233/nre-2007-22502.
[50] J. Dunne *et al.*, “The Epidemiology of Traumatic Brain Injury Due to Traffic Accidents in Latin America: A Narrative Review,” *J. Neurosci. Rural Pract.*, vol. 11, no. 2, p. 287, Apr. 2020, doi: 10.1055/S-0040-1709363.
[51] V. Brain Injury Center, “DoD Numbers for Traumatic Brain Injury Worldwide-Totals,” 2019.
[52] J. E. Capó-Aponte *et al.*, “Visual Dysfunctions at Different Stages after Blast and Non-blast Mild Traumatic Brain Injury,” *Optom. Vis. Sci.*, vol. 94, no. 1, pp. 7–15, Jan. 2017, doi: 10.1097/OPX.0000000000000825.
[53] M. M. Harper *et al.*, “Blast-mediated traumatic brain injury exacerbates retinal damage and amyloidosis in the APPswePSEND19e mouse model of alzheimer’s disease,” *Investig. Ophthalmol. Vis. Sci.*, vol. 60, no. 7, pp. 2716–2725, Jun. 2019, doi: 10.1167/iovs.18-26353.
[54] T. B. VanItallie, “Traumatic brain injury (TBI) in collision sports: Possible mechanisms of transformation into chronic traumatic encephalopathy (CTE),” *Metabolism.*, vol. 100S, Nov. 2019, doi: 10.1016/J.METABOL.2019.07.007.
[55] G. Toshkezi, M. Kyle, S. L. Longo, L. S. Chin, and L. R. Zhao, “Brain repair by hematopoietic growth factors in the subacute phase of traumatic brain injury,” *J. Neurosurg.*, vol. 129, no. 5, pp. 1286–1294, Nov. 2018, doi: 10.3171/2017.7.JNS17878.
[56] J. R. Huie, S. Mondello, C. J. Lindsell, and L. Antiga, “Biomarkers for Traumatic Brain Injury: Data Standards and Statistical Considerations,” *J. Neurotrauma*, vol. 38, no. 18, pp. 2514–2529, Apr. 2021, doi: 10.1089/neu.2019.6762.
[57] D. F. Kelly *et al.*, “Cerebral blood flow as a predictor of outcome following traumatic brain injury,” *J. Neurosurg.*, vol. 86, no. 4, pp. 633–641, 1997, doi: 10.3171/jns.1997.86.4.0633.
[58] P. Perel, J. Wasserberg, R. R. Ravi, H. Shakur, P. Edwards, and I. Roberts, “Prognosis following head injury: A survey of doctors from developing and developed countries,” *J. Eval. Clin. Pract.*, vol. 13, no. 3, pp. 464–465, Jun. 2007, doi: 10.1111/j.1365-2753.2006.00713.x.
[59] H. M. Eisenberg, R. F. Frankowski, C. F. Contant, L. F. Marshall, and M. D. Walker, “High-dose barbiture control of elevated intracranial pressure in patients with severe head injury,” *J. Neurosurg.*, vol. 69, no. 1, pp. 15–23, Jul. 1988, doi: 10.3171/jns.1988.69.1.0015.
[60] M. Aliaga *et al.*, “Diagnostic yield and safety of CT scans in ICU,” *Intensive Care Med.*, vol. 41, no. 3, pp. 436–443, Mar. 2015, doi: 10.1007/s00134-014-3592-1.
[61] D. V. Agoston, A. Shutes-David, and E. R. Peskind, “Biofluid biomarkers of traumatic brain injury,” *Brain Inj.*, vol. 31, no. 9, pp. 1195–1203, Jul. 2017, doi: 10.1080/02699052.2017.1357836.
[62] G. Teasdale and B. Jennett, “Assessment of Coma and Impared Consciousness. A Practical Scale,” *Lancet*, vol.

304, no. 7872, pp. 81–84, Jul. 1974, doi: 10.1016/S0140-6736(74)91639-0.
[63] S. Munakomi and B. Mohan Kumar, “Neuroanatomical Basis of Glasgow Coma Scale-A Reappraisal,” *Neurosci. Med.*, vol. 6, pp. 116–120, 2015, doi: 10.4236/nm.2015.63019.
[64] G. Teasdale, A. Maas, F. Lecky, G. Manley, N. Stocchetti, and G. Murray, “The Glasgow Coma Scale at 40 years: Standing the test of time,” *Lancet Neurol.*, vol. 13, no. 8, pp. 844–854, 2014, doi: 10.1016/S1474-4422(14)70120-6.
[65] M. R. Gill, D. G. Reiley, and S. M. Green, “Interrater Reliability of Glasgow Coma Scale Scores in the Emergency Department,” *Ann. Emerg. Med.*, vol. 43, no. 2, pp. 215–223, Feb. 2004, doi: 10.1016/S0196-0644(03)00814-X.
[66] M. M. Lesko *et al.*, “Comparing model performance for survival prediction using total glasgow coma scale and its components in traumatic brain injury,” *J. Neurotrauma*, vol. 30, no. 1, pp. 17–22, Jan. 2013, doi: 10.1089/neu.2012.2438.
[67] J. J. Bazarian, P. Veazie, S. Mookerjee, and E. B. Lerner, “Accuracy of mild traumatic brain injury case ascertainment using ICD-9 codes,” *Acad. Emerg. Med.*, vol. 13, no. 1, pp. 31–38, Jan. 2006, doi: 10.1197/j.aem.2005.07.038.
[68] Z. Habli, F. Kobeissy, and M. L. Khraiche, “Advances in point-of-care platforms for traumatic brain injury: recent developments in diagnostics,” *Rev. Neurosci.*, vol. 33, no. 3, pp. 327–345, Apr. 2022, doi: 10.1515/REVNEURO-2021-0103/ASSET/GRAPHIC/J_REVNEURO-2021-0103_FIG_006.JPG.
[69] N. Stocchetti *et al.*, “Inaccurate early assessment of neurological severity in head injury,” *J. Neurotrauma*, vol. 21, no. 9, pp. 1131–1140, Sep. 2004, doi: 10.1089/neu.2004.21.1131.
[70] M. D. Ward, A. Weber, V. D. Merrill, R. D. Welch, J. J. Bazarian, and R. H. Christenson, “Predictive Performance of Traumatic Brain Injury Biomarkers in High-Risk Elderly Patients,” *J. Appl. Lab. Med.*, vol. 5, no. 1, pp. 91–100, Jan. 2020, doi: 10.1093/jalm.2019.031393.
[71] C. A. Mutch, J. F. Talbott, and A. Gean, “Imaging Evaluation of Acute Traumatic Brain Injury,” *Neurosurg. Clin. N. Am.*, vol. 27, no. 4, pp. 409–439, Oct. 2016, doi: 10.1016/j.nec.2016.05.011.
[72] Y. Liu, C. Wang, Z. Pi, T. Wang, C. Zhang, and J. Cai, “Research on the Potential Biomarkers of Mild Traumatic Brain Injury: a Systematic Review and Bibliometric Analysis,” *Mol. Neurobiol.*, vol. 60, no. 8, pp. 4442–4449, Aug. 2023, doi: 10.1007/S12035-023-03350-7.
[73] L. G. F. Smith *et al.*, “Advanced neuroimaging in traumatic brain injury: an overview,” *Neurosurg. Focus*, vol. 47, no. 6, p. E17, Dec. 2019, doi: 10.3171/2019.9.FOCUS19652.
[74] A. S. Alali *et al.*, “Intracranial pressure monitoring in severe traumatic brain injury: Results from the american college of surgeons trauma quality improvement program,” *J. Neurotrauma*, vol. 30, no. 20, pp. 1737–1746, Oct. 2013, doi: 10.1089/neu.2012.2802.
[75] P. A. Perel *et al.*, “Predicting outcome after traumatic brain injury: Practical prognostic models based on large cohort of international patients,” *BMJ*, vol. 336, no. 7641, pp. 425–429, Feb. 2008, doi: 10.1136/bmj.39461.643438.25.
[76] D. Najem *et al.*, “Traumatic brain injury: Classification, models, and markers,” *Biochem. Cell Biol.*, vol. 96, no. 4, pp. 391–406, 2018, doi: 10.1139/bcb-2016-0160.
[77] O. Calcagnile, A. Anell, and J. Undén, “The addition of S100B to guidelines for management of mild head injury is potentially cost saving,” *BMC Neurol.*, vol. 16, Oct. 2016, doi: 10.1186/s12883-016-0723-z.
[78] J. K. Yue, P. S. Upadhyayula, L. N. Avalos, H. Deng, and K. K. W. Wang, “The role of blood biomarkers for magnetic resonance imaging diagnosis of traumatic brain injury,” *Med.*, vol. 56, no. 2, Feb. 2020, doi: 10.3390/medicina56020087.
[79] R. P. Berger, M. C. Pierce, S. R. Wisniewski, P. D. Adelson, and P. M. Kochanek, “Serum S100B concentrations are increased after closed head injury in children: a preliminary study,” *J. Neurotrauma*, vol. 19, no. 11, pp. 1405–1409, Nov. 2002, doi: 10.1089/089771502320914633.
[80] I. Ballocco *et al.*, “A pilot study evaluating the effect of mannitol and hypertonic saline solution in the treatment of increased intracranial pressure in 2 cats and 1 dog naturally affected by traumatic brain injury,” *J. Vet. Emerg. Crit. Care*, vol. 29, no. 5, pp. 578–584, Sep. 2019, doi: 10.1111/vec.12880.
[81] S. Agrawal, F. Abecasis, and I. Jalloh, “Neuromonitoring in Children with Traumatic Brain Injury,” *Neurocrit. Care*, Jun. 2023, doi: 10.1007/S12028-023-01779-1.
[82] B. C. D. Faria *et al.*, “The use of noninvasive measurements of intracranial pressure in patients with traumatic brain injury: a narrative review,” *Arq. Neuropsiquiatr.*, vol. 81, no. 6, pp. 551–563, Jun. 2023, doi: 10.1055/S-0043-1764411.
[83] C. Li, K. A. Shah, and R. K. Narayan, “Rapid detection of traumatic brain injury,” *Nat. Biomed. Eng.*, vol. 4, no. 6, pp. 579–580, Jun. 2020, doi: 10.1038/s41551-020-0574-1.
[84] J. B. Ware and S. Jha, “Balancing Underdiagnosis and Overdiagnosis: The Case of Mild Traumatic Brain Injury,” *Acad. Radiol.*, vol. 22, no. 8, pp. 1038–1039, 2015, doi: 10.1016/j.acra.2015.05.004.
[85] “Head Injury: Rehabilitation,” *House of Commons Health*, 2001. https://publications.parliament.uk/pa/cm200001/cmselect/cmhealth/307/30703.htm (accessed May 14, 2021).
[86] C. Childs, Y. T. in. Ong, M. M. yin. Zu, P. W. a. Aung, C. Y. Cheung, and W. S. e. Kuan, “Retinal imaging: a first report of the retinal microvasculature in acute mild traumatic brain injury,” *Eur. J. Emerg. Med.*, vol. 21, no. 5, pp. 388–389, Oct. 2014, doi: 10.1097/MEJ.0000000000000169.
[87] A. Van Gils *et al.*, “Management of mild traumatic brain injury,” *Pract. Neurol.*, vol. 20, no. 3, pp. 213–221, May 2020, doi: 10.1136/practneurol-2018-002087.
[88] J. Pundlik, R. Perna, and A. Arenivas, “Mild TBI in interdisciplinary neurorehabilitation: Treatment challenges and insights,” *NeuroRehabilitation*, vol. 46, no. 2, pp. 227–241, 2020, doi: 10.3233/NRE-192971.
[89] S. Y. Song *et al.*, “Analysis of Mortality and Epidemiology in 2617 Cases of Traumatic Brain Injury : Korean Neuro-Trauma Data Bank System 2010–2014,” *J. Korean Neurosurg. Soc.*, vol. 59, no. 5, p. 485, Sep. 2016, doi: 10.3340/JKNS.2016.59.5.485.

[90] J. V. Rosenfeld, A. I. Maas, P. Bragge, M. C. Morganti-Kossmann, G. T. Manley, and R. L. Gruen, “Early management of severe traumatic brain injury,” *Lancet*, vol. 380, no. 9847, pp. 1088–1098, Sep. 2012, doi: 10.1016/S0140-6736(12)60864-2.
[91] A. Khellaf, D. Z. Khan, and A. Helmy, “Recent advances in traumatic brain injury,” *J. Neurol.*, vol. 266, no. 11, pp. 2878–2889, Nov. 2019, doi: 10.1007/s00415-019-09541-4.
[92] G. R. Boto, P. A. Gómez, J. De La Cruz, and R. D. Lobato, “Severe head injury and the risk of early death,” *J. Neurol. Neurosurg. Psychiatry*, vol. 77, no. 9, pp. 1054–1059, 2006, doi: 10.1136/jnnp.2005.087056.
[93] E. Park, J. D. Bell, and A. J. Baker, “Traumatic brain injury: Can the consequences be stopped?,” *CMAJ*, vol. 178, no. 9, pp. 1163–1170, Apr. 2008, doi: 10.1503/cmaj.080282.
[94] N. Marchesi, F. Fahmideh, F. Boschi, A. Pascale, and A. Barbieri, “Ocular Neurodegenerative Diseases: Interconnection between Retina and Cortical Areas,” *Cells*, vol. 10, no. 9, Sep. 2021, doi: 10.3390/CELLS10092394.
[95] P. Colligris, M. J. P. de Lara, B. Colligris, and J. Pintor, “Ocular Manifestations of Alzheimer’s and Other Neurodegenerative Diseases: The Prospect of the Eye as a Tool for the Early Diagnosis of Alzheimer’s Disease,” *J. Ophthalmol.*, vol. 2018, pp. 1–12, 2018, doi: 10.1155/2018/8538573.
[96] G. Guidoboni *et al.*, “Neurodegenerative Disorders of the Eye and of the Brain: A Perspective on Their Fluid-Dynamical Connections and the Potential of Mechanism-Driven Modeling,” *Front. Neurosci.*, vol. 14, p. 1173, Nov. 2020, doi: 10.3389/FNINS.2020.566428/BIBTEX.
[97] D. Romaus-Sanjurjo *et al.*, “Alzheimer’s Disease Seen through the Eye: Ocular Alterations and Neurodegeneration,” *Int. J. Mol. Sci. 2022, Vol. 23, Page 2486*, vol. 23, no. 5, p. 2486, Feb. 2022, doi: 10.3390/IJMS23052486.
[98] J. H. ; ; Albert *et al.*, “Mild-to-Moderate Traumatic Brain Injury: A Review with Focus on the Visual System,” *Neurol. Int. 2022, Vol. 14, Pages 453-470*, vol. 14, no. 2, pp. 453–470, May 2022, doi: 10.3390/NEUROLINT14020038.
[99] A. Shteyman and B. M. DeBroff, “Ophthalmic Manifestations, Evaluation, and Guidelines for Testing of Concussion,” *Open Ophthalmol. J.*, vol. 17, no. 1, Jan. 2023, doi: 10.2174/18743641-V17-E230111-2022-43.
[100] S. M. Jacobs and G. P. Van Stavern, “Neuro-ophthalmic deficits after head trauma,” *Curr. Neurol. Neurosci. Rep.*, vol. 13, no. 11, pp. 1–9, Nov. 2013, doi: 10.1007/s11910-013-0389-5.
[101] T. C. Yin *et al.*, “Acute axonal degeneration drives development of cognitive, motor, and visual deficits after blast-mediated traumatic brain injury in mice,” *eNeuro*, vol. 3, no. 5, pp. 1–11, Sep. 2016, doi: 10.1523/ENEURO.0220-16.2016.
[102] N. H. Guley *et al.*, “A Novel Closed-Head Model of Mild Traumatic Brain Injury Using Focal Primary Overpressure Blast to the Cranium in Mice,” *J. Neurotrauma*, vol. 33, no. 4, pp. 403–422, Feb. 2016, doi: 10.1089/neu.2015.3886.
[103] Y. J. Chen *et al.*, “Longitudinal relationship between traumatic brain injury and the risk of incident optic neuropathy: A 10-year follow-up nationally representative taiwan survey,” *Oncotarget*, vol. 8, no. 49, pp. 86924–86933, Oct. 2017, doi: 10.18632/oncotarget.21008.
[104] C. S. Gilmore *et al.*, “Association of Optical Coherence Tomography With Longitudinal Neurodegeneration in Veterans With Chronic Mild Traumatic Brain Injury,” *JAMA Netw. open*, vol. 3, no. 12, p. e2030824, Dec. 2020, doi: 10.1001/jamanetworkopen.2020.30824.
[105] A. R. Stevens, Z. Su, E. Toman, A. Belli, and D. Davies, “Optical pupillometry in traumatic brain injury: neurological pupil index and its relationship with intracranial pressure through significant event analysis,” *Brain Inj.*, vol. 33, no. 8, pp. 1032–1038, Jul. 2019, doi: 10.1080/02699052.2019.1605621.
[106] S. Chiquita *et al.*, “The Retina as a Window or Mirror of the Brain Changes Detected in Alzheimer’s Disease: Critical Aspects to Unravel,” *Mol. Neurobiol.*, vol. 56, no. 8, pp. 5416–5435, Aug. 2019, doi: 10.1007/s12035-018-1461-6.
[107] A. I. Ramirez *et al.*, “The role of microglia in retinal neurodegeneration: Alzheimer’s disease, Parkinson, and glaucoma,” *Front. Aging Neurosci.*, vol. 9, no. 214, Jul. 2017, doi: 10.3389/fnagi.2017.00214.
[108] M. Joukal, “Anatomy of the Human Visual Pathway,” in *Homonymous Visual Field Defects*, Springer International Publishing, 2017, pp. 1–16.
[109] C. Y. Cheung, V. T. T. Chan, V. C. Mok, C. Chen, and T. Y. Wong, “Potential retinal biomarkers for dementia,” *Curr. Opin. Neurol.*, vol. 32, no. 1, pp. 82–91, Feb. 2019, doi: 10.1097/WCO.0000000000000645.
[110] M. A. Cerquera-Jaramillo, M. O. Nava-Mesa, R. E. González-Reyes, C. Tellez-Conti, and A. De-La-Torre, “Visual features in Alzheimer’s disease: From basic mechanisms to clinical overview,” *Neural Plast.*, vol. 2018, pp. 1–21, 2018, doi: 10.1155/2018/2941783.
[111] E. Jones-Odeh and C. J. Hammond, “How strong is the relationship between glaucoma, the retinal nerve fibre layer, and neurodegenerative diseases such as Alzheimer’s disease and multiple sclerosis?,” *Eye*, vol. 29, pp. 1270–1284, 2015, doi: 10.1038/eye.2015.158.
[112] A. Serra, C. G. Chisari, and M. Matta, “Eye movement abnormalities in multiple sclerosis: Pathogenesis, modeling, and treatment,” *Front. Neurol.*, vol. 9, no. FEB, p. 31, Feb. 2018, doi: 10.3389/fneur.2018.00031.
[113] S. Frost *et al.*, “Retinal Amyloid Fluorescence Imaging Predicts Cerebral Amyloid Burden and Alzheimer’s Disease,” *Alzheimer’s Dement.*, vol. 10, pp. 234–235, Jul. 2014, doi: 10.1016/j.jalz.2014.04.341.
[114] J. A. Fernández-Albarral *et al.*, “Retinal glial changes in Alzheimer’s disease – A review,” *J. Optom.*, vol. 12, no. 3, pp. 198–207, Jul. 2019, doi: 10.1016/j.optom.2018.07.001.
[115] C. Childs, L. A. Barker, and M. Loosemore, “Eye and Brain Dovepress investigating possible retinal biomarkers of head trauma in Olympic boxers using optical coherence tomography,” *Eye Brain*, vol. 10, pp. 101–110, 2018, doi: 10.2147/EB.S183042.
[116] O. Mufti, S. Mathew, A. Harris, B. Siesky, K. M. Burgett, and A. C. Verticchio Vercellin, “Ocular changes in traumatic brain injury: A review,” *Eur. J. Ophthalmol.*, vol. 30, no. 5, p. 112067211986697, Aug. 2019, doi:

10.1177/1120672119866974.
[117] M. Hunfalvay, N. P. Murray, C. M. Roberts, A. Tyagi, K. W. Barclay, and F. R. Carrick, “Oculomotor Behavior as a Biomarker for Differentiating Pediatric Patients With Mild Traumatic Brain Injury and Age Matched Controls,” *Front. Behav. Neurosci.*, vol. 14, no. 581819, Nov. 2020, doi: 10.3389/fnbeh.2020.581819.
[118] S. Lemke, G. C. Cockerham, C. Glynn-Milley, R. Lin, and K. P. Cockerham, “Automated Perimetry and Visual Dysfunction in Blast-Related Traumatic Brain Injury,” *Ophthalmology*, vol. 123, no. 2, pp. 415–424, 2016, doi: 10.1016/j.ophtha.2015.10.003.
[119] R. Tzekov *et al.*, “Repetitive mild traumatic brain injury causes optic nerve and retinal damage in a mouse model,” *J. Neuropathol. Exp. Neurol.*, vol. 73, no. 4, pp. 345–361, 2014, doi: 10.1097/NEN.0000000000000059.
[120] A. Mohammed Sulaiman *et al.*, “Stereology and ultrastructure of chronic phase axonal and cell soma pathology in stretch-injured central nerve fibers,” *J. Neurotrauma*, vol. 28, no. 3, pp. 383–400, Mar. 2011, doi: 10.1089/neu.2010.1707.
[121] K. Mohan, H. Kecova, E. Hernandez-Merino, R. H. Kardon, and M. M. Harper, “Retinal ganglion cell damage in an experimental rodent model of blast-mediated traumatic brain injury,” *Investig. Ophthalmol. Vis. Sci.*, vol. 54, no. 5, pp. 3440–3450, Apr. 2013, doi: 10.1167/iovs.12-11522.
[122] R. Tzekov *et al.*, “Sub-Chronic neuropathological and biochemical changes in mouse visual system after repetitive mild traumatic brain injury,” *PLoS One*, vol. 11, no. 4, Apr. 2016, doi: 10.1371/journal.pone.0153608.
[123] N. K. Evanson, F. Guilhaume-Correa, J. P. Herman, and M. D. Goodman, “Optic tract injury after closed head traumatic brain injury in mice: A model of indirect traumatic optic neuropathy,” *PLoS One*, vol. 13, no. 5, May 2018, doi: 10.1371/journal.pone.0197346.
[124] L. Xu *et al.*, “Repetitive mild traumatic brain injury with impact acceleration in the mouse: Multifocal axonopathy, neuroinflammation, and neurodegeneration in the visual system,” *Exp. Neurol.*, vol. 275, pp. 436–449, Jan. 2016, doi: 10.1016/j.expneurol.2014.11.004.
[125] J. Wang, R. J. Hamm, and J. T. Povlishock, “Traumatic axonal injury in the optic nerve: Evidence for axonal swelling, disconnection, dieback, and reorganization,” *J. Neurotrauma*, vol. 28, no. 7, pp. 1185–1198, Jul. 2011, doi: 10.1089/neu.2011.1756.
[126] J. Christensen, D. K. Wright, G. R. Yamakawa, S. R. Shultz, and R. Mychasiuk, “Repetitive Mild Traumatic Brain Injury Alters Glymphatic Clearance Rates in Limbic Structures of Adolescent Female Rats,” *Sci. Rep.*, vol. 10, no. 1, pp. 1–9, Dec. 2020, doi: 10.1038/s41598-020-63022-7.
[127] N. A. Jessen, A. S. F. Munk, I. Lundgaard, and M. Nedergaard, “The Glymphatic System: A Beginner’s Guide,” *Neurochem. Res.*, vol. 40, no. 12, pp. 2583–2599, Dec. 2015, doi: 10.1007/s11064-015-1581-6.
[128] E. Mathieu, N. Gupta, R. L. Macdonald, J. Ai, and Y. Yucel, “Does Cerebrospinal Fluid Communicate with the Eye?,” *Investig. Ophthalmol. Vis. Sci.*, vol. 54, no. 15, p. 1903, 2013.
[129] V. Govindaraju and R. Bharathi, “Post-traumatic blepharocele in an adult,” *Sultan Qaboos Univ. Med. J.*, vol. 13, no. 3, pp. 479–481, 2013, doi: 10.12816/0003279.
[130] M. K. Rasmussen, H. Mestre, and M. Nedergaard, “The glymphatic pathway in neurological disorders,” *Lancet Neurol.*, vol. 17, no. 11, pp. 1016–1024, Nov. 2018, doi: 10.1016/S1474-4422(18)30318-1.
[131] S. Kashyap *et al.*, “Osteopathic Manipulative Treatment to Optimize the Glymphatic Environment in Severe Traumatic Brain Injury Measured With Optic Nerve Sheath Diameter, Intracranial Pressure Monitoring, and Neurological Pupil Index,” *Cureus*, vol. 13, no. 3, Mar. 2021, doi: 10.7759/cureus.13823.
[132] B. A. Plog *et al.*, “Biomarkers of traumatic injury are transported from brain to blood via the glymphatic system,” *J. Neurosci.*, vol. 35, no. 2, pp. 518–526, Jan. 2015, doi: 10.1523/JNEUROSCI.3742-14.2015.
[133] Y. M. Paez, L. I. Mudie, and P. S. Subramanian, “Spaceflight associated neuro-ocular syndrome (Sans): A systematic review and future directions,” *Eye Brain*, vol. 12, pp. 105–117, 2020, doi: 10.2147/EB.S234076.
[134] A. G. Lee *et al.*, “Spaceflight associated neuro-ocular syndrome (SANS) and the neuro-ophthalmologic effects of microgravity: a review and an update,” *npj Microgravity*, vol. 6, no. 1, pp. 1–10, Dec. 2020, doi: 10.1038/s41526-020-0097-9.
[135] T. Mader, C. Gibson, N. Miller, P. Subramanian, N. Patel, and A. Lee, “An overview of spaceflight-associated neuro-ocular syndrome (SANS),” *Neurol. India*, vol. 67, no. 8, pp. S206–S211, May 2019, doi: 10.4103/0028-3886.259126.
[136] H. E. Killer, G. P. Jaggi, J. Flammer, N. R. Miller, and A. R. Huber, “The optic nerve: a new window into cerebrospinal fluid composition?,” *Brain*, vol. 129, pp. 1027–1030, 2006, doi: 10.1093/brain/awl045.
[137] J.-W. Oh, S.-H. Kim, and K. Whang, “Traumatic Cerebrospinal Fluid Leak: Diagnosis and Management,” *Korean J. Neurotrauma*, vol. 13, no. 2, p. 63, 2017, doi: 10.13004/kjnt.2017.13.2.63.
[138] R. A. Guyer and J. H. Turner, “Delayed presentation of traumatic cerebrospinal fluid rhinorrhea: Case report and literature review,” *Allergy Rhinol.*, vol. 6, no. 3, pp. 188–190, Dec. 2015, doi: 10.2500/ar.2015.6.0132.
[139] A. O. Apkarian, S. L. Hervey-Jumper, and J. D. Trobe, “Cerebrospinal fluid leak presenting as oculorrhea after blunt orbitocranial trauma,” *J. Neuro-Ophthalmology*, vol. 34, no. 3, pp. 271–273, 2014, doi: 10.1097/WNO.0000000000000099.
[140] J. Wang, M. A. Fox, and J. T. Povlishock, “Diffuse traumatic axonal injury in the optic nerve does not elicit retinal ganglion cell loss,” *J. Neuropathol. Exp. Neurol.*, vol. 72, no. 8, pp. 768–781, Aug. 2013, doi: 10.1097/NEN.0b013e31829d8d9d.
[141] A. G. Hamedani and D. R. Gold, “Eyelid dysfunction in neurodegenerative, neurogenetic, and neurometabolic disease,” *Front. Neurol.*, vol. 8, no. JUL, p. 329, Jul. 2017, doi: 10.3389/fneur.2017.00329.
[142] C. Stiebing *et al.*, “Biochemical Characterization of Mouse Retina of an Alzheimer’s Disease Model by Raman Spectroscopy,” *ACS Chem. Neurosci.*, vol. 11, no. 20, pp. 3301–3308, Oct. 2020, doi: 10.1021/acschemneuro.0c00420.
[143] E. Martinez-Lapiscina *et al.*, “Molecular Imaging of the human retina by Raman Spectroscopy (I1-1B),” *Neurology*, vol. 84, no. 14 Supplement, 2015.

[144] I. M. Pavisic *et al.*, “Eyetracking metrics in young onset alzheimer’s disease: A Window into cognitive visual functions,” *Front. Neurol.*, vol. 8, p. 1, Aug. 2017, doi: 10.3389/fneur.2017.00377.
[145] J. M. Gelfand, D. S. Goodin, W. J. Boscardin, R. Nolan, A. Cuneo, and A. J. Green, “Retinal Axonal Loss Begins Early in the Course of Multiple Sclerosis and Is Similar between Progressive Phenotypes,” *PLoS One*, vol. 7, no. 5, p. e36847, May 2012, doi: 10.1371/journal.pone.0036847.
[146] R. Mani, L. Asper, and S. K. Khuu, “Deficits in saccades and smooth-pursuit eye movements in adults with traumatic brain injury: a systematic review and meta-analysis,” *Brain Inj.*, vol. 32, no. 11, pp. 1315–1336, Sep. 2018, doi: 10.1080/02699052.2018.1483030.
[147] U. Samadani *et al.*, “Eye tracking for classification of concussion in adults and pediatrics,” *Front. Neurol.*, vol. 13, p. 1039955, Dec. 2022, doi: 10.3389/FNEUR.2022.1039955/BIBTEX.
[148] E. Pretegiani and L. M. Optican, “Eye movements in Parkinson’s disease and inherited parkinsonian syndromes,” *Front. Neurol.*, vol. 8, no. NOV, p. 592, Nov. 2017, doi: 10.3389/fneur.2017.00592.
[149] S. Gupta, R. Zivadinov, M. Ramanathan, and B. Weinstock-Guttman, “Optical coherence tomography and neurodegeneration: are eyes the windows to the brain?,” *Expert Rev. Neurother.*, vol. 16, no. 7, pp. 765–775, Jul. 2016, doi: 10.1080/14737175.2016.1180978.
[150] K. Goto *et al.*, “Sectoral analysis of the retinal nerve fiber layer thinning and its association with visual field loss in homonymous hemianopia caused by post-geniculate lesions using spectral-domain optical coherence tomography,” *Graefe’s Arch. Clin. Exp. Ophthalmol.*, vol. 254, no. 4, pp. 745–756, Apr. 2016, doi: 10.1007/s00417-015-3181-1.
[151] J. A. Micieli, R. J. Blanch, and K. Narayana, “Teaching NeuroImages: Evolving trans-synaptic degeneration of retinal ganglion cells after occipital lobe stroke,” *Neurology*, vol. 90, no. 24, pp. 2174–2178, Jun. 2018, doi: 10.1212/WNL.0000000000005686.
[152] C. E. Super *et al.*, “Increased Optic Nerve Sheath Diameter after Mild Traumatic Brain Injury in a High-Risk Population (P2.9-054),” *Neurology*, vol. 92, no. 15 Supplement, 2019, Accessed: Jun. 15, 2020. [Online]. Available: https://n.neurology.org/content/92/15_Supplement/P2.9-054.
[153] M. Lyon *et al.*, “Effect of History of Mild Traumatic Brain Injury on Optic Nerve Sheath Diameter Changes after Valsalva Maneuver,” *J. Neurotrauma*, vol. 35, no. 4, pp. 695–702, Feb. 2018, doi: 10.1089/neu.2017.5164.
[154] S. K. Das, S. P. Shetty, and K. K. Sen, “A novel triage tool: Optic nerve sheath diameter in traumatic brain injury and its correlation to rotterdam computed tomography (CT) scoring,” *Polish J. Radiol.*, vol. 82, pp. 240–243, Apr. 2017, doi: 10.12659/PJR.900196.
[155] S. S. Sadrameli *et al.*, “Changes in Transcranial Sonographic Measurement of the Optic Nerve Sheath Diameter in Non-concussed Collegiate Soccer Players Across a Single Season,” *Cureus*, vol. 10, no. 8, Aug. 2018, doi: 10.7759/cureus.3090.
[156] J. W. Chan, N. K. Hills, B. Bakall, and B. Fernandez, “Indirect traumatic optic neuropathy in mild chronic traumatic brain injury,” *Investig. Ophthalmol. Vis. Sci.*, vol. 60, no. 6, pp. 2005–2011, May 2019, doi: 10.1167/iovs.18-26094.
[157] B. Gopinath *et al.*, “Association between head injury and concussion with retinal vessel caliber,” *PLoS One*, vol. 13, no. 7, Jul. 2018, doi: 10.1371/journal.pone.0200441.
[158] L. E. Goldstein *et al.*, “Chronic traumatic encephalopathy in blast-exposed military veterans and a blast neurotrauma mouse model,” *Sci. Transl. Med.*, vol. 4, no. 134, May 2012, doi: 10.1126/scitranslmed.3003716.
[159] C. N. Thomas *et al.*, “Assessment of necroptosis in the retina in a repeated primary ocular blast injury mouse model,” *Exp. Eye Res.*, vol. 197, Aug. 2020, doi: 10.1016/j.exer.2020.108102.
[160] A. Dadas, J. Washington, R. Diaz-Arrastia, and D. Janigro, “Biomarkers in traumatic brain injury (TBI): A review,” *Neuropsychiatr. Dis. Treat.*, vol. 14, pp. 2989–3000, 2018, doi: 10.2147/NDT.S125620.
[161] Y. Wang, P. Zhao, L. Mao, Y. Hou, and D. Li, “Determination of brain injury biomarkers by surface-enhanced Raman scattering using hollow gold nanospheres,” *RSC Adv.*, vol. 8, no. 6, pp. 3143–3150, Jan. 2018, doi: 10.1039/c7ra12410d.
[162] H. Adrian, K. Mårten, N. Salla, and V. Lasse, “Biomarkers of traumatic brain injury: Temporal changes in body fluids,” *eNeuro*, vol. 3, no. 6, pp. 1–13, Dec. 2016, doi: 10.1523/ENEURO.0294-16.2016.
[163] L. Papa *et al.*, “Serum levels of ubiquitin C-terminal hydrolase distinguish mild traumatic brain injury from trauma controls and are elevated in mild and moderate traumatic brain injury patients with intracranial lesions and neurosurgical intervention,” *J. Trauma Acute Care Surg.*, vol. 72, no. 5, pp. 1335–1344, May 2012, doi: 10.1097/TA.0b013e3182491e3d.
[164] L. Papa *et al.*, “Elevated levels of serum glial fibrillary acidic protein breakdown products in mild and moderate traumatic brain injury are associated with intracranial lesions and neurosurgical intervention,” *Ann. Emerg. Med.*, vol. 59, no. 6, pp. 471–483, Jun. 2012, doi: 10.1016/j.annemergmed.2011.08.021.
[165] S. Mondello *et al.*, “Clinical utility of serum levels of ubiquitin C-terminal hydrolase as a biomarker for severe traumatic brain injury.,” *Neurosurgery*, vol. 70, no. 3, pp. 666–675, 2012, doi: 10.1227/NEU.0b013e318236a809.
[166] T. Mehta *et al.*, “Current Trends in Biomarkers for Traumatic Brain Injury,” *Open Access J Neurol Neurosurg*, vol. 12, no. 4, pp. 86–94, 2020, doi: 10.19080/OAJNN.2020.12.555842.
[167] E. Czeiter *et al.*, “Blood biomarkers on admission in acute traumatic brain injury: Relations to severity, CT findings and care path in the CENTER-TBI study,” *EBioMedicine*, vol. 56, 2020, doi: 10.1016/j.ebiom.2020.102785.
[168] F. H. Kobeissy *et al.*, “Neuroproteomics and systems biology-based discovery of protein biomarkers for traumatic brain injury and clinical validation,” *Proteomics - Clin. Appl.*, vol. 2, no. 10–11, pp. 1467–1483, 2008, doi: 10.1002/prca.200800011.
[169] A. Rodríguez-Rodríguez *et al.*, “Role of S100B protein in urine and serum as an early predictor of mortality after severe traumatic brain injury in adults,” *Clin. Chim. Acta*, vol. 414, pp. 228–233, Dec. 2012, doi: 10.1016/j.cca.2012.09.025.

[170] C. Yeung, R. Bhatia, B. Bhattarai, and M. Sinha, “Role of Salivary Biomarkers in Predicting Significant Traumatic Brain Injury: An Exploratory Study,” *Pediatr. Emerg. Care*, vol. 37, no. 12, pp. 1371–1376, 2021, doi: 10.1097/PEC.0000000000002050.
[171] A. Ercole, E. P. Thelin, A. Holst, B. M. Bellander, and D. W. Nelson, “Kinetic modelling of serum S100b after traumatic brain injury,” *BMC Neurol.*, vol. 16, no. 1, p. 93, Jun. 2016, doi: 10.1186/s12883-016-0614-3.
[172] V. A. Guedes *et al.*, “Exosomal neurofilament light: A prognostic biomarker for remote symptoms after mild traumatic brain injury?,” *Neurology*, vol. 94, no. 23, pp. e2412–e2423, Jun. 2020, doi: 10.1212/WNL.0000000000009577.
[173] R. D. Welch *et al.*, “Ability of serum glial fibrillary acidic protein, ubiquitin C-Terminal Hydrolase-L1, and S100B to differentiate normal and abnormal head computed tomography findings in patients with suspected mild or moderate traumatic brain injury,” *J. Neurotrauma*, vol. 33, no. 2, pp. 203–214, Jan. 2016, doi: 10.1089/neu.2015.4149.
[174] S. Çevik *et al.*, “NRGN, S100B and GFAP levels are significantly increased in patients with structural lesions resulting from mild traumatic brain injuries,” *Clin. Neurol. Neurosurg.*, vol. 183, Aug. 2019, doi: 10.1016/j.clineuro.2019.105380.
[175] M. Edalatfar *et al.*, “Biofluid Biomarkers in Traumatic Brain Injury: A Systematic Scoping Review,” *Neurocrit. Care*, vol. 35, no. 2, pp. 559–572, 2021, doi: 10.1007/s12028-020-01173-1.
[176] C. Reis *et al.*, “What’s new in traumatic brain injury: Update on tracking, monitoring and treatment,” *Int. J. Mol. Sci.*, vol. 16, no. 6, pp. 11903–11965, May 2015, doi: 10.3390/ijms160611903.
[177] C. Oris, S. Kahouadji, J. Durif, D. Bouvier, and V. Sapin, “S100B, Actor and Biomarker of Mild Traumatic Brain Injury,” *Int. J. Mol. Sci.*, vol. 24, no. 7, Apr. 2023, doi: 10.3390/IJMS24076602.
[178] O. Hansson, “Biomarkers for neurodegenerative diseases,” *Nat. Med. 2021 276*, vol. 27, no. 6, pp. 954–963, Jun. 2021, doi: 10.1038/s41591-021-01382-x.
[179] A. Jeromin and R. Bowser, “Biomarkers in Neurodegenerative Diseases,” in *Advances in Neurobiology*, vol. 15, Springer New York LLC, 2017, pp. 491–528.
[180] M. U. Gutierre, J. P. M. Telles, L. C. Welling, N. N. Rabelo, M. J. Teixeira, and E. G. Figueiredo, “Biomarkers for traumatic brain injury: a short review,” *Neurosurg. Rev.*, vol. 44, no. 4, pp. 2091–2097, 2021, doi: 10.1007/s10143-020-01421-0.
[181] J. A. Pineda, K. K. W. Wang, and R. L. Hayes, “Biomarkers of proteolytic damage following traumatic brain injury,” in *Brain Pathology*, 2004, vol. 14, no. 2, pp. 202–209, doi: 10.1111/j.1750-3639.2004.tb00054.x.
[182] S. Yokobori *et al.*, “Biomarkers for the Clinical Differential Diagnosis in Traumatic Brain Injury-A Systematic Review,” *CNS Neurosci. Ther.*, vol. 19, pp. 556–565, 2013, doi: 10.1111/cns.12127.
[183] A. Ercole *et al.*, “Current and emerging technologies for probing molecular signatures of traumatic brain injury,” *Front. Neurol.*, vol. 8, Aug. 2017, doi: 10.3389/fneur.2017.00450.
[184] S. Shen, R. R. O. Loo, I. B. Wanner, and J. A. Loo, “Addressing the needs of traumatic brain injury with clinical proteomics,” *Clin. Proteomics*, vol. 11, no. 1, 2014, doi: 10.1186/1559-0275-11-11.
[185] S. M. Bloomfield, J. McKinney, L. Smith, and J. Brisman, “Reliability of S100B in predicting severity of central nervous system injury,” *Neurocrit. Care*, vol. 6, no. 2, pp. 121–138, Apr. 2007, doi: 10.1007/s12028-007-0008-x.
[186] A. Franjević, R. Pavićević, and G. Bubanović, “Differences in initial NSE levels in malignant and benign diseases of the thoracic wall,” *Clin. Lab.*, vol. 58, no. 3–4, pp. 245–252, 2012, [Online]. Available: https://pubmed.ncbi.nlm.nih.gov/22582497/.
[187] V. Sapin, R. Gaulmin, R. Aubin, S. Walrand, A. Coste, and M. Abbot, “Blood biomarkers of mild traumatic brain injury: state of art,” *Neurochirurgie*, vol. 67, no. 3, pp. 249–254, Jan. 2021, doi: 10.1016/j.neuchi.2021.01.001.
[188] P. Biberthaler *et al.*, “Evaluation of Acute Glial Fibrillary Acidic Protein and Ubiquitin C-Terminal Hydrolase-L1 Plasma Levels in Traumatic Brain Injury Patients with and without Intracranial Lesions,” *Neurotrauma reports*, vol. 2, no. 1, pp. 617–625, Dec. 2021, doi: 10.1089/NEUR.2021.0048.
[189] J. Sen *et al.*, “Extracellular fluid S100B in the injured brain: A future surrogate marker of acute brain injury?,” *Acta Neurochir. (Wien).*, vol. 147, no. 8, pp. 897–900, Aug. 2005, doi: 10.1007/s00701-005-0526-2.
[190] A. E. Böhmer *et al.*, “Neuron-specific enolase, S100B, and glial fibrillary acidic protein levels as outcome predictors in patients with severe traumatic brain injury,” *Neurosurgery*, vol. 1. Böhmer, no. 6, pp. 1624–1630, Jun. 2011, doi: 10.1227/NEU.0b013e318214a81f.
[191] D. O. Okonkwo *et al.*, “Point-of-Care Platform Blood Biomarker Testing of Glial Fibrillary Acidic Protein versus S100 Calcium-Binding Protein B for Prediction of Traumatic Brain Injuries: A Transforming Research and Clinical Knowledge in Traumatic Brain Injury Study,” *J. Neurotrauma*, vol. 37, no. 23, pp. 2460–2467, Sep. 2020, doi: 10.1089/neu.2020.7140.
[192] S. Kahouadji *et al.*, “S100B Blood Level Determination for Early Management of Ski-Related Mild Traumatic Brain Injury: A Pilot Study,” *Front. Neurol.*, vol. 11, Aug. 2020, doi: 10.3389/fneur.2020.00856.
[193] A. P. Di Battista *et al.*, “Blood biomarkers in moderate-to-severe traumatic brain injury: Potential utility of a multi-marker approach in characterizing outcome,” *Front. Neurol.*, vol. 6, no. MAY, 2015, doi: 10.3389/fneur.2015.00110.
[194] A. Kural, Ş. T. Neijmann, A. Toker, H. Doğan, N. Sever, and S. Sarıkaya, “Evaluation of rat major celluler prion protein for early diagnosis in experimental rat brain trauma model,” *Ulus. Travma ve Acil Cerrahi Derg.*, vol. 26, no. 1, pp. 1–8, Jan. 2020, doi: 10.5505/tjtes.2018.46923.
[195] E. P. Thelin, D. W. Nelson, and B. M. Bellander, “A review of the clinical utility of serum S100B protein levels in the assessment of traumatic brain injury,” *Acta Neurochir. 2016 1592*, vol. 159, no. 2, pp. 209–225, Dec. 2016, doi: 10.1007/S00701-016-3046-3.
[196] D. A. Mendoza *et al.*, “Utility of biomarkers in traumatic brain injury: A narrative review,” *Colomb. J. Anesthesiol.*, vol. 48, no. 3, pp. 155–161, Jul. 2020, doi: 10.1097/CJ9.0000000000000165.
[197] J. Gill *et al.*, “Glial fibrillary acidic protein elevations relate to neuroimaging abnormalities after mild TBI,”

Neurology, vol. 91, no. 15, pp. 1385–1389, 2018, doi: 10.1212/WNL.0000000000006321.
[198] D. O. Okonkwo *et al.*, “Point-of-Care Platform Blood Biomarker Testing of Glial Fibrillary Acidic Protein versus S100 Calcium-Binding Protein B for Prediction of Traumatic Brain Injuries: A Transforming Research and Clinical Knowledge in Traumatic Brain Injury Study,” *J. Neurotrauma*, vol. 37, no. 23, pp. 2460–2467, Dec. 2020, doi: 10.1089/NEU.2020.7140/ASSET/IMAGES/LARGE/NEU.2020.7140_FIGURE3.JPEG.
[199] L. M. Lewis, L. Papa, J. J. Bazarian, A. Weber, R. Howard, and R. D. Welch, “Biomarkers May Predict Unfavorable Neurological Outcome after Mild Traumatic Brain Injury,” *J. Neurotrauma*, vol. 37, no. 24, pp. 2624–2631, Sep. 2020, doi: 10.1089/neu.2020.7071.
[200] R. C. Gardner *et al.*, “Age-Related Differences in Diagnostic Accuracy of Plasma Glial Fibrillary Acidic Protein and Tau for Identifying Acute Intracranial Trauma on Computed Tomography: A TRACK-TBI Study,” *J. Neurotrauma*, vol. 35, no. 20, pp. 2341–2350, Oct. 2018, doi: 10.1089/neu.2018.5694.
[201] R. Diaz-Arrastia *et al.*, “Acute biomarkers of traumatic brain injury: Relationship between plasma levels of ubiquitin C-terminal hydrolase-l1 and glial fibrillary acidic protein,” *J. Neurotrauma*, vol. 31, no. 1, pp. 19–25, 2014, doi: 10.1089/neu.2013.3040.
[202] G. M. Brophy *et al.*, “Biokinetic analysis of ubiquitin C-terminal hydrolase-L1 (UCH-L1) in severe traumatic brain injury patient biofluids,” *J. Neurotrauma*, vol. 28, no. 6, pp. 861–870, Jun. 2011, doi: 10.1089/neu.2010.1564.
[203] J. Li, C. Yu, Y. Sun, and Y. Li, “Serum ubiquitin C-terminal hydrolase L1 as a biomarker for traumatic brain injury: A systematic review and meta-analysis,” *Am. J. Emerg. Med.*, vol. 33, no. 9, pp. 1191–1196, Sep. 2015, doi: 10.1016/j.ajem.2015.05.023.
[204] F. Cheng, Q. Yuan, J. Yang, W. Wang, and H. Liu, “The prognostic value of serum neuron-specific enolase in traumatic brain injury: Systematic review and meta-analysis,” *PLoS One*, vol. 9, no. 9, Sep. 2014, doi: 10.1371/journal.pone.0106680.
[205] D. Slavoaca *et al.*, “Prediction of Neurocognitive Outcome after Moderate-Severe Traumatic Brain Injury Using Serum Neuron-Specific Enolase and S100 biomarkers,” *J. Med. Life*, vol. 13, no. 3, pp. 306–313, Jul. 2020, doi: 10.25122/jml-2020-0147.
[206] K. E. DeDominicis, H. Hwang, C. M. Cartagena, D. A. Shear, and A. M. Boutté, “Cerebrospinal fluid biomarkers are associated with glial fibrillary acidic protein and αII-spectrin breakdown products in brain tissues following penetrating ballistic-like brain injury in rats,” *Front. Neurol.*, vol. 9, no. JUL, p. 490, Jul. 2018, doi: 10.3389/fneur.2018.00490.
[207] H. J. Kim, J. W. Tsao, and A. G. Stanfill, “The current state of biomarkers of mild traumatic brain injury,” *JCI insight*, vol. 3, no. 1, Jan. 2018, doi: 10.1172/jci.insight.97105.
[208] S. Mondello *et al.*, “αii-spectrin breakdown products (SBDPs): Diagnosis and outcome in severe traumatic brain injury patients,” *J. Neurotrauma*, vol. 27, no. 7, pp. 1203–1213, Jul. 2010, doi: 10.1089/neu.2010.1278.
[209] S. Schraen-Maschke *et al.*, “Tau as a biomarker of neurodegenerative diseases,” *Biomark. Med.*, vol. 2, no. 4, pp. 363–384, 2008, doi: 10.2217/17520363.2.4.363.
[210] P. Shahim *et al.*, “Time course and diagnostic utility of NfL, tau, GFAP, and UCH-L1 in subacute and chronic TBI,” *Neurology*, vol. 95, no. 6, pp. e623–e636, Aug. 2020, doi: 10.1212/WNL.0000000000009985.
[211] T. aki Nakada, K. Tomita, T. Oshima, R. Kawaguchi, and S. Oda, “Serum levels of tau protein increase according to the severity of the injury in DAI rat model,” *F1000Research*, vol. 9, 2020, doi: 10.12688/f1000research.21132.1.
[212] R. J. Shannon *et al.*, “Extracellular N-Acetylaspartate in Human Traumatic Brain Injury,” *J. Neurotrauma*, vol. 33, no. 4, pp. 319–329, Feb. 2016, doi: 10.1089/neu.2015.3950.
[213] J. J. S. Rickard, V. Di-Pietro, D. J. Smith, D. J. Davies, A. Belli, and P. G. Oppenheimer, “Rapid optofluidic detection of biomarkers for traumatic brain injury via surface-enhanced Raman spectroscopy,” *Nat. Biomed. Eng.*, vol. 4, no. 6, pp. 610–623, Feb. 2020, doi: 10.1038/s41551-019-0510-4.
[214] A. Belli *et al.*, “Extracellular N-acetylaspartate depletion in traumatic brain injury,” *J. Neurochem.*, vol. 96, no. 3, pp. 861–869, Feb. 2006, doi: 10.1111/j.1471-4159.2005.03602.x.
[215] M. R. Garnett, A. M. Blamire, R. G. Corkill, T. A. Cadoux-Hudson, B. Rajagopalan, and P. Styles, “Early proton magnetic resonance spectroscopy in normal-appearing brain correlates with outcome in patients following traumatic brain injury.,” *Brain*, vol. 123 (Pt 1, pp. 2046–54, Oct. 2000, doi: 10.1093/brain/123.10.2046.
[216] I. Pirko, S. T. Fricke, A. J. Johnson, M. Rodriguez, and S. I. Macura, “Magnetic resonance imaging, microscopy, and spectroscopy of the central nervous system in experimental animals,” *NeuroRx*, vol. 2, no. 2, pp. 250–264, 2005, doi: 10.1602/neurorx.2.2.250.
[217] B. D. Ross, “Real or imaginary? Human metabolism through nuclear magnetism,” *IUBMB Life*, vol. 50, no. 3, pp. 177–187, Sep. 2000, doi: 10.1080/152165400300001499.
[218] J. Urenjak, S. R. Williams, D. G. Gadian, and M. Noble, “Specific Expression of N-Acetylaspartate in Neurons, Oligodendrocyte-Type-2 Astrocyte Progenitors, and Immature Oligodendrocytes In Vitro,” *J. Neurochem.*, vol. 59, no. 1, pp. 55–61, 1992, doi: 10.1111/j.1471-4159.1992.tb08875.x.
[219] U. Kawoos *et al.*, “N-acetylcysteine Amide Ameliorates Blast-Induced Changes in Blood-Brain Barrier Integrity in Rats,” *Front. Neurol.*, vol. 10, no. JUN, p. 650, Jun. 2019, doi: 10.3389/fneur.2019.00650.
[220] A. Pastore, G. Federici, E. Bertini, and F. Piemonte, “Analysis of glutathione: Implication in redox and detoxification,” *Clin. Chim. Acta*, vol. 333, no. 1–2, pp. 19–39, Jul. 2003, doi: 10.1016/S0009-8981(03)00200-6.
[221] F. Sivandzade, F. Alqahtani, and L. Cucullo, “Traumatic brain injury and blood–brain barrier (BBB): Underlying pathophysiological mechanisms and the influence of cigarette smoking as a premorbid condition,” *Int. J. Mol. Sci.*, vol. 21, no. 8, Apr. 2020, doi: 10.3390/ijms21082721.
[222] G. Dogan and O. Karaca, “Evaluation of neuroprotective effect of sevoflurane in acute traumatic brain injury: An experimental study in rats,” *Turk. Neurosurg.*, vol. 30, no. 2, pp. 237–243, 2020, doi: 10.5137/1019-5149.JTN.27680-19.2.
[223] R. Rossi *et al.*, “Blood glutathione disulfide: In vivo factor or in vitro artifact?,” *Clin. Chem.*, vol. 48, no. 5, pp.

742–753, May 2002, doi: 10.1093/clinchem/48.5.742.
[224] H. K. Karnati, J. H. Garcia, D. Tweedie, R. E. Becker, D. Kapogiannis, and N. H. Greig, “Neuronal enriched extracellular vesicle proteins as biomarkers for traumatic brain injury,” *J. Neurotrauma*, vol. 36, no. 7, pp. 975–987, Apr. 2019, doi: 10.1089/neu.2018.5898.
[225] S. M. Lippa, J. K. Werner, M. C. Miller, J. M. Gill, R. Diaz-Arrastia, and K. Kenney, “Recent Advances in Blood-Based Biomarkers of Remote Combat-Related Traumatic Brain Injury,” *Curr. Neurol. Neurosci. Rep.*, vol. 20, no. 12, Dec. 2020, doi: 10.1007/s11910-020-01076-w.
[226] S. M. Lippa, J. Gill, T. A. Brickell, L. M. French, and R. T. Lange, “Blood Biomarkers Relate to Cognitive Performance Years after Traumatic Brain Injury in Service Members and Veterans,” *J. Int. Neuropsychol. Soc.*, vol. 27, no. 5, pp. 508–514, 2020, doi: 10.1017/S1355617720001071.
[227] A. Herrold, S. Kletzel, and E. Foecking, “miRNAs as Potential Biomarkers for Traumatic Brain Injury: Pathway From Diagnosis to Neurorehabilitation,” *J. Head Trauma Rehabil.*, vol. 36, no. 3, pp. 155–169, 2020, doi: 10.1097/HTR.0000000000000632.
[228] E. Pinchi *et al.*, “MicroRNAs: The New Challenge for Traumatic Brain Injury Diagnosis,” *Curr. Neuropharmacol.*, vol. 18, no. 4, pp. 319–331, Nov. 2019, doi: 10.2174/1570159x17666191113100808.
[229] Q. Zhou *et al.*, “Micrornas as potential biomarkers for the diagnosis of traumatic brain injury: A systematic review and meta-analysis,” *Int. J. Med. Sci.*, vol. 18, no. 1, pp. 128–136, 2021, doi: 10.7150/ijms.48214.
[230] L. Liu *et al.*, “Traumatic brain injury dysregulates MicroRNAs to modulate cell signaling in rat hippocampus,” *PLoS One*, vol. 9, no. 8, Aug. 2014, doi: 10.1371/journal.pone.0103948.
[231] V. Di Pietro, K. M. Yakoub, U. Scarpa, C. Di Pietro, and A. Belli, “MicroRNA signature of traumatic brain injury: From the biomarker discovery to the point-of-care,” *Front. Neurol.*, vol. 9, no. JUN, Jun. 2018, doi: 10.3389/fneur.2018.00429.
[232] A. R. Mayer *et al.*, “Survival Rates and Biomarkers in A Large Animal Model of Traumatic Brain Injury Combined with Two Different Levels of Blood Loss,” *Shock*, vol. 55, no. 4, pp. 554–562, 2020, doi: 10.1097/SHK.0000000000001653.
[233] C. K. Rhea *et al.*, “Development of a Portable Tool for Screening Neuromotor Sequelae From Repetitive Low-Level Blast Exposure,” *Mil. Med.*, vol. 182, no. S1, pp. 147–154, Mar. 2017, doi: 10.7205/milmed-d-16-00140.
[234] L. Papa *et al.*, “Time Course and Diagnostic Accuracy of Glial and Neuronal Blood Biomarkers GFAP and UCH-L1 in a Large Cohort of Trauma Patients With and Without Mild Traumatic Brain Injury,” *JAMA Neurol.*, vol. 73, no. 5, pp. 551–560, May 2016, doi: 10.1001/JAMANEUROL.2016.0039.
[235] A. Abdelhak *et al.*, “Blood GFAP as an emerging biomarker in brain and spinal cord disorders,” *Nat. Rev. Neurol.*, vol. 18, no. 3, pp. 158–172, Mar. 2022, doi: 10.1038/S41582-021-00616-3.
[236] P. Johnsson, “Markers of Cerebral Ischemia After Cardiac Surgery,” *J. Cardiothorac. Vasc. Anesth.*, vol. 10, no. 1, pp. 120–126, 1996.
[237] Š. G *et al.*, “Tau Protein Hyperphosphorylation and Aggregation in Alzheimer’s Disease and Other Tauopathies, and Possible Neuroprotective Strategies,” *Biomolecules*, vol. 6, no. 1, pp. 2–28, Jan. 2016, doi: 10.3390/BIOM6010006.
[238] Z. S. Gan *et al.*, “Blood biomarkers for traumatic brain injury: A quantitative assessment of diagnostic and prognostic accuracy,” *Front. Neurol.*, vol. 10, no. APR, p. 446, Apr. 2019, doi: 10.3389/fneur.2019.00446.
[239] B. A. Cardinell, C. P. Addington, S. E. Stabenfeldt, and J. T. La Belle, “Multi-biomarker detection following traumatic brain injury,” *Crit. Rev. Biomed. Eng.*, vol. 47, no. 3, pp. 193–206, 2019, doi: 10.1615/CritRevBiomedEng.2019026108.
[240] S. Mondello *et al.*, “Blood-Based Protein Biomarkers for the Management of Traumatic Brain Injuries in Adults Presenting to Emergency Departments with Mild Brain Injury: A Living Systematic Review and Meta-Analysis,” *J. Neurotrauma*, vol. 34, pp. 1–21, Jul. 2017, doi: 10.1089/neu.2017.5182.
[241] T. N. Sager, A. Fink-Jensen, and A. J. Hansen, “Transient Elevation of Interstitial N-Acetylaspartate in Reversible Global Brain Ischemia,” *J. Neurochem.*, vol. 68, no. 2, pp. 675–682, Nov. 1997, doi: 10.1046/j.1471-4159.1997.68020675.x.
[242] K. G. Su, G. Banker, D. Bourdette, and M. Forte, “Axonal degeneration in multiple sclerosis: The mitochondrial hypothesis,” *Curr. Neurol. Neurosci. Rep.*, vol. 9, no. 5, pp. 411–417, 2009, doi: 10.1007/s11910-009-0060-3.
[243] S. Alba-Arbalat *et al.*, “In Vivo Molecular Changes in the Retina of Patients With Multiple Sclerosis,” *Invest. Ophthalmol. Vis. Sci.*, vol. 62, no. 6, May 2021, doi: 10.1167/IOVS.62.6.11.
[244] K. L. Malisza, P. Kozlowski, G. Ning, S. Bascaramurty, and U. I. Tuor, “Metabolite changes in neonatal rat brain during and after cerebral hypoxia-ischemia: a magnetic resonance spectroscopic imaging study.,” *NMR Biomed.*, vol. 12, no. 1, pp. 31–8, Feb. 1999, doi: 10.1002/(sici)1099-1492(199902)12:1<31::aid-nbm544>3.0.co;2-m.
[245] R. H. Al-Samsam, B. Alessandri, and R. Bullock, “Extracellular N-acetyl-aspartate as a biochemical marker of the severity of neuronal damage following experimental acute traumatic brain injury,” *J. Neurotrauma*, vol. 17, no. 1, pp. 31–39, Jan. 2000, doi: 10.1089/neu.2000.17.31.
[246] T. N. Sager, H. Laursen, and A. J. Hansen, “Changes in N-acetyl-aspartate content during focal and global brain ischemia of the rat,” *J. Cereb. Blood Flow Metab.*, vol. 15, no. 4, pp. 639–646, Jul. 1995, doi: 10.1038/jcbfm.1995.79.
[247] K. Sunitha *et al.*, “N-Acetylcysteine amide: A derivative to fulfill the promises of N-Acetylcysteine,” *Free Radic. Res.*, vol. 47, no. 5, pp. 357–367, May 2013, doi: 10.3109/10715762.2013.781595.
[248] G. Bramblett, J. Harris, L. Scott, and A. Holt, “Traumatic Optic Nerve Injury Elevates Plasma Biomarkers of Traumatic Brain Injury in a Porcine Model,” *J. Neurotrauma*, vol. 38, no. 8, pp. 1000–1005, Oct. 2020, doi: 10.1089/neu.2020.7039.
[249] S. Asanad *et al.*, “Retinal nerve fiber layer thickness predicts CSF amyloid/tau before cognitive decline,” *PLoS One*, vol. 15, no. 5, p. e0232785, May 2020, doi: 10.1371/journal.pone.0232785.
[250] H. Oku *et al.*, “Tau is involved in death of retinal ganglion cells of rats from optic nerve crush,” *Investig.*

Ophthalmol. Vis. Sci., vol. 60, no. 6, pp. 2380–2387, May 2019, doi: 10.1167/iovs.19-26683.
[251] M. Chiasseu *et al.*, “Tau accumulation in the retina promotes early neuronal dysfunction and precedes brain pathology in a mouse model of Alzheimer’s disease,” *Mol. Neurodegener.*, vol. 12, no. 1, Aug. 2017, doi: 10.1186/s13024-017-0199-3.
[252] Y. Shu *et al.*, “Involvement of the optic nerve in mutated CSF1R-induced hereditary diffuse leukoencephalopathy with axonal spheroids,” *BMC Neurol.*, vol. 16, no. 1, pp. 1–6, Sep. 2016, doi: 10.1186/s12883-016-0694-0.
[253] B. J. Kelley, J. Lifshitz, and J. T. Povlishock, “Neuroinflammatory responses after experimental diffuse traumatic brain injury,” *J. Neuropathol. Exp. Neurol.*, vol. 66, no. 11, pp. 989–1001, Nov. 2007, doi: 10.1097/NEN.0b013e3181588245.
[254] A. Kumar and D. J. Loane, “Neuroinflammation after traumatic brain injury: Opportunities for therapeutic intervention,” *Brain. Behav. Immun.*, vol. 26, no. 8, pp. 1191–1201, Nov. 2012, doi: 10.1016/j.bbi.2012.06.008.
[255] C. Smith, “Review: The long-term consequences of microglial activation following acute traumatic brain injury,” *Neuropathol. Appl. Neurobiol.*, vol. 39, no. 1, pp. 35–44, Feb. 2013, doi: 10.1111/nan.12006.
[256] R. K. Narayan *et al.*, “Clinical trials in head injury,” *J. Neurotrauma*, vol. 19, no. 5, pp. 503–557, 2002, doi: 10.1089/089771502753754037.
[257] Y. H. Chu, S. Y. Chen, Y. L. Hsieh, Y. H. Teng, and Y. J. Cheng, “Low-level laser therapy prevents endothelial cells from TNF-α/cycloheximide-induced apoptosis,” *Lasers Med. Sci.*, vol. 33, no. 2, pp. 279–286, Feb. 2018, doi: 10.1007/s10103-017-2364-x.
[258] A. Abdelhak *et al.*, “Glial Activation Markers in CSF and Serum From Patients With Primary Progressive Multiple Sclerosis: Potential of Serum GFAP as Disease Severity Marker?,” *Front. Neurol.*, vol. 10, p. 280, Mar. 2019, doi: 10.3389/fneur.2019.00280.
[259] Y. S. Su, J. M. Schuster, D. H. Smith, and S. C. Stein, “Cost-Effectiveness of Biomarker Screening for Traumatic Brain Injury,” *J. Neurotrauma*, vol. 36, no. 13, pp. 2083–2091, Jul. 2019, doi: 10.1089/neu.2018.6020.
[260] “Clinical Studies,” *Banyan Biomarkers*. https://www.banyanbio.com/clinical-studies.html (accessed Jun. 14, 2020).
[261] “New Blood test for concussion,” *University of Maryland School of Medicine*, 2022. https://umem.org/educational_pearls/3401/ (accessed Mar. 31, 2021).
[262] E. Hillman, “Optical brain imaging in vivo: techniques and applications from animal to man,” *J. Biomed. Opt.*, vol. 12, no. 5, p. 051402, 2007, doi: 10.1117/1.2789693.
[263] F. F. Jöbsis, “Noninvasive, infrared monitoring of cerebral and myocardial oxygen sufficiency and circulatory parameters,” *Science (80-.).*, vol. 198, no. 4323, pp. 1264–1266, 1977, doi: 10.1126/science.929199.
[264] B. Kubas, W. Łebkowski, U. Łebkowska, W. Kułak, E. Tarasow, and J. Walecki, “Proton MR spectroscopy in mild traumatic brain injury,” *Polish J. Radiol.*, vol. 75, no. 4, pp. 7–10, 2010, Accessed: Feb. 01, 2021. [Online]. Available: http://www.polradiol.com/fulltxt.php?ICID=881333.
[265] P. K. So, B. Hu, and Z. P. Yao, “Mass spectrometry: Towards in vivo analysis of biological systems,” *Mol. Biosyst.*, vol. 9, no. 5, pp. 915–929, 2013, doi: 10.1039/c2mb25428j.
[266] J. L. Markley *et al.*, “The future of NMR-based metabolomics,” *Curr. Opin. Biotechnol.*, vol. 43, pp. 34–40, Feb. 2017, doi: 10.1016/j.copbio.2016.08.001.
[267] A. H. M. Emwas, “The Strengths and Weaknesses of NMR Spectroscopy and Mass Spectrometry with Particular Focus on Metabolomics Research,” *Methods Mol. Biol.*, vol. 1277, pp. 161–193, 2015, doi: 10.1007/978-1-4939-2377-9_13.
[268] U. Ungerstedt, “Microdialysis—principles and applications for studies in animals and man,” *J. Intern. Med.*, vol. 230, no. 4, pp. 365–373, 1991, doi: 10.1111/j.1365-2796.1991.tb00459.x.
[269] P. S. Narayana, D. Varalakshmi, T. Pullaiah, and K. R. . Sambasiva Rao, *Research Methodology in Zoology*. Scientific Publishers, 2018.
[270] M. G. Stovell *et al.*, “Assessing metabolism and injury in acute human traumatic brain injury with magnetic resonance spectroscopy: Current and future applications,” *Front. Neurol.*, vol. 8, no. SEP, Sep. 2017, doi: 10.3389/fneur.2017.00426.
[271] P. J. Larkin, *Infrared and Raman Spectroscopy: Principles and Spectral Interpretation*. Elsevier Inc., 2011.
[272] A. Lin, B. D. Ross, K. Harris, and W. Wong, “Efficacy of proton magnetic resonance spectroscopy in neurological diagnosis and neurotherapeutic decision making,” *NeuroRx*, vol. 2, no. 2, pp. 197–214, 2005, doi: 10.1602/neurorx.2.2.197.
[273] L. Shutter, K. A. Tong, and B. A. Holshouser, “Proton MRS in acute traumatic brain injury: Role for glutamate/glutamine and choline for outcome prediction,” *J. Neurotrauma*, vol. 21, no. 12, pp. 1693–1705, Dec. 2004, doi: 10.1089/neu.2004.21.1693.
[274] L. Shutter, K. A. Tong, A. Lee, and B. A. Holshouser, “Prognostic role of proton magnetic resonance spectroscopy in acute traumatic brain injury,” *J. Head Trauma Rehabil.*, vol. 21, no. 4, pp. 334–349, Jul. 2006, doi: 10.1097/00001199-200607000-00005.
[275] R. E. A. Green, “Editorial: Brain Injury as a Neurodegenerative Disorder,” *Front. Hum. Neurosci.*, vol. 9, no. JAN2016, p. 615, Jan. 2016, doi: 10.3389/fnhum.2015.00615.
[276] D. M. Jameson and J. A. Ross, “Fluorescence Polarization/Anisotropy in Diagnostics and Imaging,” *Chem. Rev.*, vol. 110, no. 5, pp. 26850–2708, 2010, doi: 10.1021/cr900267p.
[277] B. A. Smith *et al.*, “Multicolor fluorescence imaging of traumatic brain injury in a cryolesion mouse model,” *ACS Chem. Neurosci.*, vol. 3, no. 7, pp. 530–537, Jul. 2012, doi: 10.1021/cn3000197.
[278] M. Vaecha, M. Zimmermann, J. Amrichová, V. Ulman, P. Matula, and M. Kozubek, “Prediction of localization and interactions of apoptotic proteins,” *J. Biomed. Sci.*, vol. 16, no. 1, p. 59, Jul. 2009, doi: 10.1186/1423-0127-16-59.
[279] P. M. Siu, S. Bae, N. Bodyak, D. L. Rigor, and P. M. Kang, “Response of caspase-independent apoptotic factors to high salt diet-induced heart failure,” *J. Mol. Cell. Cardiol.*, vol. 42, no. 3, pp. 678–686, Mar. 2007, doi: 10.1016/j.yjmcc.2007.01.001.

[280] K. J. Huang, H. Wang, M. Ma, X. Zhang, and H. S. Zhang, “Real-time imaging of nitric oxide production in living cells with 1,3,5,7-tetramethyl-2,6-dicarbethoxy-8-(3′,4′-diaminophenyl)-difluoroboradiaza-s-indacence by invert fluorescence microscope,” *Nitric Oxide - Biol. Chem.*, vol. 16, no. 1, pp. 36–43, Feb. 2007, doi: 10.1016/j.niox.2006.05.003.
[281] J. D. Van Horn, A. Bhattrai, and A. Irimia, “Multimodal Imaging of Neurometabolic Pathology due to Traumatic Brain Injury,” *Trends Neurosci.*, vol. 40, no. 1, pp. 39–59, Jan. 2017, doi: 10.1016/j.tins.2016.10.007.
[282] S. S. Ahmad, “An introduction to DARC technology,” *Saudi J. Ophthalmol.*, vol. 31, no. 1, pp. 38–41, Jan. 2017, doi: 10.1016/j.sjopt.2016.08.001.
[283] E. M. Normando *et al.*, “A CNN-aided method to predict glaucoma progression using DARC (Detection of Apoptosing Retinal Cells),” *Expert Rev. Mol. Diagn.*, vol. 20, no. 7, pp. 737–748, Jul. 2020, doi: 10.1080/14737159.2020.1758067.
[284] M. F. Cordeiro *et al.*, “Real-time imaging of single neuronal cell apoptosis in patients with glaucoma,” *Brain*, vol. 140, no. 6, pp. 1757–1767, Jun. 2017, doi: 10.1093/brain/awx088.
[285] K. Bermond *et al.*, “Autofluorescent granules of the human retinal pigment epithelium: phenotypes, intracellular distribution, and age-related topography,” *Investig. Ophthalmol. Vis. Sci.*, vol. 61, no. 5, pp. 35–35, May 2020, doi: 10.1167/IOVS.61.5.35.
[286] A. Samy, S. Lightman, F. Ismetova, L. Talat, and O. Tomkins-Netzer, “Role of autofluorescence in inflammatory/infective diseases of the retina and choroid,” *J. Ophthalmol.*, vol. 2014, pp. 1–9, 2014, doi: 10.1155/2014/418193.
[287] R. Afridi *et al.*, “Fundus Autofluorescence Imaging in Posterior Uveitis,” in *Multimodal Imaging in Uveitis*, Springer International Publishing, 2018, pp. 69–85.
[288] M. Yung, M. A. Klufas, and D. Sarraf, “Clinical applications of fundus autofluorescence in retinal disease,” *Int. J. Retin. Vitr. 2016 21*, vol. 2, no. 1, pp. 1–25, Apr. 2016, doi: 10.1186/S40942-016-0035-X.
[289] P. Malamos *et al.*, “The Role of Fundus Autofluorescence Imaging in the Study of the Course of Posterior Uveitis Disorders,” *Biomed Res. Int.*, vol. 2015, pp. 1–11, 2015, doi: 10.1155/2015/247469.
[290] L. C. Cancio *et al.*, “Hyperspectral imaging: A new approach to the diagnosis of hemorrhagic shock,” *J. Trauma - Inj. Infect. Crit. Care*, vol. 60, no. 5, pp. 1087–1095, May 2006, doi: 10.1097/01.ta.0000217357.10617.3d.
[291] S. L. Jacques, “Optical properties of biological tissues: A review,” *Phys. Med. Biol.*, vol. 58, no. 11, p. R37, Jun. 2013, doi: 10.1088/0031-9155/58/11/R37.
[292] L. V. Wang and H. Wu, *Biomedical Optics: Principles and Imaging*. Wiley, 2007.
[293] A. K. Dunn *et al.*, “Simultaneous imaging of total cerebral hemoglobin concentration, oxygenation, and blood flow during functional activation,” *Opt. Lett.*, vol. 28, no. 1, p. 28, Jan. 2003, doi: 10.1364/ol.28.000028.
[294] L. Giannoni, F. Lange, and I. Tachtsidis, “Hyperspectral imaging solutions for brain tissue metabolic and hemodynamic monitoring: past, current and future developments,” *J. Opt.*, vol. 20, no. 4, p. 044009, Mar. 2018, doi: 10.1088/2040-8986/AAB3A6.
[295] W. R. Johnson, D. W. Wilson, W. Fink, M. Humayun, and G. Bearman, “Snapshot hyperspectral imaging in ophthalmology,” *J. Biomed. Opt.*, vol. 12, no. 1, p. 014036, 2007, doi: 10.1117/1.2434950.
[296] A. R. Harvey, J. Lawlor, A. I. McNaught, J. W. Williams, and D. W. Fletcher-Holmes, “Hyperspectral imaging for the detection of retinal disease,” *Imaging Spectrom. VIII*, vol. 4816, p. 325, Nov. 2002, doi: 10.1117/12.451693.
[297] I. B. Styles, A. Calcagni, E. Claridge, F. Orihuela-Espina, and J. M. Gibson, “Quantitative analysis of multi-spectral fundus images,” *Med. Image Anal.*, vol. 10, no. 4, pp. 578–597, Aug. 2006, doi: 10.1016/j.media.2006.05.007.
[298] A. Calcagni, J. M. Gibson, I. B. Styles, E. Claridge, and F. Orihuela-Espina, “Multispectral retinal image analysis: A novel non-invasive tool for retinal imaging,” *Eye*, vol. 25, no. 12, pp. 1562–1569, 2011, doi: 10.1038/eye.2011.202.
[299] N. L. Everdell, I. B. Styles, A. Calcagni, J. Gibson, J. Hebden, and E. Claridge, “Multispectral imaging of the ocular fundus using light emitting diode illumination,” *Rev. Sci. Instrum.*, vol. 81, no. 9, Sep. 2010, doi: 10.1063/1.3478001.
[300] H. M. Chen *et al.*, “Comparison of Multispectral Image-Processing Methods for Brain Tissue Classification in BrainWeb Synthetic Data and Real MR Images,” *Biomed Res. Int.*, vol. 2021, 2021, doi: 10.1155/2021/9820145.
[301] A. Currà *et al.*, “Near-infrared spectroscopy as a tool for in vivo analysis of human muscles,” *Sci. Rep.*, vol. 9, no. 1, pp. 1–14, Dec. 2019, doi: 10.1038/s41598-019-44896-8.
[302] B. Lagerwaard, A. G. Nieuwenhuizen, V. C. J. de Boer, and J. Keijer, “In vivo assessment of mitochondrial capacity using NIRS in locomotor muscles of young and elderly males with similar physical activity levels,” *GeroScience*, vol. 42, no. 1, pp. 299–310, Feb. 2020, doi: 10.1007/s11357-019-00145-4.
[303] T. Hamaoka and K. K. McCully, “Review of early development of near-infrared spectroscopy and recent advancement of studies on muscle oxygenation and oxidative metabolism,” *J. Physiol. Sci.*, vol. 69, no. 6, pp. 799–811, Nov. 2019, doi: 10.1007/s12576-019-00697-2.
[304] A. N. Sen, S. P. Gopinath, and C. S. Robertson, “Clinical application of near-infrared spectroscopy in patients with traumatic brain injury: a review of the progress of the field,” *Neurophotonics*, vol. 3, no. 3, p. 031409, Apr. 2016, doi: 10.1117/1.nph.3.3.031409.
[305] J. M. Murkin and M. Arango, “Near-infrared spectroscopy as an index of brain and tissue oxygenation,” *Br. J. Anaesth.*, vol. 103, no. SUPPL.1, pp. i3-13, 2009, doi: 10.1093/bja/aep299.
[306] H. Owen-Reece, M. Smith, C. E. Elwell, and J. C. Goldstone, “Near infrared spectroscopy,” *Br. J. Anaesth.*, vol. 82, no. 3, pp. 418–444, 1999.
[307] R. S. Samraj and L. Nicolas, “Near infrared spectroscopy (NIRS) derived tissue oxygenation in critical illness,” *Clin. Investig. Med.*, vol. 38, no. 5, pp. 285–295, 2015, doi: 10.25011/cim.v38i5.25685.
[308] A. Bhardwaj, H. Bhagat, and V. K. Grover, “Jugular venous oximetry,” *J. Neuroanaesth. Crit. Care*, vol. 02, no. 03, pp. 225–231, May 2018, doi: 10.4103/2348-0548.165046.

[309] C. Berry *et al.*, “Redefining hypotension in traumatic brain injury,” *Injury*, vol. 43, no. 11, pp. 1833–1837, 2012, doi: 10.1016/j.injury.2011.08.014.
[310] M. Roldán and P. A. Kyriacou, “Near-Infrared Spectroscopy (NIRS) in Traumatic Brain Injury (TBI),” *Sensors (Basel).*, vol. 21, no. 5, pp. 1–30, Mar. 2021, doi: 10.3390/S21051586.
[311] H.-B. Liu, Y. Chen, G. J. Bastiaans, and X.-C. Zhang, “Detection and identification of explosive RDX by THz diffuse reflection spectroscopy,” *Opt. Express*, vol. 14, no. 1, p. 415, Jan. 2006, doi: 10.1364/opex.14.000415.
[312] M. Bernier, F. Garet, and J. L. Coutaz, “Precise determination of the refractive index of samples showing low transmission bands by THz time-domain spectroscopy,” *IEEE Trans. Terahertz Sci. Technol.*, vol. 3, no. 3, pp. 295–301, 2013, doi: 10.1109/TTHZ.2013.2247793.
[313] G. R. Musina *et al.*, “Prospects of terahertz technology in diagnosis of human brain tumors – A review,” *J. Biomed. Photonics Eng.*, vol. 6, no. 2, pp. 1–11, 2020, doi: 10.18287/JBPE20.06.020201.
[314] H. Zhao *et al.*, “High-sensitivity terahertz imaging of traumatic brain injury in a rat model,” *J. Biomed. Opt.*, vol. 23, no. 03, p. 1, Mar. 2018, doi: 10.1117/1.JBO.23.3.036015.
[315] Y. Wang *et al.*, “Terahertz spectroscopic diagnosis of early blast-induced traumatic brain injury in rats,” *Biomed. Opt. Express*, vol. 11, no. 8, p. 4085, Aug. 2020, doi: 10.1364/boe.395432.
[316] K. Kong, C. Kendall, N. Stone, and I. Notingher, “Raman spectroscopy for medical diagnostics - From in-vitro biofluid assays to in-vivo cancer detection,” *Adv. Drug Deliv. Rev.*, vol. 89, pp. 121–134, Jul. 2015, doi: 10.1016/j.addr.2015.03.009.
[317] E. Cordero, I. Latka, C. Matthäus, I. Schie, and J. Popp, “In-vivo Raman spectroscopy: from basics to applications.,” *J. Biomed. Opt.*, vol. 23, no. 7, pp. 1–23, 2018, doi: 10.1117/1.JBO.23.7.071210.
[318] C. C. Huang and C. Isidoro, “Raman Spectrometric Detection Methods for Early and Non-Invasive Diagnosis of Alzheimer’s Disease,” *J. Alzheimer’s Dis.*, vol. 57, no. 4, pp. 1145–1156, 2017, doi: 10.3233/JAD-161238.
[319] E. B. Hanlon *et al.*, “Prospects for in vivo Raman spectroscopy,” *Physics in Medicine and Biology*, vol. 45, no. 2. pp. R1-59, Feb. 2000, doi: 10.1088/0031-9155/45/2/201.
[320] O. Terrones, J. Olazar-Intxausti, I. Anso, M. Lorizate, J. A. Nieto-Garai, and F. X. Contreras, “Raman Spectroscopy as a Tool to Study the Pathophysiology of Brain Diseases,” *Int. J. Mol. Sci.*, vol. 24, no. 3, p. 2384, Jan. 2023, doi: 10.3390/IJMS24032384.
[321] G. Devitt, K. Howard, A. Mudher, and S. Mahajan, “Raman Spectroscopy: An Emerging Tool in Neurodegenerative Disease Research and Diagnosis,” *ACS Chem. Neurosci.*, vol. 9, no. 3, pp. 404–420, Mar. 2018, doi: 10.1021/acschemneuro.7b00413.
[322] G. Açikgöz, B. Hamamci, and A. Yildiz, “Determination of ethanol in blood samples using partial least square regression applied to surface enhanced raman spectroscopy,” *Toxicol. Res.*, vol. 34, no. 2, pp. 127–132, Apr. 2018, doi: 10.5487/TR.2018.34.2.127.
[323] A. Emin, A. Hushur, and T. Mamtimin, “Raman study of mixed solutions of methanol and ethanol,” *AIP Adv.*, vol. 10, no. 6, Jun. 2020, doi: 10.1063/1.5140722.
[324] D. DePaoli *et al.*, “Rise of Raman spectroscopy in neurosurgery: a review,” *J. Biomed. Opt.*, vol. 25, no. 05, p. 1, May 2020, doi: 10.1117/1.jbo.25.5.050901.
[325] I. J. Pence *et al.*, “Clinical characterization of in vivo inflammatory bowel disease with Raman spectroscopy,” *Biomed. Opt. Express*, vol. 8, no. 2, p. 524, Feb. 2017, doi: 10.1364/boe.8.000524.
[326] J. M. Surmacki, B. J. Woodhams, A. Haslehurst, B. A. J. Ponder, and S. E. Bohndiek, “Raman micro-spectroscopy for accurate identification of primary human bronchial epithelial cells,” *Sci. Rep.*, vol. 8, no. 1, pp. 1–11, Dec. 2018, doi: 10.1038/s41598-018-30407-8.
[327] I. W. Schie, C. Stiebing, J. Popp, I. W. Schie, C. Stiebing, and J. Popp, “Looking for a perfect match: multimodal combinations of Raman spectroscopy for biomedical applications,” *J. Biomed. Opt. 2021, Vol. 26, Page 080601*, vol. 26, no. 08, p. 080601, Aug. 2021, doi: 10.1117/1.JBO.26.8.080601.
[328] A. S. Moody and B. Sharma, “Multi-metal, Multi-wavelength Surface-Enhanced Raman Spectroscopy Detection of Neurotransmitters,” *ACS Chem. Neurosci.*, vol. 9, no. 6, pp. 1380–1387, Jun. 2018, doi: 10.1021/acschemneuro.8b00020.
[329] A. S. Moody, T. D. Payne, B. A. Barth, and B. Sharma, “Surface-enhanced spatially-offset Raman spectroscopy (SESORS) for detection of neurochemicals through the skull at physiologically relevant concentrations,” *Analyst*, vol. 145, no. 5, pp. 1885–1893, Mar. 2020, doi: 10.1039/c9an01708a.
[330] T. D. Payne, A. S. Moody, A. L. Wood, P. A. Pimiento, J. C. Elliott, and B. Sharma, “Raman spectroscopy and neuroscience: from fundamental understanding to disease diagnostics and imaging,” *Analyst*, vol. 145, no. 10, pp. 3461–3480, May 2020, doi: 10.1039/d0an00083c.
[331] T. J. E. Hubbard, A. Shore, and N. Stone, “Raman Spectroscopy for Rapid Intra-Operative Margin Analysis of Surgically Excised Tumour Specimens,” *Analyst*, vol. 144, no. 22, pp. 6479–6496, Nov. 2019, doi: 10.1039/c9an01163c.
[332] C. Krafft and J. Popp, “The many facets of Raman spectroscopy for biomedical analysis,” *Anal. Bioanal. Chem.*, vol. 407, no. 3, pp. 699–717, Jan. 2015, doi: 10.1007/s00216-014-8311-9.
[333] M. Kirsch, G. Schackert, R. Salzer, and C. Krafft, “Raman spectroscopic imaging for in vivo detection of cerebral brain metastases,” *Anal. Bioanal. Chem.*, vol. 398, no. 4, pp. 1707–1713, Oct. 2010, doi: 10.1007/s00216-010-4116-7.
[334] X. Zhang *et al.*, “Robust and Universal SERS Sensing Platform for Multiplexed Detection of Alzheimer’s Disease Core Biomarkers Using PAapt-AuNPs Conjugates,” *ACS Sensors*, vol. 4, no. 8, pp. 2140–2149, 2019, doi: 10.1021/acssensors.9b00974.
[335] H. E. Parker *et al.*, “Fibre-based spectral ratio endomicroscopy for contrast enhancement of bacterial imaging and pulmonary autofluorescence,” *Biomed. Opt. Express*, vol. 10, no. 4, p. 1856, Apr. 2019, doi: 10.1364/boe.10.001856.
[336] J. Desroches *et al.*, “A new method using Raman spectroscopy for in vivo targeted brain cancer tissue biopsy,”

Sci. Rep., vol. 8, no. 1, Dec. 2018, doi: 10.1038/s41598-018-20233-3.
[337] M. Jermyn *et al.*, “Raman spectroscopy detects distant invasive brain cancer cells centimeters beyond MRI capability in humans,” *Biomed. Opt. Express*, vol. 7, no. 12, p. 5129, Dec. 2016, doi: 10.1364/boe.7.005129.
[338] M. G. Shim, B. C. Wilson, E. Marple, and M. Wach, “Study of fiber-optic probes for in vivo medical Raman spectroscopy,” *Appl. Spectrosc.*, vol. 53, no. 6, pp. 619–627, Jun. 1999, doi: 10.1366/0003702991947225.
[339] G. G. Klamminger, K. Frauenknecht, M. Mittelbronn, and F. B. K. Borgmann, “From Research to Diagnostic Application of Raman Spectroscopy in Neurosciences: Past and Perspectives,” *Free Neuropathol.*, vol. 3, pp. 19–19, Aug. 2022, doi: 10.17879/FREENEUROPATHOLOGY-2022-4210.
[340] M. S. Bergholt *et al.*, “Correlated heterospectral lipidomics for biomolecular profiling of remyelination in multiple sclerosis,” *ACS Cent. Sci.*, vol. 4, no. 1, pp. 39–51, 2018, doi: 10.1021/acscentsci.7b00367.
[341] S. Bégin *et al.*, “Local assessment of myelin health in a multiple sclerosis mouse model using a 2D Fourier transform approach,” *Biomed. Opt. Express*, vol. 4, no. 10, pp. 1–12, 2013, doi: 10.1364/boe.4.002003.
[342] C.-R. Hu, D. Zhang, M. N. Slipchenko, J.-X. Cheng, and B. Hu, “Label-free real-time imaging of myelination in the Xenopus laevis tadpole by in vivo stimulated Raman scattering microscopy,” *J. Biomed. Opt.*, vol. 19, no. 8, pp. 1–8, 2014, doi: 10.1117/1.jbo.19.8.086005.
[343] J. C. Ranasinghe, Z. Wang, and S. Huang, “Raman Spectroscopy on Brain Disorders: Transition from Fundamental Research to Clinical Applications,” *Biosensors*, vol. 13, no. 1, p. 27, Dec. 2022, doi: 10.3390/BIOS13010027.
[344] M. Paraskevaidi *et al.*, “Raman Spectroscopy to Diagnose Alzheimer’s Disease and Dementia with Lewy Bodies in Blood,” *ACS Chem. Neurosci.*, vol. 9, no. 11, pp. 2786–2794, 2018, doi: 10.1021/acschemneuro.8b00198.
[345] L. Habartová *et al.*, “Blood-based molecular signature of Alzheimer’s disease via spectroscopy and metabolomics,” *Clin. Biochem.*, vol. 72, pp. 58–63, 2019, doi: 10.1016/j.clinbiochem.2019.04.004.
[346] C. Carlomagno, M. Cabinio, S. Picciolini, A. Gualerzi, F. Baglio, and M. Bedoni, “SERS-based biosensor for Alzheimer disease evaluation through the fast analysis of human serum,” *J. Biophotonics*, vol. 13, no. 3, pp. 1–11, 2020, doi: 10.1002/jbio.201960033.
[347] R. Buividas *et al.*, “Statistically quantified measurement of an Alzheimer’s marker by surface-enhanced Raman scattering,” *J. Biophotonics*, vol. 8, no. 7, pp. 567–574, 2015, doi: 10.1002/jbio.201400017.
[348] C. Banbury *et al.*, “Development of the Self Optimising Kohonen Index Network (SKiNET) for Raman Spectroscopy Based Detection of Anatomical Eye Tissue,” *Sci. Rep.*, vol. 9, no. 1, pp. 1–9, Dec. 2019, doi: 10.1038/s41598-019-47205-5.
[349] J. M. Surmacki, L. Ansel-Bollepalli, F. Pischiutta, E. R. Zanier, A. Ercole, and S. E. Bohndiek, “Label-free monitoring of tissue biochemistry following traumatic brain injury using Raman spectroscopy,” *Analyst*, vol. 142, no. 1, pp. 132–139, Jan. 2017, doi: 10.1039/c6an02238c.
[350] D. Khalenkow, S. Donche, K. Braeckman, C. Vanhove, and A. G. Skirtach, “Added Value of Microscale Raman Chemical Analysis in Mild Traumatic Brain Injury (TBI): A Comparison with Macroscale MRI,” *ACS Omega*, vol. 3, no. 12, pp. 16806–16811, Dec. 2018, doi: 10.1021/acsomega.8b02404.
[351] X. Gao *et al.*, “A ‘hot Spot’-Enhanced paper lateral flow assay for ultrasensitive detection of traumatic brain injury biomarker S-100β in blood plasma,” *Biosens. Bioelectron.*, vol. 177, Apr. 2021, doi: 10.1016/j.bios.2021.112967.
[352] X. Gao *et al.*, “Paper-Based Surface-Enhanced Raman Scattering Lateral Flow Strip for Detection of Neuron-Specific Enolase in Blood Plasma,” *Anal. Chem.*, vol. 89, no. 18, pp. 10104–10110, Sep. 2017, doi: 10.1021/ACS.ANALCHEM.7B03015/SUPPL_FILE/AC7B03015_SI_001.PDF.
[353] D. Li, M. Yang, H. Li, L. Mao, Y. Wang, and B. Sun, “SERS based protocol using flow glass-hemostix for detection of neuron-specific enolase in blood plasma,” *New J. Chem.*, vol. 43, no. 15, pp. 5925–5931, Apr. 2019, doi: 10.1039/C8NJ02561D.
[354] M. Muhammad, C. Shao, and Q. Huang, “Label-free SERS diagnostics of radiation-induced injury via detecting the biomarker Raman signal in the serum and urine bio-samples based on Au-NPs array substrates,” *Spectrochim. Acta - Part A Mol. Biomol. Spectrosc.*, vol. 223, p. 117282, Dec. 2019, doi: 10.1016/j.saa.2019.117282.
[355] J. R. Paugh *et al.*, “Characterization of expressed human meibum using hyperspectral stimulated Raman scattering microscopy,” *Ocul Surf*, vol. 17, no. 1, pp. 151–159, 2019, doi: 10.1016/j.jtos.2018.10.003.Characterization.
[356] C. Camerlingo *et al.*, “Characterization of human tear fluid by means of surface-enhanced raman spectroscopy,” *Sensors*, vol. 19, no. 5, pp. 1–9, 2019, doi: 10.3390/s19051177.
[357] X. Xie *et al.*, “Rapid, non-invasive screening of keratitis based on Raman spectroscopy combined with multivariate statistical analysis,” *Photodiagnosis Photodyn. Ther.*, vol. 31, p. 101932, Sep. 2020, doi: 10.1016/j.pdpdt.2020.101932.
[358] S. Choi, S. W. Moon, J. H. Shin, H. K. Park, and K. H. Jin, “Label-free biochemical analytic method for the early detection of adenoviral conjunctivitis using human tear biofluids,” *Anal. Chem.*, vol. 86, no. 22, pp. 11093–11099, 2014, doi: 10.1021/ac5025478.
[359] S. Kim *et al.*, “Label-Free Surface-Enhanced Raman Spectroscopy Biosensor for On-Site Breast Cancer Detection Using Human Tears,” *ACS Appl. Mater. Interfaces*, vol. 12, no. 7, pp. 7897–7904, 2020, doi: 10.1021/acsami.9b19421.
[360] G. Cennamo *et al.*, “Surface-enhanced Raman spectroscopy of tears: toward a diagnostic tool for neurodegenerative disease identification,” *J. Biomed. Opt.*, vol. 25, no. 08, p. 1, 2020, doi: 10.1117/1.jbo.25.8.087002.
[361] A. Capaccio, A. Sasso, and G. Rusciano, “Raman analysis of tear fluid alteration following contact lense use,” *Sensors (Switzerland)*, vol. 19, no. 15, pp. 1–10, 2019, doi: 10.3390/s19153392.
[362] K. Neelam *et al.*, “Measurement of macular pigment: Raman spectroscopy versus heterochromatic flicker photometry,” *Investig. Ophthalmol. Vis. Sci.*, vol. 46, no. 3, pp. 1023–1032, 2005, doi: 10.1167/iovs.04-1032.

[363] A. Obana, M. Tanito, Y. Gohto, W. Gellermann, S. Okazaki, and A. Ohira, “Macular pigment changes in pseudophakic eyes quantified with resonance Raman spectroscopy,” *Ophthalmology*, vol. 118, no. 9, pp. 1852–1858, Sep. 2011, doi: 10.1016/j.ophtha.2011.02.017.
[364] M. Lombardo, V. Villari, N. Micali, P. Roy, S. H. Sousa, and G. Lombardo, “Assessment of trans-scleral iontophoresis delivery of lutein to the human retina,” *J. Biophotonics*, vol. 11, pp. 1–8, 2018, doi: 10.1002/jbio.201700095.
[365] J. R. Beattie *et al.*, “Multiplex analysis of age-related protein and lipid modifications in human Bruch’s membrane,” *FASEB J.*, vol. 24, no. 12, pp. 4816–4824, Dec. 2010, doi: 10.1096/fj.10-166090.
[366] J. Renwick Beattie, A. M. Pawlak, J. J. McGarvey, and A. W. Stitt, “Sclera as a surrogate marker for determining AGE-modifications in Bruch’s membrane using a raman spectroscopy-based index of aging,” *Investig. Ophthalmol. Vis. Sci.*, vol. 52, no. 3, pp. 1593–1598, Mar. 2011, doi: 10.1167/iovs.10-6554.
[367] A. Obana, H. Sasano, S. Okazaki, Y. Otsuki, T. Seto, and Y. Gohto, “Evidence of carotenoid in surgically removed lamellar hole-associated epiretinal proliferation,” *Investig. Ophthalmol. Vis. Sci.*, vol. 58, no. 121. Obana, A. et al. Evidence of carotenoid in surgically removed lamellar hole-associated epiretinal proliferation. Investig. Ophthalmol. Vis. Sci. 58, 5157–5163 (2017)., pp. 5157–5163, 2017, doi: 10.1167/iovs.17-22347.
[368] S. Woong Moon, W. Kim, S. Choi, and J. H. Shin, “Label-free optical detection of age-related and diabetic oxidative damage in human aqueous humors,” *Microsc. Res. Tech.*, vol. 79, no. 11, pp. 1050–1055, 2016, doi: 10.1002/jemt.22743.
[369] M. R. Gartia *et al.*, “Point-of-service, quantitative analysis of ascorbic acid in aqueous humor for evaluating anterior globe integrity,” *Sci. Rep.*, vol. 5, no. October, pp. 1–15, 2015, doi: 10.1038/srep16011.
[370] J. W. Evans, R. J. Zawadzki, R. Liu, J. W. Chan, S. M. Lane, and J. S. Werner, “Optical coherence tomography and Raman spectroscopy of the ex-vivo retina,” *J. Biophotonics*, vol. 2, no. 6–7, pp. 398–406, 2009, doi: 10.1002/jbio.200910022.
[371] T. Léveillard and J. A. Sahel, “Metabolic and redox signaling in the retina,” *Cell. Mol. Life Sci.*, vol. 74, no. 20, pp. 3649–3665, Oct. 2017, doi: 10.1007/s00018-016-2318-7.
[372] P. S. Bernstein, M. D. Yoshida, N. B. Katz, R. W. McClane, and W. Gellermann, “Raman detection of macular carotenoid pigments in intact human retina,” *Investig. Ophthalmol. Vis. Sci.*, vol. 39, no. 11, pp. 2003–2011, 1998, Accessed: Jan. 29, 2021. [Online]. Available: https://iovs.arvojournals.org/article.aspx?articleid=2161540.
[373] W. Gellermann, M. D. Yoshida, R. W. McClane, N. Balashov, and P. S. Bernstein, “Raman detection of pigments in the human retina,” *Opt. Biopsy II*, vol. 3250, pp. 8–17, Apr. 1998, doi: 10.1117/12.305368.
[374] R. E. Hogg, R. S. Anderson, M. R. Stevenson, M. B. Zlatkova, and U. Chakravarthy, “In vivo macular pigment measurements: A comparison of resonance Raman spectroscopy and heterochromatic flicker photometry,” *Br. J. Ophthalmol.*, vol. 91, no. 4, pp. 485–490, Apr. 2007, doi: 10.1136/bjo.2006.090936.
[375] R. E. Hogg, M. B. Zlatkova, U. Chakravarthy, and R. S. Anderson, “Investigation of the effect of simulated lens yellowing, transparency loss and refractive error on in vivo resonance Raman spectroscopy,” *Ophthalmic Physiol. Opt.*, vol. 27, no. 3, pp. 225–231, 2007, doi: 10.1111/j.1475-1313.2007.00478.x.
[376] M. Marro *et al.*, “Dynamic molecular monitoring of retina inflammation by in vivo Raman spectroscopy coupled with multivariate analysis,” *J. Biophotonics*, vol. 7, no. 9, pp. 724–734, 2014, doi: 10.1002/jbio.201300101.
[377] R. J. Erckens *et al.*, “Noninvasive Raman spectroscopic identification of intraocular lens material in the living human eye,” *J. Cataract Refract. Surg.*, vol. 27, no. 7, pp. 1065–1070, Jul. 2001, doi: 10.1016/S0886-3350(00)00828-2.
[378] R. Michael *et al.*, “Absence of amyloid-beta in lenses of Alzheimer patients: A confocal Raman microspectroscopic study,” *Exp. Eye Res.*, vol. 119, pp. 44–53, 2014, doi: 10.1016/j.exer.2013.11.016.
[379] O. Masihzadeh, D. A. Ammar, M. Y. Kahook, and T. C. Lei, “Coherent Anti-Stokes Raman Scattering (CARS) Microscopy: A Novel Technique for Imaging the Retina,” *Invest. Ophthalmol. Vis. Sci.*, vol. 54, no. 5, pp. 3094–3101, May 2013, doi: 10.1167/IOVS.13-11642.
[380] T. Akiyama, H. Segawa, Y. Kaji, T. Oshika, and H. Kano, “Label-Free Spectroscopic Imaging of Rat Eye Tissue Using Multimodal and Multiphoton Microscopy,” *J. Japan Soc. Laser Surg. Med.*, vol. 36, no. 2, pp. 201–209, Jul. 2015, doi: 10.2530/JSLSM.JSLSM-36_0030.
[381] J. Li *et al.*, “Harnessing the power of Raman spectroscopic imaging for ophthalmology,” *Front. Chem.*, vol. 11, p. 1211121, May 2023, doi: 10.3389/FCHEM.2023.1211121/BIBTEX.
[382] S. Li, Y. Li, R. Yi, L. Liu, and J. Qu, “Coherent Anti-Stokes Raman Scattering Microscopy and Its Applications,” *Front. Phys.*, vol. 8, p. 598420, Dec. 2020, doi: 10.3389/FPHY.2020.598420/BIBTEX.
[383] S. Xu, C. H. Camp, and Y. J. Lee, “Coherent anti-Stokes Raman scattering (CARS) microscopy for polymers,” *J. Polym. Sci.*, vol. 60, no. 7, pp. 1244–1265, Apr. 2022, doi: 10.1002/POL.20210317.
[384] G. I. Petrov, R. Arora, V. V. Yakovlev, X. Wang, A. V. Sokolov, and M. O. Scully, “Comparison of coherent and spontaneous Raman microspectroscopies for noninvasive detection of single bacterial endospores,” *Proc. Natl. Acad. Sci. U. S. A.*, vol. 104, no. 19, pp. 7776–7779, May 2007, doi: 10.1073/PNAS.0702107104/ASSET/EE3A3296-8E34-41E1-AAFD-B800E27F770F/ASSETS/GRAPHIC/ZPQ0160760440005.JPEG.
[385] W. Gellermann, I. V. Ermakov, R. W. McClane, and P. S. Bernstein, “Raman imaging of human macular pigments,” *Opt. Lett.*, vol. 27, no. 10, p. 833, May 2002, doi: 10.1364/ol.27.000833.
[386] P. S. Bernstein, D. Y. Zhao, S. W. Wintch, I. V. Ermakov, R. W. McClane, and W. Gellermann, “Resonance Raman measurement of macular carotenoids in normal subjects and in age-related macular degeneration patients,” *Ophthalmology*, vol. 109, no. 10, pp. 1780–1787, Oct. 2002, doi: 10.1016/S0161-6420(02)01173-9.
[387] W. Gellermann, I. V. Ermakov, M. R. Ermakova, R. W. McClane, D.-Y. Zhao, and P. S. Bernstein, “In vivo resonant Raman measurement of macular carotenoid pigments in the young and the aging human retina,” *J. Opt. Soc. Am. A*, vol. 19, no. 6, p. 1172, Jun. 2002, doi: 10.1364/josaa.19.001172.
[388] I. V. Ermakov, R. W. McClane, W. Gellermann, and P. S. Bernstein, “Resonant Raman detection of macular

pigment levels in the living human retina," *Opt. Lett.*, vol. 26, no. 4, pp. 202–204, Feb. 2001, doi: 10.1364/ol.26.000202.
[389] I. Ermakov, M. Ermakova, W. Gellermann, and P. S. Bernstein, "Macular pigment Raman detector for clinical applications," *J. Biomed. Opt.*, vol. 9, no. 1, pp. 139–148, 2004, doi: 10.1117/1.1627776.
[390] M. Sharifzadeh, D.-Y. Zhao, P. S. Bernstein, and W. Gellermann, "Resonance Raman imaging of macular pigment distributions in the human retina," *J Opt Soc Am A Opt Image Sci Vis*, vol. 25, no. 4, pp. 947–957, 2008.
[391] K. Neelam, N. O'Gorman, J. Nolan, O. O'Donovan, K. G. Au Eong, and S. Beatty, "Macular pigment levels following successful macular hole surgery," *Br. J. Ophthalmol.*, vol. 89, no. 9, pp. 1105–1108, Sep. 2005, doi: 10.1136/bjo.2004.063834.
[392] D. Y. Zhao, S. W. Wintch, I. V. Ermakov, W. Gellermann, and P. S. Bernstein, "Resonance Raman measurement of macular carotenoids in retinal, choroidal, and macular dystrophies," *Arch. Ophthalmol.*, vol. 121, no. 7, pp. 967–972, 2003, doi: 10.1001/archopht.121.7.967.
[393] A. Obana *et al.*, "Effect of age and other factors on macular pigment optical density measured with resonance Raman spectroscopy," *Graefe's Arch. Clin. Exp. Ophthalmol.*, vol. 252, no. 8, pp. 1221–1228, 2014, doi: 10.1007/s00417-014-2574-x.
[394] H. Yoshizako, K. Hara, Y. Takai, S. Kaidzu, A. Obana, and A. Ohira, "Comparison of macular pigment and serum lutein concentration changes between free lutein and lutein esters supplements in Japanese subjects," *Acta Ophthalmol.*, vol. 94, no. 6, pp. e411–e416, Sep. 2016, doi: 10.1111/aos.13106.
[395] P. S. Bernstein, D. Y. Zhao, M. Sharifzadeh, I. V. Ermakov, and W. Gellermann, "Resonance Raman measurement of macular carotenoids in the living human eye," *Arch. Biochem. Biophys.*, vol. 430, no. 2, pp. 163–169, Oct. 2004, doi: 10.1016/J.ABB.2004.07.004.
[396] R. Arunkumar, C. M. Calvo, C. D. Conrady, and P. S. Bernstein, "What do we know about the macular pigment in AMD: The past, the present, and the future," *Eye*, vol. 32, no. 5, pp. 992–1004, May 2018, doi: 10.1038/s41433-018-0044-0.
[397] O. Howells, F. Eperjesi, and H. Bartlett, "Measuring macular pigment optical density in vivo: A review of techniques," *Graefe's Arch. Clin. Exp. Ophthalmol.*, vol. 249, no. 3, pp. 315–347, Mar. 2011, doi: 10.1007/s00417-010-1577-5.
[398] B. Li, E. George, and P. S. Bernstein, "Imaging Lutein and Zeaxanthin in the Primate Macula by Confocal Resonance Raman Microscopy | IOVS | ARVO Journals," *Invest. Ophthalmol. Vis. Sci.*, vol. 59, no. 9, Jul. 2018, [Online]. Available: https://iovs.arvojournals.org/article.aspx?articleid=2693089.
[399] A. Obana *et al.*, "Spatial distribution of macular pigment estimated by autofluorescence imaging in elderly Japanese individuals," *Jpn. J. Ophthalmol.*, vol. 64, pp. 160–170, 2020, doi: 10.1007/s10384-020-00716-5.
[400] C. Stiebing *et al.*, "Nonresonant Raman spectroscopy of isolated human retina samples complying with laser safety regulations for in vivo measurements," *Neurophotonics*, vol. 6, no. 04, p. 1, Sep. 2019, doi: 10.1117/1.nph.6.4.041106.
[401] A. Katz, E. F. Kruger, G. Minko, C. H. Liu, R. B. Rosen, and R. R. Alfano, "Detection of glutamate in the eye by Raman spectroscopy," *J. Biomed. Opt.*, vol. 8, no. 2, pp. 167–172, 2003, doi: 10.1117/1.1559726.
[402] I. V. Ermakov, "Raman Spectroscopy of Ocular Tissue," in *Emerging Raman Applications and Techniques in Biomedical and Pharmaceutical Fields, Biological and Medical Physics, Biomedical Engineering*, Springer-Verlag, 2010, p. 285.
[403] C. Banbury *et al.*, "Spectroscopic detection of traumatic brain injury severity and biochemistry from the retina," *Biomed. Opt. Express*, vol. 11, no. 11, pp. 6249–6261, Nov. 2020, doi: 10.1364/boe.399473.
[404] P. Villoslada, M. Marro, A. Taubes, B. Moreno, and D. Petrov, "Raman Spectroscopy Analysis of the Retina Reveals Changes in Glutamate, N-Acetyl-Aspartate, NADH and Phosphatidylcholine in Neuroinflammation (P01.166)," *Neurology*, vol. 78, no. 1 Supplement, 2012.
[405] M. Marro, A. Taubes, P. Villoslada, and D. Petrov, "Detection of neuroinflammation through the retina by means of Raman spectroscopy and multivariate analysis," *Biophotonics Photonic Solut. Better Heal. Care III*, vol. 8427, p. 842715, Jun. 2012, doi: 10.1117/12.921358.
[406] M. Mowbray, C. Banbury, J. J. S. Rickard, D. J. Davies, and P. Goldberg Oppenheimer, "Development and Characterization of a Probe Device toward Intracranial Spectroscopy of Traumatic Brain Injury," *ACS Biomater. Sci. Eng.*, vol. 7, pp. 1252–1262, Mar. 2021, doi: 10.1021/acsbiomaterials.0c01156.
[407] A. Prasad, A. Chaichi, D. P. Kelley, J. Francis, and M. R. Gartia, "Current and future functional imaging techniques for post-traumatic stress disorder," *RSC Adv.*, vol. 9, no. 42, pp. 24568–24594, Aug. 2019, doi: 10.1039/c9ra03562a.
[408] I. J. Jahn, A. Grjasnow, H. John, K. Weber, J. Popp, and W. Hauswald, "Noise sources and requirements for confocal raman spectrometers in biosensor applications," *Sensors*, vol. 21, no. 15, Aug. 2021, doi: 10.3390/S21155067/S1.
[409] J. Smulko, M. S. Wrobel, and I. Barman, "Noise in biological Raman spectroscopy," *2015 Int. Conf. Noise Fluctuations, ICNF 2015*, Oct. 2015, doi: 10.1109/ICNF.2015.7288562.
[410] I. Barman, N. C. Dingari, G. P. Singh, J. S. Soares, R. R. Dasari, and J. M. Smulko, "Investigation of noise-induced instabilities in quantitative biological spectroscopy and its implications for noninvasive glucose monitoring," *Anal. Chem.*, vol. 84, no. 19, pp. 8149–8156, Oct. 2012, doi: 10.1021/AC301200N/SUPPL_FILE/AC301200N_SI_001.PDF.
[411] M. Jermyn *et al.*, "Intraoperative brain cancer detection with Raman spectroscopy in humans," *Sci. Transl. Med.*, vol. 7, no. 274, Feb. 2015, doi: 10.1126/SCITRANSLMED.AAA2384.
[412] K. V. Chalam, J. Chamchikh, and S. Gasparian, "Optics and Utility of Low-Cost Smartphone-Based Portable Digital Fundus Camera System for Screening of Retinal Diseases," *Diagnostics 2022, Vol. 12, Page 1499*, vol. 12, no. 6, p. 1499, Jun. 2022, doi: 10.3390/DIAGNOSTICS12061499.
[413] C. Cacciuttolo, V. Guzmán, P. Catriñir, E. Atencio, S. Komarizadehasl, and J. A. Lozano-Galant, "Low-Cost

Sensors Technologies for Monitoring Sustainability and Safety Issues in Mining Activities: Advances, Gaps, and Future Directions in the Digitalization for Smart Mining," *Sensors (Basel).*, vol. 23, no. 15, Aug. 2023, doi: 10.3390/S23156846.

[414] J. M. Smulko, N. C. Dingari, J. S. Soares, and I. Barman, "Anatomy of Noise in Quantitative Biological Raman Spectroscopy," *Bioanalysis*, vol. 6, no. 3, pp. 411–421, Feb. 2014, doi: 10.4155/BIO.13.337.

Chapter 2

Obtaining Retinal Spectra using a 635 nm Portable Raman Device for Eye-Based Traumatic Brain Injury Diagnostics

This chapter outlines the contributions I made towards the testing of the 635 nm portable Raman Device (EyeD) for which a patent has been granted (US20220338788A1), a journal article published (stated below) and funding for a university spin-out approved. Being involved in this work allowed me to become acclimatised to the world of medical device conception and commercialisation, as all components were confirmed for the system, but the signal needed to be improved and first retinae spectra obtained. Alongside this, the strengths and weaknesses of the EyeD would later be utilised in the development of my own portable Raman device in the following chapters.

As Traumatic Brain Injury (TBI), a major cause of morbidity and mortality worldwide, is hard to diagnose due to patients often exhibiting no clinical symptoms, there is an urgent need for rapid point-of-care (PoC) diagnostics to enable timely intervention. The Advanced Nano-Materials Structures and Applications (ANMSA) group at the University of Birmingham developed a technology for eye-based Raman spectroscopy to satisfy this need, implementable outside of laboratory settings without any sample preparation. This system is combined with a commercial smartphone attachment for portable fundus imaging to obtain biochemical and structural information. The device is therefore capable of rapid and non-invasive acquisition of molecular fingerprints of TBI-biochemistry to safely measure proxies for cerebral injury through the eye, providing a path towards non-invasive point-of-care neurodiagnostics.

Here, I sourced an eye model for continuous Raman testing, explored tissue preparation, ensuring retinal layer preservation using Optical Coherence Tomography (OCT), a technique for externally obtaining structural cross-sections of a patient's retinal layers. I optimised the EyeD signal and compared the performance against a commercial Raman system, achieving enhancement of high-wavenumber bands in fresh *ex vivo* porcine eyes' as well as detection of biomarkers in the posterior of fresh *ex vivo* porcine eyes. Spectral changes in retina are identified following trauma and first stages towards injury profiling with prospective TBI biomarkers was initiated. The EyeD is designed to maximise Raman spectroscopy portability, alongside obtaining relevant diagnostic information for rapid triage, to allow clinicians to objectively assess TBI at the PoC, as well as identify long-term changes in brain biochemistry indicative of neurodegenerative diseases.

Acknowledgement of contributing material and authors

Content within this chapter has been published in the following journal paper:

- C. Banbury, G. Harris, M. Clancy, R. J. Blanch, J. J. S. Rickard, P. Goldberg Oppenheimer, Window into the mind: Advanced handheld spectroscopic eye-safe technology for point-of-care neurodiagnostic. *Sci. Adv.* **9** (2023).

2.1 Introduction

Traumatic brain injury (TBI) has become a leading clinical challenge of the 21st century, as the cascade of biochemical changes evolve immediately after the initial trauma yet, many individuals display very few clinical symptoms at the early stages which can develop long-term, persistent, neurodegenerative deficits[1]–[3]. As the brain tissue lacks regenerative capacity, early diagnosis is crucial for improving outcomes. Life-critical decisions, which influence patients' prognoses and the efficacy of treatment must be made within the first hour after trauma (*i.e.,* the "Golden Hour")[4], [5]. These decisions must not only be rapid but also accurate, as it is known that in TBI, misdiagnosis or delay in treatment in the pre-hospital settings is where most of the acute, cerebral damage occurs[6]. As discussed in **Chapter 1,** neuroimaging is expensive and cannot be used in a timely manner at the point-of-care. Instead, the only current TBI diagnostic technique employed at the Point-of-Care (PoC) involve cognitive assessment, where the ambulance crew still relies on subjective observational triage tools with macro-descriptors transmitted *via* third-party intermediaries to clinicians. Limitations of inter-rater reliability, predictive validity and requiring patient information beforehand prevent full PoC suitability [7].

Alongside these shortfalls, current TBI diagnostic methods are unable to detect small changes in TBIs, which can be present without any detectable physiological abnormalities. It is therefore vital that an alternative technique is harnessed which obtains quantifiable information, without any prerequisite knowledge of the patient and employable outside of a hospital environment. Currently, no point-of-care technology exists for quantitative assessment of TBI with sufficient sensitivity and timeliness to aid the stratification and early diagnosis whether this is at the pitch side in contact sports, or the roadside after motor vehicle collisions. This is exacerbated by the long-term consequences of mild TBI and concussion[8], [9], with cumulative effects from multiple sustained injuries for athletes and the military[10], [11].

Raman spectroscopy is a rapid and highly specific analytical technique, which can provide real-time, quantitative diagnostic information both *in-vivo* and *ex-vivo* by measuring subtle changes to inelastically scattered light, accurately identifying changes in disease or injury-specific biomarkers with diagnostic capabilities[12]–[15]. In ophthalmology, Raman spectroscopy has been applied to study disease states *ex-vivo*[16]–[18]. Further findings highlight the ability to identify malignant tissue in the brain, acting as a surgical guide, however, these required direct and invasive access to the brain[12]. The retina contains all retinal ganglion cell bodies, and the optic disc is where all retinal ganglion cell axons leave through carrying visual information captured to the brain through the optic nerve. Ganglion cells in the retina are unmyelinated, meaning that changes assessed there relate directly to neuronal biology, whilst the optic nerve is myelinated and surrounded by cerebrospinal fluid, continuous with that surrounding the rest of the Central Nervous System (CNS). The retina and optic nerve have long been known to display physically measurable changes because of increased intracranial pressure, where its monitoring is of significance for intensive care in TBI[19]–[22]. It has also been found that retinal degeneration after TBI is directly caused by CNS damage involving the visual pathways, which comprise 30% of the cerebral cortex[23], [24]. Whilst the retinal changes detected in animal models closely associate with TBI severity, the markers considered (and other potential markers) detected in the retina may also associate

with local pathology and afferent visual dysfunction. Given that up to 80% of patients with mild TBI have long term visual complaints, the ability to detect and predict long-term visual dysfunction after TBI would be extremely valuable.

In contrast to biochemical information obtained using Raman Spectroscopy, Optical Coherence Tomography (OCT) is a non-invasive imaging technique, commonplace in an ophthalmology clinic as a valuable tool, which externally produces images of the retina and optic nerve head[25], [26]. OCT uses optical backscattering, like ultrasound, to produce high-resolution cross-sectional images for *in vivo* measurements of retinal layers[27]. There are many cases of OCT being implemented to determine the presence and extent of elevated intracranial pressure (ICP) and resulting idiopathic intracranial hypertension (IIH) through structural manifestations[28]–[30]. Raised ICP and IIH can result from many cases such as obesity, head injury, tumours or stroke, and IIH can lead to vision loss due to the numerous complications created at the optic nerve[30]. Potential retinal manifestations lead to the implementation of OCT in IIH diagnostics, by determining changes in retinal nerve fibre layer (RNFL) thickness[25], [26]. As ocular manifestations of TBI are more frequently being explored, OCT has been used to assess whether changes in retinal structure could indicate brain trauma, and studies have found RNFL thinning even in mild TBI cases[31]–[33]. Whilst OCT is a potential parallel method for eye-based Raman spectroscopy, as shown in this study, there are limitations that prevent OCT being a suitable singular TBI diagnostic method, such as inability to distinguish RNFL thickness due to factors introduced by edema which is commonplace following TBI[25], along with accessibility issues when considering PoC implementation.

Raman spectroscopy provides information on the biochemical composition and therefore, the metabolic state of the neuro-retina, which is only indirectly available with structural imaging modalities, such as using OCT angiography or fluorescein angiography, which may reveal reduced blood flow, from which clinicians could infer retinal ischaemia. Whilst magnetic resonance spectroscopy is unable to examine the retina due to the minimum voxel size being too large, it could examine the vitreous and has occasionally been used for this purpose in research, however, there is a limited relationship between vitreous and retinal findings.

There are examples of technologies being explored to probe the molecular signatures of TBI[34], however, the specificity in multi-disease settings has not been sufficiently established. All approaches used clinically today and many of the proposed methods, *e.g.,* measuring S100B concentration, lack specificity[35], and whilst the latter has been implemented in Scandinavian countries, it is rarely used elsewhere[36]. The high sensitivity for the combination of GFAP and neuro-UCH-L1 measured within 12h of injury[37], formed the basis of the first FDA-approved TBI test for triaging the need for CT, however, is affected by poor specificity (36.5%), low-positive predictive value (9.2%) and long-analysis times, defeating its purpose [38]. GCS despite being highly subjective, remains the only ground truth for clinical and academic understanding of TBI that can span the entire patient journey as well as injury severity.

Previous to this study, the ANMSA group have demonstrated a number of paths towards the use of Raman spectroscopy for the detection of biochemical changes indicative of TBI in brain tissue, retinal tissue and biofluids such as blood. Rickard *et* al. developed a microfluidic system and demonstrated that a range of validated

biomarkers, particularly N-acetyl-aspartate (NAA), were rapidly and continuously released from injured neurons into the blood following TBI, reflecting biochemical changes occurring in the brain and creating temporal profiles of extracellular activity post-TBI[39]. **Fig. 2.1a** features the key finding of NAA detection in the blood following TBI at two different acute time-points using a 785 nm laser wavelength. Raman spectroscopy is an inherently weak signal, which is exacerbated when utilising low power lasers to stay within eye safety guidelines, therefore the ANMSA group established a machine learning software: Self Organising Kohonen Index Network (SKiNET). It can be used to embrace noisy data to perform dimensionality reduction and organise spectra into self-organised maps (SOMs) for clear, visual separation. Using this interface, TBI was successfully classified from spectral data of mice using 785 nm laser wavelengths, by detecting tissue-specific signatures of each anatomical layer on eye-sections using a commercial Raman system and clearly separating them, as shown in **Fig. 2.1b**[40], [41]. SKINET was featured within the paper this chapter contributed to, observing changes in brain chemistry by acquiring spectra from retinal tissue to identify TBI in an *ex-vivo* murine model and established a high-accuracy differentiation between control and brain injury tissue using a 633 nm laser wavelength to model potential outputs of the 635 nm EyeD[42], as well as in a separate study at a 785 nm excitation wavelength capable of detecting injury for both of mild and severe severity, using a commercial laboratory-based Raman spectroscopy for both cases[43].

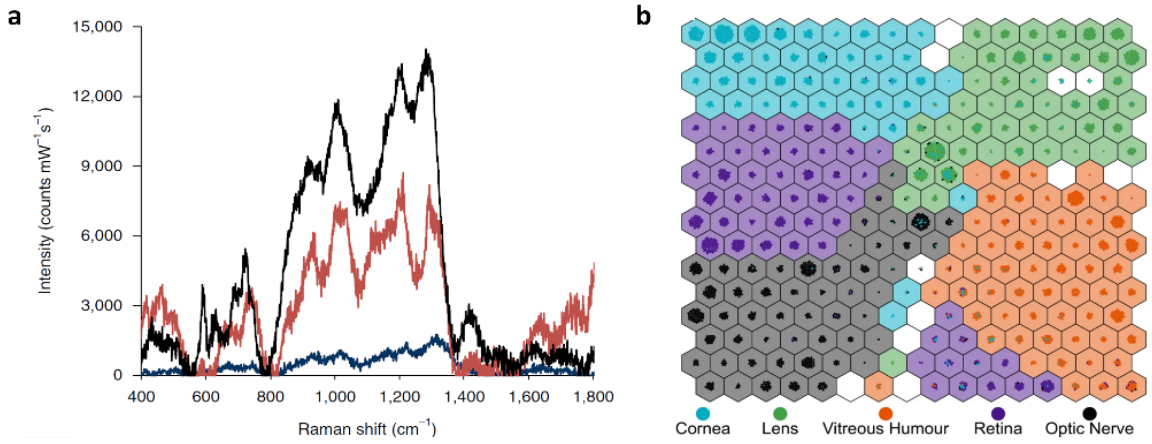

Figure 2.1. Examples of the ANMSA group utilising Raman Spectroscopy for the detection of biochemical changes indicative of TBI in tissue and biofluids. ***a*** *Raman spectrum produced of blood samples using a 785 nm laser wavelength, a clear difference can be seen between the healthy control (navy), NAA at t = 0 hours (black) and NAA at t = 8 hours (red) post TBI, suggesting that there are temporal changes of NAA levels even in the acute phase on TBI, detectable by Raman spectroscopy [39].* ***b*** *Self-organised map (SOM) separating spectra obtained of murine eye tissue using a 785 nm laser wavelength. The clear clustering of colours shows good separation of small spectral differences, discernible by Raman spectroscopy [41].*

To address the challenges associated with early-stage detection of TBI, the ANMSA group have developed a 635 nm laser-based spectroscopic technology focused on accessing the retina and optic nerve at the back of the eye (posterior), as a projection of brain tissue *via* the ocular tract. This structure is the only external extension of the CNS, providing an optically clear window into the biochemistry of the brain[44]–[48]. By targeting CNS biochemical changes, we reduce the need to filter out confounding (non-CNS) compounds, measuring the brain side of the blood-brain barrier, increasing specificity. The eye-safe device, based upon using multiplex resonance Raman spectroscopy, can characterise specific TBI biomarkers or ‘molecular fingerprints’, as

proxies for disease and injury. Such markers for “brain health” include structural changes in brain specific lipids and biochemicals due to local tissue damage such as cardiolipin and cytochrome C or neuromarkers such as S100B, GFAP and NAA, which have demonstrated strong correlation with injury severity in the acute TBI phase, relating to both radiological, surgical and physiological findings[39], [40], [49]–[51].

In this chapter, an appropriate validation platform is established using OCT, allowing for testing of the portable 635 nm Raman device (EyeD), obtaining spectra from fresh, ocular tissue. Performance of the EyeD is compared to a commercial Raman system and spectral differences between trauma and control retinal samples are identified using the machine learning platform SKiNET. First steps towards injury profiling is established with prospective TBI biomarkers Cytochrome C and cardiolipin. This work is the final stage of device testing before considering commercialisation.

2.2 Pre-Existing Device Design and Build

The portable and non-invasive eye-safe 635 nm Raman device (EyeD) utilises modified optics with a Class I collimated laser introduced into the optical path and focused by the eye, without using ionising radiation. The unique device permits simultaneous Raman spectroscopy and fundus imaging by isolating the Raman and white light paths. Raman scatter is collected using an external portable spectrometer and processed using an external laptop with spectral software. The ultimate plan is to modify the device to be streamlined with the ANMSA Self Organising Kohonen Index Network (SKiNET), to be classified using the developed artificial neural networks algorithm as a decision support tool[41]. SKiNET performs visual separation to identify the underlying chemical differences between classes, providing accurate classification for rich information and high classification specificity, even for low laser powers and short acquisition times, representative of the real-world point-of-care conditions. Integrating the EyeD with SKiNET to investigate the retina, as an extension of the brain environment after injury, will rapidly distinguish TBI from control groups, yielding an automated classification of the acquired Raman data and assignment to particular neuromarkers, tissue type or disease state. This tool, along with the successful demonstration that high-frequency Raman bands indicative of early-stage TBI can be safely measured from the retina will enable important steps for translation of the developed platform technology to real-world clinical point-of-care neurological diagnostic applications.

The EyeD is designed for use on-site for immediate, confident decision-making and treatment. Measuring abnormal changes in the retina at the point-of-care that are indicative of TBI, providing a quantitative assessment of trauma at the earliest stages whilst simultaneously helping to quantify the damage. It would be interpreted by clinicians as an indication to treat the patients according to TBI guidance without delay and help in triaging *e.g.,* directing to major trauma centres with neurosurgical facilities or conversely allowing the patient to return to military service or high impact sport. Previous but limited studies have explored the feasibility of utilising Raman spectroscopy to obtain spectra of *in vivo* retina, such as studies by Marro, M. *et* al. and Stiebing, C. *et* al. which used a standard Raman arrangement and flat mounted or cultured tissue[52], [53]. However, the major obstacle to *in vivo* imaging has been the use of high magnification, high numerical aperture objective lenses, which are typically required for Raman spectroscopy. Such objectives have a natural

incompatibility with imaging the eye posterior since the eye itself can be considered as a lens with a combined positive power of 60D (Diopters)[54]. Therefore, the EyeD set-up uses a collimated beam incident on the cornea, allowing the eye to naturally focus the beam onto the retina. Ermakov *et* al. employed the compound power of the cornea and lens as an objective lens in 2001 towards the identification of age-related macular degeneration, by exploiting resonance Raman of macular pigments[55]. Such an effect dramatically enhances the available signal, which helps to mitigate the restricted laser power and absence of high-power optics, however, little progress has been made in this application of Raman spectroscopy since, most likely due to the weak Raman signal and low laser powers required for *in vivo* retinal probing, which can be mitigated with the introduction of SKiNET.

The Raman spectroscopy path schematically demonstrated in **Fig. 2.2a,** it involves a 635nm class I laser (9600 Series, Kingfisher) **(1)**, "cleaned up" by a 635 nm Laser Line filter (FL05635-10, ThorLabs) **(2)**, redirected by a 625 nm edge BrightLine single-edge short-pass standard epi-fluorescence dichroic beamsplitter (FF625-SDi01-25x36, Semrock) **(3)**, redirected again by a 635 nm BrightLine single-edge super resolution dichroic beamsplitter (Di03-R635-t1-25x36, Semrock) **(4)** to reach the eye, the Raman scatter then returns back along this path but passing through the 625 nm dichroic beamsplitter **(3)** and finally reaching a 650 nm Longpass Filter (FEL0650, ThorLabs) **(5)** which blocks out any Rayleigh scatter before being the beam is collected at the exit fibre port and fed to a portable spectrometer (635 nm QEPro, Ocean Insight) *via* an optical fibre.

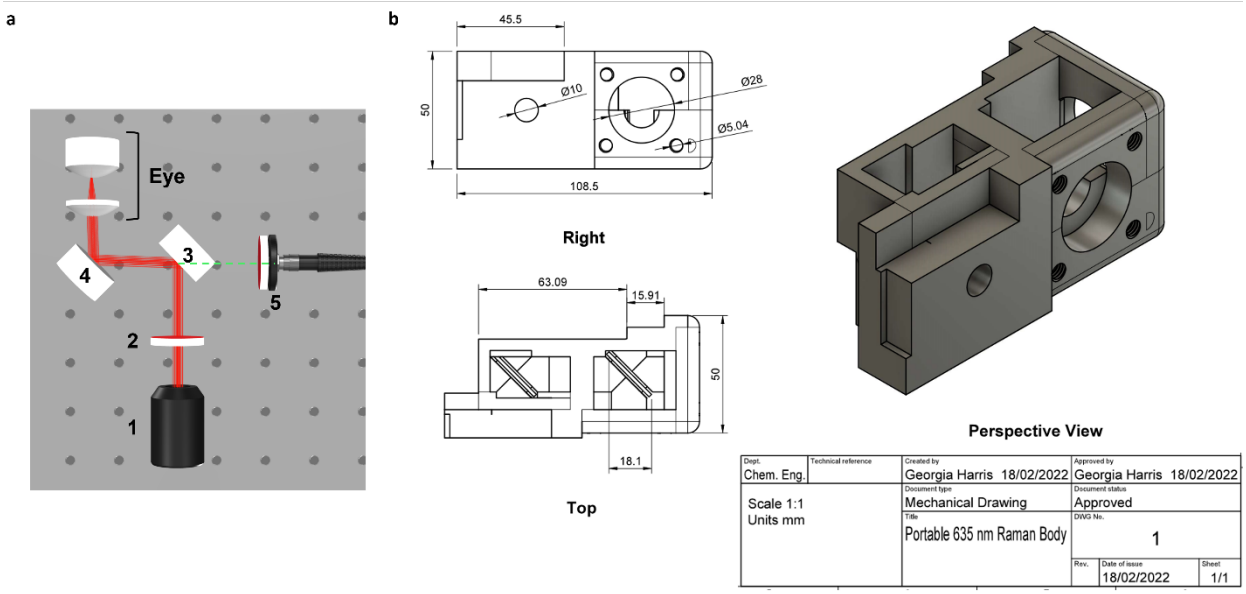

Figure 2.2. Illustrations of the EyeD beam path and portable 3D-printed housing. ***a*** *Schematic diagram of the beam path within the EyeD starting at the 635 nm laser [1], passing through the clean-up filter [2], redirected 45º by a dichroic beamsplitter [3] and redirected again by a second dichroic beamsplitter [4] before reaching the patient's eye and the Raman scatter is once again redirected by the dichroic beamsplitter [4] but this time passing through the dichroic beamsplitter [3] to reach the exit fibre port where any Rayleigh scatter is blocked by the longpass filter [5]. This signal is fed from the system to a portable spectrometer via a fibre port, and the spectrometer is connected to a laptop where the spectrum can be viewed.* ***b*** *Mechanical drawing of the CAD designed housing including dimensions. This main body shows all slots in which mirrors and filters can be placed, along with threads to screw fibre port mounts onto.*

The use of fibre optics allows for design and engineering freedom, enabling bulky components to be kept away from the patient, ensuring a compact imaging system. Silica used in fibre optics normally yields additional interference due to its own Raman signal in the fingerprint region (500-2000 cm-1). However, in the high wavenumber region, there is no Raman contribution from silica. The overall engineered EyeD consists of the combined fundus imaging optical path and eye-safe Raman spectroscopy path contained within a 3D-printed housing. The design that houses the optics is based on a 3D printed hollow casing. The housing is illustrated in **Fig. 2.2b** with labelled dimensions**,** and an additional indented lid to overlap the housing and lid components when secured, limiting external light entering the system. **Fig. 2.3** provides a mechanical drawing of the entire system when the smartphone mount and lid are present, suitable for handheld use. Optical components fit into a cradle and allow for easy adjustments and optimisation in free space with an open-on-top section for alignment during optimisation, a 3D digital render of the housing sliced to expose all of the internal components present and the patient eye location is provided in **Fig. 2.4**. Images of the 3D printed housing with all components inserted and smartphone with attached D-Eye module can be seen in **Fig. 2.5a.**

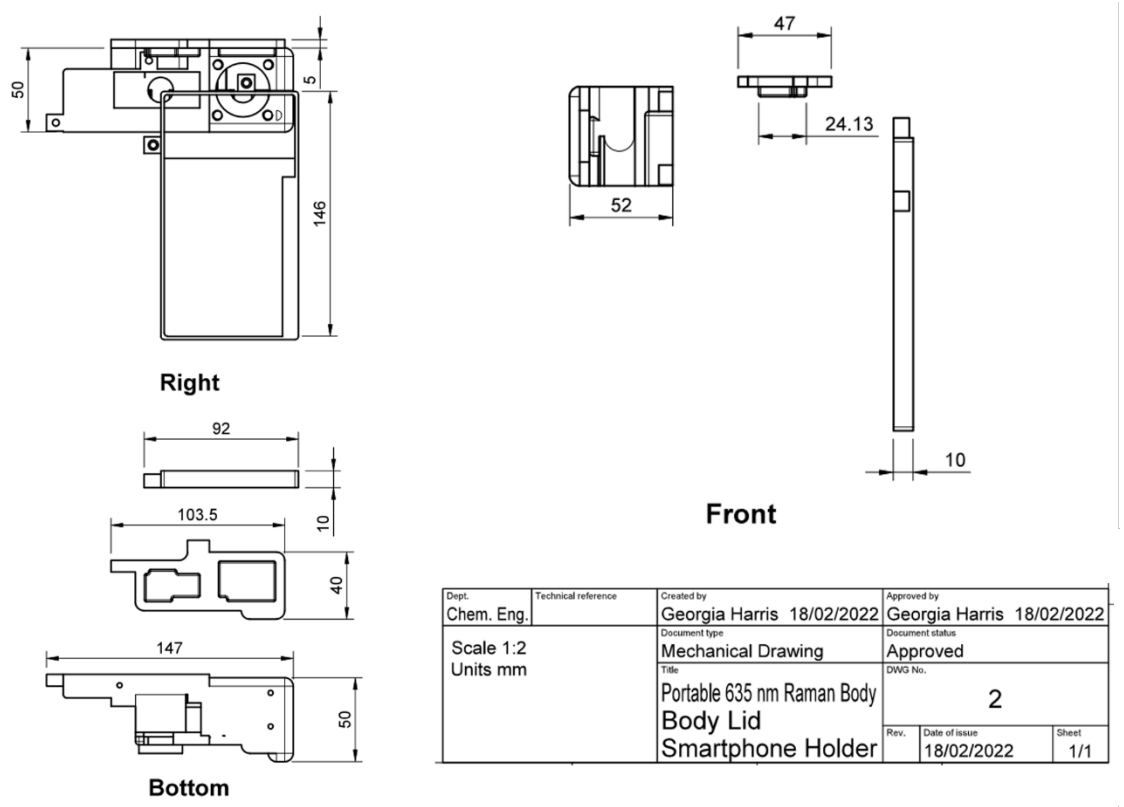

Figure 2.3. Mechanical drawing of the Right, Bottom and Front view of the full EyeD device with the dimensions labelled, the lid to prevent stay light exiting or entering and the mount to attach the smartphone with the D-Eye fundus module are featured.

To measure Raman spectra from the eye posterior segment, a co-aligned imaging system was required to target a region of interest on the retina, such as the optic disc. Thus, a D-EYE smartphone fundus camera was used for optical imaging of the retina, which utilises the flash from a smartphone camera for illumination and the phone camera for imaging. The D-EYE is a compact optical module providing a direct

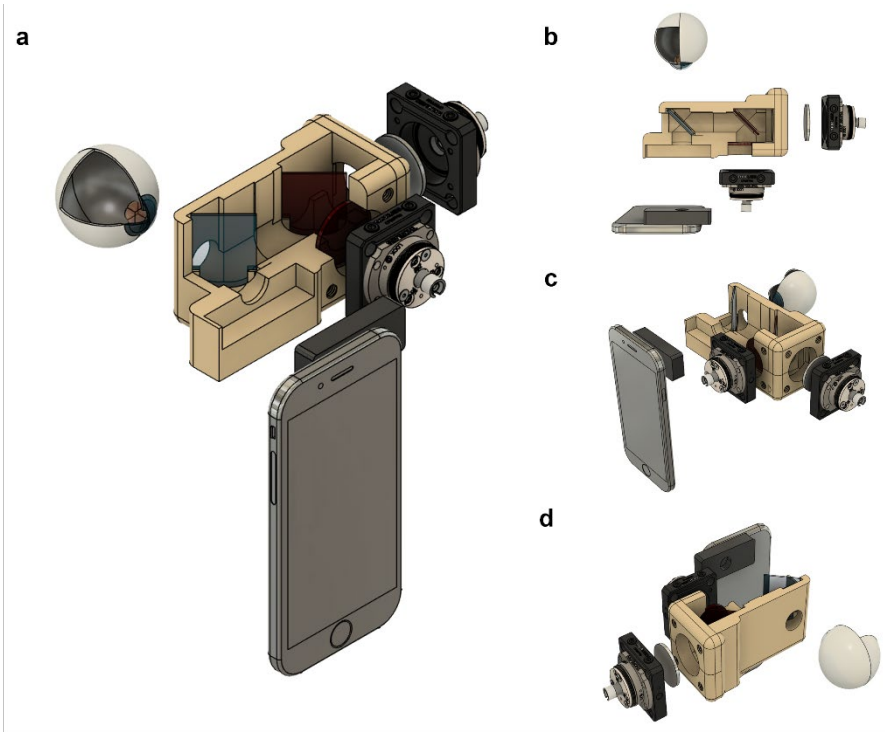

Figure 2.4. Schematic diagrams of the 3D CAD design for the EyeD housing with accessories in shaded with visible edges only visual style. ***a*** *Perspective view with all accessories fully or partially visible. Slot for the D-EYE attachment and a clear path directly to the eye sample.* ***b*** *Top view of the alignment of each component with both dichroic beamsplitters set at 45º to the beam path.* ***c*** *Side view of both fibre ports which mount the clean-up and Rayleigh filters.* ***d*** *Back view illustrating the unobstructed beam path out of the system into the eye, with no components touching the patient's face.*

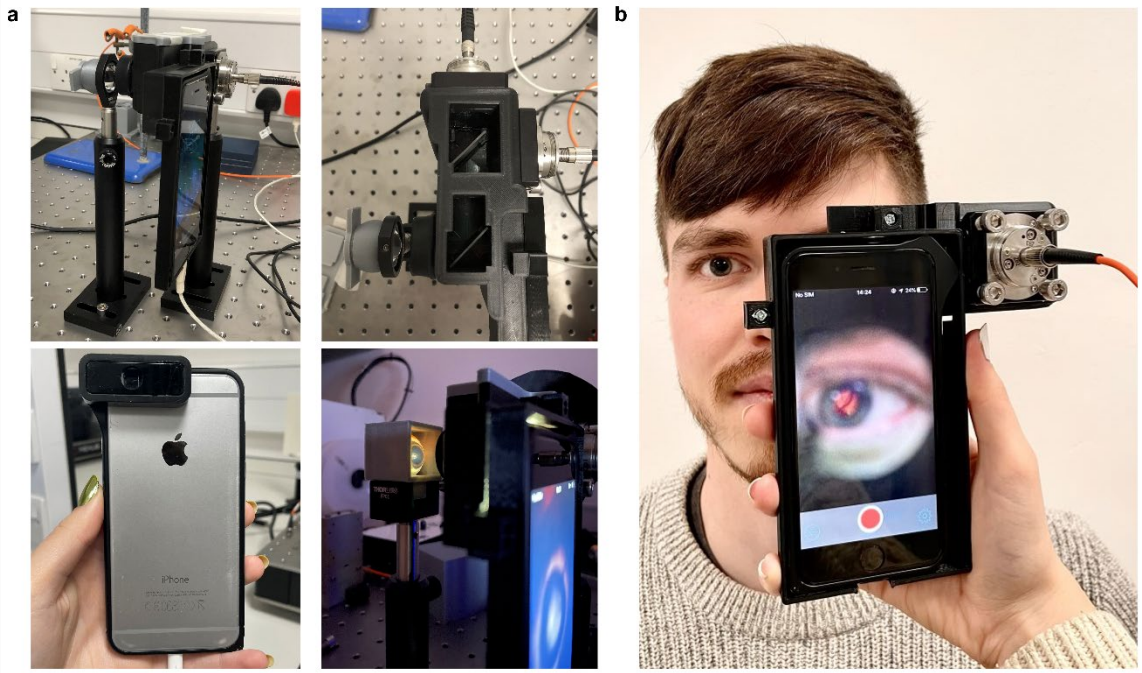

Figure 2.5. Images of the EyeD prototype. ***a*** *The EyeD prototype including 3D printed housing, the smartphone mount (top left) to attach the D-Eye fundus imaging module (bottom left), the internal components, and fibre ports (top right) and the patient eye location demonstrated with a fresh, ex vivo porcine eye (bottom right).* ***b*** *Demonstration of how the EyeD portable device is held and positioned in front of the patient's eye for fundus images. The optical fibre (orange) allows for the portable spectrometer and laptop to be placed tabletop at a distance from the patient and operator.*

illumination and therefore, can be used without pupil dilation of the patient. The fundus imaging path consists of a smartphone with a fundus imaging smartphone attachment module (D-Eye), passing through the previously mentioned 625 nm short pass dichroic beamsplitter (component **(4)** in **Fig. 2.2a**) and the patient's eye. **Fig. 2.5b** provides a demonstration of how the device is held and the smartphone interface a healthcare provider would view during a fundus imaging examination.

2.3 Determining an Eye Model

Previously mentioned ANMSA studies exploring retinal Raman spectra have been demonstrated with formalin fixed samples to maximise usage and reduce laser damage, however, the process of fixing changes the molecular bonds of the tissue which will affect the Raman spectrum. When moving towards device commercialisation, it is vital to consider the most clinically relevant model to test the EyeD with, that is fresh upon data collection, accessible and affordable.

The human eye is a highly complex system, illustrated in **Fig. 2.6a**. The compound power of the human cornea and lens is equal to +58.60D, producing a focal length of 17 mm, within the average 22.6 mm eye length[55]. Kaschke *et* al. describe the optical system of the eye in Chapter 2 *Optics of the Human Eye* in "Optical Devices in Ophthalmology and Optometry", stating that the human retina has a thickness between 180 μm at the fovea and 200 to 400 μm elsewhere[56].

Porcine eyes have many similarities with human eyes that make them appropriate models for *ex-vivo* prototype testing, when thinking of optical properties both eyes share the same dimensionality, photoreceptor density and retinal layer distribution[57], [58]. Further, they are phylogenetically similar such as sclera shape and thickness, cones are present in the external retina[59]. Hammer *et* al. demonstrated the structural similarities between human and porcine retinal layers, noting the lack of macula and thicker RNFL layer in porcine eyes. However, in the same study, OCT revealed that the porcine retinal structures were well-preserved 7 hours post-mortem[60], and alongside this, porcine lenses allow the whole visible spectrum through with little attenuation (95% transmission)[61], this makes them suitable as a model to use for testing the EyeD within this Chapter, along with the further work in following chapters, and similarities can be observed when comparing the human fundus in **Fig. 2.6a** with **2.6c** and **2.6d.**

Porcine eyes were sourced from large white pigs (Liverpool Medical Meat Supplies). Death was induced as an electrical stun shock directly to the brain, followed by an incision to the neck [following United Kingdom Food Standards Agency (UK FSA) health guidelines as part of standard abattoir slaughtering practice]. Porcine eyes were enucleated before searing to avoid damage and later clouding to the cornea, a clear cornea is shown in **Fig. 2.6b.** Despite the preservation of retinal structures, literature mentions corneal opacity increasing by 8 hours after death[62], some studies state that enucleated porcine eyes must be used within 6 hours post-mortem [63], whilst

others claim that retinal blood vessel segmentation takes place within 30 minutes to 2 hours [64], making *ex vivo* porcine eyes time-sensitive and costly.

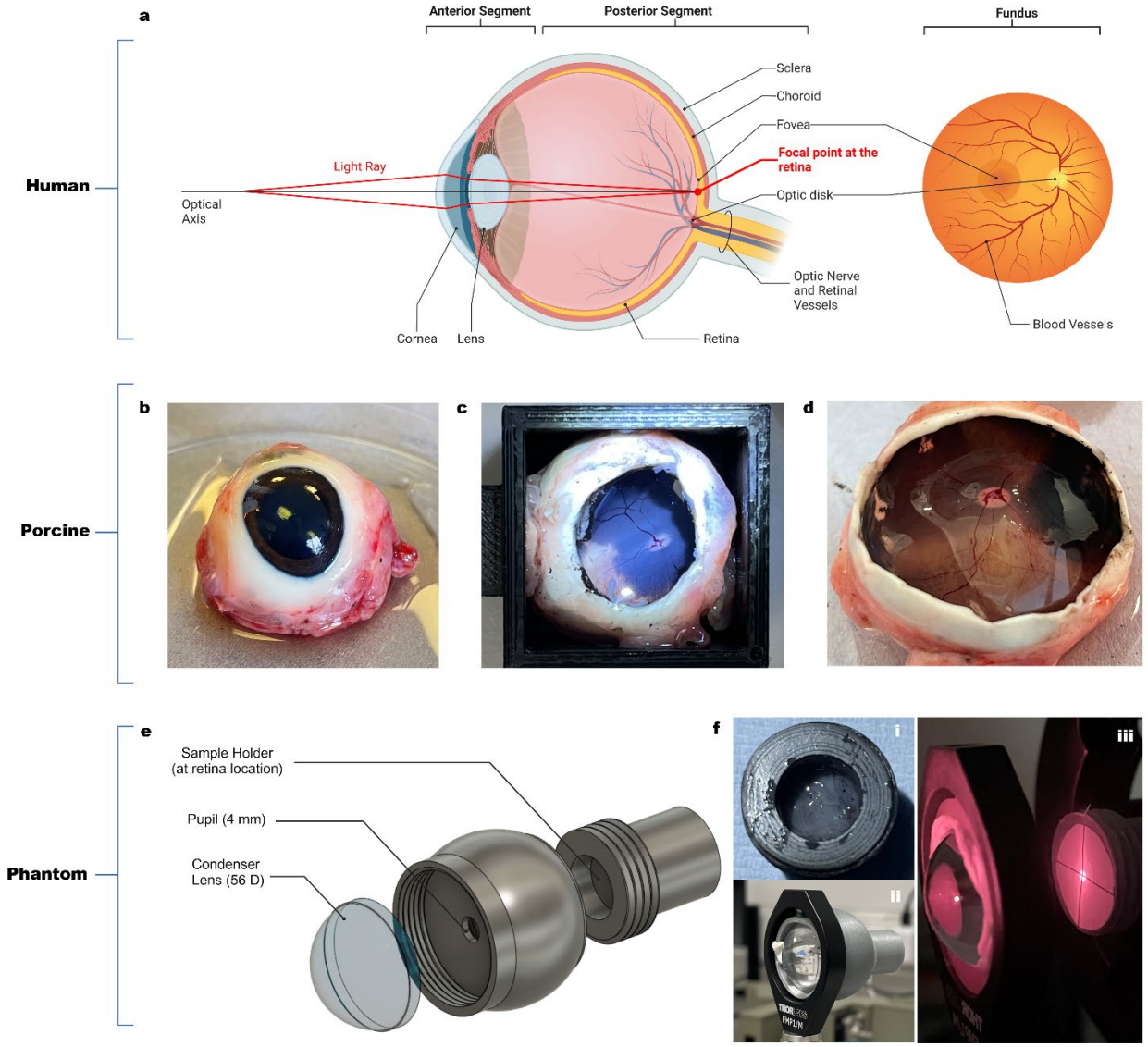

Figure 2.6. The eye models explored in the development and testing of the handheld fundus camera system. ***a*** *Schematic of the human eye illustrating the light path when imaging a nearby object. A view of a healthy fundus is shown. These main structures are the aim to visualise with the fundus camera. Figure created with Biorender.com* ***b*** *Fresh ex vivo porcine eye, intercepted before searing to avoid corneal clouding.* ***c*** *Porcine eye with anterior segment removed. The fundus can be viewed through the vitreous humour.* ***d*** *Posterior segment of the porcine eye.* ***c*** *and* ***d*** *nicely compliment the fundus schematic shown in* ***a,*** *highlighting the similarities between human and porcine eyes.* ***e*** *Digital render of the 3D printed phantom eye model, with dimension comparable to the human eye, lens which mimics that of a human in power (56 D) and numerical aperture (0.52), and non-mydriatic pupil aperture (4 mm).* ***f*** *Images of the 3D printed phantom eye* ***i*** *Showing the sample holder with porcine retina inside* ***ii*** *showing the mounted system and* ***iii*** *Showing the open version which allows the light path to be viewed at crosshairs at the retina location.*

Time-sensitivity was explored by comparing corneal clarity and fundus visibility with a commercial ophthalmoscope after freeze-thawing. Freeze-thawing would allow for porcine eyes to be received and utilised over multiple days. The freeze-thaw experiment involved freezing whole enucleated porcine eyes in either ambient space or submerged in Phosphate-Buffered Saline (PBS) and freezing in different formats. These included freezing for 24 hours at -20°, -80° or initially in -20° for 1 hour before

moving to -80°. The results from the commercial smartphone-based fundus imaging system (D-Eye) are shown in **Fig. 2.7a,** with poor visual acuity from all freezing methods but the best three being both ambient state and PBS submerged at -20° and in PBS moving from -20° to -80°. These were then dissected to assess damage and retinal detachment, shown in **Fig. 2.7b,** where PBS submerged eyes seemed to have the most corneal cloudiness and retinal damage, whereas the ambient state eye had only retinal detachment. Overall, very poor results were seen when freeze-thawing the eyes when compared to four examples shown in **Fig. 2.7c** of fresh porcine eyes (~5 hours post-mortem) using the D-Eye fundus module. For small, frequent iterations, testing on porcine eyes is not feasible and therefore an alternative is necessary.

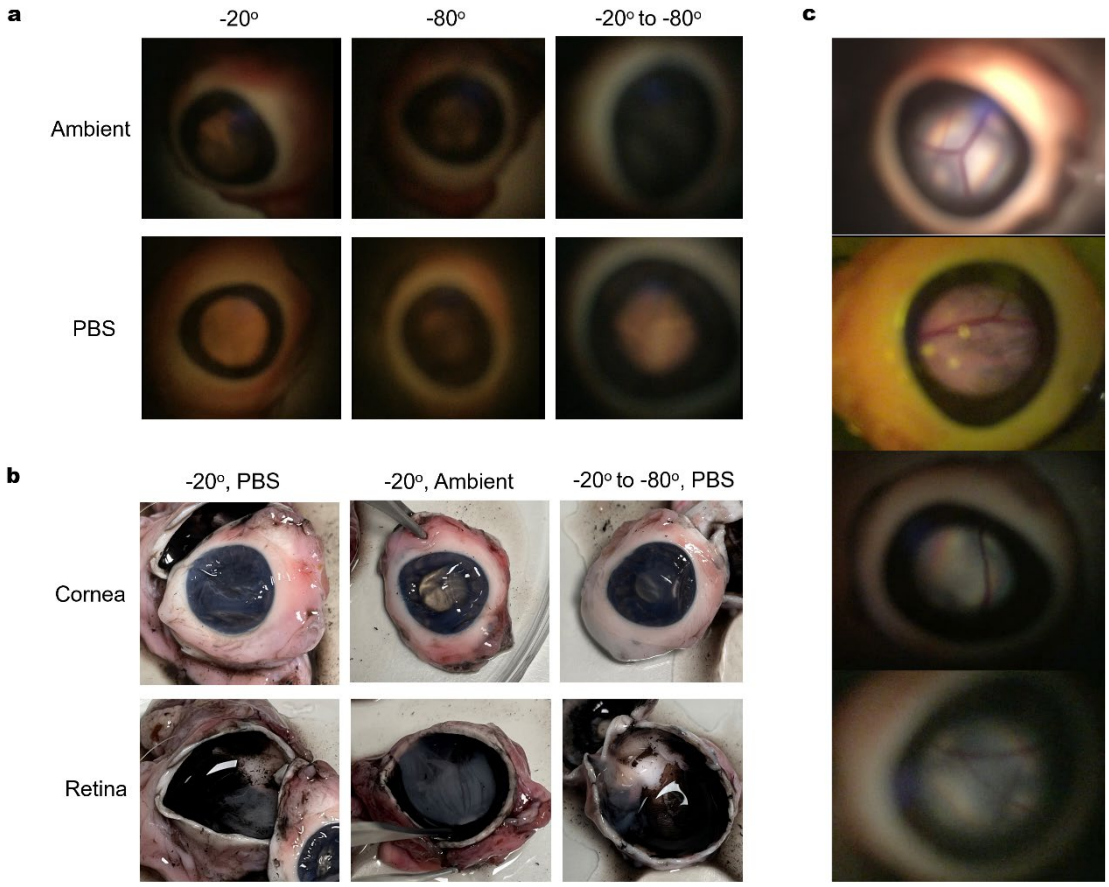

Figure 2.7. Results from the freeze-thaw study to determine if one porcine eye order could be used over multiple days. ***a*** *Fundus images from a commercial smartphone-based ophthalmoscope (D-Eye) carried out on thawed porcine eyes which were frozen in 6 different methods. Eyes were frozen either submerged in PBS or in ambient space, then placed in a -20° or -80° freezer for 24 hours, or frozen at -20° for 1 hour before being moved to a -80° freezer. The best three were both -20° frozen eyes (left), and the eye frozen in PBS at -20 then -80° (bottom right).* ***b*** *The best three were then dissected to observe corneal clarity and any posterior damage. Both PBS submerged eyes had increased corneal opacity and significant posterior damage. The ambient eye has good corneal clarity and clear retinal detachment.* ***c*** *Four examples of fresh ex vivo porcine eyes imaged with the commercial D-Eye system as a reference for how easily the fundus can be viewed.*

Developing a novel eye-based technology that relies on the optical power of the eye to focus the Raman laser requires a controlled testing environment with fixed optics. A phantom eye model was developed to mimic the physical dimensions and optical characteristics of the eye, whilst providing a realistic Raman signature of the retina. The model was developed by previous Postdoctoral Researcher Michael Clancy, for simplicity, a single lens is used to mimic the combined power, restricted by a 4mm

diameter pinhole representing the un-dilated pupil and housed in a 3D printed case. **Fig. 2.6e** shows an expanded digital render featuring the aspheric lens (ACL2018U, ThorLabs) with power 56 D, the main body with dimensions comparable to a human eye and the sample holder where samples can be placed in the position of the retina (18 mm from the front of the eye) shown in **Fig. 2.6f(i).** Ray diagrams of the chosen single lens compared to a model of light entering the human eye are presented in **Figure 2.8,** demonstrating compatibility between focal lengths and dimensionality. The tissue characteristics of the retina are then simulated by placing porcine tissue into a removable sample holder. The sample holder is screwed in place using 3D-printed threads, which allows for small focus adjustments to compensate for differences in the thickness of different tissue samples. The 3D printed model can be seen in **Fig. 2.6f(ii),** whilst an open version of the phantom eye is given in **Fig. 2.6f(iii)** which allows the light path to be viewed and the retinal location to be externally illuminated. These crosshairs are clear targets to be visually acquired with a successful fundus imaging system, being 250 µm thick they are comparable to the blood vessels shown in **Fig. 2.6a** and **2.6c** which are on average between 123 – 151 µm in diameter[65].

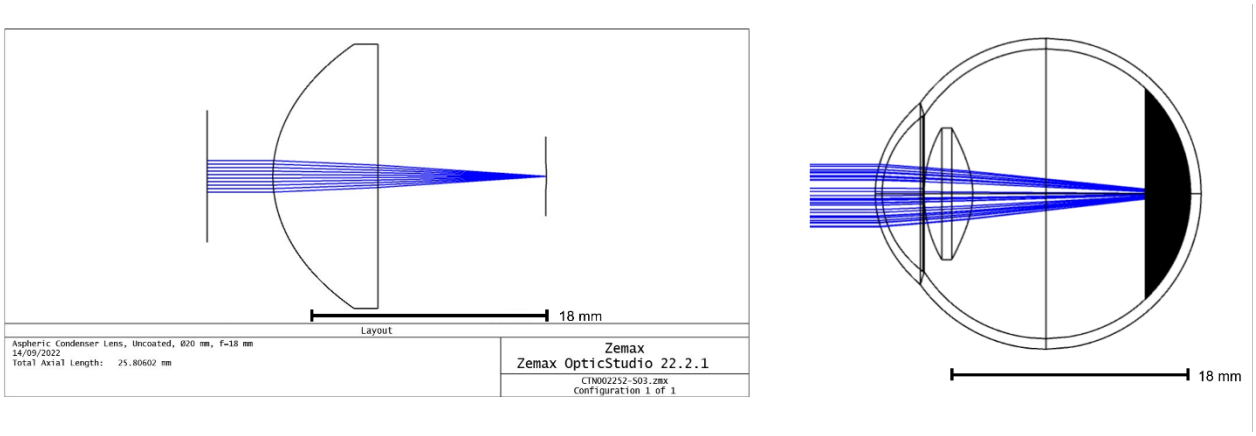

Figure 2.8. Zemax ray diagram comparison between the single aspheric condenser lens (left) with an 18 mm focal length (ACL2018U, ThorLabs) and the combined power of the human lens and cornea (right). This illustrates the suitability both in dimensionality and optics of the phantom eye model as a test platform for the eye-based laser systems. Diagrams produced using Zemax OpticsStudio with files from ThorLabs and Zemax Knowledgebase.

2.3 Quality Checking Porcine Eyes

Once an eye model was chosen, a validation study was completed to determine the extent of post-mortem structural change in the trauma porcine eyes using optical OCT, a technique commonly used in ophthalmology (**Fig. 2.9**). This was to confirm that the eyes being delivered were not crushed, torn nor damaged internally that may not be detectable with fundus imaging. 24 OCT scans were obtained from whole porcine eyes (n_{Live} = 12, $n_{Post\text{-}Mortem}$ = 12) and a live view was assessed during image collection by an ophthalmologist Dr Richard Blanch to determine if regular structure had been disturbed. Upon confirming regular structure, scans were saved for analysis of the RNFL and ganglion cell layer (GCL) thickness post-TBI.

The post-mortem eyes were obtained from the same supplier as the porcine eyes assessed in **Section 2.2,** and therefore are classed as TBI samples due to the nature of death, whilst the live eyes are the control group without trauma. The post-mortem eyes displayed qualitatively less clear separation of retinal layers than the live porcine

eyes, with a lower signal-to-noise ratio, which could relate to degradation of the optically clear optical media (such as the cornea) after death and delivery, as well as being due to cellular cytotoxic oedema occurring in the ischaemic and post-mortem tissue.

Examples of OCT images obtained from post-mortem and *in vivo* eyes are shown in **Fig. 2.9a** and **Fig. 2.9b,** respectively, with clear visual similarities. For consistency, a distance of 3000 and 4500 µm from the optic disc were measured and are shown as blue and red lines in **Fig. 2.9**, and RNFL and GCL thicknesses were measured at these points. In all cases, retinal layer thicknesses were higher in the retinal images obtained post-mortem than in live porcine eyes. An f-test was completed to determine that the variance of both populations per tissue type were equal, therefore a two-sample t-test assuming equal variance was completed. OCT measurements from the RNFL displayed an average increase of 6.4% with a p-value of 0.305, suggesting low statistical significance in the thickness increase observed post-mortem. Whilst a 21.6% increase was measured in the GCL with a p-value of 0.004, illustrated in **Fig 2.9c,** was measured. It would be necessary to obtain OCT data from additional living and post-mortem eyes to determine if an RNFL thickness increase is likely following trauma, whilst the increase in GCL thickness can be considered statistically significant and likely to be observed when repeating the experiment. This is consistent with the early cytotoxic oedema predominantly affecting the cell bodies with the corresponding standard error mean thicknesses presented as error bars in the chart. Together, these findings are consistent with the abattoir-supplied porcine eyes being in the early stages of post-mortem degradation at the time of Raman imaging, with relative preservation of inner retinal structure, however still determined suitable for experimental testing.

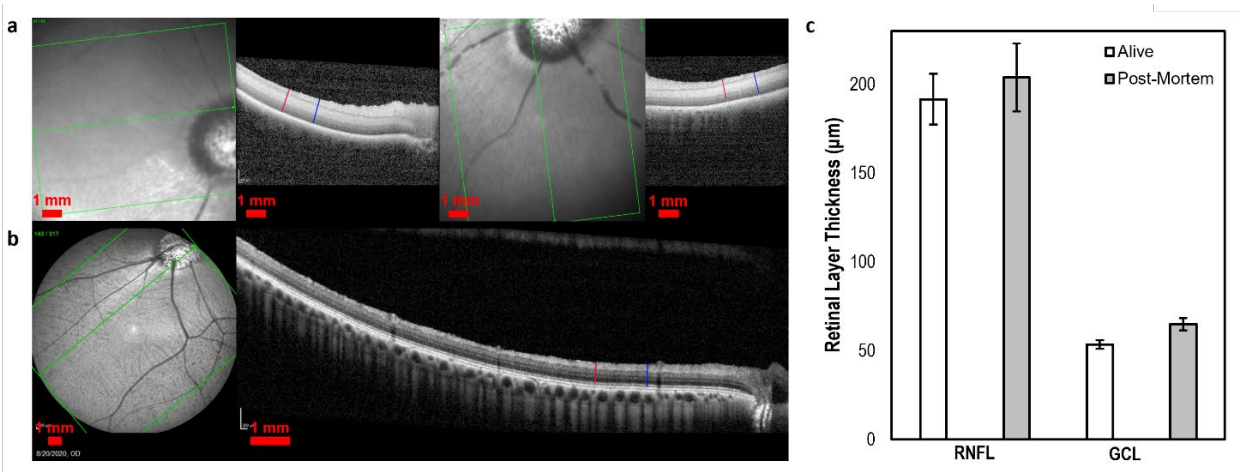

Figure 2.9. ***a*** *Representative OCT images of post-mortem, ex vivo, trauma porcine eyes, measurement locations at 3000 and 4500µm are shown as blue and red lines, respectively.* ***b*** *Example of an OCT image obtained from alive in vivo eyes from healthy patients, showing the optic disc margin on the left of the en-face image and a horizontal arrow marking the location of the cross-section running through the fovea shown on the right. Comparison to the porcine eye reveals the same retinal layers, although the foveal dip is absent in the pig eye.* ***c*** *Retinal layer thicknesses of two prominent layers: the retinal nerve fibre layer (RNFL) and ganglion cell layer (GCL) in both alive and post-mortem eyes imaged using OCT and measured using ImageJ. Retinal layer thickness was greater in post-mortem samples, with increase of 6.4% (p-value 0.305) and 21.6% (p-value 0.004) in the RNFL and GCL, respectively, consistent with the early cytotoxic oedema predominantly affecting the cell bodies post death. Standard error of the mean (SEM) are illustrated as error bars with supporting information for these calculations found in* ***Appendix A.***

2.4 Fresh *Ex Vivo* Porcine Retinal Spectra

Upon determining the best possible eye model to test the eye-based Raman spectroscopy systems with, the EyeD could be used to obtain spectra of fresh, *ex vivo* porcine retinal samples placed into the sample holder of the phantom eye. Spectra measured from the retina were taken from an area in close proximity to the optic disc for each eye. The ultimate aim when obtaining spectra from the low-power (0.63 mW) portable system is to observe a resonance effect strong enough to sit above the auto-fluorescent signal from the tissue.

A comparison study was completed between the in-house built portable EyeD and commercial Raman spectrometer *InVia* Qontor (Renishaw plc). A total of 180 spectra were collected from porcine retinal samples (n_{EyeD} = 9, n_{InVia} = 12). From these measurements, several characteristic bands are observed in the high-wavenumber band in the region of 2800-3200cm^{-1}, attributed to resonant overtones of vibrational modes in the fingerprint region. Studies have shown that high wavenumber region bands can be used to distinguish a number of tissue types, including the difference between myelinated and unmyelinated nerves. In this high wavenumber region, there appears to be good agreement between the EyeD and the commercial InVia system, as shown in **Fig. 2.10a.**

The high wavenumber region was explored further by investigating spectral differences between the trauma porcine samples using the EyeD and spectra obtained from control porcine eyes previously under comparative parameters with a commercial Raman system. A total of 510 measurements were collected from the retinal samples (n_{TBI} = 39, $n_{Control}$ = 12). SKINET was used to extract a self-organising map discriminant index (SOMDI), to further identify features in the Raman data that may not be discerned visually in the raw spectra. The specific differences in these features may originate from biochemical variations in the eye after TBI reflected in the Raman spectra, indicating the changes in molecular composition. The SOMDI identified peaks are shown in **Fig. 2.10b,** highlighted with four grey bars at 2850, 2880, 2930 and 2955 cm^{-1}. The 2880 and 2955 cm^{-1} peaks are assigned as CH_3 *symmetric stretching* and *asymmetric* stretching, respectively, constituting the grey matter with the further *C=O* and *C=C* coupled bond *stretching* from the unsaturated fatty acid residues[66]–[69]. The two peaks of main interest, 2850 and 2930 cm-1 are assigned as CH_2 *symmetric* and *asymmetric* stretching, respectively which are present in lipids (*i.e.* Cardiolipin, $C_{81}H_{140}Na_2O_{17}P_2$) and proteins (*i.e.,* Cytochrome C, ($C_{42}H_{52}FeN_8O_6S_2$)).

Raman spectra of raw Cytochrome C and Cardiolipin were produced using a 633 nm excitation wavelength on the commercial *InVia* Qontor system shown in **Fig. 2.10c.** Grey bars highlight the presence of peaks at 2850 and 2930 cm-1 which, as the SOMDI suggested, presented differently in the trauma and control porcine retinal spectra. This is an initial, first-stage indicator that low-power Raman spectroscopy can obtain spectral information indicative of the presence of TBI biomarkers, with the use of SKiNET, for which there is opportunity to explore further upon the procurement of improved fresh retinal samples.

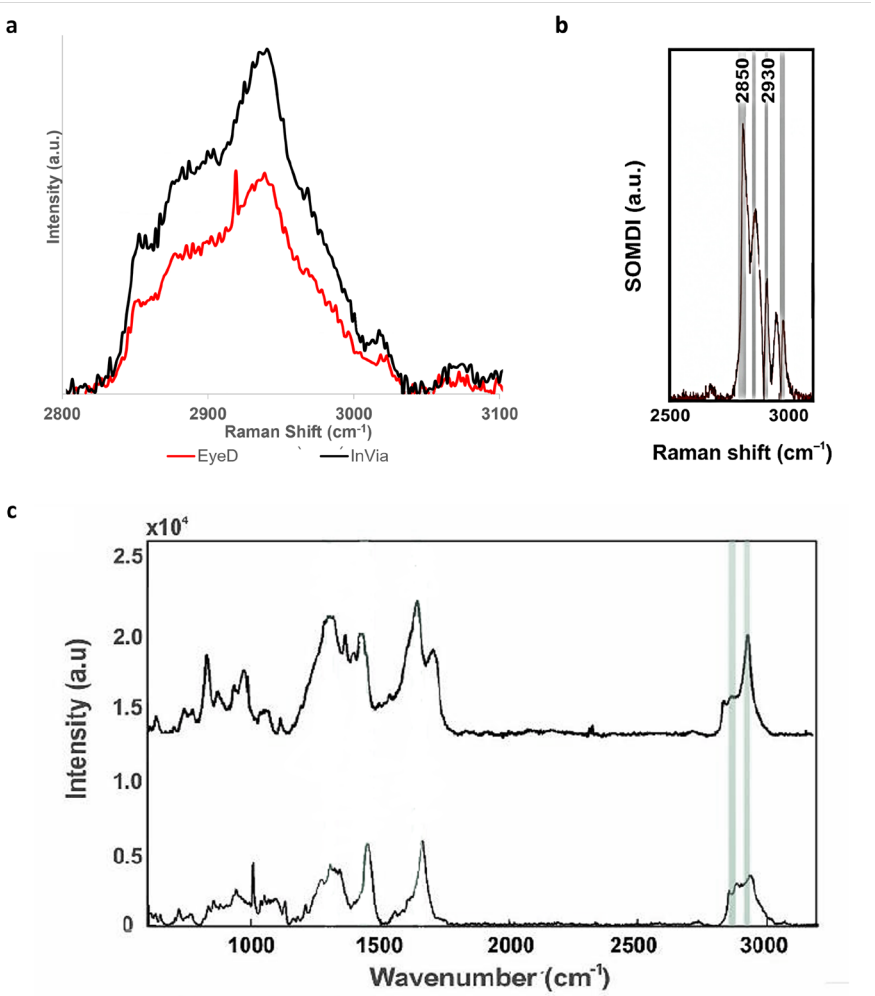

Figure 2.10. ***a*** *Comparison study between the EyeD and commercial Raman Spectrometer InVia Qontor (Renishaw plc). Spectra were collected on both systems using comparable settings of power, acquisition time and post-processing. In the high wavenumber region (2800 – 3100 cm-1) there was good agreement in spectral peak shapes between the EyeD (red) and InVia (black).* ***b*** *The self-organised map discriminant index (SOMDI) produced from the (**b**), extracting spectral differences between the control and trauma samples, suggesting biochemical changes in the retina post-TBI. High wavenumber peaks extracted are 2880 and 2955 cm-1 indicating grey matter and unsaturated fatty acid residues, along with 2850 and 2930 cm-1 peaks that could represent lipids and proteins such as Cardiolipin and Cytochrome C, respectively, both prospective TBI biomarkers.* ***c*** *Spectra obtained of raw Cytochrome C (top) and Cardiolipin (bottom) using a commercial Raman spectrometer, grey bars highlight the two peaks of interest showing spectral changes in the control vs trauma SOMDI.*

2.5 Discussion and Conclusion

The presence of Cytochrome C indicates cell death (apoptosis) and is found in the mitochondrial inner membrane, and as a result is a prospective biomarker of TBI in literature[70], [71]. Membranes of cells are the primary target for injury and determining damage as they are highly dependent on their physical properties and lipid organisation, affecting membrane fluidity, which is a key property for maintaining cell functionality. Cell membranes depend on lipid composition and cell environment, leading to distortions, deformations and decrease of mechanical stability[72]–[74]. Cardiolipin undergoes oxidation during the pathophysiological cascade in TBI, with literature identifying an accumulation of similar oxidation products in the region of injury[75][76]. A further link has been established between the spectral changes and

apoptosis *via* comparison to immunohistochemistry of TBI in mice using Raman spectroscopy[77].

Retinal degeneration after TBI is proposed to be directly caused by central nervous system damage affecting the visual pathways, accounting for 30% of the cerebral cortex[32], [78], [79]. The detected retinal changes in literature are found to closely associate with TBI, eliciting subtle spectral changes which can be linked to variation in Cardiolipin and Cytochrome C, indicating metabolic disruption. These lipid rich fatty substances encompass the brain tissue[80], especially with the brain containing nearly 60% fat and the Raman signatures for twelve major and minor brain-specific lipids have been well characterized[81], [82].

It has been shown that there is an increase in cerebral cortical free fatty acids (used as predictive markers of injury outcome) following cortical impact brain injuries in rats and human cerebral spinal fluid (CSF)[83], [84]. This suggests TBI activated changes in the environment of hydrocarbon chains of lipid molecules, resulting in strong effects on the C-H stretching vibration region of the Raman spectra which can be used to indicate different states of order. When the hydrocarbon chains Cardiolipin are in a natural state, the *symmetric* stretching vibrations of the CH_2 groups at the 2850cm^{-1} band dominate. However, when the Cardiolipin undergoes environmental strain, such as in the case of TBI, it has been shown that the relative intensity of the 2930cm^{-1} band, in relation to the other C-H stretching vibration, is increased relative to the intensity of the 2850cm^{-1} as well as compared to the 2885m^{-1} peaks in hydrocarbon chain region[85], due to the disorder induced in the hydrocarbon chains. As the environment changes increase during the pathophysiological cascade in TBI, the 2930cm^{-1} peak may increase successively compared to the other C-H stretching vibration peaks. Thus, an increase in the Cardiolipin concentration as well as the presence of the Cytochrome C could provide sufficient change in the neighbourhood of the CH_2 and CH_3, yielding detectable changes in the 2930/2850 peak ratio, characterised by portable Raman spectroscopy.

The feature bands in the high wavenumber region, identified as strong SOMDI weights derived from the SKiNET analysis, closely reflect the Cardiolipin and Cytochrome C molecular structures and the corresponding variations as predicted by literature, indicating that in the earliest stages after TBI, the concentration ratio of these biomarkers' changes in the retina could provide a prognostic information for triaging. Two main peaks at 2850cm^{-1} and 2930cm^{-1} were found to be associated with the *CH_2 stretching* of lipids / *CH_3 symmetric* stretching of proteins, further revealing information on the type of lipid-protein biomarker interaction due to the metabolic cascade following TBI, the environment of the hydrocarbon chains of the lipid and the state of order of the chains.

In summary, the ANMSA group have demonstrated a novel concept of measuring changes to brain neuro-chemistry non-invasively *via* the eye, overcoming the strict constraints of *in-vivo* imaging which are highly unfavourable for Raman spectroscopy, and shown first evidence that spectra of the neuro-retina can be used to identify TBI. The successful implementation of the EyeD shows that by using the eye alone to focus a collimated beam onto the retina, high wavenumber Raman bands can be measured, whilst simultaneously performing fundus imaging. These results established the potential for high wavenumber bands *alone* to be used to identify TBI from the retina

and subsequently, this work outlines the design of a portable device for eye-safe data acquisition in a realistic synthetic model of the human eye, providing the first tangible path towards non-invasive point-of-care diagnostics of the brain using Raman spectroscopy.

Measuring the biochemical compounds *via* EyeD from the retina directly, as an accessible part of the central nervous system, circumvents many of the drawbacks of TBI detection, particularly with specificity. Known biomarkers once thought to be highly specific for the brain have later been found to have additional extracranial sources, which reduces reliability. In the case of the compounds detected by the EyeD, there is no biological reason to infer that extracranially derived metabolites would accumulate in any large quantities in the retina, as the blood-retinal barrier prevents the entrance of systemic compounds from circulation. We can therefore measure the changes directly from the blood-brain-barrier side, probing both the local brain biology *via* the neuro-retina and the global brain *via* the optic nerve. Thus, the non-invasive *in-vivo* spectroscopic EyeD technology, which could be combined with a parallel blood test, would be reflective of both global brain pathology (*via* probing the optic nerve) and any local neurological disease (*via* detecting from the neuro-retina), representing the first opportunity for an alternative to GCS, whilst simultaneously offering greater fundamental mechanistic insights to further our understanding of the underlying pathobiology of TBI.

In the longer term, the EyeD technology has the potential to offer crucial clinical insights about a patient's brain without any preparation. By developing an eye-safe fundamental mechanism that combines fundus imaging and Raman spectroscopy, the translational gap is bridged *via* additive manufacturing, smartphone technology and machine learning. Whilst we have demonstrated that high wavenumber bands detected in the eye can be used to diagnose TBI, Raman spectroscopy EyeD has the potential to also be applied to a multitude of neurological conditions. Importantly, the measurements are made portable and non-invasive, therefore enabling routine point-of-care use and long-term patient monitoring. The final portable EyeD will be used to detect neurotrauma at point-of-care *e.g.,* roadside, pitch-side, austere combat environment, where no expert evaluation or urgent radiological investigations are immediately available. This has the potential to revolutionise how TBI and neurological conditions are diagnosed and triaged, which in turn, would provide substantial healthcare savings, improved clinical outcomes and save many lives.

2.6 Next Steps

When considering my next steps for refining the design and technology developed for the EyeD, I assessed the shortfalls in the current set-up and capabilities. The most fundamental aspect is the visible red laser utilised for 635 nm Raman excitation wavelengths, a bright light that, despite being eye-safe, may dazzle the patient, creating a negative patient experience, or reducing the amount of time a patient can withstand measurements. Therefore, the sister system to the EyeD will be built using a near-infrared laser wavelength, also creating the potential for exciting different molecular bonds in samples, or producing lower levels of fluorescence for greater signal to noise ratio in tissue spectra.

During the development of the EyeD, the company manufacturing the D-Eye went into administration rendering the smartphone fundus attachment module obsolete. This requires exploration of alternative portable fundus camera systems that do not utilise a smartphone. While smartphone camera-based systems are portable, easy to use and can be coupled with Artificial Intelligence (AI) diagnostic support, there are a number of limitations that raise the need for an alternative. Telemedicine using smartphones is ideal for personal use, introducing medical care into a device already owned by the patient for seamless integration. However, medical devices built upon smartphones for healthcare providers are less intuitive if the phone is only utilised for that singular purpose. This is exacerbated by smartphones not being universal, and quickly becoming outdated with frequent software and hardware updates, especially when considering the constant improvement and redesign of phone cameras. An alternative that allows for complete modification in the prototype stage is required, to allow for fundus imaging, data collection and SKiNET analysis platforms along with cloud storage capabilities.

Whilst the innovative engineered eye phantom, mimicking the physical dimensions and optical characteristics of the eye, opens a new avenue for straightforward studies of ocular tissues in conjunction with Raman spectroscopy, an improved eye model is desirable for the future testing of the EyeD technology. The phantom eye model does not feature all the eye anatomy which may affect the Raman spectroscopy signal and performance of fundus imaging, especially in low-power, portable conditions. The fresh, *ex vivo* porcine eye model is suitable for early-stage tissue analysis, however, a sustainable and consistent alternative is needed to appropriately characterise TBI with Raman spectroscopy whilst validating device eye-safety. The nature of this research utilising lasers, even at low powers, puts restrictions on device testing, next steps towards improving the quality of data collection would be obtaining the approval of *in vivo* testing or utilising an advanced *in vitro* model.

There is great potential for the handheld EyeD with integrated SKiNET to simultaneously provide dimensionality reduction, feature extraction and multiclass classification to act as a decision support tool, dramatically improving the speed and cost of diagnosis. The EyeD readout would form part of a protocolised decision-making tree combined with cognitive assessment. Further, by levering cloud data upload, data analysis could be performed remotely on any device that has a web browser and is designed to be user-friendly to clinicians.[30] To achieve this, it would be necessary to incorporate the portable spectrometer into the handheld, ergonomic design and eliminating the need for a laptop by creating a smartphone platform to perform all data collection, SKiNET analysis and display a result for accessible readout without the need for a specialist healthcare provider.

2.7 Methods and Materials

Porcine Eye Study. Pig eyes were acquired from large white pigs (Liverpool Medical Meat Supplies). Traumatic focal brain injuries, representative of a cortical impact, to the pigs' brain (frontal and parietal) were induced as an electrical stun shock directly to the brain, followed by an incision to the neck (following UK FSA health guidelines as part of standard abattoir slaughtering practice). These injury forces, led to clinically relevant histopathological outcomes including cellular damage and death, skull fracture, disruption and haemorrhage of the cortical surface, swelling, oedema and

contusions[86], representing the head injuries acquired from falls, which account for over 35% of all sustained TBIs and over 50% of TBIs in children younger than 14 years[87]. Control eye samples were acquired from Yorkshire pigs dying a natural death post-euthanasia. All eyes remained optically clear and were analysed 2-4 hours after extraction. Retinae were dissected out and analysed in flat mounts on aluminium covered, microscope slides using the Renishaw inVia system or placed in the phantom eye sample holder lined with a silicon wafer.

Design and Fabrication of the EyeD Technology. CAD designs for 3D printing were made using Autodesk Fusion 360 and printed by the fused filament fabrication (FFF) method in polylactic acid (PLA) using an Ultimaker 3 Extended (Ultimaker BV). The combined Raman spectroscopy/fundus photography setup consisted of the following components: iPhone (Apple Inc), D-EYE Smartphone-Based Retinal Imaging System (D-EYE Srl), 625nm edge BrightLine single-edge shortpass standard epi-fluorescence dichroic beamsplitter (FF625-SDi01-25x36, Semrock, 635 nm BrightLine single-edge super resolution dichroic beamsplitter (Di03-R635-t1-25x36, Semrock), 650nm long pass filter (FEL0650, ThorLabs), 635nm laser line filter (FL0635-10, ThorLabs), 2x FiberPort (input: (PAF2S-11B, ThorLabs) and output: (PAF2P-11A, ThorLabs)), FC/PC 100mm 0.22 NA multi-mode input fiber, SMASMA 100mm 0.22 NA multi-mode output fiber (M15L01, ThorLabs), 635nm class I Laser (KI9807A VFL, Kingfisher International), QE Pro Spectrometer optimised for 638nm (Ocean Optics Inc).

The phantom eye model consisted of a 3D printed housing encasing an aspheric condenser lens with a focal length of 18mm (ACL2018U,ThorLabs Inc). Fundus photograph of a human eyes (approved by UoB ethics committee for healthy controls, Ethics Reference: ERN_22-1129) were taken using unmodified D-EYE camera attachment.

Raman Spectroscopy. For the system comparison study, the commercial system utilised as the *InVia* Qontor confocal Raman (Renishaw) spectrometer equipped with 514, 633, 785 and 830 nm lasers, which was adjusted for optimal throughput, fluorescence control and sensitivity, was used to acquire the standard and comparative data. Raman spectra were acquired using both the *InVia* Qontor (Renishaw plc) 633 nm laser and the engineered EyeD technology equipped with a 635nm laser. Surface maps over an area of 2500 mm^2 were acquired for each sample using the *InVia* Qontor, with laser power 0.47 mW, an acquisition time of 60s and using a 20x Leica objective (0.40 NA), with scans recorded in the range 2032-3466 cm^{-1}. Optical measurements were carried out with a specially adapted research grade microscope (Leica DM 2700 M) equipped with an incoherent white light source, allowing confocal measurements with 2.5µm depth resolution. EyeD spectra were collected at the set power of 0.63 mW with an acquisition time of 60s, as single spectra saved individually using OceanView software (Ocean Optics Inc.). Post-processing of spectra was performed in WiRE 5.3, cosmic rays were removed from each map using the nearest neighbour method, followed by baseline subtraction using a 9^{th} order polynomial and the noise tolerance of 1.50 was applied. The average was taken from each map resulting in a single spectrum per sample.

To compare TBI and control porcine retinal tissue, EyeD scans were obtained as outlined above and control tissue spectra was taken from a previous databank for which Raman maps were generated using the *InVia* Qontor in a Streamline mode scan

with 1s acquisition, 3 accumulations at 633 nm. A 50× objective with an NA of 0.75 was used for Raman measurements. Spectra obtained from the Cytochrome C and Cardiolipin biomarkers were done so using the *InVia* Qontor 633 nm laser set to 0.38 mW power, collecting 10s acquisitions and 4 accumulations.

Optical Coherence Tomography (OCT). In determining the extent of changes in the retinal structure of living and post-mortem eyes, Yorkshire pigs eyes were imaged using a Heidelberg Spectralis OCT platform (for both post-mortem and in vivo imaging), using the manufacturer's "Posterior Pole" protocol to acquire volumetric retinal scans in 61 horizontal b-scans averaged over at least 9 frames in a 30°×25° volume centred temporal to the optic disc in the expected location of the pig visual streak. OCT images were exported in tiff format and analysed using ImageJ. The retinal nerve fibre layer and ganglion cell layer were manually segmented, and thicknesses measured at 3000 and 4500 µm from the optic disc orientated in the axis of the visual streak.

Living eyes were imaged from patient recruited to the Ophthalmic and Neurocognitive Assessment in the Management of Critically Ill Patients study: 19/YH/0113, approved by the NHS Research Ethics Service and conducted in the Ophthalmology Department at the Queen Elizabeth Hospital Birmingham of University Hospitals Birmingham NHS Foundation Trust (UK), as previously described. Inclusion criteria were patients over the age of 18 years with planned esophagectomy. Exclusion criteria were individuals with pre-existing retinal pathology, optic nerve pathology or known neurological conditions. Patients were approached in clinic by members of the clinical care team and, if they expressed a willingness to participate, were given a patient information leaflet, had the opportunity to discuss the study and were invited to participate by a member of the research team, providing written, informed consent if they agreed. All documents were approved by the NHS Research Ethics Service and the Hospital Trust.

Artificial Neural Network Data Analysis and Classification. SKiNET, an open-source analysis tool with an accompanying Raman Toolkit web interface was used to generate SOM models from the training data and perform predictions against the test data. 20% of the data was randomly selected from each group and used as test data with the remaining 80% of data used for training. To achieve higher accuracy of the SOM size, these models were optimised by performing cross-validation on the training data, tuning the number of neurons (hexagons), initial learning rate, empiric testing of the number of epochs and number of training steps, with classification accuracy determined using a 10-fold cross-validation. The final model used a 10x10 grids of neurons (for each group), 57,600 training steps (9 epochs), with an initial learning rate of 0.3.

2.8 References

[1] J. Haarbauer-Krupa, M. J. Pugh, E. M. Prager, N. Harmon, J. Wolfe, and K. Yaffe, "Epidemiology of Chronic Effects of Traumatic Brain Injury," *J. Neurotrauma*, vol. 38, no. 23, pp. 3235–3247, Dec. 2021, doi: 10.1089/NEU.2021.0062.

[2] S. Koljenović *et al.*, "Tissue characterization using high wave number Raman spectroscopy," *J. Biomed. Opt.*, vol. 10, no. 3, p. 031116, 2005, doi: 10.1117/1.1922307.

[3] A. Van Gils *et al.*, "Management of mild traumatic brain injury," *Pract. Neurol.*, vol. 20, no. 3, pp. 213–221, May 2020, doi: 10.1136/practneurol-2018-002087.

[4] C. D. Newgard *et al.*, "Revisiting the 'Golden Hour': An Evaluation of Out-of-Hospital Time in Shock and

Traumatic Brain Injury," *Ann. Emerg. Med.*, vol. 66, no. 1, p. 30, Jul. 2015, doi: 10.1016/J.ANNEMERGMED.2014.12.004.
[5] M. M. Dinh, K. Bein, S. Roncal, C. M. Byrne, J. Petchell, and J. Brennan, "Redefining the golden hour for severe head injury in an urban setting: the effect of prehospital arrival times on patient outcomes," *Injury*, vol. 44, no. 5, pp. 606–610, May 2013, doi: 10.1016/J.INJURY.2012.01.011.
[6] C. Peixoto, D. Buchanan, and R. Nahas, "Missed Emergency Department Diagnosis of Mild Traumatic Brain Injury in Patients with Chronic Pain After Motor Vehicle Collision," *Pain Physician*, vol. 1, pp. 101–110, 2023.
[7] Y. G. Bodien *et al.*, "Diagnosing Level of Consciousness: The Limits of the Glasgow Coma Scale Total Score," *J. Neurotrauma*, vol. 38, no. 23, pp. 3295–3305, Dec. 2021, doi: 10.1089/NEU.2021.0199.
[8] K. Kunker, D. M. Peters, and S. Mohapatra, "Long-term impact of mild traumatic brain injury on postural stability and executive function," *Neurol. Sci.*, vol. 41, no. 7, pp. 1899–1907, Jul. 2020, doi: 10.1007/S10072-020-04300-0/TABLES/3.
[9] P. J. A. Dean and A. Sterr, "Long-term effects of mild traumatic brain injury on cognitive performance," *Front. Hum. Neurosci.*, vol. 7, no. JAN, p. 29277, Jan. 2013, doi: 10.3389/FNHUM.2013.00030/BIBTEX.
[10] C. M. Tate *et al.*, "Serum brain biomarker level, neurocognitive performance, and self-reported symptom changes in soldiers repeatedly exposed to low-level blast: A breacher pilot study," *J. Neurotrauma*, vol. 30, no. 19, pp. 1620–1630, Oct. 2013, doi: 10.1089/neu.2012.2683.
[11] B. L. Edlow *et al.*, "Long-Term Effects of Repeated Blast Exposure in United States Special Operations Forces Personnel: A Pilot Study Protocol," *J. Neurotrauma*, vol. 39, no. 19–20, p. 1391, Oct. 2022, doi: 10.1089/NEU.2022.0030.
[12] J. Desroches *et al.*, "A new method using Raman spectroscopy for in vivo targeted brain cancer tissue biopsy," *Sci. Rep.*, vol. 8, no. 1, Dec. 2018, doi: 10.1038/s41598-018-20233-3.
[13] P. Gao *et al.*, "The Clinical Application of Raman Spectroscopy for Breast Cancer Detection," *J. Spectrosc.*, vol. 2017, pp. 1–10, 2017, doi: 10.1155/2017/5383948.
[14] J. H. Granger, M. C. Granger, M. A. Firpo, S. J. Mulvihill, and M. D. Porter, "Toward development of a surface enhanced Raman scattering (SERS) based cancer diagnostic immunoassay panel," *Analyst*, vol. 138, no. 2, pp. 410–416, Jan. 2013, doi: 10.1039/C2AN36128K.
[15] M. Höhl, C. Zeilinger, B. Roth, M. Meinhardt-Wollweber, and U. Morgner, "Multivariate discrimination of heat shock proteins using a fiber optic Raman setup for in situ analysis of human perilymph," *Rev. Sci. Instrum.*, vol. 90, no. 4, Apr. 2019, doi: 10.1063/1.5030301.
[16] IJ C. Bauer, J. P. Wicksted, F. H. M Jongsma, W. F. March, F. Hendrikse, and M. Motamedi, "Noninvasive assessment of the hydration gradient across the cornea using confocal Raman spectroscopy.," *Invest. Ophthalmol. Vis. Sci.*, vol. 39, no. 5, pp. 831–835, Apr. 1998.
[17] A. Katz, E. F. Kruger, G. Minko, C. H. Liu, R. B. Rosen, and R. R. Alfano, "Detection of glutamate in the eye by Raman spectroscopy," *J. Biomed. Opt.*, vol. 8, no. 2, pp. 167–172, 2003, doi: 10.1117/1.1559726.
[18] A. Obana *et al.*, "Macular Carotenoid Levels of Normal Subjects and Age-Related Maculopathy Patients in a Japanese Population," *Ophthalmology*, vol. 115, no. 1, pp. 147–157, Jan. 2008, doi: 10.1016/j.ophtha.2007.02.028.
[19] S. K. Das, S. P. Shetty, and K. K. Sen, "A novel triage tool: Optic nerve sheath diameter in traumatic brain injury and its correlation to rotterdam computed tomography (CT) scoring," *Polish J. Radiol.*, vol. 82, pp. 240–243, Apr. 2017, doi: 10.12659/PJR.900196.
[20] H. E. Killer, G. P. Jaggi, J. Flammer, N. R. Miller, and A. R. Huber, "The optic nerve: a new window into cerebrospinal fluid composition?," *Brain*, vol. 129, pp. 1027–1030, 2006, doi: 10.1093/brain/awl045.
[21] O. Mufti, S. Mathew, A. Harris, B. Siesky, K. M. Burgett, and A. C. Verticchio Vercellin, "Ocular changes in traumatic brain injury: A review," *Eur. J. Ophthalmol.*, vol. 30, no. 5, p. 112067211986697, Aug. 2019, doi: 10.1177/1120672119866974.
[22] S. S. Sadrameli *et al.*, "Changes in Transcranial Sonographic Measurement of the Optic Nerve Sheath Diameter in Non-concussed Collegiate Soccer Players Across a Single Season," *Cureus*, vol. 10, no. 8, Aug. 2018, doi: 10.7759/cureus.3090.
[23] S. M. Cansler and N. K. Evanson, "Connecting endoplasmic reticulum and oxidative stress to retinal degeneration, TBI, and traumatic optic neuropathy," *J. Neurosci. Res.*, vol. 98, no. 3, pp. 571–574, Mar. 2020, doi: 10.1002/JNR.24543.
[24] M. Das *et al.*, "CCL20-CCR6 axis modulated traumatic brain injury-induced visual pathologies," *J. Neuroinflammation*, vol. 16, no. 1, pp. 1–12, May 2019, doi: 10.1186/S12974-019-1499-Z.
[25] V. Vijay *et al.*, "Using Optical Coherence Tomography as a Surrogate of Measurements of Intracranial Pressure in Idiopathic Intracranial Hypertension," *JAMA Ophthalmol.*, vol. 138, no. 12, pp. 1264–1271, Dec. 2020, doi: 10.1001/JAMAOPHTHALMOL.2020.4242.
[26] M. Skau, H. Yri, B. Sander, T. A. Gerds, D. Milea, and R. Jensen, "Diagnostic value of optical coherence tomography for intracranial pressure in idiopathic intracranial hypertension," *Graefe's Arch. Clin. Exp. Ophthalmol.*, vol. 251, no. 2, pp. 567–574, Feb. 2013, doi: 10.1007/S00417-012-2039-Z.
[27] J. G. Fujimoto, C. Pitris, S. A. Boppart, and M. E. Brezinski, "Optical coherence tomography: an emerging technology for biomedical imaging and optical biopsy," *Neoplasia*, vol. 2, no. 1–2, pp. 9–25, 2000, doi: 10.1038/SJ.NEO.7900071.
[28] Y. M. Huang-Link, A. Al-Hawasi, T. Oberwahrenbrock, and Y. P. Jin, "OCT measurements of optic nerve head changes in idiopathic intracranial hypertension," *Clin. Neurol. Neurosurg.*, vol. 130, pp. 122–127, 2015, doi: 10.1016/J.CLINEURO.2014.12.021.

[29] M. Dreesbach *et al.*, “Optic Nerve Head Volumetry by Optical Coherence Tomography in Papilledema Related to Idiopathic Intracranial Hypertension,” *Transl. Vis. Sci. Technol.*, vol. 9, no. 3, 2020, doi: 10.1167/TVST.9.3.24.
[30] P. Nichani and J. A. Micieli, “Retinal Manifestations of Idiopathic Intracranial Hypertension,” *Ophthalmol. Retin.*, vol. 5, no. 5, pp. 429–437, May 2021, doi: 10.1016/J.ORET.2020.08.016.
[31] H. S. Lyons *et al.*, “A systematic review of optical coherence tomography findings in adults with mild traumatic brain injury,” *Eye 2024*, pp. 1–7, Jan. 2024, doi: 10.1038/s41433-023-02845-w.
[32] C. S. Gilmore *et al.*, “Association of Optical Coherence Tomography With Longitudinal Neurodegeneration in Veterans With Chronic Mild Traumatic Brain Injury,” *JAMA Netw. open*, vol. 3, no. 12, Dec. 2020, doi: 10.1001/JAMANETWORKOPEN.2020.30824.
[33] R. Kardon *et al.*, “Prevalence of Structural Abnormalities of the Retinal Nerve Fiber Layer (RNFL) and Ganglion Cell Layer Complex (GCLC) by OCT in Veterans with Traumatic Brain Injury (TBI),” *Invest. Ophthalmol. Vis. Sci.*, vol. 54, no. 15, pp. 2360–2360, Jun. 2013.
[34] A. Ercole *et al.*, “Current and emerging technologies for probing molecular signatures of traumatic brain injury,” *Front. Neurol.*, vol. 8, Aug. 2017, doi: 10.3389/fneur.2017.00450.
[35] R. E. Andersen, L. O. Hansson, O. Nilsson, R. Dijlai-Merzoug, and G. Settergren, “High serum S100B levels for trauma patients without head injuries,” *Neurosurgery*, vol. 48, no. 6, pp. 1255–1260, 2001, doi: 10.1097/00006123-200106000-00012.
[36] M. Minkkinen *et al.*, “Prospective Validation of the Scandinavian Guidelines for Initial Management of Minimal, Mild, and Moderate Head Injuries in Adults,” *J. Neurotrauma*, vol. 36, no. 20, pp. 2904–2912, Oct. 2019, doi: 10.1089/NEU.2018.6351.
[37] J. J. Bazarian *et al.*, “Serum GFAP and UCH-L1 for prediction of absence of intracranial injuries on head CT (ALERT-TBI): a multicentre observational study,” *Lancet. Neurol.*, vol. 17, no. 9, pp. 782–789, Sep. 2018, doi: 10.1016/S1474-4422(18)30231-X.
[38] I. Banyan Biomarkers, “Evaluation of Automatic Class III Designation for Banyan Brain Trauma Indicator Decision Memorandum,” 2018.
[39] J. J. S. Rickard, V. Di-Pietro, D. J. Smith, D. J. Davies, A. Belli, and P. G. Oppenheimer, “Rapid optofluidic detection of biomarkers for traumatic brain injury via surface-enhanced Raman spectroscopy,” *Nat. Biomed. Eng.*, vol. 4, no. 6, pp. 610–623, Feb. 2020, doi: 10.1038/s41551-019-0510-4.
[40] C. Banbury *et al.*, “Spectroscopic detection of traumatic brain injury severity and biochemistry from the retina,” *Biomed. Opt. Express*, vol. 11, no. 11, pp. 6249–6261, Nov. 2020, doi: 10.1364/boe.399473.
[41] C. Banbury *et al.*, “Development of the Self Optimising Kohonen Index Network (SKiNET) for Raman Spectroscopy Based Detection of Anatomical Eye Tissue,” *Sci. Rep.*, vol. 9, no. 1, pp. 1–9, Dec. 2019, doi: 10.1038/s41598-019-47205-5.
[42] C. Banbury, G. Harris, M. Clancy, R. J. Blanch, J. J. S. Rickard, and P. Goldberg Oppenheimer, “Window into the mind: Advanced handheld spectroscopic eye-safe technology for point-of-care neurodiagnostic,” *Sci. Adv.*, vol. 9, no. 46, Nov. 2023, doi: 10.1126/SCIADV.ADG5431/SUPPL_FILE/SCIADV.ADG5431_SM.PDF.
[43] C. Banbury and P. G. Oppenheimer, “Towards developement of technology for point of care diagnostics for traumatic brain injury,” University of Birmingham, 2021.
[44] F. Z. Javaid, J. Brenton, L. Guo, and M. F. Cordeiro, “Visual and Ocular Manifestations of Alzheimer’s Disease and Their Use as Biomarkers for Diagnosis and Progression,” *Front. Neurol.*, vol. 7, p. 55, 2016, doi: 10.3389/fneur.2016.00055.
[45] M. Joukal, “Anatomy of the Human Visual Pathway,” in *Homonymous Visual Field Defects*, Springer International Publishing, 2017, pp. 1–16.
[46] S. Lemmens, A. Devulder, K. Van Keer, J. Bierkens, P. De Boever, and I. Stalmans, “Systematic Review on Fractal Dimension of the Retinal Vasculature in Neurodegeneration and Stroke: Assessment of a Potential Biomarker,” *Front. Neurosci.*, vol. 14, p. 16, Jan. 2020, doi: 10.3389/FNINS.2020.00016/BIBTEX.
[47] N. Marchesi, F. Fahmideh, F. Boschi, A. Pascale, and A. Barbieri, “Ocular Neurodegenerative Diseases: Interconnection between Retina and Cortical Areas,” *Cells*, vol. 10, no. 9, Sep. 2021, doi: 10.3390/CELLS10092394.
[48] P. J. Snyder *et al.*, “Retinal imaging in Alzheimer’s and neurodegenerative diseases,” *Alzheimers. Dement.*, vol. 17, no. 1, pp. 103–111, Jan. 2021, doi: 10.1002/ALZ.12179.
[49] L. Papa *et al.*, “Elevated levels of serum glial fibrillary acidic protein breakdown products in mild and moderate traumatic brain injury are associated with intracranial lesions and neurosurgical intervention,” *Ann. Emerg. Med.*, vol. 59, no. 6, pp. 471–483, Jun. 2012, doi: 10.1016/j.annemergmed.2011.08.021.
[50] J. Sen *et al.*, “Extracellular fluid S100B in the injured brain: A future surrogate marker of acute brain injury?,” *Acta Neurochir. (Wien).*, vol. 147, no. 8, pp. 897–900, Aug. 2005, doi: 10.1007/s00701-005-0526-2.
[51] R. J. Shannon *et al.*, “Extracellular N-Acetylaspartate in Human Traumatic Brain Injury,” *J. Neurotrauma*, vol. 33, no. 4, pp. 319–329, Feb. 2016, doi: 10.1089/neu.2015.3950.
[52] M. Marro *et al.*, “Dynamic molecular monitoring of retina inflammation by in vivo Raman spectroscopy coupled with multivariate analysis,” *J. Biophotonics*, vol. 7, no. 9, pp. 724–734, 2014, doi: 10.1002/jbio.201300101.
[53] C. Stiebing *et al.*, “Nonresonant Raman spectroscopy of isolated human retina samples complying with laser safety regulations for in vivo measurements,” *Neurophotonics*, vol. 6, no. 04, p. 1, Sep. 2019, doi:

10.1117/1.nph.6.4.041106.
[54] G. Smith and D. A. Atchison, “The eye and visual optical instruments,” p. 816, 1997, Accessed: Feb. 21, 2024. [Online]. Available: https://books.google.com/books/about/The_Eye_and_Visual_Optical_Instruments.html?id=Jg68339LQeQC.
[55] I. V. Ermakov, R. W. McClane, W. Gellermann, and P. S. Bernstein, “Resonant Raman detection of macular pigment levels in the living human retina,” *Opt. Lett.*, vol. 26, no. 4, pp. 202–204, Feb. 2001, doi: 10.1364/ol.26.000202.
[56] M. F. Kaschke, K.-H. Donnerhacke, and M. S. Rill, *Optical devices in ophthalmology and optometry : technology, design principles and clinical applications*, 1st ed. John Wiley and Sons Inc., 2014.
[57] M. J. Chandler, P. J. Smith, D. A. Samuelson, and E. O. Mackay, “Photoreceptor density of the domestic pig retina,” *Vet. Ophthalmol.*, vol. 2, no. 3, pp. 179–184, 1999, doi: 10.1046/J.1463-5224.1999.00077.X.
[58] S. Regal, D. O’Connor, P. Brige, R. Delattre, T. Djenizian, and M. Ramuz, “Determination of optical parameters of the porcine eye and development of a simulated model,” *J. Biophotonics*, vol. 12, no. 11, p. e201800398, Nov. 2019, doi: 10.1002/JBIO.201800398.
[59] T. W. Olsen, S. Sanderson, X. Feng, and W. C. Hubbard, “Porcine sclera: thickness and surface area,” *Invest. Ophthalmol. Vis. Sci.*, vol. 43, no. 8, pp. 2529–2532, 2002.
[60] M. Hammer *et al.*, “Fundus autofluorescence beyond lipofuscin: lesson learned from ex vivo fluorescence lifetime imaging in porcine eyes,” *Biomed. Opt. Express, Vol. 9, Issue 7, pp. 3078-3091*, vol. 9, no. 7, pp. 3078–3091, Jul. 2018, doi: 10.1364/BOE.9.003078.
[61] C. Artigas, A. Navea, M. M. López-Murcia, A. Felipe, C. Desco, and J. M. Artigas, “Spectral transmission of the pig lens: Effect of ultraviolet A + B radiation,” *J. Fr. Ophtalmol.*, vol. 37, no. 10, pp. 773–779, Dec. 2014, doi: 10.1016/J.JFO.2014.06.006.
[62] J. W. Brooks, “Postmortem Changes in Animal Carcasses and Estimation of the Postmortem Interval,” *Vet. Pathol.*, vol. 53, no. 5, pp. 929–940, Mar. 2016, doi: 10.1177/0300985816629720.
[63] E. M. S. Hood, C. A. Curcio, and D. Lipinski, “Isolation, culture, and cryosectioning of primary porcine retinal pigment epithelium on transwell cell culture inserts,” *STAR Protoc.*, vol. 3, no. 4, Dec. 2022, doi: 10.1016/J.XPRO.2022.101758.
[64] R. Shrestha, T. Kanchan, and K. Krishan, “Methods of Estimation of Time Since Death,” *StatPearls*, May 2023, Accessed: Nov. 23, 2023. [Online]. Available: https://www.ncbi.nlm.nih.gov/books/NBK549867/.
[65] D. Goldenberg, J. Shahar, A. Loewenstein, and M. Goldstein, “Diameters of retinal blood vessels in a healthy cohort as measured by spectral domain optical coherence tomography,” *Retina*, vol. 33, no. 9, pp. 1888–1894, Oct. 2013, doi: 10.1097/IAE.0B013E31829477F2.
[66] G. Socrates, *Infrared and Raman Characteristic Group Frequencies: Tables and Charts. 3rd ed.* John Wiley & Sons, Ltd, 2004.
[67] L. Giannoni, F. Lange, M. Sajic, K. J. Smith, and I. Tachtsidis, “A hyperspectral imaging system for mapping haemoglobin and cytochrome-c-oxidase concentration changes in the exposed cerebral cortex,” *IEEE J. Sel. Top. Quantum Electron.*, vol. 27, no. 4, Jul. 2021, doi: 10.1109/JSTQE.2021.3053634.
[68] J. P. Kitt, D. A. Bryce, S. D. Minteer, and J. M. Harris, “Raman Spectroscopy Reveals Selective Interactions of Cytochrome c with Cardiolipin That Correlate with Membrane Permeability,” *J. Am. Chem. Soc.*, vol. 139, no. 10, pp. 3851–3860, Mar. 2017, doi: 10.1021/JACS.7B00238/ASSET/IMAGES/LARGE/JA-2017-00238Q_0006.JPEG.
[69] V. Russo *et al.*, “Key Role of Cytochrome C for Apoptosis Detection Using Raman Microimaging in an Animal Model of Brain Ischemia with Insulin Treatment,” *Appl. Spectrosc.*, vol. 73, no. 10, pp. 1208–1217, Oct. 2019, doi: 10.1177/0003702819858671.
[70] P. G. Sullivan, J. N. Keller, W. L. Bussen, and S. W. Scheff, “Cytochrome c release and caspase activation after traumatic brain injury,” *Brain Res.*, vol. 949, no. 1–2, pp. 88–96, Sep. 2002, doi: 10.1016/S0006-8993(02)02968-2.
[71] W. Li *et al.*, “Study on the relationship between brain temperature and cytochrome c in hyperacute phase of mouse traumatic brain injury,” *https://doi.org/10.1117/12.2687355*, vol. 12770, p. 1277004, Nov. 2023, doi: 10.1117/12.2687355.
[72] J. D. Unsay, K. Cosentino, Y. Subburaj, and A. J. García-Sáez, “Cardiolipin effects on membrane structure and dynamics,” *Langmuir*, vol. 29, no. 51, pp. 15878–15887, Dec. 2013, doi: 10.1021/LA402669Z.
[73] M. O. Ripple, M. Abajian, and R. Springett, “Cytochrome c is rapidly reduced in the cytosol after mitochondrial outer membrane permeabilization,” *Apoptosis*, vol. 15, no. 5, pp. 563–573, May 2010, doi: 10.1007/S10495-010-0455-2.
[74] V. E. Kagan *et al.*, “Oxidative lipidomics of apoptosis: redox catalytic interactions of cytochrome c with cardiolipin and phosphatidylserine,” *Free Radic. Biol. Med.*, vol. 37, no. 12, pp. 1963–1985, Dec. 2004, doi: 10.1016/J.FREERADBIOMED.2004.08.016.
[75] J. Ji *et al.*, “Lipidomics identifies cardiolipin oxidation as a mitochondrial target for redox therapy of brain injury,” *Nat. Neurosci.*, vol. 15, no. 10, pp. 1407–1413, Oct. 2012, doi: 10.1038/NN.3195.
[76] P. V. Cvijin, J. J. O’Brien, G. H. Atkinson, W. K. Wells, J. I. Lunine, and D. M. Hunten, “Methane overtone absorption by intracavity laser spectroscopy,” *CPL*, vol. 159, no. 4, pp. 331–336, Jul. 1989, doi: 10.1016/0009-2614(89)87495-0.
[77] Y. LI *et al.*, “Rapid detection of nasopharyngeal cancer using Raman spectroscopy and multivariate statistical analysis,” *Mol. Clin. Oncol.*, vol. 3, no. 2, pp. 375–380, Mar. 2015, doi: 10.3892/MCO.2014.473.

[78] C. Childs, L. A. Barker, A. Gage, and M. Loosemore, “Investigating possible retinal biomarkers of head trauma in Olympic boxers using optical coherence tomography,” *Eye Brain*, vol. 10, pp. 101–110, 2018, doi: 10.2147/EB.S183042.
[79] L. Vien, C. Dalporto, and D. Yang, “Retrograde Degeneration of Retinal Ganglion Cells Secondary to Head Trauma,” *Optom. Vis. Sci.*, vol. 94, no. 1, pp. 125–134, Jan. 2017, doi: 10.1097/OPX.0000000000000899.
[80] T. Minamikawa, Y. Harada, and T. Takamatsu, “Ex vivo peripheral nerve detection of rats by spontaneous Raman spectroscopy,” *Sci. Rep.*, vol. 5, no. 1, pp. 1–11, Nov. 2015, doi: 10.1038/srep17165.
[81] C.-Y. Chang, D.-S. Ke, and J.-Y. Chen, “Essential fatty acids and human brain,” *Acta Neurol. Taiwan.*, vol. 18, no. 4, pp. 231–241, 2009.
[82] C. Krafft, L. Neudert, T. Simat, and R. Salzer, “Near infrared Raman spectra of human brain lipids,” *Spectrochim. Acta Part A Mol. Biomol. Spectrosc.*, vol. 61, no. 7, pp. 1529–1535, May 2005, doi: 10.1016/J.SAA.2004.11.017.
[83] P. Homayoun, N. E. Parkins, J. Soblosky, M. E. Carey, E. B. Rodriguez De Turco, and N. G. Bazan, “Cortical impact injury in rats promotes a rapid and sustained increase in polyunsaturated free fatty acids and diacylglycerols,” *Neurochem. Res.*, vol. 25, no. 2, pp. 269–276, 2000, doi: 10.1023/A:1007583806138/METRICS.
[84] J. G. Pilitsis *et al.*, “Free fatty acids in cerebrospinal fluids from patients with traumatic brain injury,” *Neurosci. Lett.*, vol. 349, no. 2, pp. 136–138, Oct. 2003, doi: 10.1016/S0304-3940(03)00803-6.
[85] S. Yue, J. M. Cárdenas-Mora, L. S. Chaboub, S. A. Lelivre, and J. X. Cheng, “Label-Free Analysis of Breast Tissue Polarity by Raman Imaging of Lipid Phase,” *Biophys. J.*, vol. 102, no. 5, p. 1215, Mar. 2012, doi: 10.1016/J.BPJ.2012.01.023.
[86] A. C. Duhaime, “Large animal models of traumatic injury to the immature brain,” *Dev. Neurosci.*, vol. 28, no. 4–5, pp. 380–387, Aug. 2006, doi: 10.1159/000094164.
[87] CDC, “Traumatic Brain Injury in the United States,” 2002. Accessed: Jan. 13, 2020. [Online]. Available: www.cdc.gov/TraumaticBrainInjury.

Chapter 3

Developing a Non-Mydriatic Fundus Imaging System for Portable, Point-of-Care Neurodiagnostics

In this chapter, first steps were taken towards establishing a new portable Raman system for eye-based diagnostics by developing a handheld fundus camera set-up that can be combined with the Raman light paths to replace the smartphone fundus attachment “D-Eye” module which has been discontinued. A Raspberry Pi module and accessories were used to build the handheld fundus camera, allowing for complete modification, along with clear telemedicine capabilities.

Ophthalmoscopes were explored, and how the fundamental and simplistic indirect ophthalmoscopy has been developed to establish several handheld fundus cameras on the current market, identifying the current limitations, leading to the realisation that fundus imaging utilising Volk lenses require optical systems with long working distances that limit their use in handheld devices. Careful consideration and many iterations were therefore tested in the development of the fundus system in this chapter to reduce the working distance and increase the suitability for point-of-care use in this portable eye-based Raman device.

Alongside this, Light Emitting Diode (LED) illumination was optimised in both cases of light wavelength and focus to reduce the amount of patient pupil contraction all whilst seamlessly integrating with the optical paths of the Raman spectroscopy system. Once achieved, the final fundus camera design was tested for non-mydriatic use, eliminating the need for any artificial pupil dilation the final piece required for complete point-of-care application, ready to be implemented into this portable eye-based Raman device for simultaneous biochemical and structural TBI diagnostics.

3.1 Introduction

The human fundus is a highly investigated structure that plays an important role in medicine as it has direct vascular links to the brain and central nervous system (CNS) whilst also able to be visualised externally and non-invasively. Since its invention in 1851, the ophthalmoscope has been vital for diagnosing retinal, choroidal, and cardiovascular diseases and screening for early causes of blindness such as diabetic retinopathy, age-related macular degeneration, and glaucoma[1]–[5]. As fundus cameras advance, there are increasing cases of visual morbidity being prevented through early identification [6], alongside taking advantage of the unique opportunity the retina provides in acting as an embryological extension of the brain[7].

Fundus photography, specifically utilising indirect ophthalmoscopy, is a commonplace technique in opticians and ophthalmic clinics, in which visible light is scattered at the fundus and produces an image of the important structures: the retina, optic nerve head, macula fovea, blood vessels and arteries. There is increasing research utilising fundus imaging to diagnose and monitor neurodegenerative diseases and disorders[5], [7]–[10], and point-of-care brain trauma diagnostics[11]–[14], as the retina is viewed as an extension of the CNS[15]. However, traditional fundus cameras are large and expensive systems that require the upkeep of technicians and significant training before use[6]. Panwar *et* al. outline several modern table-top fundus cameras and, along with highlighting the limitation of patients needing to be sat upright for extended periods which is not suitable for point-of-care applications, ultimately conclude that most models require add-on features to be utilised fully, creating larger and non-portable systems[6].

Therefore, there is a need for hand-held fundus cameras that are accessible, affordable, high-resolution, and intuitive to use by healthcare professionals without extensive training. This is a growing market with some systems available to buy either as handheld units or attachments for smartphones[3], [16], [17]. However, there are common limitations for hand-held fundus systems, one being the requirement for pupil dilation. Artificial pupil dilation (mydriasis) is not only an invasive procedure but also creates an additional 30-minute waiting period before imaging, pushing diagnosis outside of the vital acute phase in point-of-care applications. Mydriasis also leaves the patient with blurred vision for 4-6 hours following the imaging[18], which could hinder any diagnostic techniques utilised after the imaging such as cognitive assessments typical in neurodiagnoses, and also has the small risk of inciting acute angle-closure glaucoma[19], therefore a non-mydriatic fundus camera is imperative when considering point-of-care and long-term monitoring uses.

A desirable feature for the future of hand-held fundus cameras is by combination with another parallel ophthalmic technique such as Optical Coherent Tomography (OCT) or Raman Spectroscopy. OCT is another non-invasive technique that utilises low coherent interferometry to produce cross-sectional images of the retina and is more frequently being used for early diagnosis of neurodegenerative disorders such as Alzheimer’s disease[9], [20]. Raman Spectroscopy is a rapid, label-free technique that

utilises inelastically scattered light to obtain a spectrum of peaks that represent a sample's molecular bond vibrations[21]. The non-destructive nature and portability potential of Raman spectroscopy has brought increased interest in its application in clinical settings, specifically for neurodegeneration[22], [23], and more experimentally in the retina[24]–[26].

Another limitation of hand-held fundus cameras, specifically smartphone-based systems, is the systems are not universal and quickly becoming obsolete as smartphone models update. This was the case for the D-Eye, which was previously employed in the portable EyeD Raman system utilising visible 635 nm wavelengths[24], discussed in Chapter 2. We already faced limitations as the most current smartphone model the company catered for was the iPhone 8 with no plans to update, and then the company went obsolete. Thus, for the continued development of the portable Raman spectroscopy technology explored in this work, we needed a fundus imaging system that would be hand-held and adaptable, whilst also compatible with near-infrared wavelengths.

Combining biochemical and structural changes in the retina would level up the application value of the fundus system. In this chapter, we design a new portable, non-mydriatic fundus imaging system that utilises a Raspberry Pi module to obtain images of the back of a phantom eye model and *ex-vivo* porcine eyes.

3.2 Current Fundus Imaging Market

Indirect ophthalmoscopy is implemented for handheld and smartphone fundus camera systems, providing a true, horizontally and vertically inverted image of the retina, using a condensing lens to achieve a 50-degree field of vision and x3 magnification, whereas direct ophthalmoscopy creates a 5-degree field of vision with an x15 magnification but requires significant training[27]. Corr *et* al. outline the 3 fundamental conditions that the inventor of the first ophthalmoscope, Hermann von Helmholtz, stated were essential to view the human fundus *in vivo.* These are as follows: correction of refractive errors, sufficient illumination to the retina and for the light source and observer's eyes to be aligned along the same optical axis[27]. Most handheld systems, especially smartphone-based, unfortunately, make a compromise in the 3 Helmholtz values to achieve portability.

The simplest form of indirect ophthalmoscopy consists of a condenser lens (typically 20 D Volk lens), an observer and a patient, illustrated in **Fig. 3.1a.** This can be simply translated into a handheld system by replacing the observer with a camera or smartphone, capable of capturing images for distributing or analysis post-examination. A popular 3D printed housing for this set-up mounts a 20 D lens and a smartphone along a single axis as a simple and cost-effective set-up and is available for open access on AutoDesk Instructables[28], and is shown with results in **Fig. 3.1b**. Examples of the fundus view are shown in **Fig. 3.1c,** both in darkness and with room lighting, and retinal arterioles can be seen. This system does not uphold the 3

Helmholtz criteria as the smartphone LED light source is not aligned along the same axis as the smartphone camera, therefore, reflections from the LED flashlight can be seen and obscures the view.

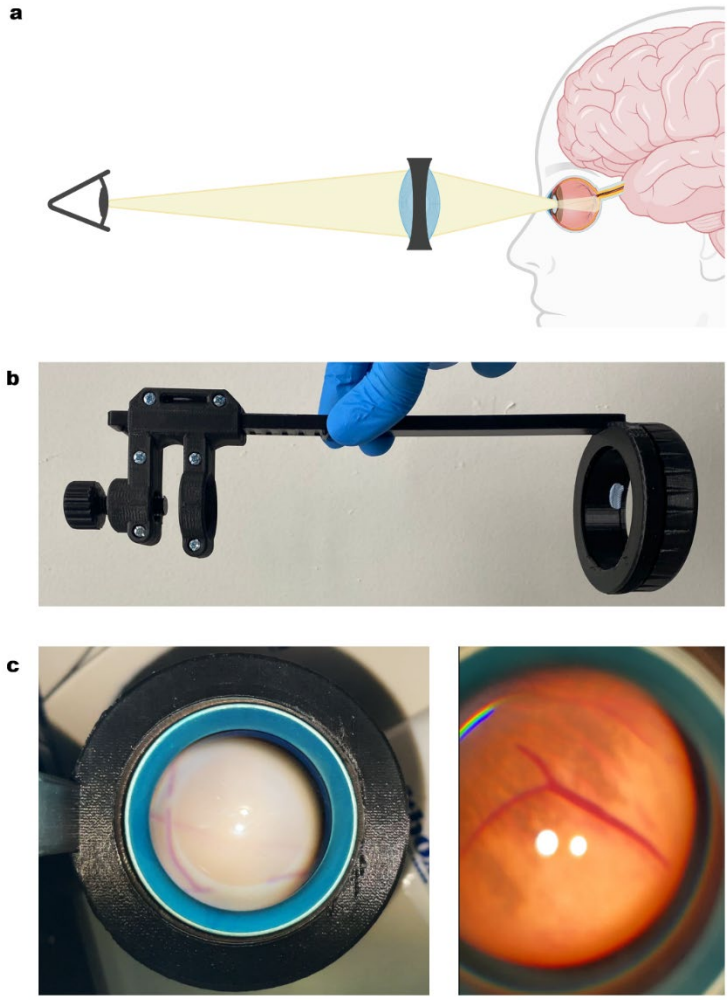

Figure 3.1. ***a*** *Schematic diagram of simple indirect ophthalmoscopy using a condensing lens. Created using Biorender.com* ***b*** *Openaccess 3D printed housing for the simple indirect ophthalmoscopy technique using a 20 Dioptre condensing lens and an smartphone to view the fundus.* ***c*** *Results from utilising the openaccess 3D printed housing with 20 D condensing lens, demonstrated with ex vivo porcine eyes.* ***(left)*** *implemented in room lighting with smartphone LED flash* ***(right)*** *demonstrated in darkness with smartphone LED flash.*

A selection of portable systems that are still available to purchase have been summarised in **Table 3.1**, where information on dimensions, weight and costs were available as of November 2023; choosing only three smartphone-based systems. This representation of the market will be utilised in the future development of this portable fundus system to ensure parameters are chosen to fit within desirable traits. There is a considerable price increase when minimum pupil sizes decrease from 5 mm as these are mydriatic systems requiring pupil dilation. It is noted that the Remido Fundus on Phone, Volk iNview and Volk VistaView are all smartphone-compatible systems with prices excluding the mobile device.

Smartphone-compatible fundus cameras have been a topic of interest in literature, and many have been reviewed for their clinical utility[3], [16], [17], [29]. Typically, smartphone-based fundus cameras utilise indirect ophthalmoscopy without a condensing lens, so they require the phone to be 4-5 cm from the patient's eye and for the pupil to be dilated with mydriatic eye drops[27]. This is confirmed in the D-Eye patent, which suggests that the entire premise of the device is redirecting the iPhone light/LED into the same plane as the camera. The design also features polarised filters between the iPhone camera and the eye, and the diaphragm and second beamsplitter, these are the main factors for reducing glare from the eye[30].

Prayago *et* al. completed an up-to-date sweep of smartphone-based retinal photography systems for diabetic retinopathy screening, observing a price range of £108-351 when converting from United States (US) dollars to Great British Pounds (GBP)[3]. This is a significant drop in cost compared to the current-market portable systems reviewed in **Table 3.1.** Karakaya *et* al. compared four smartphone-based fundus systems with the simplistic 20 D indirect ophthalmoscopy technique, evaluating their classification accuracy within their deep learning network: iExaminer (61%), D-Eye (62%), Peek Retina (69%), iNview (75%)[29]. The smartphone-based retinal imaging systems are compared in **Fig. 3.2,** where it is notable that most systems are compatible with iPhone models 5 – 7 which were released between 2012 – 2016, despite the study being completed in 2020. This exemplifies the inability of companies to keep up with the fast-moving smartphone market and is demonstrated further as 3 of the 4 systems are now obsolete, with the Volk iNview only available to purchase new.

	iExaminer	**D-Eye**	**Peek Retina**	**iNview**	**20 D Lens**
Compatible Smartphones	iPhone 6	iPhone 6/7	Universal	iPhone 5/6/6S	Universal
Illumination Source	Inside	Flashlight	Inside	Flashlight	Flashlight
Dilation dependency	Not Required	Required	Required	Not Required	Required
Degree of Retinal View	25	6-20	20-30	50	46
Working Distance (mm)	22	22	22	65	50
Size (mm)	70/220/162	68/135/7	25/75/35	180/76/180	50/50/10
Weight (g)	390	25	43	332	50
Price ($)	693	400	235	799	113
Type of captured data	Image	Video	Image/Video	Image	N/A
# of Image / Duration of Video	5 images	30 seconds	N/A	9 images	N/A
Size of Images/Video	320x280	640x480	640x480	640x480	N/A

Figure 3.2. Smartphone-based retinal imaging system study completed by Karakaya et al. where four systems available on the market were compared to a simplistic 20 D condensing lens [29].

Table 3.1. Summary of portable fundus imaging systems currently on the market, including both tabletop and handheld devices. Dimensions that state “two parts” require the purchase of a small module as well as an additional attachment, reducing portability and cost-effectiveness.

Name	Company	Price (£)	Dimensions (mm)	Weight (g)	Resolution (megapixel)	Min pupil size (mm)	Refs
iNview	Volk	720.00	94 x 180	413	8	5.0	[31]
VistaView	Volk	1492.00	88 x 202 x 103	560	48	5.0	[32]
Hand Held Non-Mydriatic HD Fundus Camera HFC	Hanson Medical	3287.00	160 x 90 x 190	450	2.1	2.5	[33]
Signal	Topcon Health	4109.00	127 x 202 x 240	785	5	3.1	[34]
VersaCam	NIDEK	4520.00	89 x 40 x 203 118 x 43 (two parts)	445	5	3.5	[35]
The Fundus on Phone	Remido	4600.00	93 x 284 x 226	1100	12	3.0	[16]
Pictor Plus	Volk	5664.00	82 x 166 x 66 67 x 73 x 160 (two parts)	700	4.9	3.0	[36]
Visuscout 100	Zeiss	5753.00	115 x 216 x 199	800	5	3.5	[37]
Aurora IQ	Optomed	6919.75	406 x 381 x 152	2722	4.24	3.1	[38]
Pictor Prestige	Volk	7245.00	122 x 202 x 97 69 x 74 x 160 (two parts)	797	4.24	3.0	[39]

3.3 Designing & Building

3.3.2. Initial Design

As demonstrated in the ophthalmoscope literature review, portable fundus systems based on smartphones are not universal and quickly become redundant due to the fast turnaround of new models. Therefore, an alternative platform is required that is

handheld, user-friendly, and easy to modify, and a Raspberry Pi-based camera system fits all these requirements. There are some examples in literature of Raspberry Pi's being utilised for fundus imaging, due to its compatibility with near-infrared (near-IR) wavelengths to achieve non-mydriatic ophthalmoscopy and telemedicine capabilities but, as a standard, lack autofocus which is a strength in smartphone-based fundus imaging[5], [40], [41].

Yan *et* al. describe a low-cost Raspberry Pi stereoscopic fundus imaging system that uses 3 RasPi cameras and a Volk lens (unspecified power but likely to be 20 D)[42]. Whilst this setup produces good quality images, the system is large and not handheld. Palacios *et* al. highlights the necessity for handheld systems, stating the limitations of desktop fundus imaging to be bulkiness, an associated steep learning curve and high costs[40]. Instead, they propose a large field-of-view retinal imaging system using a RasPi board and a 90 D Volk lens, choosing Raspberry Pi over Arduino due to the limitations in processor performance and programming language. The camera they produce has dimensions: 220 x 200 x 135 mm and a weight: of 997 grams[40], making it a good competitor with the current handheld fundus imaging systems on the market shown in **Table 3.1.**

Shen *et* al. employ near-IR wavelengths with a dual IR and white LEDs in their RasPi-based fundus camera which is combined with a Raspberry Pi module with a NoIR camera, a 5-inch touchscreen display and a 20 D condensing lens[43]. Whilst this system is small (133 x 91 x 45 mm), lightweight (386 grams) and cost-effective ($185.20, which is ~£146), the set-up requires the user to hold the 20D lens at the appropriate distance from the patient's eye and then the camera at a further, highly specific distance to view the fundus in focus, potentially requiring two users to achieve consistent results. The system is successful in obtaining non-mydriatic fundus images with portable parameters but still would need training before use. A lot of the features of this set-up are highly desirable but would need to be re-designed to meet all portable ophthalmoscopy requirements for neurodiagnostics.

The initial design for a handheld fundus camera featured the Raspberry Pi 4 module (Raspberry Pi) and NoIR camera (Raspberry Pi), an 800 nm LED (LED800L, ThorLabs), a 14D Volk single aspheric lens (Birmingham Optical) and 7" Touchscreen Display (Raspberry Pi), shown in **Fig. 3.3a**. The 14D Volk lens allowed for the longest working distance (75 mm) that we could source, in which other components could be added for additional neurodiagnostics such as for Raman Spectroscopy. The NoIR RasPi camera was run on Python scripts titled "RasPi_ NoIR_ FundusCam_ Motion" and "RasPi_ NoIR_ FundusCam _Static" which inverted the image to remove the mirroring effect from the Volk lens, and optional cropped view to maximise and centralise the image. It also allowed continuous viewing for adjustments, whilst saving images and pictures. When the phantom eye and Volk lens are placed at the correct 75 mm working distance, and the NoIR camera is moved between 0 and 90 mm, illustrated in **Fig. 3.3b**, the crosshairs that represent the retina could only be viewed as in-focus when the NoIR camera sits 24 mm away from the Volk lens, results shown

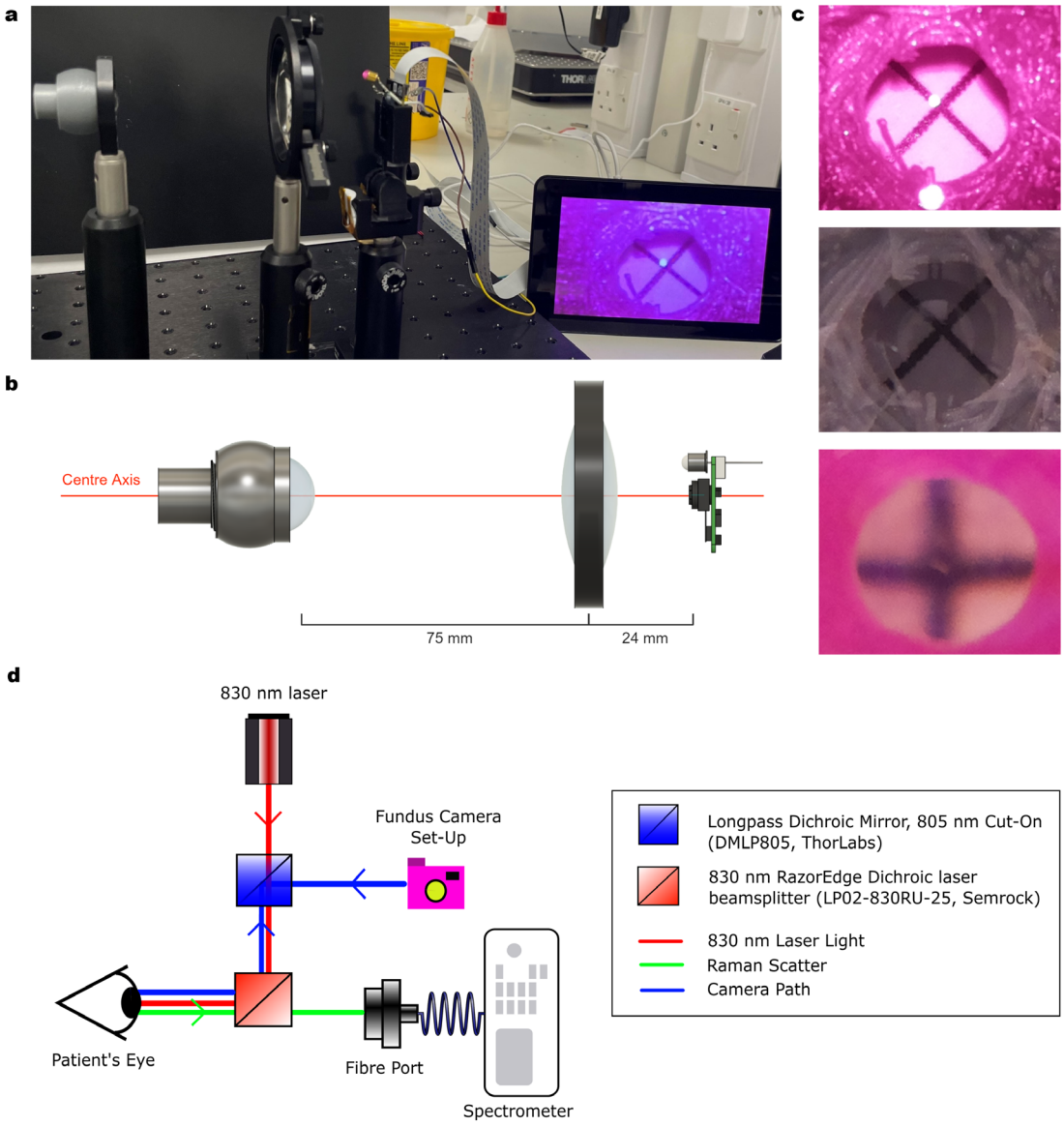

Figure 3.3. ***a*** *Picture of the initial fundus camera set-up built on an optical table showing (from left to right) the phantom eye model, the 14 D Volk condenser lens, the Raspberry Pi NoIR camera module, the 800 nm LED and the Raspberry Pi 7" Touchscreen display. The display shows the camera view of the crosshairs located at the retinal position of the phantom eye, the crosshairs are positioned where they are focused, not at the correct 18 mm retinal distance.* ***b*** *A schematic diagram of the initial fundus camera set-up.* ***c*** *Examples of camera views captured on the touchscreen module. The top and middle panel shows the crosshairs in focus as the closest possible position to the phantom lens, the first using the LED to illuminate and the second using room lighting. The bottom panel shows the crosshairs at the correct 18 mm position of the retina, but it is out of focus.* ***d*** *Schematic diagram of the prospective 830 nm portable Raman set-up, illustrating the proposed path of the fundus camera and the shared optics with the Raman spectroscopy path.*

in **Fig. 3.3c** top and middle panels with the 800 nm IR LED on and with regular room lighting. When the crosshairs are in the correct retinal position (18 mm from the front of the eye), the crosshairs appear out of focus and distorted, as shown in the bottom panel of **Fig. 3.3c.** Alongside obtaining a focused image of the crosshairs at the retinal position of the phantom eye model, the objective is to minimise the path distance of the fundus camera set-up e.g. the distance between the Volk lens and NoIR camera (currently 24 mm) for portability whilst maximising the path distance between the phantom eye and the Volk lens (currently 75 mm), illustrated in **Fig. 3.3b.** The

maximsied path is essential to allow for the shared optics required to combine the fundus imaging with Raman spectroscopy, as shown in the schematic diagram for the proposed 830 nm portable Raman device shown in **Fig. 3.3d.**

Upon further reading, Colenbrander *et* al. outlined the basic principles of indirect ophthalmoscopy, providing calculations of distances between the patient and observer depending on the condenser lens[44]. A 20 D Volk lens, which is commonplace for indirect ophthalmoscopy, requires a distance of 30 – 45 cm between the lens and observer, whilst a 13 D lens needs 32.7 – 47.7 cm[44]. The 14 D Volk lens, chosen for a maximum working distance for a portable Raman spectroscopy set-up to be implemented alongside, will therefore require approximately the same range.

Following the guidance from Colenbrander *et* al., an improvement was noticed with increased distances and fundus imaging of the crosshairs at the retinal position was achieved at a distance of 30 cm from the 14 D Volk lens, as shown in **Fig. 3.4**. Whilst good image quality was still achieved at this distance, demonstrated in the bottom right panel of **Fig. 3.4,** these parameters are not ideal when implementing a camera as the observer, all enclosed in a hand-held housing, as the entire working path of the optical system would be around 1 metre long, outside of the range for an effective point-of-care device. The next steps in this process would be to reduce the entire path length, specifically between the camera and Volk lens.

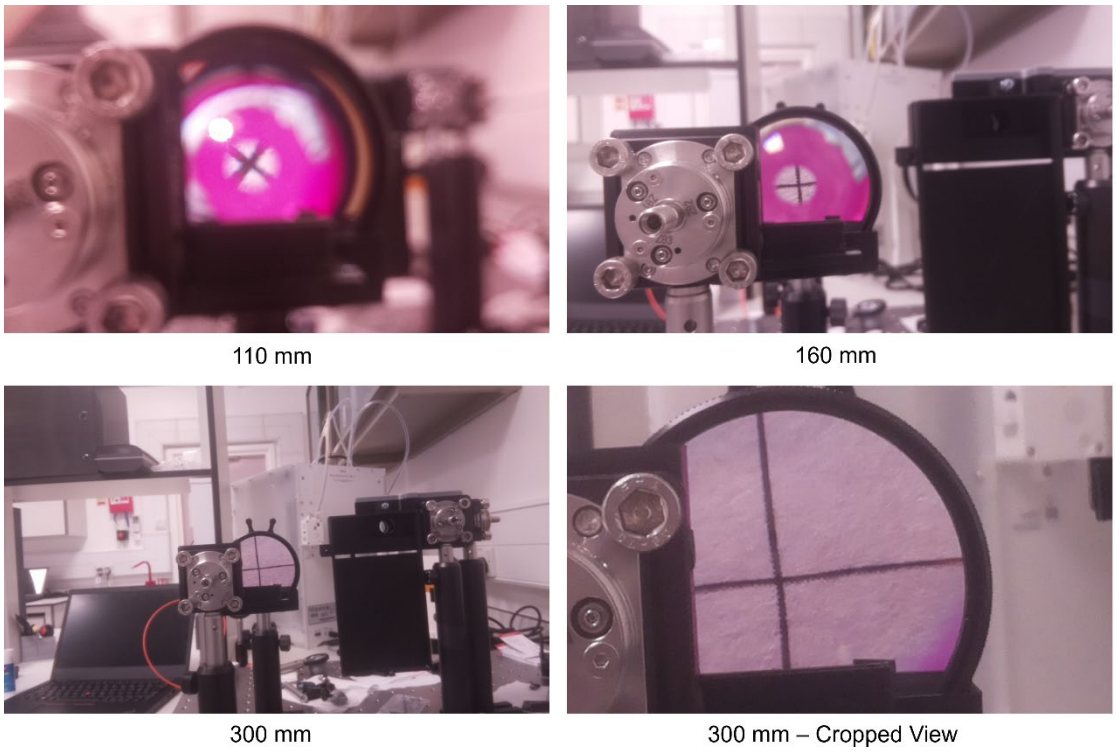

Figure 3.4. Demonstration of improved focus on the crosshairs as the distance between the 14 D Volk lens and the RasPi NoIR camera module is increased from 24 mm to 110, 160 then 300 mm. At 300 mm (bottom panels), good focus and image quality is achieved even when using a Python command to crop the camera view (bottom right panel). This 300 m distance makes the entire fundus camera set-up large and bulky, not ideal for handheld, point-of-care use.

3.3.3 Reducing Path Length

To reduce the working distance path length, the beam focused by the Volk lens to the camera needs to be done so closer to the Volk lens, I started by mixing and matching different positions between the 3 components, i.e. moving away from the 75 mm working distance of the Volk lens, shown in **Fig. 3.5a.** I found an example of a NoIR camera user adjusting the camera lens to shorten the working distance[45], this was implemented alongside the reconfiguring of the distances between components to determine what would be the most optimised version of the initial fundus camera set-up, shown in **Fig. 3.5b.** The view of the crosshairs was being restricted in two of the configurations in **Fig. 3.5a** and all of the results from adjusting the NoIR camera lens.

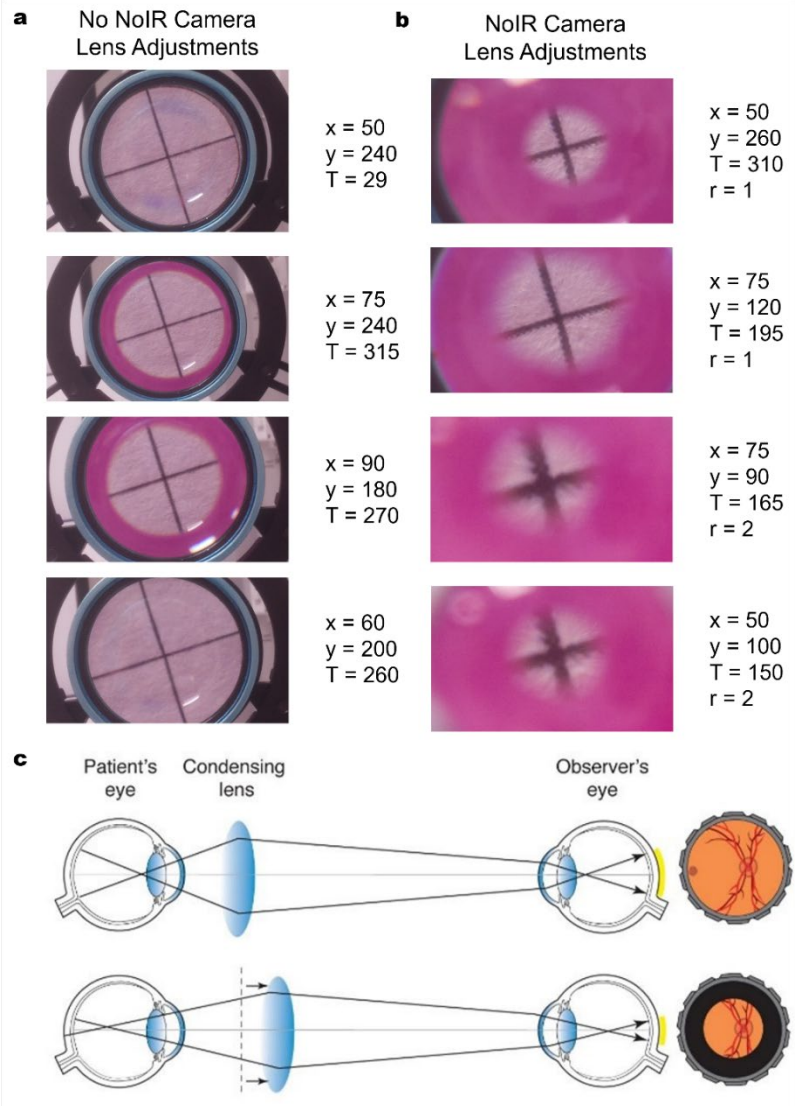

Figure 3.5. ***a*** *Adjusting the combination of distances between our initial fundus camera set-up. Where distance between eye and Volk lens = x; Distance between camera and Volk lens = y; total working distance of system = T; all in millimetres (mm). In our initial system: x = 75 mm, y = 300 mm, T = 375 mm and the aim is to reduce this as much as possible.* ***b*** *Adjusting the NoIR camera module lens moving further away (anticlockwise) where number of anticlockwise lens rotations = r.* ***c*** *Illustrates that the effect created when the Volk (condensing) lens is too far from the patient's eye, light from the peripheral of the patient's retina will not reach the observer. This is the effect we observe in in some of the configurations in* ***a*** *and all of the results from adjusting the NoIR camera lens in* ***b****[46].*

Atebara *et* al. describe how this effect is also observed when the condenser lens is too close to the patient's eye, blocking light from the periphery of the retina reaching the observer, illustrated in **Fig. 3.5c**[46]. The only improvement from these efforts was reducing the total working distance by 3 cm, shown in the bottom panel of **Fig. 3.5a,** and adjusting the NoIR camera doesn't achieve the desired effect without restricting the view. The next step is to look into adding an additional lens to reduce the path between the condenser lens and the NoIR camera, to focus the beam closer to the lens and to avoid the effect shown in **Fig. 3.5c** by adjusting the condenser lens working distance, this is of best interest also as this working distance needs to be as long as possible to ensure enough space for Raman Spectroscopy components to sit.

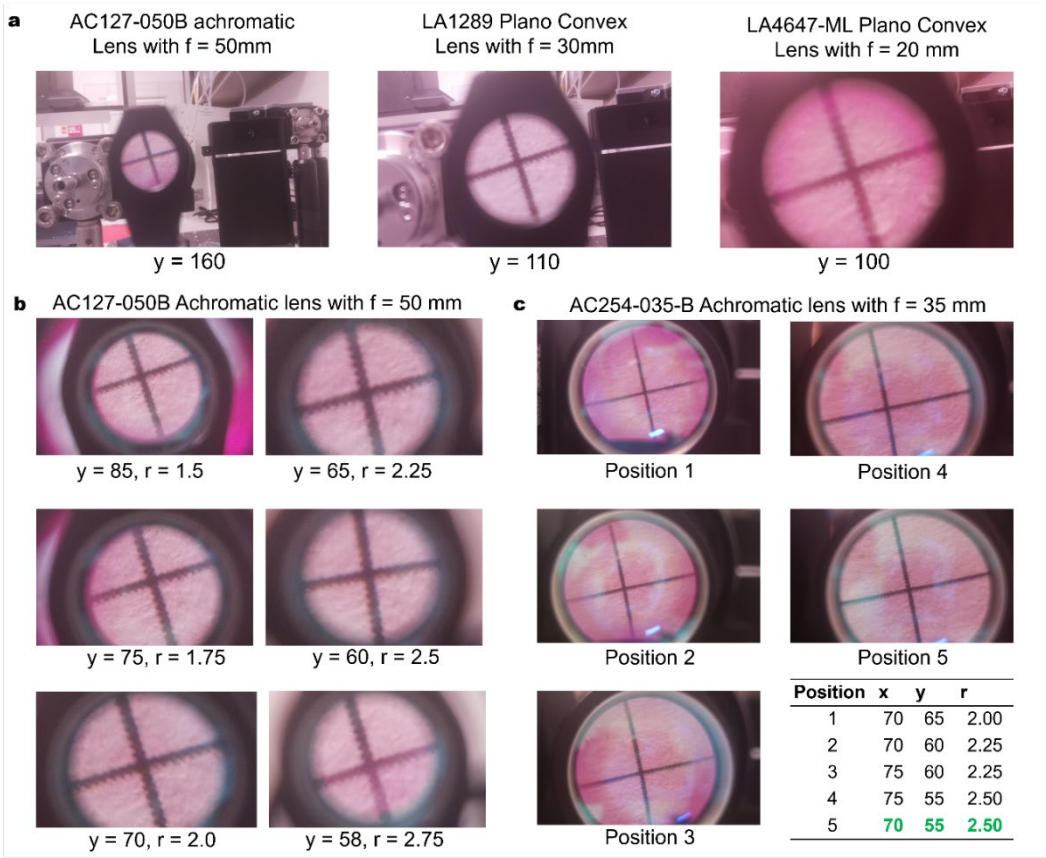

Figure 3.6. NoIR camera results when introducing four different lenses between the camera and Volk lens, as well as altering NoIR camera lens position. ***a*** *Comparison between three lenses placed in between the 14D Volk condenser lens and the NoIR camera module to shorten the working distance (y) from 300 mm. Good results from all.* ***b*** *Comparison when adjusting the NoIR camera lens whilst placing the 50 mm focal length achromatic lens between the 14D Volk condenser lens and the NoIR camera module, further shortening the working distance (y).* ***c*** *Adjusting configuration of all components in the initial fundus camera design plus a 35 mm focal length achromatic lens between the 14D Volk condenser lens and the NoIR camera module. This achieved the shortest working distance (y) and widest field of view, suitable for handheld fundus camera applications. Where distance between eye and condenser lens = x; Distance between camera and condenser lens = y; number of anticlockwise lens rotations = r.*

Achromatic and plano-convex lenses were tested to observe any improvements, these included: a 50 mm focal length achromatic lens (AC127-050B, ThorLabs), a 30 mm focal length plano-convex lens (LA1289-B, ThorLabs) and a 20 mm focal length plano-convex lens (LA4647-ML, ThorLabs). The 14 D Volk condenser lens was placed back at the regular working distance of 75 mm from the phantom eye model and test lenses

were placed between the condenser lens and NoIR camera module to make this distance as short as possible. This was achieved with all three lenses, as shown in **Fig. 3.6a**, and the NoIR camera lens was once again adjusted to determine any improvement. For the plano-convex lenses, adjusting the NoIR lens anticlockwise would require the camera to be moved further away from the lens, thus cancelling out the effect, however, improvement in focus was observed when combined with the achromatic lens 50 mm focal length achromatic lens, which is shown in **Fig. 3.6b.** Visual acuity and focus was suitable when using this achromatic lens but could be improved upon, and the small size (12.7 mm) limited the camera view. A second achromatic lens was ordered and tested, with a 35 mm focal length to shorten the working distance even further and a diameter of 25.4 mm. Good results were observed when adjusting the NoIR camera lens between 2-2.5 anticlockwise turns, so this was explored with the new, bigger lens, to achieve a new, optimised configuration for the fundus camera set-up, these results are given in **Fig. 3.6c,** reducing the distance between condenser lens and observer from 300 mm to 55 mm.

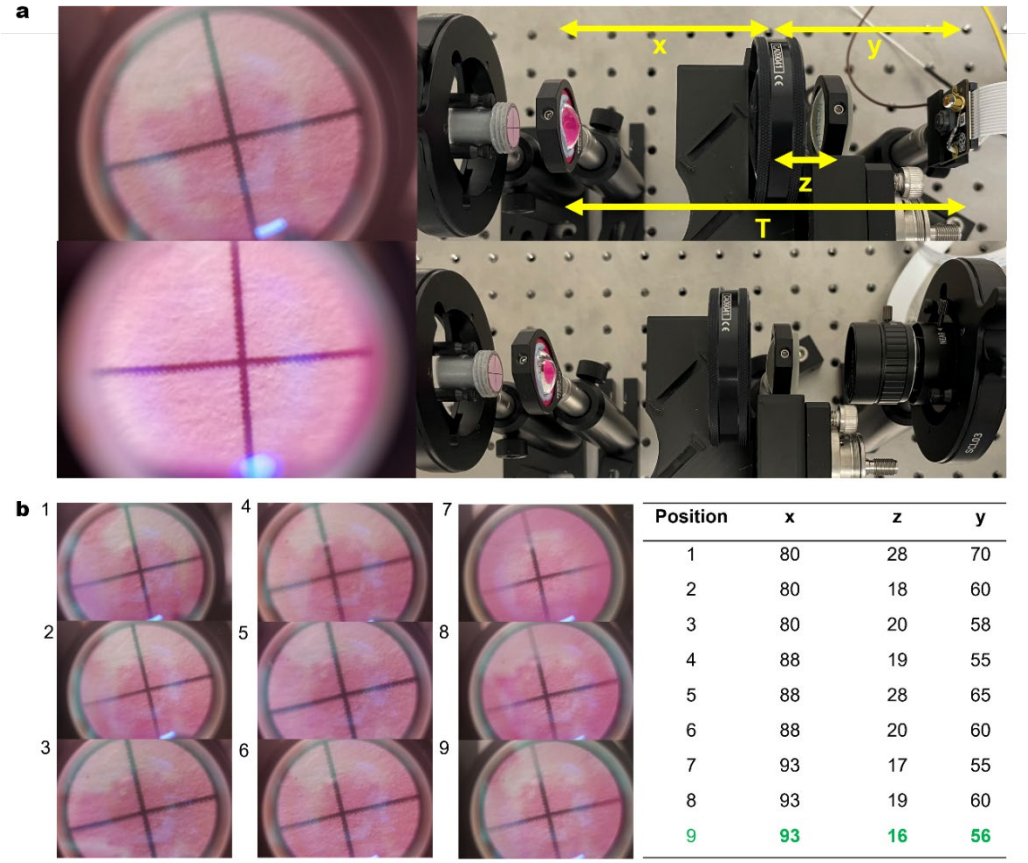

Position	x	z	y
1	80	28	70
2	80	18	60
3	80	20	58
4	88	19	55
5	88	28	65
6	88	20	60
7	93	17	55
8	93	19	60
9	93	16	56

Figure 3.7. ***a*** *Comparison between the camera view and size of the Raspberry Pi NoIR camera module (top) and the Raspberry Pi HQ camera with 6mm wide angle lens (bottom). The high resolution and autofocus of the HQ camera allows a shorter working distance and slightly improved camera view but not worth the large increase in overall weight to the portable system.* ***b*** *Adjusting configurations of the initial fundus design once a lens was chosen to shorten the working distance (b) between the 14D Volk condenser lens and the NoIR camera module, and once a lens position was finalised for the NoIR camera. The aim was to increase the internal distance (x) between the phantom eye model and the 14D Volk condenser lens to allow for Raman Spectroscopy components to be placed, without increasing the working distance (y) which would negatively impact portability. Where distance between eye and condenser lens = x; Distance between camera and condenser lens = y.*

An alternative Raspberry Pi camera module was purchased to compare with the performance of the NoIR camera module once a sufficient working distance was achieved for portable, handheld applications. A Raspberry Pi High-Quality Camera Module (Raspberry Pi, SC0818) with a 6 mm Wide Angle Camera Lens (Raspberry Pi, SC0124) was purchased for higher resolution and auto-focus capabilities, as this feature is referred to as one of the biggest pros for smartphone-based fundus camera systems[29], [47], [48]. Comparisons between the systems are shown in **Fig. 3.7a,** and overall, it was determined that the visual improvements do not outweigh the negative impact the High-Quality camera module would have due to its larger size (visible in **Fig. 3.7a**) and mass of 85 g versus the lightweight 3-gram NoIR camera module.

Upon finalising the NoIR camera module and 2.50 anticlockwise turns from the starting position (roughly measured as a 22 mm focal length, previously 50 cm[45]), the entire configuration was tweaked to maximise the distance between the phantom eye and condenser lens to allow as much space as possible for Raman Spectroscopy components to be placed, without reducing the portable suitability or quality of the image. These adjustments are shown in **Fig. 3.7b,** and it can be observed that very little difference was made in the image quality of crosshairs. A Raman working distance of 93 mm was achieved, which is intended to be redirected along right angles, therefore not reducing the portability of the entire system, and an optimised portable fundus set-up was achieved.

A visible red laser (635 nm wavelength) was utilised with a viewing board and microscope camera to view how the collimated beam was passing through the entire fundus camera set-up, example shown in **Fig. 3.8ii.**, to produce a ray diagram. Images were taken of the beam spot size along the beam path and the diameter was measured using ImageJ afterwards. A scaled ray diagram was drawn up and a digital render of the portable fundus camera set-up is presented in **Fig. 3.8i.**

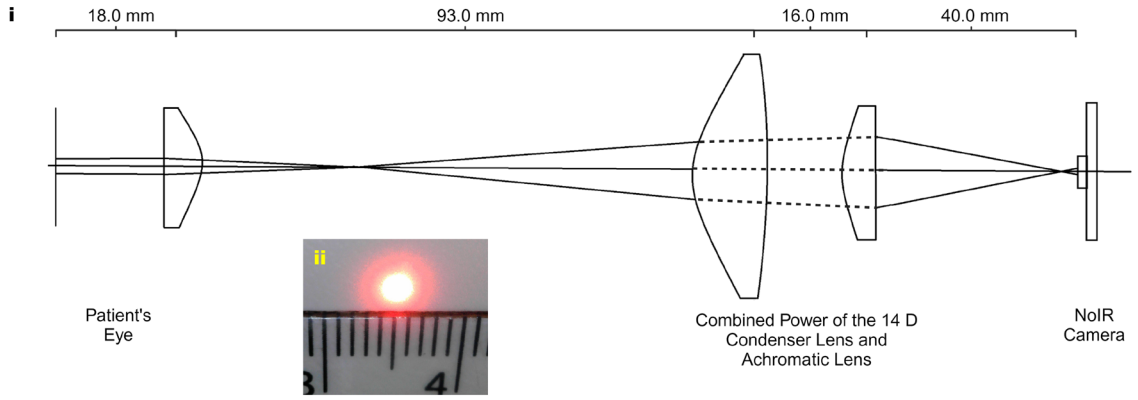

*Figure 3.8. **i** Digital schematic diagram of the portable fundus camera set-up, drawn to scale. **ii** Example of the microscope camera view of a red laser beam spot size. These images were taken along the beam path and diameter was measured using ImageJ to trace the beam throughout the entire system. The dotted line represents the modelled ray path that would be taken to achieve this ray diagram from the combined power of the 14 D (Volk) condenser lens and achromatic lens, however, not the actual light behaviour of these lenses.*

3.4 Optimising LED Illumination

3.4.1 LED Wavelength

The main challenge, once creating a portable set-up, is how to appropriately illuminate the retinal fundus without obstructing the reflected light passing back through the pupil towards the camera[49]. A large reason for exploring the use of a near-infrared (NIR) excitation wavelength was for a better patient experience when completing spectral acquisitions and illuminating the eye for fundus imaging should do the same. Cui *et* al. utilised NIR light to prevent pupil contractions when imaging the fundus. However, they discuss the limitations of this including low-resolution imaging due to backscattering from different tissue depths and less clear retinal vasculature, whereas visible light penetrates less into the retina and is absorbed much more in the haemoglobin[49]. To mitigate this, they implemented an image processing technique to produce higher-quality images.

Longer wavelengths in the NIR region have lower frequency and greater penetration than “white” LEDs[50]. Alongside this, literature explores LED light sources as an alternative to conventional flash fundus photography, as this tends to be oversaturated in the red region whilst washed out in the green and blue regions, resulting in flat and red-hued images[51]. Therefore, implementing an LED for the portable fundus camera system would create another benefit over smartphone-based systems.

An 800 nm wavelength LED was chosen (LED800L, ThorLabs), to create the best patient experience, and to avoid interference with the Raman Spectroscopy components when implemented with an 830 nm excitation wavelength. When completing the experiments in Section 3.3, the open version of the phantom eye model shown in **Fig. 3.7a** was used with the room light on, however, when using the final phantom eye, room light cannot illuminate the crosshairs/retina and LED will be the only form of light. Therefore, the type and position of the LED are vital for sufficient fundus image capture. The 800 nm LED was placed in different locations throughout the portable fundus camera set-up, above and to the right of the NoIR camera, at the achromatic lens and at the condenser lens, as shown in **Fig. 3.9a.** The LED at these locations provided little illumination to the crosshairs and created glare. I decided to direct the LED into the camera axis using a mirror, illustrated in the bottom panel of **Fig. 3.9a**, as this is one of the fundamental properties of smartphone-based fundus cameras which feature little to no additional lenses to achieve ophthalmoscopy[27]. This created a better camera view, with a spotlight on the “retina” allowing visibility of the crosshairs, in position 5 of **Fig. 3.9b.**

13 porcine eyes were tested with the portable fundus set-up, using the open access 3D printed 20D Volk lens mount with an iPhone 12 (discussed in Section 2 in **Fig. 3.1**) and the D-Eye, with the iPhone 6, to confirm good corneal clarity and that there was no damage to the internal structures beforehand, shown in the top panel of **Fig. 3.9c**. As shown in the middle panel of **Fig. 3.9c,** there was very little illumination of the porcine eye globe when placing the eye just outside of the focal point and glare from

the 800 nm LED can be seen. As the porcine eye is moved closer to the camera, reaching the focal point, the corneal glare overwhelms the camera view until it is all the camera is able to focus on, as shown in the bottom panel of **Fig. 3.9c.**

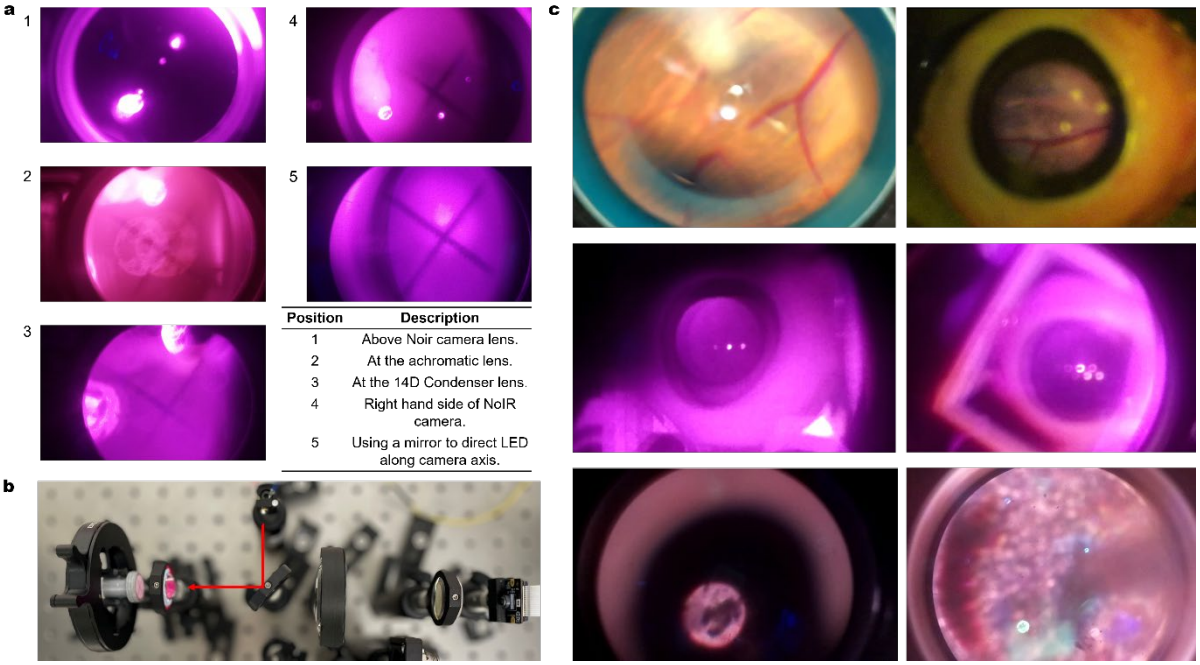

Figure 3.9. ***a*** *(1-5) NoIR camera view of the crosshairs at the retinal position of the phantom eye model with the 800 nm LED placed in different positions throughout the set-up. Bottom right panel shows a key describing each position.* ***b*** *Top view of the set-up on the optical table, showing how the LED is brought into the system along the camera axis when achieving "Position 5".* ***c (top)*** *Shows the performance of the two smartphone-based fundus systems on the fresh, ex vivo porcine eyes: 3D printed open access 20D lens mount using an iPhone 12 (left) and the D-Eye using an iPhone 6 (right).* ***(middle)*** *Examples of how the portable fundus set-up with 800 nm LED does not illuminate the porcine eyes at a distance.* ***(bottom)*** *Illustrating closer views of the glare created by the 800 nm LED on the porcine eyes.*

There is no evidence in the literature that ~800 nm wavelengths would behave differently passing through porcine cornea and lenses compared to a human eye, and Artigas *et* al. show that porcine eyes are similar to that of a human eye in the visible spectrum, allowing 95% transmission[52]. However, we were having little success translating the near-IR LED from the phantom model to *ex vivo* porcine eyes, so other LED wavelengths were explored, with the intention of remaining non-mydriatic and not to dazzle the patient. Whilst Lobato-Rincon *et* al. determined that human eyes have the largest pupillary response to white and green (510 nm) light when exploring laser wavelengths[53], Schmitz-Volckenberg *et* al. showed impressive results when utilising green and blue emissions for *in vivo* fundus autofluorescence imaging, which makes best use of the natural autofluorescence from the retina[54], and Everdell *et* al. utilise wavelengths 504, 525 and 557 nm to obtain multispectral images of the fundus.

The fresh, *ex vivo,* porcine eye test was repeated with LED wavelengths: 525, 570, 750, 800 and 850 nm, with results on both the open phantom eye model and *ex vivo* porcine eyes shown in **Fig. 3.10.** The 525 nm LED produced a spotlight onto the retina location but little contrast between the paper and printed crosshairs, the porcine eye globe appears illuminated, but the fundus could not be viewed. The 570 nm LED

illuminated a very dim spotlight onto the crosshairs, but very little of the eye was seen and no illumination of the fundus. The near-IR LEDs created a general illumination, much like the effect of having the room light on, due to the compatibility with the NoIR camera, but the 750 nm created a very faint spotlight onto the crosshairs and no retinal structures could be seen, whilst the 850 nm LED produced a clear spot, not as bright as the original 800 nm, but again the fundus could not be viewed.

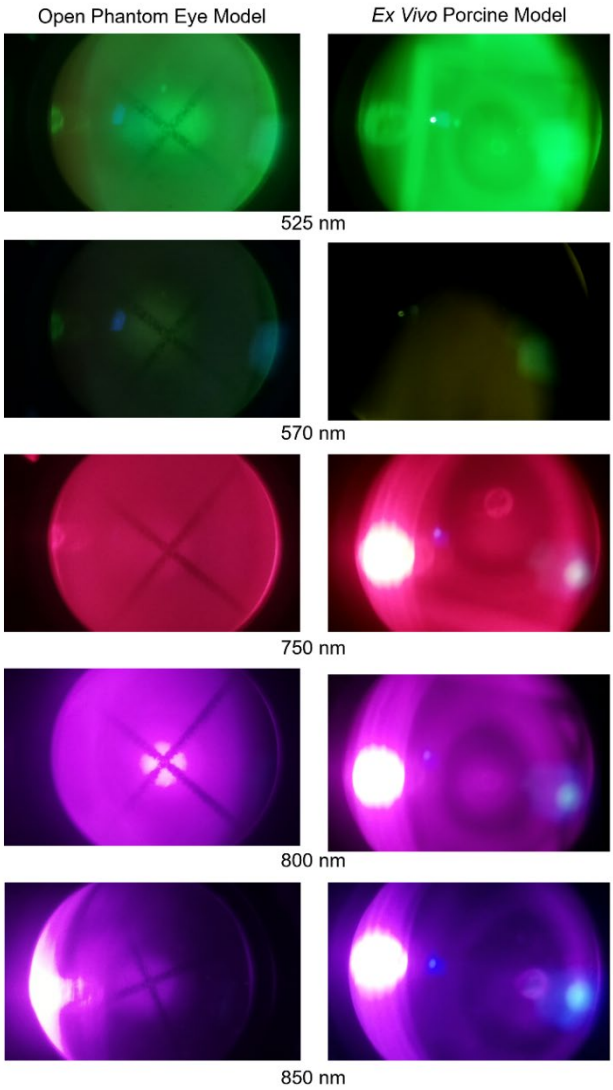

Figure 3.10. Comparison between different LED wavelengths: 525, 570, 750, 800 and 850 nm using both the open phantom eye model and ex vivo porcine eye model. Very little clarity and contrast from the green LEDs and best results from the near infrared. The clearest illumination was achieved using the 800 nm LED.

3.4.2. Extra Aperture

Another approach was taken, in response to Palmer *et* al. discussing that the entrance pupil diameter must be smaller than the patient's pupil to eliminate vignetting in the camera. This method is employed in some smartphone-based fundus camera systems, such as the D-Eye, which utilises a diaphragm with an aperture to collimate the dispersing LED light and reduce glare. This was explored with an adjustable iris aperture (ID15/M, ThorLabs) placed in between the LED light and the eye model, and results using the phantom eye with crosshairs and a bird's eye view of the set-up are

shown in **Fig. 3.11a** and **3.11b,** respectively. Little difference is seen in the phantom eye model, and no improvement was observed in fresh, *ex vivo* porcine eyes. An opposite thought process was followed, placing a black dot in the middle of the LED to soften or disperse the light further in hopes of reducing the glare. A visual of this method is shown on a white LED in **Fig. 3.11c,** again, no improvement was made.

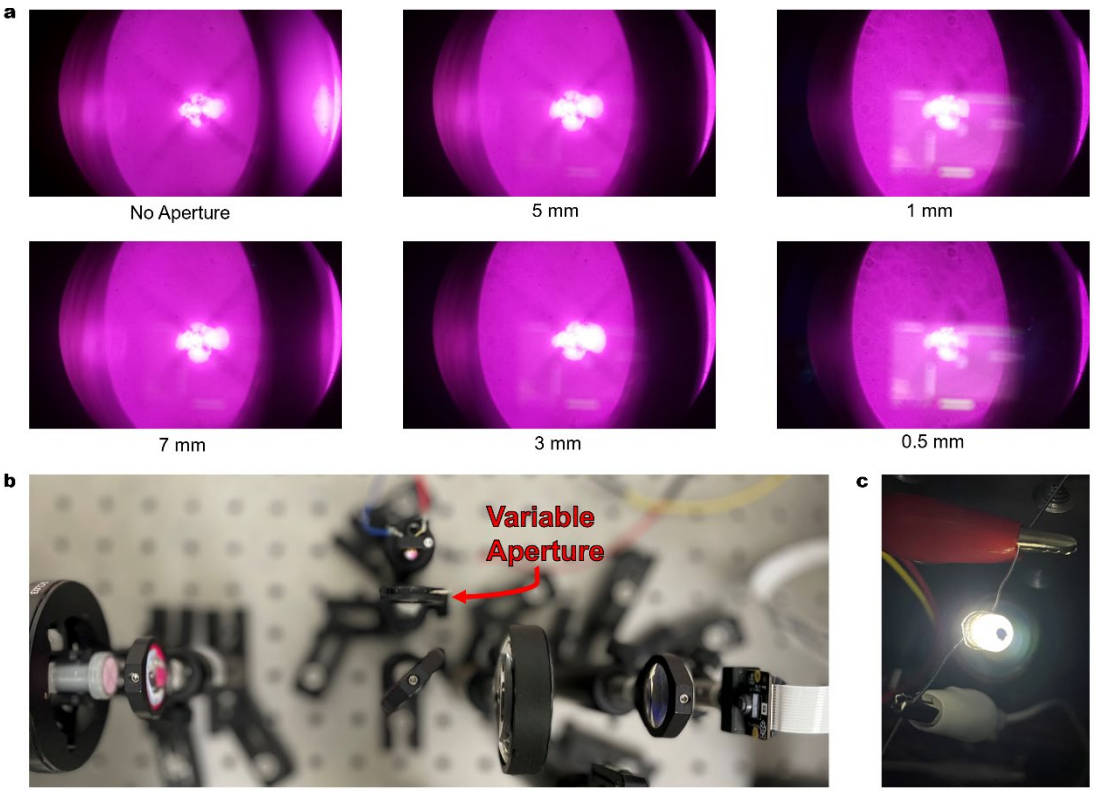

Figure 3.11. ***a*** *Aperture test introducing a variable iris to achieve better illumination. Aperture was decreased from 7 to 0.5 mm. No improvement was observed.* ***b*** *Top view of the fundus set-up on the optical table illustrating where the variable aperture iris was placed.* ***c*** *Black dot placed on an LED to soften the illumination and reduce glare, which did not produce positive results.*

3.4.3. Additional Lenses

Upon observing no improvement, the original 800 nm LED was once again utilised, but removing the lens, and then vitreous humour, of the *ex vivo* porcine eyes, in case the dead, unresponsive cornea and lens were the reason for no image being formed, as Palmer *et* al. state that the most anterior corneal surface has the most contribution to producing glare[55]. We were obtaining good results using the phantom eye, so the anterior of the porcine eye was replaced with the phantom lens and the dissected posterior of the eye was placed in the retinal location. The fundus can be viewed clearly even with a regular smartphone set-up through the vitreous humour, seen in **Fig. 3.12a,** including the optic disc. The full fundus still could not be seen once replacing the porcine cornea and lens with the phantom lens but some structures were beginning to come into view like in the top right-hand corner of **Fig. 3.12b.** Once removing the vitreous humour, the structures of the fundus could be obtained in clear focus, confirming that the resolution of the portable fundus set-up was not the issue

as **Fig. 3.12c** shows the intricate details of the retinal arteries and veins **(i)** and the optic disc **(ii)**.

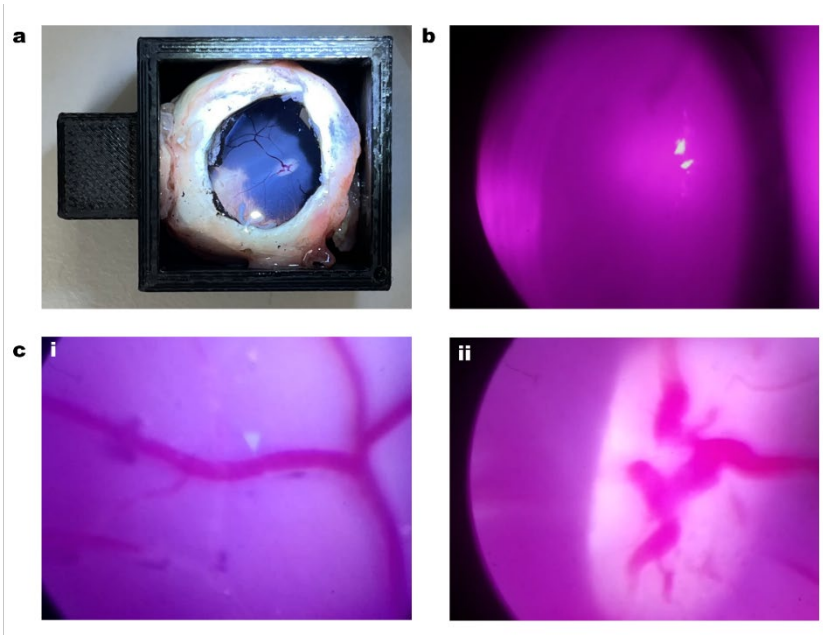

Figure 3.12. ***a*** *Example of how the fundus including small details of optical disc and veins can be viewed smartphone through the vitreous humour without any additional attachments once the lens and cornea are removed.* ***b*** *NoIR camera view through the vitreous humour once the lens and cornea are removed from porcine eye, still little visibility.* ***c*** *Examples of improved visibility and focus onto the fundus once the vitreous humour is removed and the porcine lens and cornea are replaced with the phantom eye lens, achieving clear view of retinal veins* ***(i)*** *and the optic disc* ***(ii).***

If the compound power of the dead porcine cornea and lens were proving the problem, as the deformed structures may be behaving differently to that of the approximate power of 60 D in living eyes, then the next stage was to introduce lenses between the LED and patient eye to manipulate the focus of the illuminating light. It seemed that as the LED is moved away from the phantom lens, a concentric ring shape is created rather than even distribution, shown in **Fig. 3.13a**, and the LED cannot be brought closer to the lens as it must not disturb the camera view, and therefore must sit around 50-60 mm away from the phantom eye model. Three plano-convex lenses were introduced to improve the illuminated spot at an appropriate distance for the portable fundus set-up, with focal lengths: 50.8, 75 and 100 mm. The illuminated spot produced by these lenses at ~60 mm from the axis is shown in **Fig. 3.13b.** The 50.8 mm focal length plano-convex lens produced the largest spot size with the lowest saturation which allows the crosshairs to be seen. The area of illumination is evened out when the lens is moved to 86 mm away from the axis, as shown in **Fig. 3.13c(i)** but this is considerably further away, reducing the suitability of the system for a handheld device and it is of interest to reduce this.

Multiple lenses were introduced to the 50.8 mm focal length lens (49-846, Edmund Optics) to create a compound power, and the best result was created by an additional 30 mm focal length plano-convex lens (LA1085, ThorLabs), shown in **Fig. 3.13c(ii)**, at a suitable LED distance of 20 mm from the axis. A compound lens mount was

designed, and 3D printed to securely fix the two lenses together for optical table use, illustrated in **Fig. 3.13d.** Despite the visual improvement with the phantom eye model, the fundus still could not be viewed by the portable fundus camera set-up when using fresh, *ex vivo,* porcine eyes.

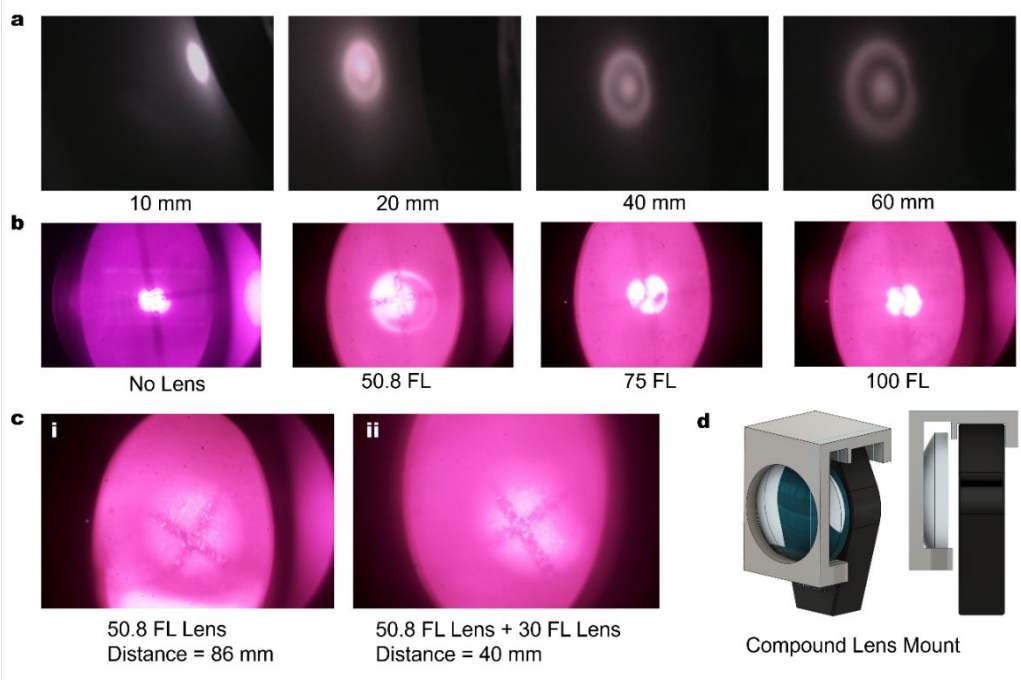

Figure 3.13. ***a*** *Smartphone images of the LED illuminated through the phantom eye lens onto a viewing board. The LED is moved further away from the lens and board, and a concentric ring shape is created.* ***b*** *NoIR camera view upon introducing plano-convex lenses 60 mm from the phantom eye model to increase the spot size.* ***c*** *Exploration of the best suited lens with 50.8 focal length at the best location* ***(i)*** *and at decreased distance with added secondary lens of 30 mm focal length* ***(ii).*** ***d*** *CAD design of a mount which combines the two lenses. Where FL = focal length.*

3.5 Optimised Design

3.5.1 Fundus Imaging

Throughout these stages, the D-Eye system using an iPhone 6 and the open access 3D printed 20D Volk lens mount with an iPhone 12 effortlessly obtain images of the fundus with the same porcine eyes, using the standard iPhone flashlight. Despite efforts to utilise a near-IR LED source to create the best possible patient experience, it was necessary to test a white LED to deduce that the illumination source was the last remaining issue. Flash-light sources in photography provide natural colours to images but dazzle patients, whilst LED sources emit a less dispersive light spectrum[50], therefore still providing a better patient experience over standard fundus ophthalmoscopy. Five fresh, *ex vivo* porcine eyes were used to test the portable fundus camera system with the newly introduced white LED (LEDW7E, ThorLabs) and plano-convex lenses, example shown in **Fig. 3.14a.** This set-up finally produced an image of the fundus, with retinal veins of approximate diameter of 123 – 136 µm, shown in the portable fundus camera images in **Fig. 3.14b,** where the top row has clear view of blood vessels, the middle row shows some glare from the LED still present and the bottom row illustrates how, in some eyes, the LED glare disrupts the view of the

fundus. This is an issue that will need to be rectified in future work but the improvement from the initial set-up is very promising.

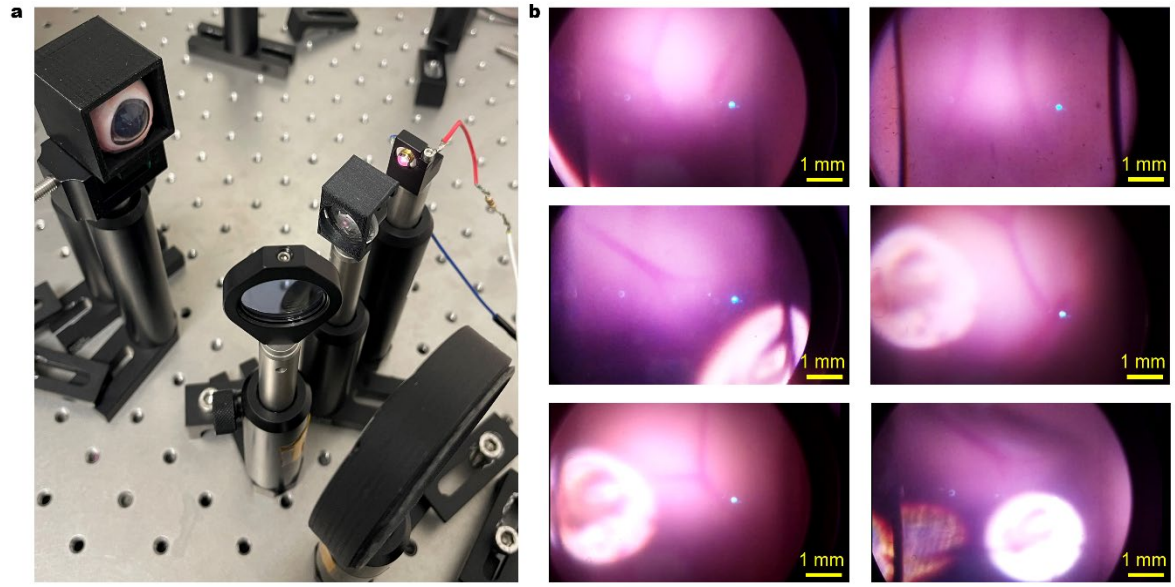

Figure 3.14. ***a*** *Optical table set-up of the white LED being reflected into the camera axis with the added compound lenses, using fresh porcine eyes at the patient location.* ***b*** *Examples of fundus imaging results using the white LED, showing clear view of blood vessels. Glare is also present and in the bottom panel disrupts the camera view.*

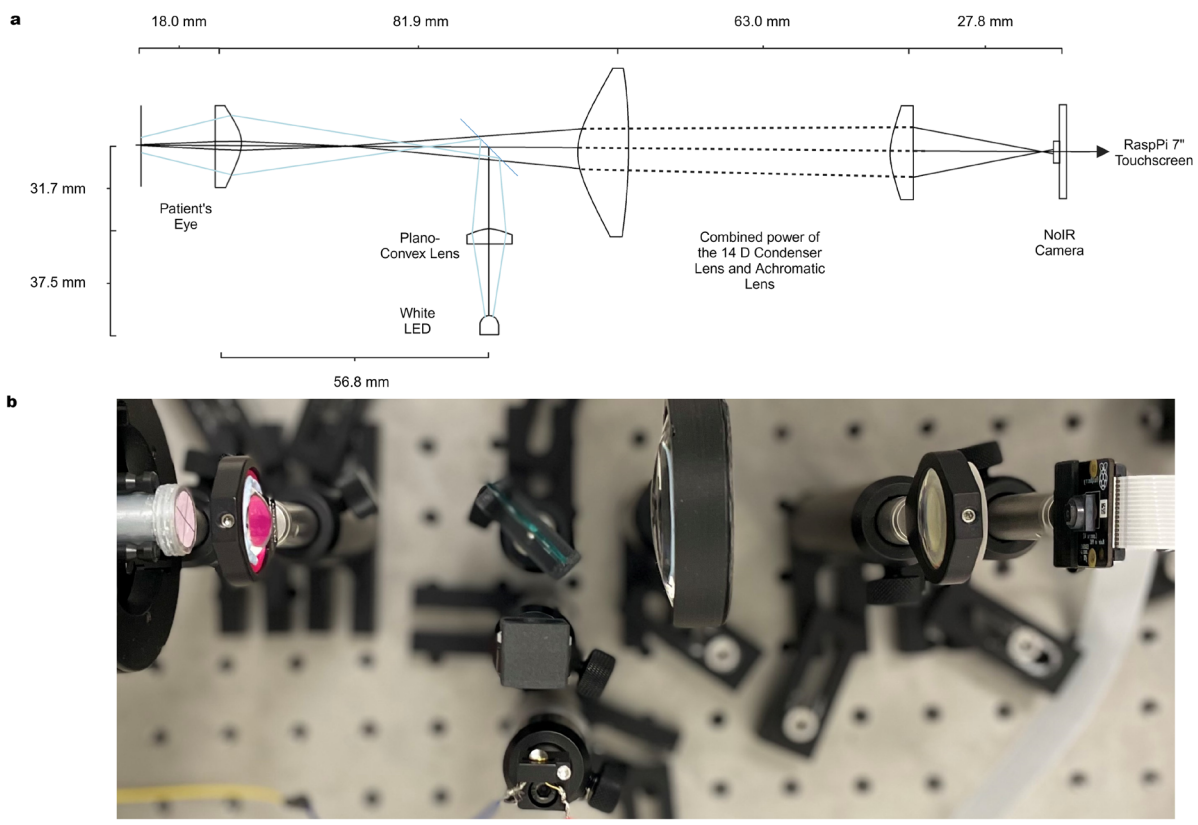

Figure 3.15. ***a*** *Final ray diagram and schematic of the portable fundus camera set-up.* ***b*** *Top view of the optical table portable fundus camera set-up. The dotted line represents the modelled ray path that would be taken to achieve this ray diagram from the combined power of the 14 D (Volk) condenser lens and achromatic lens, however, not the actual light behaviour of these lenses.*

Upon further adjustments and for simplicity, the compound lens was removed and only the 30 mm plano-convex lens was featured in the final portable fundus design, sitting 31.7 mm from the axis, and creating a soft, even illumination spot with simpler mounting. To maximise patient comfort, a potentiometer was introduced to allow the LED brightness to be controlled per measurement, which can also be altered to avoid saturation. A final ray diagram was created from all of the aforementioned iterations and is presented in **Fig. 3.15a,** alongside this, a bird's eye view image is presented of the components on the optical table in **Fig. 3.15b,** both without the potentiometer as this was mounted in the 3D printed system.

3.5.2 Non-Mydriatic Use

Once the portable fundus set-up was confirmed to use a white LED for illumination, the system needed to be tested on different pupil sizes to ensure its suitability for non-mydriatic use. The open phantom eye model was utilised as the porcine eye pupil could not be controlled. Natural pupils can have diameters between 2 and 7 mm[56], this holder has an aperture that mimics the eye's pupil with a 4 mm diameter which is the approximate size of a human eye in regular room lighting. When the eye is in darkness the diameter will be around 6 mm but can be as large as 8 mm when artificially dilated with tropicamide (mydriasis), 3 mm when exposed to bright light and as small as 2 mm under certain trauma or drugs (miosis)[57]. For point-of-care use, the portable fundus system should be able to be implemented on a patient with little preparation or knowledge of their condition, and in a timeframe too short for artificial dilation or to wait for drugs to subside, and therefore must be functional in all

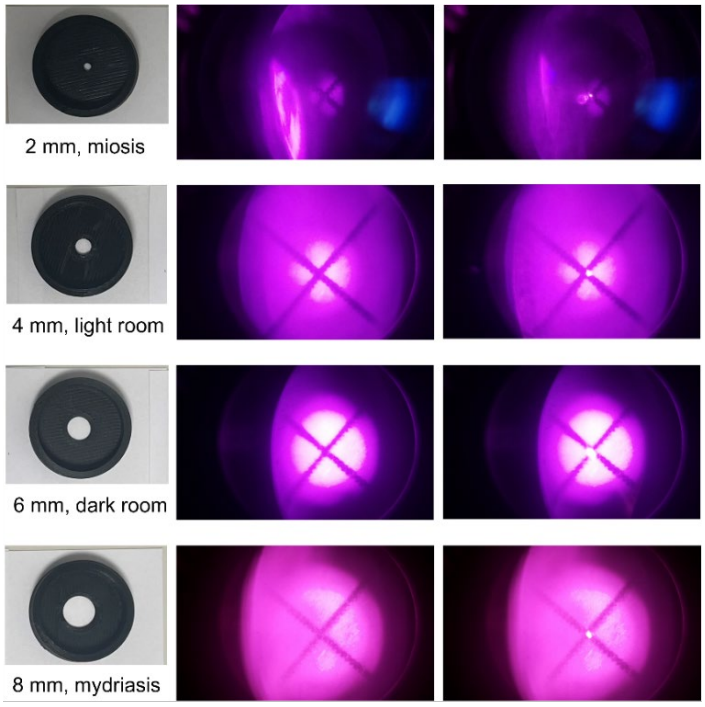

Figure 3.16. Demonstration of non-mydriatic capabilities of the portable fundus camera system. Each row shows the 3D printed pupil, noIR camera view of the crosshairs at the retinal location of the phantom eye model and the same view with a 830 nm laser aligned with the camera axis for potential secondary diagnostic techniques. Pupil diameters of 2, 4, 6 and 8 mm were explored for all patient circumstances.

conditions. The 3D-printed pupils can be seen in the left column of **Fig. 3.16,** whilst the portable fundus camera view is shown middle column, illustrating that the system can be utilised under all circumstances. An 830 nm laser was passed along the camera axis onto the centre of the crosshairs to also display compatibility with an external laser-based technique such as Raman Spectroscopy, found in the right column of **Fig. 3.16.**

3.5.3 Creating a Portable Housing

Once the portable fundus camera set-up was finalised, the 3D-printed housing could be designed and printed, ensuring all components fit securely for portable use and that the potentiometer could be mounted. The CAD design is presented in **Fig. 3.17,** with **(a)** showing the internal components, **(b)** an isometric view with the device lid to reduce stray light entering **(c)** a side view displaying the additional grips for user comfort and a patient eye to demonstrate the comfortable distance.

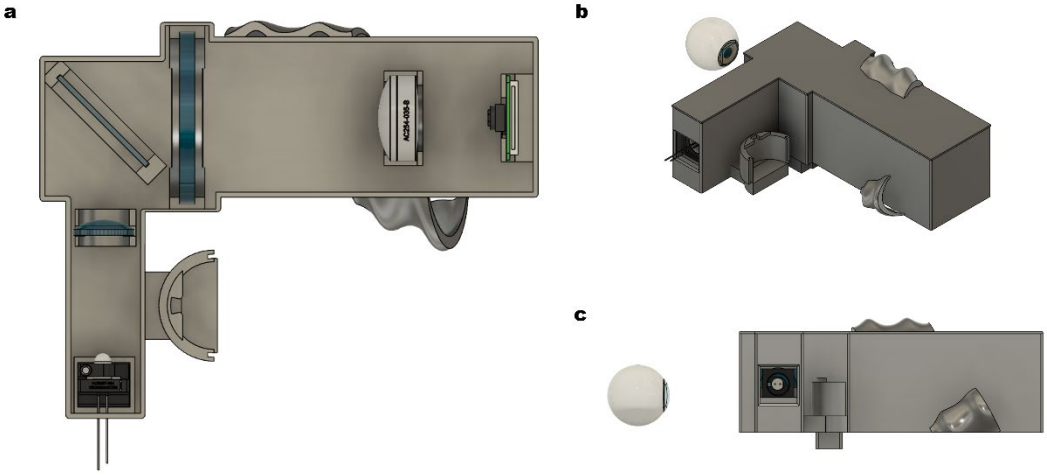

Figure 3.17. Renderings of the 3D housing of the portable fundus camera device with an eye model in the patient position. ***a.*** *Top view without the lid to expose the internal components of NoIR camera, 2 lenses, fundus lens, glass slide and LED.* ***b.*** *Isometric view of the portable fundus camera with lid attached.* ***c.*** *Side view of portable fundus camera with lid attached.*

The design was Fused Filament Fabrication (FFF) 3D printed using matte PLA (183-0245, RS Pro) to reduce scattered light and is presented with the lid removed to show the internal optics and potentiometer present in **Fig. 3.18a** and alongside the attached 7” touchscreen module in **Fig. 3.18b(i),** along with an example of how the system is handheld, made more comfortable with the hand grips shown in **Fig. 3.18b(ii).** Once fabricated, the system could be weighed and measured for final mass and size to compare against the current handheld fundus systems on the market. The system weighed in at ~547 g and measured 117 x 148 x 56 mm for an approximate cost of £500, the most expensive item being the 14 D Volk lens. The parameters achieved with the portable fundus camera design allow this system to compete with the current handheld ophthalmoscope market, outlined previously in **Table 3.1.**

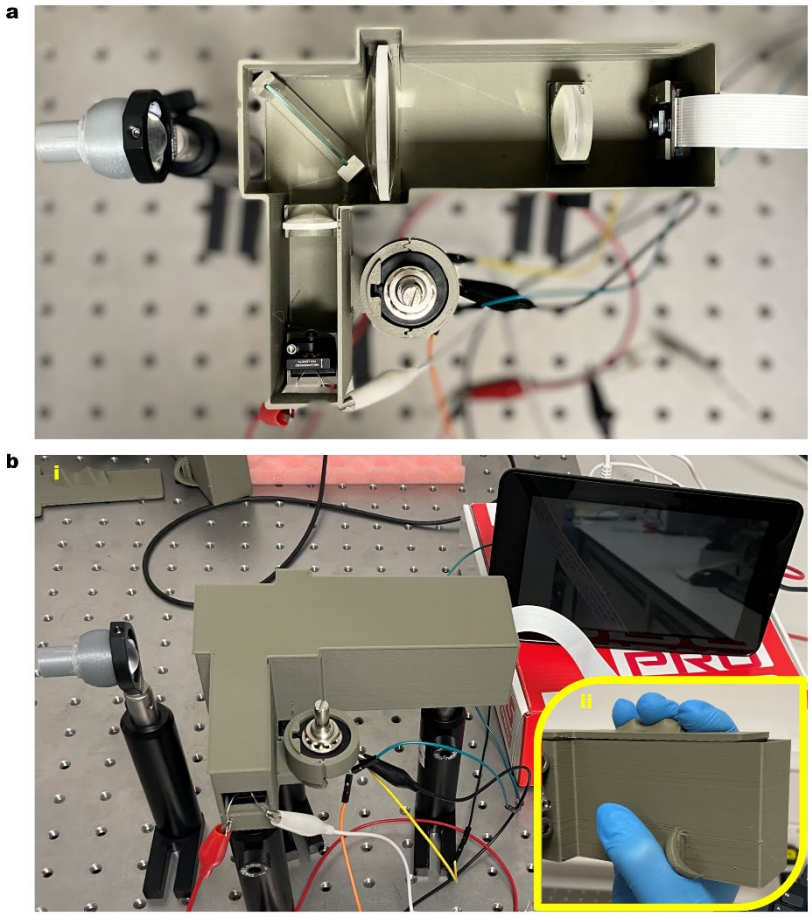

Figure 3.18. Photographs of the portable fundus camera device with the phantom eye model in the patient position. ***a*** *Top view of the components mounted into the 3D printed housing of the portable fundus camera system with the potentiometer present* ***b (i)*** *Image taken of the final portable fundus camera system prototype placed onto the optical table, with the lid on to reduce external stray light and with the 7" touchscreen module present.* ***(ii)*** *Example of ergonomic design achieved by additional hand grips onto the 3D printed system.*

3.6 Discussion and Conclusion

The current progress of the portable fundus camera design is satisfactory and is suitable for the next stages to introduce Raman Spectroscopy as a principal diagnostic technique for which fundus imaging will accompany. Despite the fundus being in view, there are still issues remaining concerning glare and contrast. Palmer *et* al. explore glare-free fundus imaging by using glare masking which ignores part of the light field that corresponds to glare whilst blending references to integrate to a single point from a range of different views in the light field to 'look around" the glare. They also deliver LED light to the eye from 3 different off-axis locations to move corneal glare away from the centre of the pupil[55]. This suggests two potential pathways for future steps, either using glare masking as a processing technique or revisiting the LED set-up to allow for glare-free imaging live.

When considering the patient experience inspiration can be taken, again, from Palmer *et* al. introducing an eye fixation system to their portable fundus device, encouraging

the patient to fix their eye at infinity by focusing on an LED-backlit fixation target at a retinal conjugate plane[55]. Another addition could be introducing a chin rest to aid stability and make the device more user-intuitive when the patient can be sat upwards. Chin rests can be priced around £500, but an open-access GitHub page describes the materials and files needed for a low-cost and portable research-grate chin rest for around £50[58].

Alongside optimising this portable fundus imaging set-up, utilising phantom eye or porcine eye models, the next stages would involve testing in more human-relevant environments. Human volunteers could be obtained as subjects of fundus imaging, collecting feedback on the patient experience, the quality of images and whether the design is user-friendly. The success of this design, not only creates the opportunity to patent a novel set-up for portable fundus imaging but also, opens up more prospects for telemedicinal ophthalmology where patients can receive more care in the comfort of their own homes, hopefully encouraging more frequent monitoring of ocular-related injuries and diseases which may usually go undetected, underdiagnosed, or identified too late for recovery. This will create better outcomes for, and knowledge of pathologies related to eye health, reducing the number of patients affected by loss of sight or neurological diseases and disorders.

3.7 References

[1] A. Calcagni and P. J. Gibson, “Imaging of the Human Fundus in the Clinical Setting: Past, Present and Future,” *US Ophthalmic Rev.*, vol. 06, no. 01, p. 42, 2013, doi: 10.17925/USOR.2013.06.01.42.

[2] Y. Wang, X. Gu, and Y. Chen, “Advances in multi-modal non-invasive imaging techniques in the diagnosis and treatment of polypoidal choroidal vasculopathy,” *Front. Med.*, vol. 10, 2023, doi: 10.3389/FMED.2023.1221846.

[3] M. E. Prayogo *et al.*, “Accuracy of Low-Cost, Smartphone-Based Retinal Photography for Diabetic Retinopathy Screening: A Systematic Review,” *Clin. Ophthalmol.*, vol. 17, pp. 2459–2470, 2023, doi: 10.2147/OPTH.S416422.

[4] C. Mishra and K. Tripathy, “Fundus Camera,” *Compend. Biomed. Instrum.*, pp. 853–856, Jul. 2023, doi: 10.1002/9781119288190.ch158.

[5] M. A. P. Vilela, A. Arrigo, M. B. Parodi, and C. da S. Mengue, “Smartphone Eye Examination: Artificial Intelligence and Telemedicine,” *Telemed. J. E. Health.*, 2023, doi: 10.1089/TMJ.2023.0041.

[6] N. Panwar *et al.*, “Fundus Photography in the 21st Century—A Review of Recent Technological Advances and Their Implications for Worldwide Healthcare,” *Telemed. J. e-Health*, vol. 22, no. 3, p. 198, Mar. 2016, doi: 10.1089/TMJ.2015.0068.

[7] N. Marchesi, F. Fahmideh, F. Boschi, A. Pascale, and A. Barbieri, “Ocular Neurodegenerative Diseases: Interconnection between Retina and Cortical Areas,” *Cells*, vol. 10, no. 9, Sep. 2021, doi: 10.3390/CELLS10092394.

[8] A. H. Kashani *et al.*, “Past, present and future role of retinal imaging in neurodegenerative disease,” *Prog. Retin. Eye Res.*, vol. 83, Jul. 2021, doi: 10.1016/J.PRETEYERES.2020.100938.

[9] P. J. Snyder *et al.*, “Retinal imaging in Alzheimer’s and neurodegenerative diseases,” *Alzheimers. Dement.*, vol. 17, no. 1, pp. 103–111, Jan. 2021, doi: 10.1002/ALZ.12179.

[10] Y. Zhang, Y. Wang, C. Shi, M. Shen, and F. Lu, “Advances in retina imaging as potential biomarkers for early diagnosis of Alzheimer’s disease,” *Transl. Neurodegener.*, vol. 10, no. 1, pp. 1–9, Dec. 2021, doi: 10.1186/S40035-021-00230-9/TABLES/2.

[11] M. S. Andersen, C. B. Pedersen, and F. R. Poulsen, “A new novel method for assessing intracranial pressure using non-invasive fundus images: a pilot study,” *Sci. Rep.*, vol. 10, no. 1, pp. 1–7, Aug. 2020, doi: 10.1038/s41598-020-70084-0.

[12] C. Childs, Y. T. in. Ong, M. M. yin. Zu, P. W. a. Aung, C. Y. Cheung, and W. S. e. Kuan, “Retinal imaging: a first report of the retinal microvasculature in acute mild traumatic brain injury,” *Eur. J. Emerg. Med.*, vol. 21, no. 5, pp. 388–389, Oct. 2014, doi: 10.1097/MEJ.0000000000000169.

[13] J. W. Chan, N. K. Hills, B. Bakall, and B. Fernandez, “Indirect traumatic optic neuropathy in mild chronic traumatic brain injury,” *Investig. Ophthalmol. Vis. Sci.*, vol. 60, no. 6, pp. 2005–2011, May 2019, doi: 10.1167/iovs.18-26094.

[14] B. Gopinath *et al.*, “Association between head injury and concussion with retinal vessel caliber,” *PLoS*

One, vol. 13, no. 7, Jul. 2018, doi: 10.1371/journal.pone.0200441.
[15] L. P. Evans *et al.*, “Acute vitreoretinal trauma and inflammation after traumatic brain injury in mice,” *Ann. Clin. Transl. Neurol.*, vol. 5, no. 3, pp. 240–251, Mar. 2018, doi: 10.1002/acn3.523.
[16] S. Das *et al.*, “Feasibility and clinical utility of handheld fundus cameras for retinal imaging,” *Eye*, vol. 37, no. 2, pp. 274–279, Jan. 2022, doi: 10.1038/s41433-021-01926-y.
[17] C. DeBuc, “Retinal Imaging On the Go,” *Review of Ophthalmology*, 2020. https://www.reviewofophthalmology.com/article/retinal-imaging-on-the-go (accessed Oct. 25, 2023).
[18] Y. Ou, “Pupil Dilation Test: Why a Dilated Eye Exam Is Important,” *BrightFocus Foundation*, 2023. https://www.brightfocus.org/glaucoma/article/dilated-eye-exam-why-its-so-important (accessed Nov. 15, 2023).
[19] G. Liew, P. Mitchell, J. J. Wang, and T. Y. Wong, “Fundoscopy: to dilate or not to dilate?,” *BMJ*, vol. 332, no. 7532, p. 3, Jan. 2006, doi: 10.1136/BMJ.332.7532.3.
[20] C. Czakó *et al.*, “Retinal biomarkers for Alzheimer’s disease and vascular cognitive impairment and dementia (VCID): implication for early diagnosis and prognosis,” *GeroScience*, vol. 42, no. 6, pp. 1499–1525, Dec. 2020, doi: 10.1007/S11357-020-00252-7/TABLES/1.
[21] G. Harris *et al.*, “Review: Emerging Eye-Based Diagnostic Technologies for Traumatic Brain Injury,” *IEEE Rev. Biomed. Eng.*, vol. 16, pp. 530–559, 2023, doi: 10.1109/RBME.2022.3161352.
[22] A. R. Stevens *et al.*, “Raman Spectroscopy as a Neuromonitoring Tool in Traumatic Brain Injury: A Systematic Review and Clinical Perspectives,” *Cells*, vol. 11, no. 7, pp. 1–22, Apr. 2022, doi: 10.3390/CELLS11071227.
[23] G. Devitt, K. Howard, A. Mudher, and S. Mahajan, “Raman Spectroscopy: An Emerging Tool in Neurodegenerative Disease Research and Diagnosis,” *ACS Chem. Neurosci.*, vol. 9, no. 3, pp. 404–420, Mar. 2018, doi: 10.1021/acschemneuro.7b00413.
[24] C. Banbury, G. Harris, M. Clancy, R. J. Blanch, J. J. S. Rickard, and P. Goldberg Oppenheimer, “Window into the mind: Advanced handheld spectroscopic eye-safe technology for point-of-care neurodiagnostic,” *Sci. Adv.*, vol. 9, no. 46, Nov. 2023, doi: 10.1126/SCIADV.ADG5431/SUPPL_FILE/SCIADV.ADG5431_SM.PDF.
[25] M. Marro, A. Taubes, P. Villoslada, and D. Petrov, “Detection of neuroinflammation through the retina by means of Raman spectroscopy and multivariate analysis,” *Biophotonics Photonic Solut. Better Heal. Care III*, vol. 8427, p. 842715, Jun. 2012, doi: 10.1117/12.921358.
[26] C. Stiebing *et al.*, “Nonresonant Raman spectroscopy of isolated human retina samples complying with laser safety regulations for in vivo measurements,” *Neurophotonics*, vol. 6, no. 04, p. 1, Sep. 2019, doi: 10.1117/1.nph.6.4.041106.
[27] R. H. Corr, “Fundoscopy in the smartphone age: current ophthalmoscopy methods in neurology,” *Arq. Neuropsiquiatr.*, vol. 81, no. 5, pp. 502–509, 2023, doi: 10.1055/S-0043-1763489.
[28] Opthalmicdocs, “Smartphone Ophthalmoscope ODocs Fundus,” *Autodesk Intructables*, 2015. https://www.instructables.com/Retinal-Imaging-Device-OphthalmicDocs-Fundus/ (accessed Nov. 16, 2023).
[29] M. Karakaya and R. E. Hacisoftaoglu, “Comparison of smartphone-based retinal imaging systems for diabetic retinopathy detection using deep learning,” *BMC Bioinformatics*, vol. 21, no. 4, pp. 1–18, Jul. 2020, doi: 10.1186/S12859-020-03587-2/TABLES/3.
[30] “Optical Accessory For A Mobile Device,” Apr. 2014.
[31] “iNview for iPhone 6 & 6s,” *Volk Optical*, 2023. https://www.volk.com/products/inview-for-iphone-6-6s (accessed Nov. 17, 2023).
[32] “VistaView,” *Volk Optical*, 2023. https://www.volk.com/pages/vistaview™ (accessed Nov. 17, 2023).
[33] “Hanson Instruments Hand Held Non Mydriatic HD Fundus Camera,” *Hanson Medical*, 2023. https://www.hansoninstruments.co.uk/optometric/fundus-cameras/hand-held-non-mydriatic-hd-fundus-camera-hfc (accessed Nov. 17, 2023).
[34] “SIGNAL Handheld Retinal Camera,” *Topcon Healthcare*, 2023. https://topconhealthcare.com/products/signal-handheld-retinal-camera/ (accessed Nov. 17, 2023).
[35] “VersaCam Digital Medical Scope Specifications,” *NIDEK*, 2016. .
[36] “Pictor Plus Fundus Camera,” *Volk Optical*, 2023. https://www.volk.com/products/pictor-plus-fundus-camera (accessed Nov. 17, 2023).
[37] “VISUSCOUT 100 Handheld Fundus Camera,” *Zeiss*, 2023. https://navaophthalmic.com/product/visuscout-100/ (accessed Nov. 17, 2023).
[38] “Aurora User Manual,” *Optomed*, 2023. www.optomed.com (accessed Nov. 17, 2023).
[39] “Pictor Prestige,” *Volk Optical*, 2023. https://www.volk.com/pages/prestige (accessed Nov. 17, 2023).
[40] D. R. Palacios *et al.*, “Wide field of view handheld smart fundus camera for telemedicine applications,” *J. Med. Imaging*, vol. 8, no. 2, Mar. 2021, doi: 10.1117/1.JMI.8.2.026001.
[41] Z. Howard, “Smartphone Fundus Camera,” *Autodesk Intructables*. https://www.instructables.com/Smartphone-Fundus-Camera/ (accessed Oct. 25, 2023).
[42] M. Yan, J. K. To, A. N. Vu, and A. W. Browne, “Low-Cost Raspberry Pi Stereoscopic Fundus Imaging System,” *Invest. Ophthalmol. Vis. Sci.*, vol. 62, no. 8, Jun. 2021.
[43] B. Y. Shen and S. Mukai, “A Portable, Inexpensive, Nonmydriatic Fundus Camera Based on the Raspberry Pi® Computer,” 2017, doi: 10.1155/2017/4526243.
[44] A. Colenbrander, “Chapter 63. Principles of Ophthalmoscopy,” in *Duane’s Ophthalmology*, 2006.
[45] “Infrared Bird Box,” *Raspberry Pi Foundation*. https://projects.raspberrypi.org/en/projects/infrared-bird-

box/6 (accessed Dec. 04, 2023).
[46] N. H. Atebara and C. H. Wooley, “Indirect Ophthalmoscopy,” *American Academy of Ophthalmology*. https://www.aao.org/education/image/indirect-ophthalmoscopy#disqus_thread (accessed Dec. 04, 2023).
[47] K. Jin, H. Lu, Z. Su, C. Cheng, J. Ye, and D. Qian, “Telemedicine screening of retinal diseases with a handheld portable non-mydriatic fundus camera,” *BMC Ophthalmol.*, vol. 17, no. 1, pp. 1–7, Jun. 2017, doi: 10.1186/S12886-017-0484-5/TABLES/4.
[48] R. N. Maamari, J. D. Keenan, D. A. Fletcher, and T. P. Margolis, “A mobile phone-based retinal camera for portable wide field imaging,” *Br. J. Ophthalmol.*, vol. 98, no. 4, pp. 438–441, Apr. 2014, doi: 10.1136/BJOPHTHALMOL-2013-303797.
[49] Y. Cui, T. Takamatsu, K. Shimizu, and T. Miyake, “Near-infrared fundus imaging system with light illumination from an electronic contact lens,” *Appl. Phys. Express*, vol. 15, 2022, doi: 10.35848/1882-0786/ac4675.
[50] F. Galli, “A comparison of light sources in retinal imaging,” *Eye News*, vol. 28, no. 3, p. 1, 2021, [Online]. Available: https://www.eyenews.uk.com/features/allied-professions/post/a-comparison-of-light-sources-in-retinal-imaging.
[51] V. Sarao, D. Veritti, E. Borrelli, S. V. R. Sadda, E. Poletti, and P. Lanzetta, “A comparison between a white LED confocal imaging system and a conventional flash fundus camera using chromaticity analysis,” *BMC Ophthalmol.*, vol. 19, no. 1, pp. 1–10, Nov. 2019, doi: 10.1186/S12886-019-1241-8/FIGURES/7.
[52] C. Artigas, A. Navea, M. M. López-Murcia, A. Felipe, C. Desco, and J. M. Artigas, “Spectral transmission of the pig lens: Effect of ultraviolet A + B radiation,” *J. Fr. Ophtalmol.*, vol. 37, no. 10, pp. 773–779, Dec. 2014, doi: 10.1016/J.JFO.2014.06.006.
[53] L. L. Lobato-Rincón, M. del C. Cabanillas-Campos, C. Bonnin-Arias, E. Chamorro-Gutiérrez, A. Murciano-Cespedosa, and C. S. R. Roda, “Pupillary behavior in relation to wavelength and age,” *Front. Hum. Neurosci.*, vol. 8, no. 1 APR, Apr. 2014, doi: 10.3389/FNHUM.2014.00221.
[54] S. Schmitz-Valckenberg *et al.*, “Fundus autofluorescence imaging,” *Prog. Retin. Eye Res.*, vol. 81, Mar. 2021, doi: 10.1016/J.PRETEYERES.2020.100893.
[55] D. W. Palmer *et al.*, “Glare-free retinal imaging using a portable light field fundus camera,” *Biomed. Opt. Express*, vol. 9, no. 7, p. 3178, Jul. 2018, doi: 10.1364/BOE.9.003178.
[56] L. Franssen, J. Tabernero, J. E. Coppens, and T. J. T. P. Van Den Berg, “Pupil Size and Retinal Straylight in the Normal Eye,” *Invest. Ophthalmol. Vis. Sci.*, vol. 48, no. 5, pp. 2375–2382, May 2007, doi: 10.1167/IOVS.06-0759.
[57] Y. D. Shin, J. H. Bae, E. J. Kwon, H. T. Kim, T. S. Lee, and Y. J. Choi, “Assessment of pupillary light reflex using a smartphone application,” *Exp. Ther. Med.*, vol. 12, no. 2, p. 720, Aug. 2016, doi: 10.3892/ETM.2016.3379.
[58] A. Murphy, “RestEasy: An open source chin rest for human psychophysics experiments,” *GitHub*, 2018. https://github.com/nimh-nif/SCNI_Toolbar/wiki/RestEasy:-An-open-source-chin-rest-for-human-psychophysics-experiments (accessed Dec. 18, 2023).

Chapter 4

Laser Profiling for Portable and Eye-Safe Raman Spectroscopy

This chapter explores the parameters of the 830 nm laser diode proposed to be use in a near-infrared eye-based Raman system, to profile key aspects for future designs and begin verifying eye-safety. It is a short, but necessary, pitstop in the long journey to establishing a medical device with modifiable features, especially in the case of laser-based systems, to ensure complete compatibility not only with other components in the design but also with eye safety regulations.

All equipment and laser settings are outlined, along with methods for verifying collimation, laser wavelength and power density, whilst highlighting the challenges introduced when utilising a low-power laser that is not visible to the human eye. Complete familiarity with the chosen laser diode will aid troubleshooting when designing and building the entire 830 nm portable Raman system, unexpected outputs from the optical design will be easily identified or discarded as being a result of the laser.

The UK and European standards for laser safety (BS EN 60825) are assessed to determine approximate parameters for beam width and power for the chosen 830 nm laser wavelength. A maximum laser power output of 2.72 mW when completing 30-second exposures was calculated, which is a realistic measurement time for patients.

To investigate further, a collaborating with the Defence Science and Technology Laboratory (Dstl) was established to observe laser damage on Porcine primary retinal pigment epithelial cells (PRPEpiC). The goal was to observe an area of damaged cells from the laser spot size, then establish the safety limits i.e. at what power and exposure times are cells damaged. Whilst an experimental set-up was established, there were limitations in time, laser modification and cell availability to obtain numerical results, as cells did not show signs of damage following even 40 mW exposures. The results indicate that an increased power density is required to observe a positive result to confirm that the staining techniques being used are appropriate.

4.1 Introduction

Research surrounding the ocular manifestations of neurodegeneration is a small but growing sector, where the physical and biochemical structure of the eye can be assessed externally to gain insight into pathology taking place inside the skull [1]–[7]. Current methods for obtaining diagnostic information on neurological disorders involve invasive techniques from blood samples to neuroimaging[8], [9]. These methods are costly, time-consuming and invasive, and techniques that utilise the eye's optical path to obtain neurodegenerative information are starting to revolutionise the patient journey.

Optical imaging such as Optical Coherence Tomography (OCT), vascular retinal imaging and fundus imaging have been explored in identifying neurodegeneration[10]–[15], utilising the eye's optical path and direct links to the brain to produce images and gain diagnostic information with structural changes. Conversely, Raman spectroscopy utilises the inelastic scattering of light to produce a spectrum of peaks that represent a sample's molecular bond vibrations. This technique uses laser light and the use of Raman spectroscopy for neurodiagnostics is of increasing interest in literature[16]–[21].

There are hugely influential, but unfortunately limited, examples of Raman spectroscopy being implemented with ocular tissue or *in-vitro* to obtain diagnostic information[22]–[26]. The lack of progress in this field is largely due to limitations when combining laser light with human eyes, as retinal damage is common as high emission of collimated light is being focused by the large combined lens power of the human cornea and lens. The UK and European standards, the "BS EN 60825-1:2014+A11:2021 Safety of laser products – Equipment classification and requirements" document outlines the current laser regulations, providing an indication of Maximum Permissible Exposure (MPE) based on laser wavelength, exposure time and eye tissue[27].

In this work, we develop a laser diode set-up suitable for portable Raman Spectroscopy, operating at a wavelength that is invisible to the human eye for an ideal patient experience. The BS EN 60825 classification and requirements are used to calculate emission limits, and an experiment is designed to explore and identify damage to primary porcine retinal cells following 830 nm laser exposure and the safety limitations when adhering to these calculated regulations.

4.2 Driver Set-Up

The portable Raman device utilises an 830 nm excitation wavelength, at laser powers low enough to meet the BS EN 60825 standard of MPE. To allow full customisation and optimisation, a 50 mW GaAlAs laser diode (HL8338MG, ThorLabs) was used.

The laser diode set-up includes the 50 mW Gallium – Aluminium – Arsenide (GaAlAs) laser diode, a collimation tube (LTN330-B, ThorLabs), a constant power LD driver

(MLD203P2E, ThorLabs), an evaluation board (MLDEVAL, ThorLabs), an ESD Protection and Strain Relief Cable (SR9C-DB9, ThorLabs) and a USB cable (USB-AB-72, Thorlabs). All work was carried out on a static control ESD table mat (TM2448, ThorLabs), to dissipate static charges, with a grounding wrist strap connected to the user and the mat connected to an earthing socket.

The set-up mode used for the laser driver evaluation board was MLD203PxE Module (CP) as the laser diode utilised in this work uses pin code C, illustrated in **Fig. 4.1a**. The monitor current for the laser diode is $I_{PD,\,MAX}$ = 0.50 mA, which is equivalent to the maximum optical output power. The resistance R_{COMP} was calculated using the equation:

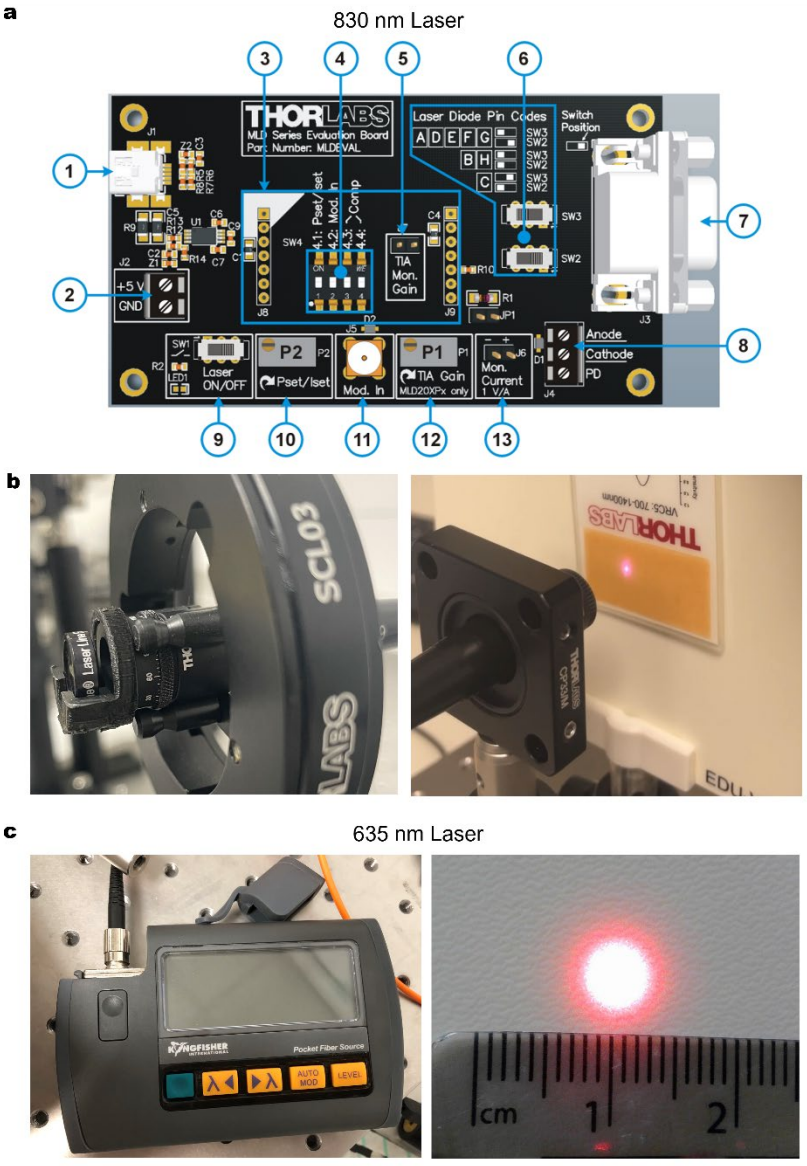

Figure 4.1. ***a*** *Schematic of the laser driver evaluation board (MLD203PxE, ThorLabs) Module, provided in the ThorLabs "MLDEVAL User Manual". Key features labelled 1-13 utilised to power and control the 830 nm laser diode (LTN330-B, ThorLabs) with the laser driver (MLDEVAL, ThorLabs)].* ***b (left)*** *Laser diode set-up within the collimation tube (LTN330-B, ThorLabs) and with the additional laser line clean-up filter (LL01-830-12.5, Semrock) attached.* ***(right)*** *Near-infrared beam visible when utilising a viewing card.* ***c (left)*** *Visible 635 nm portable laser (KI 9800 Series Light Source, Kingfisher).* ***(right)*** *Collimated 635 nm laser exiting FC/PC optical fibre and imaged on a viewing board.*

$$R_{COMP}[k\Omega] = \frac{2.5\ V}{I_{PD,MAX}\ [mA]} \quad (4.1)$$

Where R_{COMP} is resistance, V is the potential difference, $I_{PD,\ MAX}$ is the monitor current.

Giving a result of R_{COMP} = 5 kΩ. This was set using a Tenma 72-7730a ohmmeter connected to the constant power monitor connector pins J7 (5 in **Fig. 4.1a**) to measure and adjust the resistance through P1 (12 in **Fig. 4.1a**).

The LD driver is inserted into the sockets J8 and J9 (within 3 in **Fig.4.1a**) of the evaluation board. The laser diode was placed into the collimator package and strain relief cable and connected to the DB9 output connector (7 in **Fig. 4.1a**). Power is supplied through the USB cable connected to the mains and the USB power supply terminal (1 in **Fig. 4.1a**). Once the laser is turned on using the evaluation board switch (9 in **Fig. 4.1a)**, the power is measured using a 400-1100 nm photodiode power sensor (S121C, ThorLabs) which is adjusted using the evaluation board potentiometer P2 (10 in **Fig. 4.1a**). The laser power was initially set to 1 mW.

4.3 Collimation

The portable Raman systems utilise the patient's eye as an objective lens, focusing a collimated beam to the retina, thus complete collimation of the laser is required. The visible laser used for the 635 nm portable Raman system (KI 9800 Series Light Source, Kingfisher) shown in **Fig. 4.1c (left)**, requires an FC/PC optical fibre to be connected for use and does not require collimation (spot shown in **Fig. 4.1c (right)**). However, the laser diode used in the 830 nm set-up does need collimating, it is placed within an adjustable collimation tube (LTN330-B, ThorLabs) that holds an aspheric lens (collimation optic) and attached to a strain relief cable. This setup is shown in **Fig. 4.1b (left)** with the additional laser line clean-up filter (LL01-830-12.5, Semrock) and the near-infrared beam is visible when using a viewing card as shown in **Fig 4.1b (right)**. Laser collimation is adjusted by moving the aspheric lens closer/further away.

The set-up for testing collimation is shown in **Fig. 4.2a** and includes a viewing board with a scale bar mounted and an infrared microscope camera, both stationary. The laser is moved away from the board between distances of 5 and 135 cm. The camera captures images over this distance (example shown in **Fig. 4.2b**) and ImageJ is used to analyse the beam diameter. It is noted that the laser diode shape is elliptical (shown in **Fig. 4.2c**) and the microscope camera must sit slightly off-axis to capture images. This is repeated and optimised until collimation is reached, as shown in **Fig. 4.2d**.

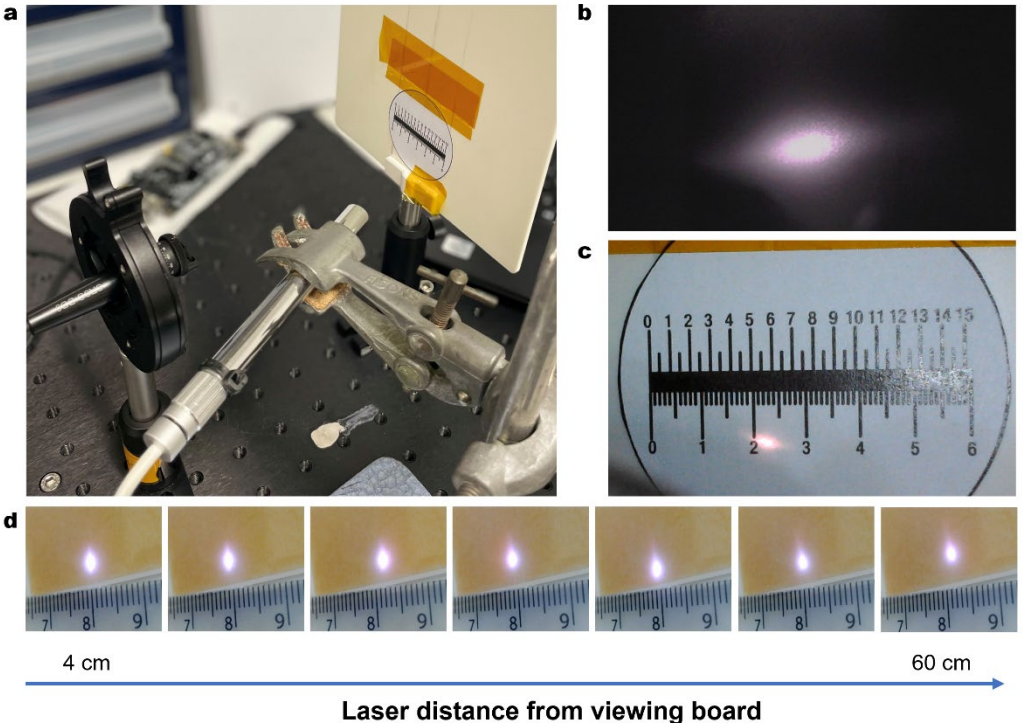

Figure 4.2. Photographs of the experimental set-up and viewing board to collimate the 830 nm laser diode. ***a*** *Example of laser diode elliptical shape, raw laser beam without collimation tube.* ***b*** *Infrared microscope camera view focused onto scale bar. Scale bar utilised in ImageJ and diameters recorded.* ***c*** *Collimation set-up demonstrating the stationary viewing board with scale bar and the infrared microscope camera (silver cylinder), laser diode is mounted but free to move along the optical table.* ***d*** *Microscope camera view of collimated laser diode beam over increasing distanced from 5 to 135 cm from viewing board.*

4.4 Laser Wavelength Validation

ThorLabs provide a wavelength error of ± 10 nm for the 830 nm laser diode, whilst Kingfisher quote an error of ± 5 nm for the 635 nm portable laser [28]. It is essential to investigate these errors to determine what wavelength the laser is producing in practice to ensure compatibility with the portable Raman system's filters and mirrors. Here three methods are experimented with to compare and confirm the working laser diode wavelength.

4.4.1 Spectrometer Method

The first method used was by determining the Rayleigh peak position when feeding unscattered laser light into the portable spectrometer. If the true laser wavelength is the same as how it is labelled, then the Rayleigh peak will be centred about 0 nm.

For the 635 nm laser, this was repeated 4 times, changing the focus each time to obtain a range of counts for the Rayleigh peak. A large feature to note is that the peak is very steep, going from minimum values to the maximum peak value between 648.10 nm and 652.45 nm on the left-hand side, but wide and sloped on the right-hand side in **Fig. 4.3a (top)**. When fully focused, the Rayleigh peak is rounded with a turning point before meeting the origin (635 nm). This was repeated with the 830 nm laser diode, this time the Rayleigh peak was consistently sharp with no sign of a turning point in **Fig. 4.3a (bottom)**, suggesting that the actual wavelength is lower than 830

nm. A more numerical method is required, as the turning points are below the origin it is not possible to observe where the peak is located.

4.4.2 Diffraction Method

A simple diffraction method using a single slit was utilised for the visible 635 nm laser, shown in **Fig. 4.3b (top)**. A microscope camera connected to a laptop was used to view the diffraction pattern and ImageJ was used to measure the distance (*d*) between bright spots visible in **Fig. 4.3b (bottom)**. Pythagoras can then be used, with the length (L) between the single slit and viewing board, to calculate the angle of diffraction (θ) and the laser wavelength (λ) can be found using the single slit diffraction equation:

$$n\lambda = dsin(\theta) \qquad (4.2)$$

Where *n* is the order, *λ* is wavelength, *d* is distance between bright spots and *θ* is the angle of diffraction.

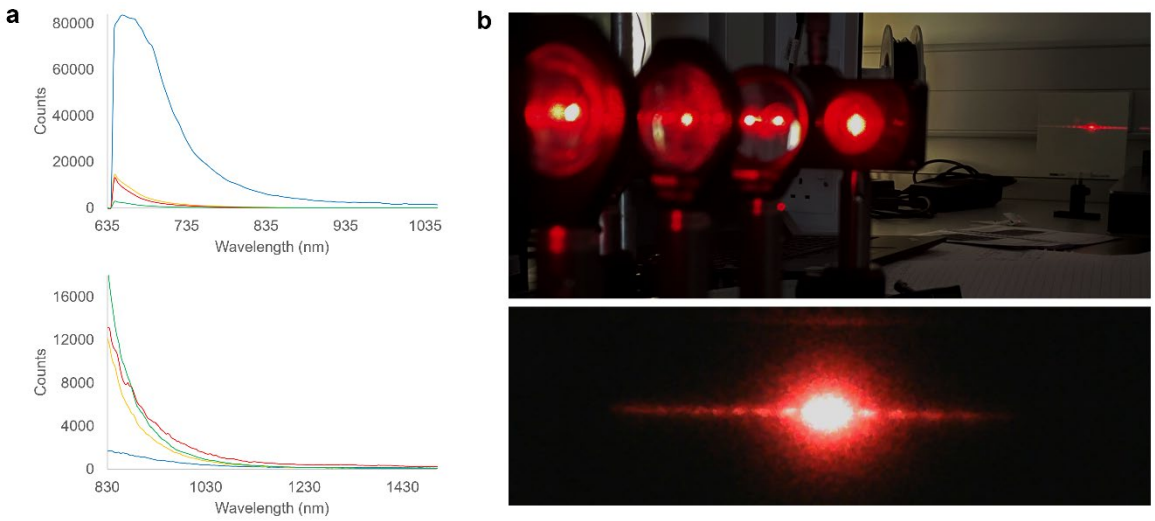

Figure 4.3. ***a*** *Lasers fed into portable spectrometers with no filters and taking 10 us acquisitions.* ***(top)*** *The 635 nm laser (KI 9800 Series Light Source, Kingfisher) is paired with a custom portable spectrometer (QE Pro, Ocean Insight), changing level of focus to alter counts, and repeated 4 times. The Rayleigh peak is steep, going from minimum values to the maximum peak value over 4.35 nm on the left-hand side, but wide and sloped on the right-hand side. It is not certain where the true turning point of the Rayleigh peak is.* ***(bottom)*** *The same method is utilised for the 830 nm laser diode (HL8338MG, ThorLabs). The Rayleigh peak is consistently sharp with no sign of a turning point, suggesting that the wavelength is lower than 830 nm.* ***b (top)*** *Image of the diffraction method for determining the true laser wavelengths, using the 635 nm laser.* ***(bottom)*** *Close-up of the diffraction pattern produced by the 635 nm laser that is uploaded to ImageJ for analysis.*

Due to the large length (*L*) required to create a clear enough diffraction pattern to measure a distance (*d*) with confidence, significant errors are introduced. This method was repeated with positioning and an average of 683 nm was calculated with a huge error of ± 218 nm. This method also introduced challenges when applied to the 830 nm laser diode due to the lack of visibility in a highly sensitive set-up. It was proposed that it would be sensible to acquire a Wavemeter to measure these directly and accurately.

4.4.3 Wavemeter Method

To obtain accurate wavelength readings of both the 635 and 830 nm lasers utilised in the portable Raman systems, a Digital Optical Wavemeter (TQ8325, Advantest) was utilised, which measures wavelength using Michelson interference and a Helium – Neon (He-Ne) laser as the standard wavelength. This machine requires an FC/PC fibre connector input, compatible with the 635 nm portable laser, but more difficult for the 830 nm laser diode.

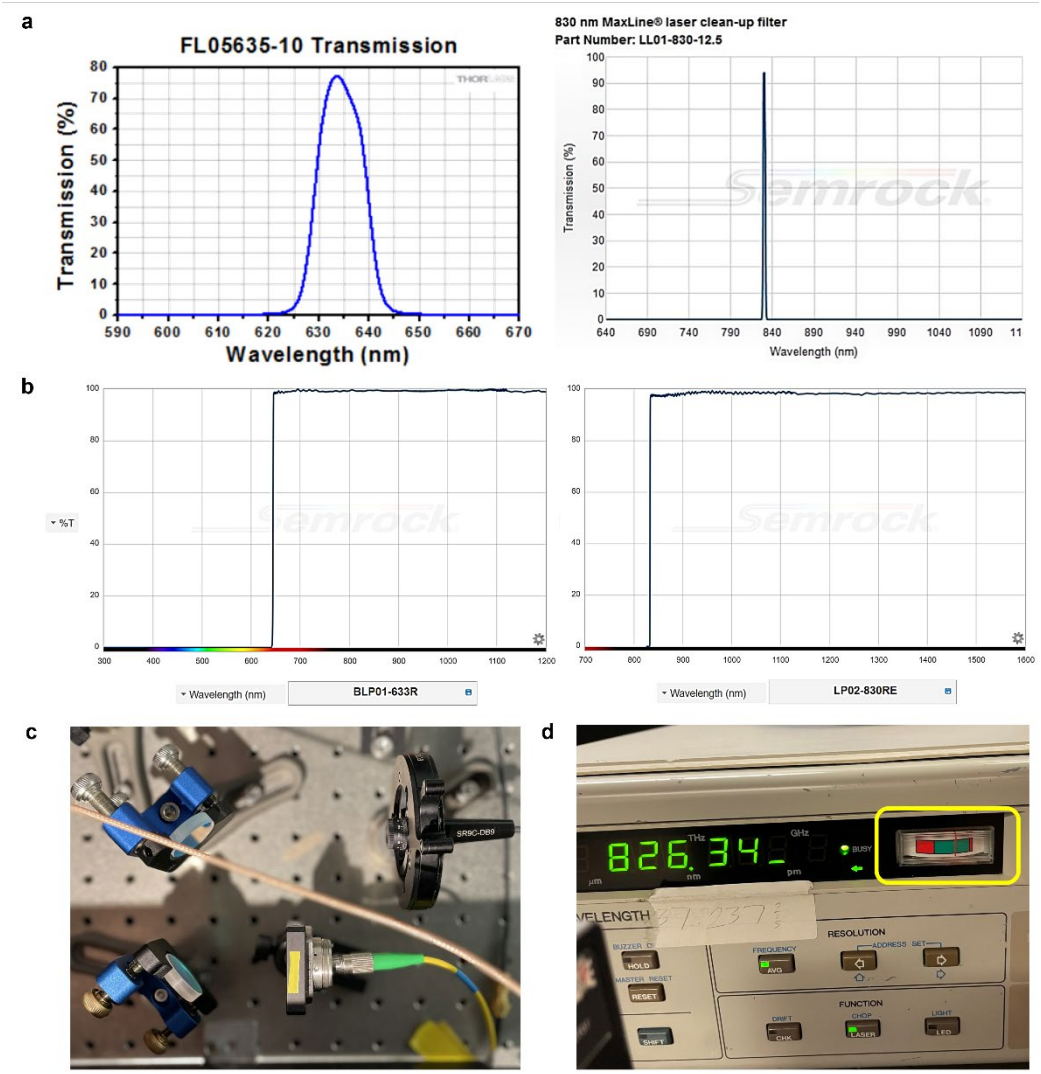

Figure 4.4. ***a (left)*** *Transmission graph for 635 nm clean-up filter (FL05635-10, ThorLabs) illustrating the Full Width Half Maximum (FWHM) of 10 nm.* ***(right)*** *Transmission graph for 830 nm clean-up filter (LL01-830-12.5, Semrock) illustrating the Full Width Half Maximum (FWHM) of 3.2 nm****. b (left)*** *Transmission graph for the Long-pass Rayleigh filter (BLP01-633R, Semrock) used within the 635 nm portable Raman design. This filter has a transmission band 650.5-1200 nm and an edge wavelength 645 nm [31]* ***(right)*** *Transmission graph for the long-pass edge filter (LP02-830RE-25, Semrock) used within the 830 nm portable Raman design. This filter has a transmission band 835.4 – 1872.2 nm and an edge wavelength 832.5 nm [32].* ***c*** *Fibre coupled set-up for the 830 nm laser diode to ensure sufficient power is supplied to the wavemeter.* ***d*** *Digital Optical Wavemeter (TQ8325, Advantest) output, measuring 826.34 nm, with a 0.0025% accuracy. The yellow box highlights the red pointer within the green zone indicating sufficient power has been supplied to the wavemeter.*

The 635 nm portable laser was easily connected and measured a wavelength of 637.67 nm with a measurement accuracy of 0.0025%[29], which is within the

manufacturer's given errors. Thus, the measured laser wavelength passes through the clean-up filter (FL05635-10, ThorLabs) with a large Full Width Half Maximum (FWHM) of 10 nm, shown in **Fig 4.4a**[30]**,** and suitably blocked from the spectrometer by the long-pass Rayleigh filter (BLP01-633R, Semrock) used within the 635 nm portable Raman system design, which has an edge wavelength 645 nm shown in **Fig. 4.4b (left)**[31].

The 830 nm laser diode required fibre coupling for sufficient power to be detected by the wavemeter, this involved guiding the beam into a fibre port using 2 mirrors on adjustable mounts to utilise all degrees of rotation (**Fig. 4.4c**). The laser input power was kept at at ~0.5 mW as this is the current approximate power designed to reach the eye within the portable system, a 15.3% transmission efficiency was calculated from the fibre coupled set-up with the single mode fibre, so the laser diode power was increased to 3.66 mW to obtain an output power of 0.56 mW. This was sufficient to reach the green zone of the wavemeter input levels, outlined in a yellow box in **Fig. 4.4d**. The wavemeter stabilised at 826.34 nm, which is within the ±10 nm error provided by the laser diode manufacturer and may explain why the Rayleigh peak centre sits below the spectrometer origin. The measured laser wavelength of 826.34 nm should be suitably blocked by the spectrometer using the long-pass Rayleigh filter (BLP01-633R, Semrock), used within the first draft of the 830 nm portable Raman system, as the filter has an edge wavelength 832.5 nm, shown in **Fig. 4.4b (right)**[32], however, the transmission of the laser diode is most likely reduced by the presence of the clean-up filter (LL01-830-12.5, Semrock) as the FWHM is very narrow at 3.2 nm, giving a lower wavelength of 826.8 nm, illustrated in **Fig. 4.4a (right)**. Thus, the laser power may need to be increased to obtain sufficient power at the spectrometer.

4.5 Beam Profiling

4.5.1 Spot Size

A beam profiler (BC106N-VIS/M, ThorLabs) was used with the provided software (ThorLabs Beam Application) to visualise and model the 830 nm laser diode beam. This was a borrowed system and seemed to need power calibration as 0.26 mW laser power would be detected as 244 mW by the profiler. The highest neutral density (ND) filter was used to prevent the software saturation, using the B-type AR (anti-reflective) coating (650-1050 nm) in filter slot number 6, for reference[33].

Using this software, the laser spot size of both the collimated beam and the retinal spot size through the phantom lens could be measured. The collimated beam spot size (with 6 cm between the laser and profiler) is shown in the 2D projection in **Fig. 4.5a.** Parameters are logged alongside this, in text form, including the major and minor diameters of the elliptical beam shape, which were used to calculate an elliptical area of $A_{collimated}$ = 0.0100 cm^2. A 3D projection and an X profile of the collimated beam are produced to ensure no irregularities, given in **Fig. 4.5b** and **4.5c,** respectively. Beam stability was also measured, collecting 270 counts over 2 minutes, producing a stability graph shown in **Fig. 4.5d**, where the dark blue line traces the centroid position, and

the light blue circle plots the smallest enclosing area around the centroid position scatter. The white line traces the plotted Gauss-fitted centroid position, in which the data is fitted to a Gaussian distribution. The red plot indicates the reference position trace which was set as the centre of the centroid position scatter, illustrating a drift of 2.5 μm.

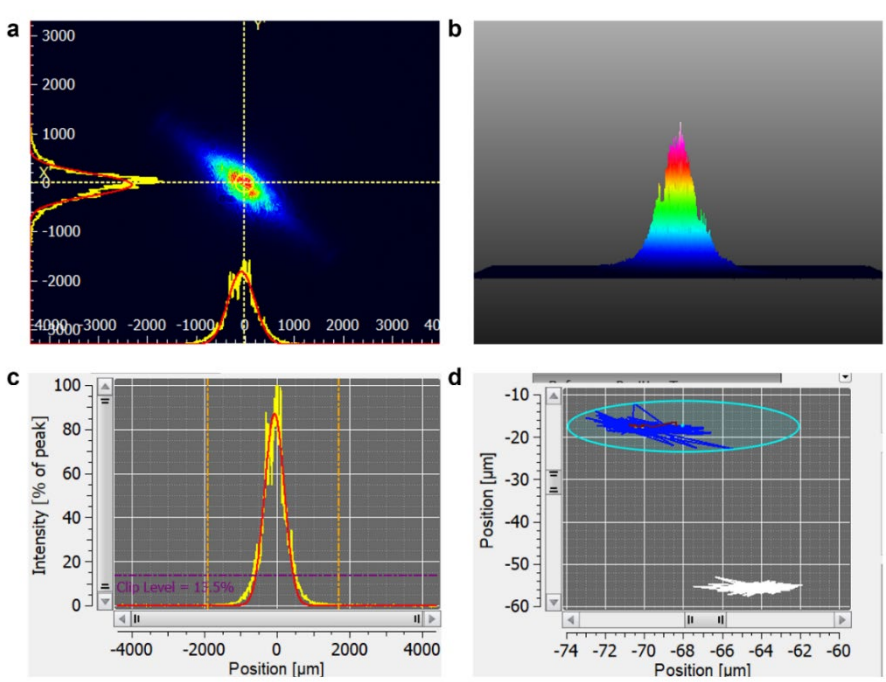

Figure 4.5. Beam profiling of the collimated 830 nm laser beam using the ThorLabs BC106N-VIS/M beam profiler and ThorLabs Beam Application software. ***a*** *2D projection of collimated beam, showing elliptical area calculated as 0.0100 cm^2.* ***b*** *3D projection showing no beam irregularities.* ***c*** *X profile of beam showing no irregularities.* ***d*** *Beam stability graph tracking centroid position (dark blue) encircled with the centroid position scatter (light blue), the Gaussian distribution (white) and the reference trace of the centre of the centroid position scatter (red), drifting a total of 2.5 µm.*

This process was repeated with the phantom eye lens (ACL2018U, ThorLabs) focusing the collimated 830 nm laser beam and the beam profiler at the retinal location, where the crosshairs are located (18 mm from the lens) in **Fig. 4.6a.** The spot size created by the phantom lens is shown in **Fig. 4.6b,** along with the 2D projection in **Fig. 4.6c.** The elliptical area was obtained using the extracted parameters and calculated to be $A_{Focused}$ = 0.0014 cm^2. Again, a 3D projection and an X profile of the collimated beam illustrate no irregularities in the beam, given in **Fig. 4.6d** and **4.6e,** respectively. **Fig. 4.6f.** shows the beam stability and there is a clear decrease in centroid position scattering shown in dark blue, creating a much smaller light blue circle, and the red trace indicating the centre of the centroid position scatter only spans 1.5 μm. This comparison indicates an increase in beam stability through the phantom lens which is beneficial for maximising the photon number at the retina for the inherently weak Raman signal fed back to the spectrometer.

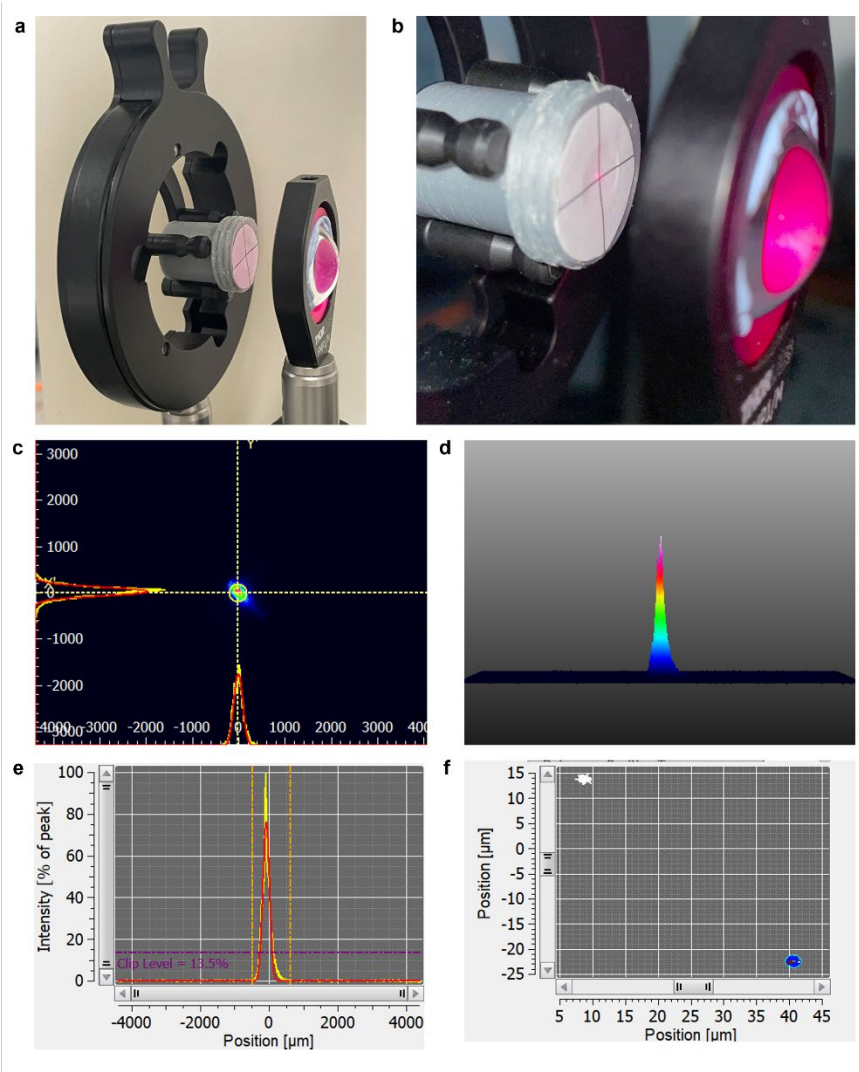

Figure 4.6. Beam profiling of the 830 nm laser beam focused by the phantom eye lens (ACL2018U, ThorLabs) using the ThorLabs BC106N-VIS/M beam profiler and ThorLabs Beam Application software. ***a*** *Set-up of the mounted phantom eye lens with crosshairs in the retinal location (18 mm) which is later replaced with the beam profiler.* ***b*** *Close-up view of the focused 830 nm laser spot size.* ***c*** *2D projection of collimated beam, showing elliptical area calculated as 0.0014 cm^2.* ***d*** *3D projection showing no beam irregularities.* ***e*** *X profile of beam showing no irregularities.* ***f*** *Beam stability graph tracking centroid position (dark blue) encircled with the centroid position scatter (light blue), the Gaussian distribution (white) and the reference trace of the centre of the centroid position scatter (red), drifting a total of 1.5 µm.*

4.5.2 Power Density

The beam profiler was used to produce a power density graph illustrating the change with radius as the beam is focused by the phantom eye lens. Parameters for ellipse area and major radius were obtained from the ThorLabs Beam Application software whilst power measurements were taken with the ThorLabs S121C photodiode power sensor to ensure high accuracy compared to the incorrect values produced by the profiler. Parameters were collected with the profiler and power sensor at increasing distances from 5 to 140 mm, to produce the power density graph shown in **Fig. 4.7**. The red plot indicates the focal point located at the focal length of the phantom eye lens (18 mm), where the power density rapidly increases.

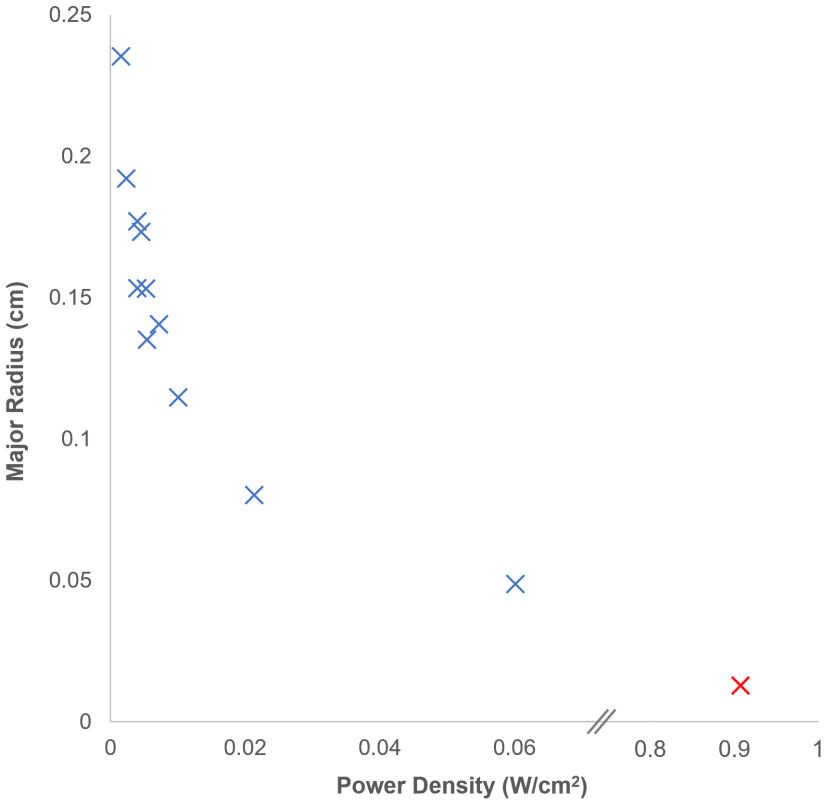

Figure 4.7. Power density graph of the 830 nm laser focused by the phantom eye lens (ACL2018U, ThorLabs). Elliptical major radii and areas obtained using the ThorLabs BC106N-VIS/M beam profiler whilst power measurements were taken with the ThorLabs S121C photodiode power sensor. The red plot indicates the phantom eye lens focal point at 18 mm from the back of the eye, where power density rapidly increases.

4.6 Laser Safety Regulations

Unlike the 635 nm visible laser which is Class 1 and sold on the market as “eye safe”, the 830 nm laser diode is Class 3 and needs to be utilised with care when designing a non-invasive eye-based device. When designing the system for the UK and European standards, the “BS EN 60825-1:2014+A11:2021 Safety of laser products – Equipment classification and requirements” document was referred to[27]. Damage to biological tissue is highly influenced by wavelength, pulse duration and radiation exposure, though absorption occurs at a molecular level and is wavelength specific, therefore changing device set-up per laser wavelength is important in this context[34].

In the 400 to 1400 nm range, the greatest hazard is retinal damage, whilst the cornea, aqueous humour, lens, and vitreous humour are transparent to radiation of these wavelengths[27], [34]. This is why lasers emitting UV and far infra-red radiation represent a corneal hazard whilst visible and near infra-red wavelengths will be transmitted and damaging to the retina[27].

Accessible Emission Limits can be calculated from the regulations outlined in the “BS EN 60825-1:2014+A11:2021” document, specifically in Table 7 for Class 3 laser products in the wavelength range 400 – 1400 nm that pose a retinal hazard. The

equation for accessible emission limits can be deduced by outlining an emission duration of 10 to 3x10^4 seconds for a laser wavelength of 700 to 1050 nm:

$$E[J] = 3.5 \times 10^{-3} t^{0.75} C_4 C_6 \quad (4.3)$$

Where *E* is the emission limit, *t* is emission duration and *C* are correction factors, which were identified using Table 9 in the "BS EN 60825-1:2014+A11:2021" document. $C_4 = 10^{0.002(\lambda-700)}$ for spectral region 700 – 1050 nm. $C_6 = 1$ for $\alpha \leq \alpha_{min}$ which is true for a collimated beam with α (divergence) less than or equal to 1.5 mrad[34], [35].

A realistic emission duration is approximately 30 seconds, which should allow time for sufficient Raman signal to be collected in a Raman acquisition without causing much strain on the patient. This could be shortened to 10 seconds and accumulated 3 times in data processing to reduce emission limit, mimicking a blink mechanism. Soleimani *et* al. explore burn intensity in retinal laser photocoagulation based on laser parameters, with results showing that shorter pulses in laser surgery were associated with significantly lower pain levels.

However, a "blink" mechanism is not the simple answer, whilst high powers in long pulses will give rise to progressively enlarging lesions, short pulses will create a risk of explosive rupture of cells and damage due to physical displacement[27]. This can be explored further when assessing the quality of Raman spectra with the low-power, portable system. In the preliminary stage, $t = 30$ s is suitable and produces an emission limit of $E = 0.081$ J which is equal to a laser power of 2.72 mW. This would be the maximum power within regulation, and all design and prototype efforts will be set far below this to assess how successful the system could be within real-world applications.

4.7 Investigation of Laser Damage to Primary Porcine Retinal Cells

A collaborative project was completed with the Defence Science and Technology Laboratory (Dstl) to explore the effect of the 830 nm laser on eye-relevant cells to gain insight into the safety of using the laser diode within a diagnostic device. The main aim was to identify the upper limit of laser exposure for a realistic timeframe that eye-based Raman readings may require, exploring whether "blink" mechanisms would be appropriate to implement, such as splitting a 30-second Raman acquisition into three 10-second measurements.

4.7.1 Materials and Method

Porcine primary retinal pigment epithelial cells (PRPEpiC, Innoprot) were plated at 51,000 cells per cm^2 on inserts 22 days post seeding, without passage. Inserts were used to enable cells to be removed from the media for exposure to avoid the laser being absorbed by the surrounding liquid. The collimation tube was altered to create a larger spot size of $A_{RAW} = 7.8540$ cm^2 for better visibility of cell damage, this can be calculated as power density and modelled back to the regular spot size utilised for the final portable Raman system.

The cells were initially exposed to the collimated beam at 40 mW, 10 mW and 1 mW for 30 seconds to model what the cornea would be subjected to. Metabolic activity was assessed using Presto Blue (1:10 dilution, 600 µL per well and 300 µL per insert, incubated at 37°C for 45 minutes). Metabolic activity was measured using a Flexstation in stop-read fluorescence mode, with excitation and emission wavelengths 544 nm and 590 nm, respectively.

After 20 minutes, the cells were stained for apoptosis and necrosis using a 3-colour staining kit (Apoptotic, Necrotic and Healthy Cells Quantitation Kit, Biotium) containing stains: CF488A Annexin-V for staining apoptotic cells green, Hoechst 33342 to stain nuclei blue and Ethidium Homodimer III to stain necrotic cells red. Apoptotic cell staining was proving an issue with this kit and the Annexin-V stain was therefore swapped for Calcein AM to stain live cells green, for this a set of the exposed cells were incubated at 37°C with 5% CO_2 for 24 hours. A set of wells was uncovered in the fume hood environment for 30 seconds without laser exposure and then underwent the same staining process as control readings.

4.7.2 Set-up

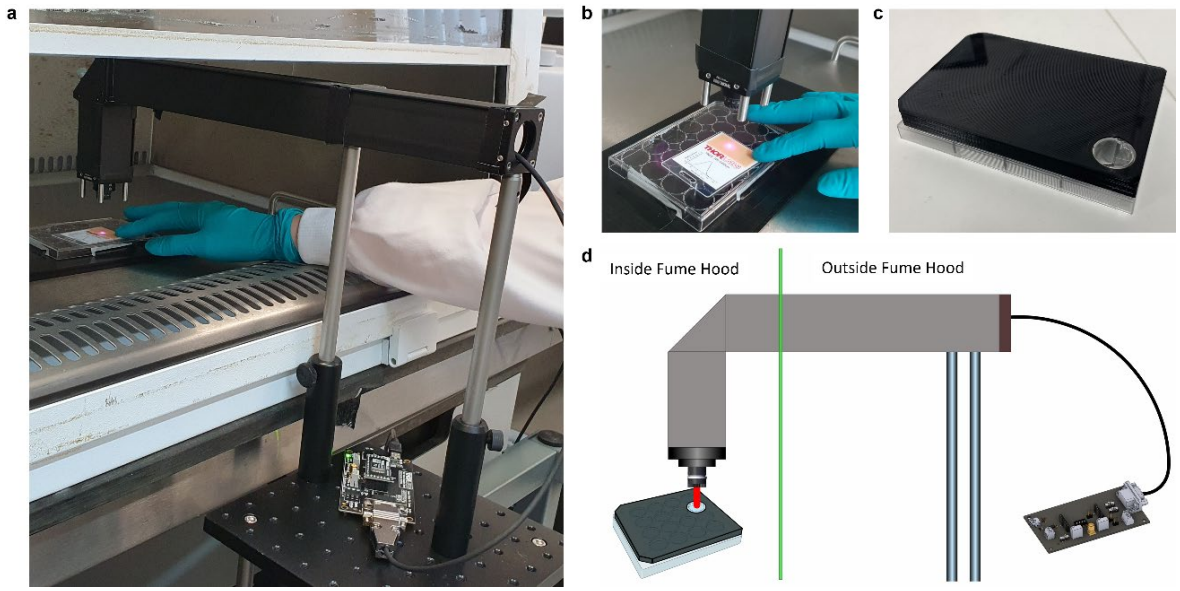

Figure 4.8. Photographs and schematic diagram of the laser enclosure set-up to allow the laser to enter the cabinet without sterilising the electronics. ***a*** *Image taken of the entire set-up during calibration. The laser driver and optical posts can be seen on the portable optical table which dampens vibrations to increase laser stability. The strain relief cable connected that powers the laser diode from the driver is fed into the cage system on the right-hand-side (outside the cabinet). On the left-hand-side (inside the cabinet), the laser diode mounted in the collimation tube exits the cage and shines on the viewing card at the transwell plate location.* ***b*** *A close-up view of the left-hand-side of the set-up inside the cabinet.* ***c*** *3D printed transwell plate lid to reduce cell exposure to stray laser beam and probability of infection. Multiple lids were printed with different hole locations to create consistency with exposure location and to allow multiple cell exposure without disturbing cells.* ***d*** *Schematic of the entire set-up created with Inkscape.*

Working with sensitive primary porcine retinal cells required a sterile set-up within a microbiological safety cabinet. A laser set-up had to be designed to allow the laser to enter the cabinet without sterilising the electronics, this is shown in **Fig. 4.8a.** and a schematic is given in **Fig. 4.8d.** The laser driver and optical posts were mounted onto

a portable optical table to dampen vibrations and increase laser stability. The strain relief cable connected that powers the laser diode from the driver is fed into the cage system on the right-hand-side (outside of the cabinet) and exits on the left-hand-side (inside the cabinet), the laser diode mounted in the collimation tube exits the cage and shines on the cells within inserts of a 24 transwell plate, **Fig. 4.8b** shows a close-up of the set-up inside the cabinet. To guide the laser location, reduce secondary exposure to stray laser light and minimise the amount of time the cells are left uncovered, a 3D-printed transwell plate lid was designed, shown in **Fig. 4.8c.**

4.7.3. Results

In the first round of preliminary experiments, there was no observed reduction in metabolic activity of the cells after the 20-minute wait period, however, there was evidence of an increased in metabolic activity after 40 and 1 mW exposure. An increase metabolic activity following laser exposure is of interest, as near-infrared wavelengths, such as 830 nm, have shown potential as therapeutic photobiomodulation techniques, specifically in neurodegeneration[36]–[38]. After metabolic activity was measured, the retinal cells were stained for evidence of apoptosis or necrosis (as well as a nuclear stain). Staining at T = 0 hours (T0) provided no positive apoptotic control in any of the cell exposures, and the stain was swapped out for T = 24 hours (T24) staining to the more reliable Calcein AM. Assessing visually, there was no difference in the amount of necrotic staining between the control and any of the cells exposed to the 830 nm laser, nor significant evidence of cell death. It was unclear whether this is because apoptosis was not present in the samples or if staining was unsuccessful (no positive apoptotic control). The experiment was rescheduled and repeated with improved methodology in determining the location of laser exposure and staining.

The methodology was improved by marking the location of laser exposure within the cabinet that could be relocated during microscopic imaging. The PRPEpiC were exposed again to the 40 mW laser for 30 seconds to compare to cells under control conditions. **Fig. 4.9** shows the resulting stains of this experimental run, with little visual difference between the control and 40 mW exposure cells other than a slightly lower concentration of green stain (live cells) but no increase of red stain (dead cells). ImageJ was used to quantify area of cell fluorescence from each stain, by separating the individual fluorescent channels, converting into greyscale images and using the threshold analysis tool to identify green/blue/red staining and measure this as a percentage of the image area. Following exposure, the area of dead (red) cells increased from 0.23% to 4.87%, whilst the area of living (green) cells decreased from 34.99% to 15.12%. At a 40 mW laser power, the visual impact of the laser exposure was expected, however this quantification suggests some cell damage. Conversely the areas of blue stain indicative of nuclei increased from 6.83% to 14.79%, suggesting

an increase in undamaged cells following exposure. Unfortunately, there was still no clear area observed that would indicate the laser spot exposed to the cells.

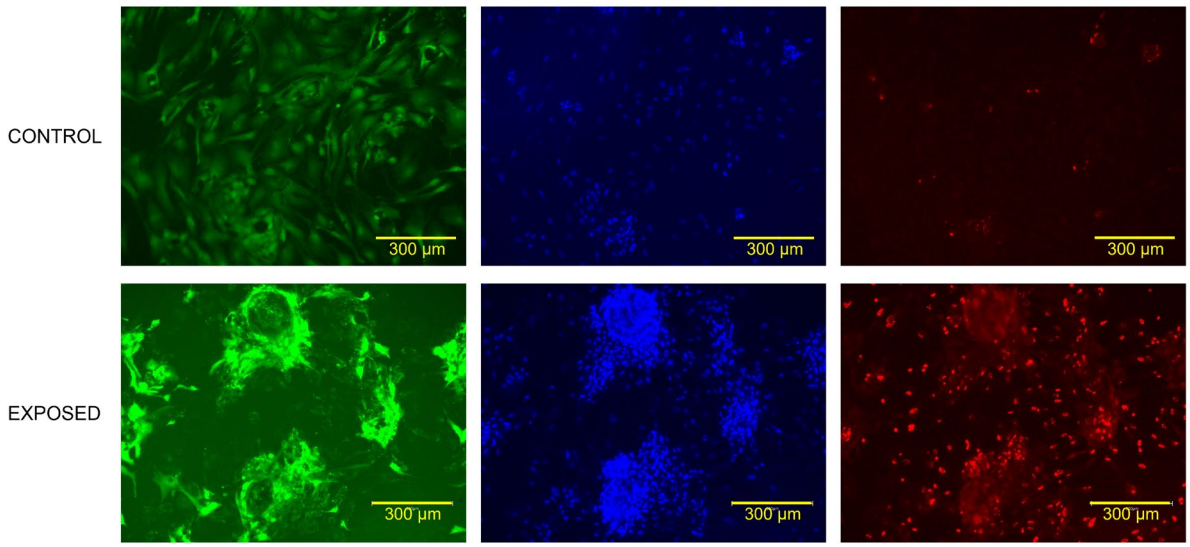

Figure 4.9. Images of the improved methodology of PRPEpiC cells exposed to 40 mW collimated 830 nm laser for 30 seconds with markers present to locate exposed area. Cells were stained with Calcein AM (green, live) Hoechst (blue, all nuclei) Ethidium Homodimer III (red, dead) and imaged immediately at x10 magnification. ***Top*** *Shows the control cells without laser exposure.* ***Bottom*** *shows the location of the 40 mW laser exposure. Stains show little difference between the control and 40 mW exposure cells, lower concentration of green stain (live cells) but no increase of red stain (dead cells), which was reflected when measuring cell florescence using ImageJ. No clear area indicating laser spot was observed.*

A large reason that laser safety is so important is due to the huge increase in power density as the collimated beam is focused by the strong compound 60 D (Dioptre) power from the cornea and lens, causing damage. Thus, the experimental method was repeated with the introduction of the phantom eye lens (ACL2018U, ThorLabs) to increase the power density of the laser and mimic what the retina is exposed to. Due to the large lens power, the power density was sufficiently increased to expect cell damage, reducing the area from $A_{collimated}$ = 0.0100 cm^2 to $A_{Focused}$ = 0.0014 cm^2. Unfortunately, with the focused laser spot size covering a tiny area of the insert surface, a damaged area could not be observed.

Due to the lack of positive results showing an area of damage in the laser exposed location, the PRPEpiC were once again grouped as control, exposed and sham (following starvation and heat), and exposed to the same laser at 50 mW power for 10 minutes. These cells were seeded at P2; markers were placed underneath the inserts to ensure consistency between the laser exposure spot and the location of microscopy. This experimental step was made to ensure a positive result to dictate further power exposures to be chosen based more closely on the EU (European Union) safety regulations. We hypothesised that cell damage would be observed, due to the calculated emission limit power of 2.72 mW for a 30-second exposure established in **Section 4.6**.

Unfortunately, no visibly damaged areas of dead cells were observed in the inserts. Despite this, the staining shown in **Fig. 4.10** revealed some observations that could

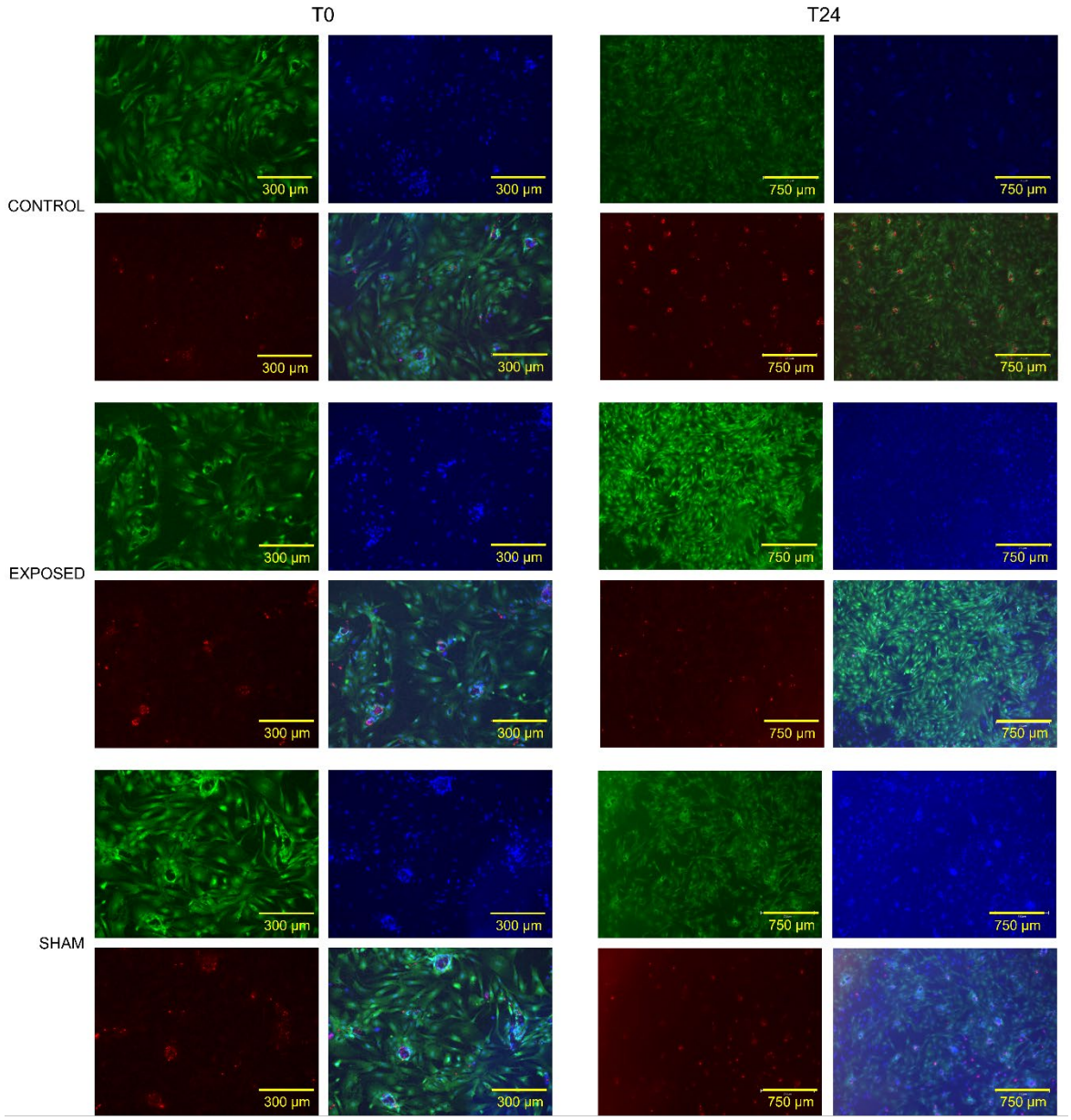

Figure 4.10. Images of stained PRPEpiC cells seeded at P2 and investigated at day 65, exposed to 830 nm laser set to 50 mW for 10 minutes. Stains were completed at both T= 0 hours and T = 24 hours. No areas of damage indicating the laser spot were observed. At T0, there are clearer formations of red cells (dead) in the exposed and sham plates which reflected in quantitative analysis. Visual differences are difficult to determine between T0 and T24, and quantitative analysis suggests percentage area of living (green) cells decreased but stayed constant in the exposed cells and even increased in the sham model. Quantitative measurements of cell fluorescence can be found in ***Appendix B.***

be made regarding cell behaviour following laser exposure. At T0, clearer formations of red cells can be observed in the exposed and sham inserts, compared to that of the control which has very few dead cells that are scattered more evenly, which was shown by slight quantitative differences using ImageJ fluorescence analysis with area percentage of dead cells being 0.2% in the T0 control versus 0.6% and 1.3% in the exposed and Sham samples, respectively. At T24, on the other hand, more clumps of dead cells can be observed in the control insert, whereas a lower concentration of even scatter is present in the exposed and sham inserts, measuring as being 2.0% in the T24 control versus 5.2% and 6.6% in the exposed and Sham samples,

respectively. The exposed cells having fewer dead cells than the Sham model suggests that the strain/danger the cells are being put under with a 50 mW laser for 10 minutes is less impactful than keeping the cells in sub-optimal conditions, this is unlikely and experimental repeats are required to confirm this relationship. Another quantitative observation that justifies more cell data to be collected is due to the area percentage of green (living) cells behaving as expected for controls (e.g. decreasing from 35.0% to 8.1% after 24 hours), but then measuring the same area percentage after 24 hours following laser exposure (19.0% to 19.0%) and even increasing in area percentage in the Sham model (18.9% to 24.4%); extracted area percentage values can be found in **Appendix B**. Though the aforementioned themes of the therapeutic properties of near-IR wavelengths is a possibility and was explored in a side project in **Appendix H,** there is not enough evidence in the set-up of this study to conclude a definite safe laser power for retinal cell exposure in the continued use of the portable 830 nm Raman device.

4.8 Discussion and Conclusion

The work in this chapter involves the profiling and testing of the 830 nm laser diode with the intended use of a portable, eye-safe Raman device, along with an exploration of eye safety guidelines which are vital to consider for a project with commercial applications. Laser parameters such as wavelength, power and collimation are essential for effective use in a low-power and highly aligned system and have therefore been verified. This work will aid the next steps of this thesis project to build an optical path and 3D housing for eye-based Raman spectroscopy, specifically in choosing components such as mirrors and filters.

Alongside laser profiling, an investigation for further validation was established in collaboration with Dstl. For this, eye-relevant tissue needed to be tested so Porcine primary retinal pigment epithelial cells were grown at Dstl Porton Down labs, for later laser exposure and staining. Metabolic activity following laser exposure was also tested before staining, as the first steps in observing any patterns between metabolism and 830 nm laser exposure. The slight increase in metabolic activity following 1 and 40 mW laser powers suggests grounds for further work to determine if there is a definite relationship and what are the limits, for which a therapeutic application to the Raman device could be established.

Though obstacles of identifying suitable staining kits for the cell type and building a set-up to allow for sterile laser exposure were overcome, the biggest issue in the study was identifying the location of laser exposure to assess any damage to the cells. Further issues with the cell line also caused complications in the time-limited study, such as the cells not forming a uniform layer, producing small gaps and clumps of dead cells at which the small laser spot size may be hitting, resulting in an inability to locate using staining. Alternatively, the laser could be hitting an area of healthy cells and having no effect.

Overall, this chapter provides useful information on the laser diode proposed for portable and eye-safe Raman spectroscopy which aided decision making in building the 830 nm Raman device in the following chapter. Unfortunately, time constraints and limitations in laser set-up at Dstl prevented a complete set of final results from being produced to accompany the 830 nm Raman device with validation of eye safety. However, the cell damage study produced clear foundations for a future study for which the set-up and methodology would be replicated, alongside the laser being modified to fill a larger area of the insert surface, at a power density comparable to that at the retina once passing through the human cornea and lens.

4.9 References

[1] A. G. Hamedani and D. R. Gold, “Eyelid dysfunction in neurodegenerative, neurogenetic, and neurometabolic disease,” *Front. Neurol.*, vol. 8, no. JUL, p. 329, Jul. 2017, doi: 10.3389/fneur.2017.00329.

[2] A. I. Ramirez *et al.*, “The role of microglia in retinal neurodegeneration: Alzheimer’s disease, Parkinson, and glaucoma,” *Front. Aging Neurosci.*, vol. 9, no. 214, Jul. 2017, doi: 10.3389/fnagi.2017.00214.

[3] R. Mancino *et al.*, “Neurodegenerative Process Linking the Eye and the Brain,” *Curr. Med. Chem.*, vol. 26, no. 20, pp. 3754–3763, Mar. 2018, doi: 10.2174/0929867325666180307114332.

[4] J. A. Fernández-Albarral *et al.*, “Retinal glial changes in Alzheimer’s disease – A review,” *J. Optom.*, vol. 12, no. 3, pp. 198–207, Jul. 2019, doi: 10.1016/j.optom.2018.07.001.

[5] N. Marchesi, F. Fahmideh, F. Boschi, A. Pascale, and A. Barbieri, “Ocular Neurodegenerative Diseases: Interconnection between Retina and Cortical Areas,” *Cells*, vol. 10, no. 9, Sep. 2021, doi: 10.3390/CELLS10092394.

[6] J. H. ; ; Albert *et al.*, “Mild-to-Moderate Traumatic Brain Injury: A Review with Focus on the Visual System,” *Neurol. Int. 2022, Vol. 14, Pages 453-470*, vol. 14, no. 2, pp. 453–470, May 2022, doi: 10.3390/NEUROLINT14020038.

[7] P. Colligris, M. Jesus Perez De Lara, B. Colligris, and J. Pintor, “Ocular Manifestations of Alzheimer’s and Other Neurodegenerative Diseases: The Prospect of the Eye as a Tool for the Early Diagnosis of Alzheimer’s Disease,” *J. Ophthalmol.*, vol. 2018, pp. 1–12, 2018, doi: 10.1155/2018/8538573.

[8] A. Jeromin and R. Bowser, “Biomarkers in Neurodegenerative Diseases,” in *Advances in Neurobiology*, vol. 15, Springer New York LLC, 2017, pp. 491–528.

[9] O. Hansson, “Biomarkers for neurodegenerative diseases,” *Nat. Med. 2021 276*, vol. 27, no. 6, pp. 954–963, Jun. 2021, doi: 10.1038/s41591-021-01382-x.

[10] P. J. Snyder *et al.*, “Retinal imaging in Alzheimer’s and neurodegenerative diseases,” *Alzheimers. Dement.*, vol. 17, no. 1, pp. 103–111, Jan. 2021, doi: 10.1002/ALZ.12179.

[11] A. H. Kashani *et al.*, “Past, present and future role of retinal imaging in neurodegenerative disease,” *Prog. Retin. Eye Res.*, vol. 83, Jul. 2021, doi: 10.1016/J.PRETEYERES.2020.100938.

[12] C. S. Gilmore *et al.*, “Association of Optical Coherence Tomography With Longitudinal Neurodegeneration in Veterans With Chronic Mild Traumatic Brain Injury,” *JAMA Netw. open*, vol. 3, no. 12, Dec. 2020, doi: 10.1001/JAMANETWORKOPEN.2020.30824.

[13] S. Gupta, R. Zivadinov, M. Ramanathan, and B. Weinstock-Guttman, “Optical coherence tomography and neurodegeneration: are eyes the windows to the brain?,” *Expert Rev. Neurother.*, vol. 16, no. 7, pp. 765–775, Jul. 2016, doi: 10.1080/14737175.2016.1180978.

[14] C. Childs, L. A. Barker, and M. Loosemore, “Eye and Brain Dovepress investigating possible retinal biomarkers of head trauma in Olympic boxers using optical coherence tomography,” *Eye Brain*, vol. 10, pp. 101–110, 2018, doi: 10.2147/EB.S183042.

[15] S. Jung *et al.*, “Retinal neurodegeneration in patients with end-stage renal disease assessed by spectral-domain optical coherence tomography,” *Sci. Rep.*, vol. 10, no. 1, pp. 1–10, Mar. 2020, doi: 10.1038/s41598-020-61308-4.

[16] A. R. Stevens *et al.*, “Raman Spectroscopy as a Neuromonitoring Tool in Traumatic Brain Injury: A Systematic Review and Clinical Perspectives,” *Cells*, vol. 11, no. 7, pp. 1–22, Apr. 2022, doi: 10.3390/CELLS11071227.

[17] G. Devitt, K. Howard, A. Mudher, and S. Mahajan, “Raman Spectroscopy: An Emerging Tool in Neurodegenerative Disease Research and Diagnosis,” *ACS Chem. Neurosci.*, vol. 9, no. 3, pp. 404–420, Mar. 2018, doi: 10.1021/acschemneuro.7b00413.

[18] M. Paraskevaidi *et al.*, “Raman Spectroscopy to Diagnose Alzheimer’s Disease and Dementia with Lewy Bodies in Blood,” *ACS Chem. Neurosci.*, vol. 9, no. 11, pp. 2786–2794, 2018, doi: 10.1021/acschemneuro.8b00198.

[19] O. Terrones, J. Olazar-Intxausti, I. Anso, M. Lorizate, J. A. Nieto-Garai, and F. X. Contreras, “Raman Spectroscopy as a Tool to Study the Pathophysiology of Brain Diseases,” *Int. J. Mol. Sci.*, vol. 24, no. 3,

p. 2384, Jan. 2023, doi: 10.3390/IJMS24032384.
[20] A. S. Moody and B. Sharma, “Multi-metal, Multi-wavelength Surface-Enhanced Raman Spectroscopy Detection of Neurotransmitters,” *ACS Chem. Neurosci.*, vol. 9, no. 6, pp. 1380–1387, Jun. 2018, doi: 10.1021/acschemneuro.8b00020.
[21] C. C. Huang and C. Isidoro, “Raman Spectrometric Detection Methods for Early and Non-Invasive Diagnosis of Alzheimer’s Disease,” *J. Alzheimer’s Dis.*, vol. 57, no. 4, pp. 1145–1156, 2017, doi: 10.3233/JAD-161238.
[22] R. J. Erckens *et al.*, “Noninvasive Raman spectroscopic identification of intraocular lens material in the living human eye,” *J. Cataract Refract. Surg.*, vol. 27, no. 7, pp. 1065–1070, Jul. 2001, doi: 10.1016/S0886-3350(00)00828-2.
[23] W. Gellermann, I. V. Ermakov, R. W. McClane, and P. S. Bernstein, “Raman imaging of human macular pigments,” *Opt. Lett.*, vol. 27, no. 10, p. 833, May 2002, doi: 10.1364/ol.27.000833.
[24] M. Marro, A. Taubes, P. Villoslada, and D. Petrov, “Detection of neuroinflammation through the retina by means of Raman spectroscopy and multivariate analysis,” *Biophotonics Photonic Solut. Better Heal. Care III*, vol. 8427, p. 842715, Jun. 2012, doi: 10.1117/12.921358.
[25] P. Villoslada, M. Marro, A. Taubes, B. Moreno, and D. Petrov, “Raman Spectroscopy Analysis of the Retina Reveals Changes in Glutamate, N-Acetyl-Aspartate, NADH and Phosphatidylcholine in Neuroinflammation (P01.166),” *Neurology*, vol. 78, no. 1 Supplement, 2012.
[26] C. Stiebing *et al.*, “Nonresonant Raman spectroscopy of isolated human retina samples complying with laser safety regulations for in vivo measurements,” *Neurophotonics*, vol. 6, no. 04, p. 1, Sep. 2019, doi: 10.1117/1.nph.6.4.041106.
[27] British Standards Institution, “BS EN 60825-1:2014+A11:2021 Safety of laser products. Part 1, Equipment classification and requirements.,” p. 140.
[28] “KI 9600 Series Power Meter KI 9800 Series Light Source,” *Kingfisher*, 2021. https://www.kingfisherfiber.com/media/ozskdcqx/usermanual_ki9000.pdf (accessed Nov. 02, 2023).
[29] “TQ8325 Advantest (Digital Optical Wavelength Meter) | ArtisanTG™.” https://www.artisantg.com/TestMeasurement/51634-2/Advantest-TQ8325-Digital-Optical-Wavelength-Meter (accessed Feb. 22, 2024).
[30] “FL05635-10 - Ø1/2" Laser Line Filter, CWL = 635 ± 2 nm, FWHM = 10 ± 2 nm,” *ThorLabs*. https://www.thorlabs.com/thorproduct.cfm?partnumber=FL05635-10.
[31] “632.8 nm EdgeBasic™ best-value long-pass edge filter,” *IDEX Health & Science*. https://www.idex-hs.com/store/product-detail/blp01_633r_25/fl-008543.
[32] “830 nm RazorEdge® ultrasteep long-pass edge filter,” *IDEX Health & Science*. https://www.idex-hs.com/store/product-detail/lp02_830re_25/fl-009064.
[33] “BC106N M2MS-BC106N Operation Manual,” *ThorLabs*. https://www.thorlabs.com/drawings/e8c1d66fa1d153b7-6A9BB3F8-D4B9-A0D9-F5604F0B94F60ED9/BC106N-VIS_M-Manual.pdf.
[34] M. F. Kaschke, K.-H. Donnerhacke, and M. S. Rill, *Optical devices in ophthalmology and optometry : technology, design principles and clinical applications*, 1st ed. John Wiley and Sons Inc., 2014.
[35] K. Schulmeister, “‘The Apparent Source’-A Multiple Misnomer,” *Int. Laser Saf. Conf.*, pp. 91–98, 2005, Accessed: Nov. 13, 2023. [Online]. Available: http://laser-led-lamp-safety.seibersdorf-laboratories.at/newsletterhttp://laser-led-lamp-safety.seibersdorf-laboratories.at.
[36] W. tong Pan, P. miao Liu, D. Ma, and J. jun Yang, “Advances in photobiomodulation for cognitive improvement by near-infrared derived multiple strategies,” *J. Transl. Med.*, vol. 21, no. 1, p. 135, Dec. 2023, doi: 10.1186/S12967-023-03988-W.
[37] A. S. C. Foo, T. W. Soong, T. T. Yeo, and K. L. Lim, “Mitochondrial Dysfunction and Parkinson’s Disease—Near-Infrared Photobiomodulation as a Potential Therapeutic Strategy,” *Front. Aging Neurosci.*, vol. 12, Apr. 2020, doi: 10.3389/FNAGI.2020.00089.
[38] A. Abijo, C.-Y. Lee, C.-Y. Huang, P.-C. Ho, and K.-J. Tsai, “The Beneficial Role of Photobiomodulation in Neurodegenerative Diseases,” *Biomedicines*, vol. 11, no. 7, p. 1828, Jun. 2023, doi: 10.3390/BIOMEDICINES11071828.

Chapter 5

Designing, Building and Testing an Eye-Based Raman Device with Fundus Imaging for Biochemical and Structural Traumatic Brain Injury Detection

Herein, all of the lessons learnt, and techniques developed in the previous chapters of this thesis are utilised to design, build, and test a novel portable device harnessing invisible 830 nm laser wavelengths and a handheld fundus imaging set-up built upon a Raspberry Pi module to achieve spectra from fresh, *ex vivo* retinae suitable for point-of-care diagnostics and complete telemedicine applications.

Finalising the device design involved decision-making towards the most compact positioning of the 830 nm system's components that would not disrupt the optical paths of the fundus camera. Once this was complete, all components were built upon the optical table using commercial and custom 3D-printed mounts. This was iterated until complete alignment was achieved where the input laser path met the centre of the retinal sample holder of the phantom eye model along with the simulated exit laser path.

The biggest challenge was translating the finely tuned alignment into a CAD design and 3D-printed housing. A first draft for component mounting was completed first and, upon testing alignment, was utilised to obtain spectra of fresh, *ex vivo* porcine retinae, assigning characteristic peaks.

Many versions had to be created, tested, and discarded before achieving full alignment in the first functioning prototype with slots or attachments for all components and a lid to reduce stray light. This was due to limitations in mounting, resolution, and the need for support material.

The remaining limitation of this project that will prevent progression, with both the EyeD and the 830 nm Raman Device prototype, is a lack of viable eye tissue to test with. Narratives surrounding spectral data obtained with such low-power Raman spectroscopy and adherence to laser safety regulations cannot be concluded without a new eye model that has the capabilities to be prepared as either healthy or TBI subjects.

5.1 Introduction

There is an undeniable need for a new technology to diagnose Traumatic Brain Injury (TBI) at the point of care (PoC). Despite approximately 70 million people sustaining a TBI worldwide each year[1], [2], and studies estimating that half of the world's population is likely to have at least one TBI in their lives[3], the techniques used to identify TBI are frequently failing patients. A TBI is sustained following rapid movement or trauma to the skull, commonly following falls, assaults, and vehicle accidents. Issues in TBI diagnostics arise from the fact that TBI is not a single pathophysiological phenomenon, but a complex disease process generating structural and biochemical functional damage[4].

A TBI can be categorised as either mild, moderate, or severe, where symptoms worsen from disorientation, impaired consciousness, vomiting, dysfunctional memory, and prolonged unconsciousness[4], [5]. The overlap and subtleties between symptoms make TBI classification difficult and the subsequent patient management inconsistent. Making TBI diagnostics more challenging is the further classification of primary and secondary injuries, where the former occurs at the time of injury as a direct result of impact such as hematoma and contusions, whilst the latter is a biochemical cascade of neurodegeneration leading to elevated intracranial pressure (ICP) and tissue death taking place between hours and days following injury[5].

Characterising incidents of TBI by severity produces the estimated separation: 81% mild, 11% moderate and 8% severe[2]. The overwhelming rate of mild TBI (mTBI) and the lack of distinctive symptoms has coined TBI the descriptor a "silent epidemic"[2], [4]. There is an overwhelming presence of mTBI which is most likely underestimated as many mTBI patients never seek medical assistance nor are treated by GP[4]. Even when assessed by a healthcare professional, mTBI often goes undetected as it has been shown that multiple instances of mTBI were not associated with cognitive impairment in the chronic phase, and some had better visual working memory than controls[6], rendering cognitive assessment techniques such as the Glasgow Coma Scale (GCS) ineffective. Even the golden standard TBI diagnostic techniques such as neuroimaging are not ideal for mTBI as it does not typically present as structural brain changes detectable with Magnetic Resonance Imaging (MRI)[7], and large percentages of mTBI patients have no indicators when assessed with Computed Tomography (CT) scans[2].

The drastic influence of mTBI towards the global incidence numbers and the difficulties presented in identifying it highlights the importance of new methods for accurate and rapid TBI diagnostics. Characterising TBI at the PoC is important, not only for making triaging decisions about whether medical assistance is required but also, in making early plans for the patient journey as the mTBI therapeutic and diagnostic window ranges from minutes to hours[7].

In recent years, novel innovations have been developed to find an alternative method to diagnose TBI using biofluids[8], outlined in **Chapter 1,** such as mass spectrometry,

magnetic resonance spectroscopy (MRS), enzyme-linked immunosorbent assays (ELISAs), near-infrared spectroscopy (NIRS) and hyperspectral imaging[9], [10]. These techniques identify biochemical changes that characterise TBI in biofluid coined “biomarkers” for which their presence or change in concentration can confirm a diagnosis, termed a liquid biopsy[11]. Whilst there are many prospective biomarkers for TBI and neurodegenerative diseases explored in literature[2], [12]–[15], and introduced in **Chapter 1,** only one biomarker has been integrated into healthcare systems. S100B has been introduced as a biomarker of TBI in French and Scandinavian guidelines to triage patients for CT scans[2], [7]. Although two prospective TB biomarkers, GFAP and UCHL1, have been approved by the FDA for monitoring TBI patients[16], issues regarding standardisation and selectivity prevent more TBI biomarkers from being introduced into healthcare practices.

An avenue for exploring and characterising biochemical, neurologically relevant information for TBI diagnostics is by utilising the direct links the eye has with the brain *via* the optical tract. The retina can therefore be explored as an extension of the central nervous system (CNS)[17], and there is a growing field of research looking at ocular neurodegenerative diseases like age-related macular degeneration and glaucoma[18], as well as how degeneration in the brain can present in the retina and optic nerve[19]–[23]. This direct connection is strengthened by studies showing that oculomotor behaviour could correctly identify mTBI[24], [25], as eye movement deficits are present in 38 – 51.3% of mTBI patients[24], and oculomotor behaviour has been shown to correctly identify mTBI in 75.3% of patients[25]. Shteyman *et* al. provide an extensive review of ophthalmic manifestations of mTBI/concussion, highlighting the necessity for more research in this field when considering that 40-90% of TBI sufferers experience eye movement deficits[26]. This is unsurprising as the brain areas that are responsible for eye movements are susceptible to damage from mTBI[26].

Raman spectroscopy is a newly established biochemical technique in the medical field, after being utilised primarily in inorganic materials and physical science environments since the 1960s. Raman spectroscopy harnesses the inelastic scattering of light to characterise the vibrations of molecular bonds in a sample to produce a spectrum of peaks that illustrate the chemical composition. The clinical potential of Raman spectroscopy has been reviewed extensively outlining its increasing application in cancer differentiation, disease detection, assisting surgery[11], [27]–[29], and more recently, in liquid biopsies using blood, urine, tears and saliva[30]–[34].

The use of Raman spectroscopy for liquid biopsies has shown great success, mostly drying samples down onto surfaced-enhanced Raman spectroscopy (SERS) substrates to obtain clinically relevant information[33], [35]–[37]. However, a growing sector is the application of Raman spectroscopy for diagnostics using the eye, by capitalising on the in-built optical system and the neurologically relevant changes at the retina due to its connections within the CNS[38]–[44]. There are many challenges introduced by laser power and tissue damage that prevent *in vitro* testing but, there

are several examples of attempts[45]–[48], and developments in eye models open up opportunities in the near future[49]–[56].

This work contributes to the limited but growing field of eye-based Raman spectroscopy by building a portable near-infrared Raman system for combined with a handheld fundus camera set-up for *in vivo* biochemical and structural diagnostic information without requiring artificial dilation or transport to emergency healthcare centres. In **Chapter 3** a handheld fundus camera system was developed, ready for integration into the 830 nm Raman optical set-up developed herein. An 830 nm excitation wavelength is chosen due to invisibility to the human eye for an improved patient experience from **Chapter 2**, low fluorescent levels in the high wavenumber region[57], and the therapeutic potential that has been explored in literature and discussed in **Chapter 4**[58]**.**

A signal is obtained using the Raman device to confirm low power spectra can be achieved and is then tested on fresh, *ex vivo* porcine retinae and characteristic peaks assigned to a potential injury profile. A 3D printed housing was then designed and built to safely mount all internal components, along with the fibre ports, potentiometer and 830 nm laser for easy handheld use. The integration of a Raspberry Pi-based fundus camera opens up opportunities for integrating spectroscopic data collection and subsequent machine-learning analysis for rapid and intuitive TBI diagnostics to triage patients with high confidence to reduce the number of facilities being used for non-TBI sufferers and increase the number of patients receiving the care they need.

5.2 Choosing Appropriate Filters and Mirrors

The 830 nm Raman spectroscopy set-up was designed to be integrated into the fundus camera developed in **Chapter 3**. Therefore, the mirror and filter specifications must direct the 830 nm laser source to the eye and the Raman scatter to the collection fibre port connected to the spectrometer, whilst allowing the camera path to reach the eye and reflect back to the camera. This setup is illustrated in the schematic diagram **Fig. 5.1a,** where the optical paths were designed to create a portable, handheld system. The set-up is shown on an optical table with all components mounted and hand-aligned in **Fig. 5.1b(i)** without the white LED mounted.

The additional components for Raman spectroscopy include a 50 mW GaAlAs laser diode by Ushio (HL8338MG, ThorLabs), a collimation tube (LTN330-B, ThorLabs), a constant power LD driver (MLD203P2E, ThorLabs), an evaluation board (MLDEVAL, ThorLabs), an ESD Protection and Strain Relief Cable (SR9C-DB9, ThorLabs) and a USB cable (USB-AB-72, Thorlabs), a SMA 600-1050 nm Fibre Port (PAF2S-11B, ThorLabs), and a portable 830 nm spectrometer (QEPRO-Raman-Plus, Ocean Insight). The filters and mirrors include an 830 nm MaxLine laser clean-up filter (LL01-830-12.5, Semrock), a long-pass 805 nm cut-on dichroic mirror (DMLP805, ThorLabs), an 830 nm RazorEdfe dichroic laser beamsplitter (LP02-830RU-25, Semrock) and an 830 nm RazorEdge ultra-steep long-pass edge filter (LP02-830RE-

25, Semrock) which removes the Rayleigh peak. The NoIR camera module view is provided in **Fig. 5.1b(ii),** showing the retinal view using the closed phantom model, the white LED and all of the additional Raman spectroscopy components in place.

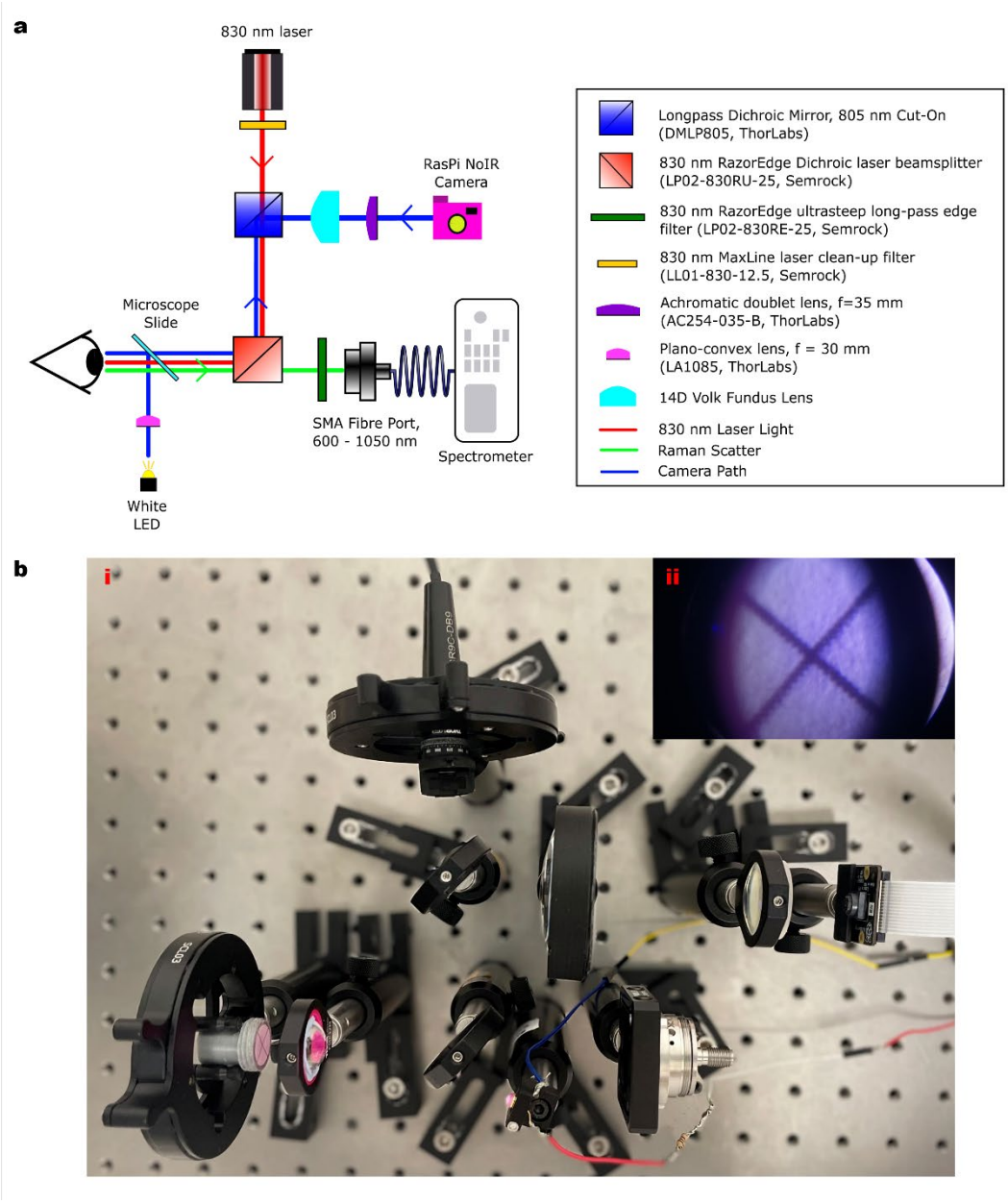

Figure 5.1. ***a*** *Schematic diagram of the full 830 nm portable Raman system with integrated fundus camera. The diagram features part number and specifications for all the lenses and mirrors chosen. Not to scale.* ***b*** ***(i)*** *Optical table set-up of the 830 nm portable Raman system with integrated fundus camera. All components mounted and hand-aligned.* ***(ii)*** *NoIR camera view of the crosshairs at the retinal location through the phantom eye model, following the path dictated by the dichroic mirrors and illuminated with the white LED.*

5.3 Optimising Alignment

Building the portable Raman set-up onto the optical table allows for fast adjustments but makes alignment more difficult. Fundus camera alignment is simple and easy to determine, as a focused image of the retinal crosshairs is produced on the 7”

touchscreen module connected to the NoIR camera module. However, for the 830 nm laser to be aligned, it must pass through the centre of the cornea and lens, reach the retinal sample holder, and scatter from the eye to the collection fibre port opposite the eye. By connecting a red laser to the back of the fibre port, the beam path mimics the Raman scatter, mapping the alignment. This process is illustrated in **Fig. 5.2a**, the 830 nm laser points near the centre of the crosshairs, and the red laser from the fibre port hits the same spot. **Fig. 5.2b** provides an external view of this overlap with an Andonstar x500 endoscope microscope camera.

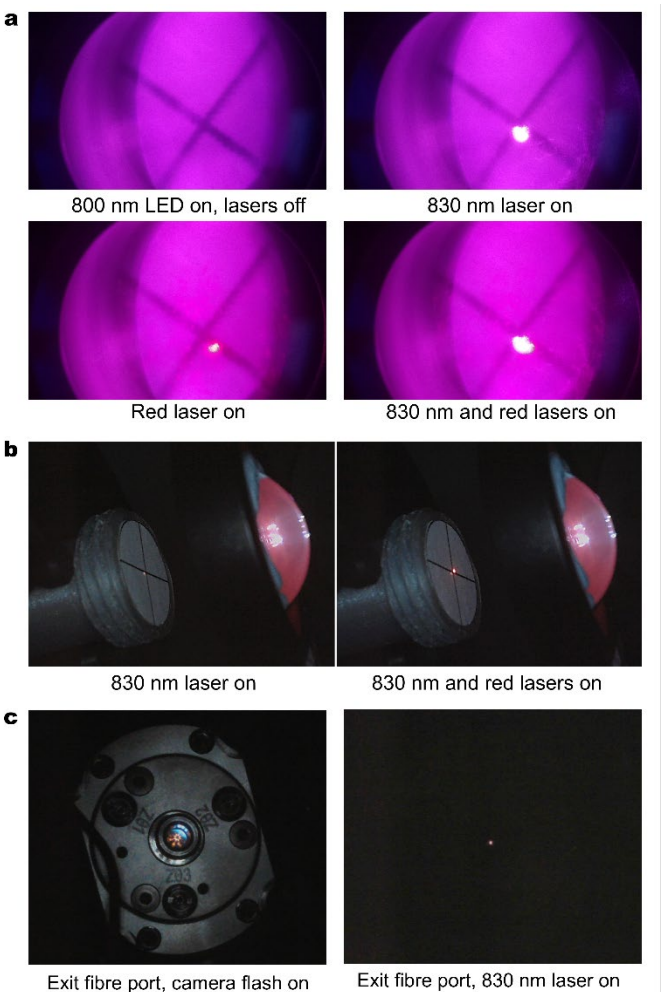

Figure 5.2. NoIR camera view and external photographs of optical table alignment methods used. Open phantom eye model used to align then replaced with the closed model to better mimics the patient's eye. 800 nm LED utilised to illuminate the crosshairs so white LED could be mounted. ***a*** *NoIR camera view of the retinal crosshairs. Red laser is connected to the fibre port which collects Raman scatter to mimic the Raman scatter path from the retina to spectrometer. The 830 nm source laser reaches the centre of the retinal crosshairs and the red laser "exit path" hits the same point.* ***b*** *Alternative external view the 830 nm source laser and red exit laser hitting the centre of the crosshairs.* ***c*** *Microscope camera view of the back side of the fibre port where the Raman scatter is fed into the spectrometer. The crosshairs were replaced with a silicon wafer in the retina location. Left shows the fibre port with flashlight, right shows the 830 nm source laser reflected from the silicon in the phantom eye model and shining through the fibre port, showing alignment.*

When the retinal crosshairs are replaced with a silicon wafer, much more laser light is reflected, increasing the intensity of the Raman scatter reaching the fibre port. So when a silicon wafer is used in the retinal sample holder and the 830 nm laser power is increased, the scatter can be seen passing through the fibre port using the

microscope camera, as shown in **Fig. 5.2c.** Once this is achieved, we can expect a signal of 830 nm laser when the spectrometer is connected, and then optimise alignment further by maximising the spectrometer counts.

Before optimised alignment, the portable spectrometer was connected to the Raman system using an optical fibre attached to the fibre port, and spectrometer was also connected to a laptop with the OceanView software. In this alignment, the spectrometer was saturated when the Rayleigh and laser-line filters (green and yellow filters in **Fig. 5.1a**) were removed (shown in **Fig. 5.3a(i)**), and when only the laser-line filter was removed (**Fig. 5.3a(ii)**), but had no signal when both filters were in place (**Fig. 5.3a(iii)**); here the laser power was set to 0.51 mW and spectra had 100 ms acquisition times. Optimised alignment was then determined by maximising the Rayleigh peak. If the spectrometer was saturated, the acquisition time was decreased, and the process was repeated.

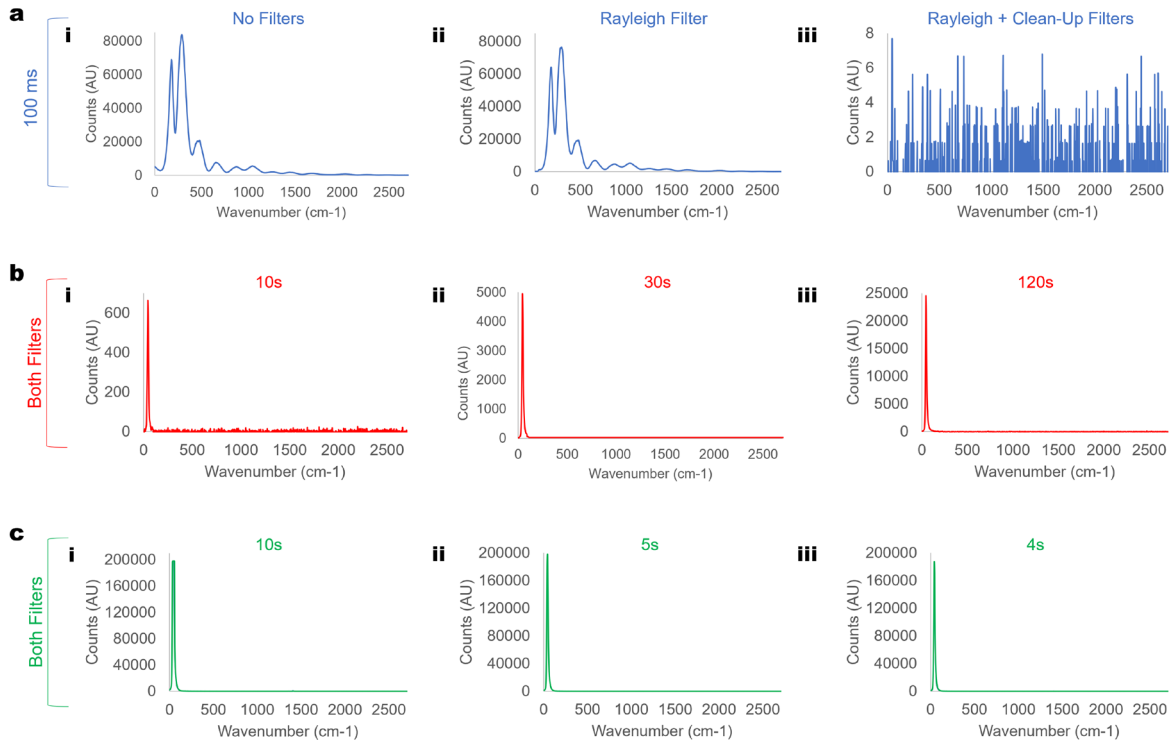

Figure 5.3. First signal detected from the portable Raman set-up using the Ocean Insight 830 nm spectrometer and OceanView software. 830 nm laser diode set to 0.78 mW. Where AU is Arbitrary Units. ***a*** *100 ms acquisition time using silicon wafer as a sample, with* ***(i)*** *ultra-steep longpass Rayleigh filter (LP02-830RE-25, Semrock) and laser clean-up filter (LL01-830-12.5, Semrock) removed.* ***(ii)*** *Only Rayleigh filter present.* ***(iii)*** *Both Rayleigh filter and clean-up filter present.* ***b*** *Still utilising silicon wafer as a sample, both Rayleigh and clean-up filters present, and increasing acquisition times of* ***(i)*** *10 seconds.* ***(ii)*** *30 seconds.* ***(iii)*** *120 seconds.* ***c*** *Realigned system with Rayleigh and clean-up filters present. Ink on silicon wafer used as sample. Saturation (20,000 counts) of the Rayleigh peak occurred above 4 seconds but with no other spectral information, shown with acquisition times of* ***(i)*** *10 seconds* ***(ii)*** *5 seconds* ***(iii)*** *4 seconds.*

Once this was completed with the minimum acquisition time of 4 µs, the silicon wafer sample was replaced with an ink-covered silicon wafer. **Fig. 5.3b** demonstrates the improved counts from the first round of realignment with this method, and some signal is being collected with both filters present, but only the Rayleigh peak is visible with no other spectral information when using increasing acquisition times of **(i)** 10, **(ii)** 30 and

(iii) 120 seconds. However, even when completing a second round of optimised alignment, only the Rayleigh peak was present and the spectrometer was saturating above 4 seconds, as shown in **Fig. 5.3c.** The presence of the saturating Rayleigh peak at such low laser powers not only prevents further alignment and power increase to obtain spectral information, but also suggests that the current Rayleigh filter is not suitable for the set-up, and a replacement should be found to continue alignment.

The current Rayleigh filter is the 830 nm long-pass filter (LP02-830RE-25, Semrock), which has a transmission band = 835.4 – 1872.2 nm and edge wavelength = 832.5 nm. A potential replacement with a higher edge wavelength is the 830 nm EdgeBasic best-value long-pass edge filter (BLP01-830R-25 Semrock) with a transmission band = 853.2-1600 nm and edge wavelength = 846 nm. This was purchased and tested, immediately improving, allowing the 830 nm laser to be increased to a high power of 30 mW to ensure a signal could be obtained. **Fig. 5.4a(i)** shows the first spectrum collected using a silicon wafer in the sample holder of the phantom eye model, with a 120-second acquisition time which would typically be the maximum time a patient would sit for an eye scan, and 4 repeats averaged. This is swapped for ink on silicon in **Fig. 5.4a(ii),** and clear ink peaks can be observed in the 1000 – 1500 cm^{-1} wavenumber region.

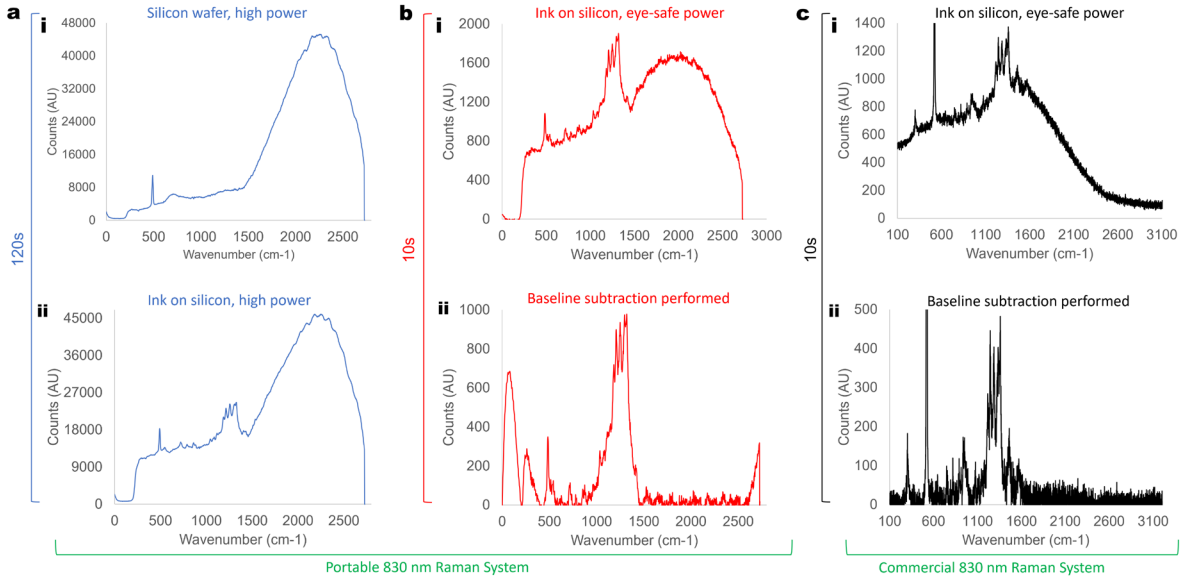

Figure 5.4. First spectra produced by the portable 830 nm Raman set-up using ink on silicon. ***a*** *120 second scan (doesn't saturate and is max. time a patient would probably have a scan), 4 accumulations averaged, 30 mW.* ***(i)*** *Silicon, clear 520 cm-1 silicon peak at 491 cm-1.* ***(ii)*** *Ink on silicon wafer, more spectral information.* ***b*** *Spectra of ink on silicon using the portable Raman system with optimised focus and low power of 1.3 mW. Single spectrum of 10 second acquisition both* ***(i)*** *Raw and* ***(ii)*** *Baseline subtracted.* ***c*** *Comparison spectra of ink on silicon using the Renishaw InVia Raman spectroscopy system with an 830 nm laser at 1.3 mW. Single spectrum of 10 second acquisition using a x20 objective lens, both* ***(i)*** *Raw and* ***(ii)*** *Baseline subtracted.*

Once the new Rayleigh filter was shown to make a large improvement, the system was realigned for a final time using the maximised Rayleigh peak method. A single spectrum of 10-second acquisition time was collected of ink on silicon with a laser wavelength of 1.3 mW to mimic a low power system suitable for the eye at a realistic measurement time, **Fig. 5.4b(i)** shows the raw data collected, whilst **(ii)** is the spectrum following baseline subtraction. The Renishaw inVia confocal Raman system

with an 830 nm laser was used at similar measurement parameters (1.3 mW power, x20 lens objective, 10-second acquisition) to obtain a single spectrum of the same ink on silicon sample as illustrated in **Fig. 5.4c(i)** and **(ii).** Good agreement is observed between both systems and counts in the 1000-1500 cm^{-1} region are even higher than the Renishaw Raman spectrometer following baseline subtraction. Seven characteristic peaks were selected from the Renishaw inVia ink on silicon spectra and an offset was observed when compared to the portable Raman system of 43 ± 8 cm^{-1}, which will be considered in future measurements. The characteristic peaks were assigned based on the Renishaw inVia Raman shift values and are provided in **Table 5.1.**

Table 5.1. Characteristic peaks identified in both spectra of ink on silicon produced by the Renishaw InVia Confocal Raman Spectroscopy system and the portable 830 nm Raman system developed in this chapter. Peaks produced by the portable system are consistently offset by ~ 43 cm^{-1}. Ink peaks are assigned based on the wavenumber location produced by the commercial Renishaw InVia system. ν = stretching; s = symmetric; a = anti-symmetric.

Peak (cm^{-1})		Assignment	Ref.
InVia	**Portable**		
521	484	ν_s(Si)	[59]
1358	1319	$\nu_a(NO^{3-})$	[60]
1334	1294	ν_s(N-O)	[61]
1286	1250	ν_s(C-O)	[62]
1244	1204	ν_s(C-O)	[63]
1241	1182	ν_s(C-N)	[64]
1461	1412	ν_s(CN)	[65]

5.4 Obtaining Fresh *ex vivo Retina Spectra*

Upon achieving successful spectra comparable to that of a commercial Raman spectroscopy system and at parameters suitable for patient use, i.e. low laser power and short acquisition times, the portable Raman set-up and alignment could be deemed optimised, and a 3D printed housing could be built. This housing was simplified at first to determine all of the component mounts were suitable and in the correct position, as shown in **Fig. 5.5a.** The system could then be tested on fresh *ex vivo* porcine retinal samples, with the 830 nm laser diode set to 2.4 mW. Beforehand, a single 30-second acquisition was collected through the closed phantom eye model without the sample holder present to confirm there was no background contribution, produced in **Fig. 5.5b.** 12 best quality retinas were selected, ten 30-second single spectra were collected per retina, and all 120 scans were averaged to produce the raw spectrum in **Fig. 5.5c,** and baseline subtraction was completed in **Fig. 5.5d.** Good spectral information can be seen by eye, without any further post-processing, in the

500-2000 cm-1 fingerprint region but very few peaks seen in the high wavenumber region.

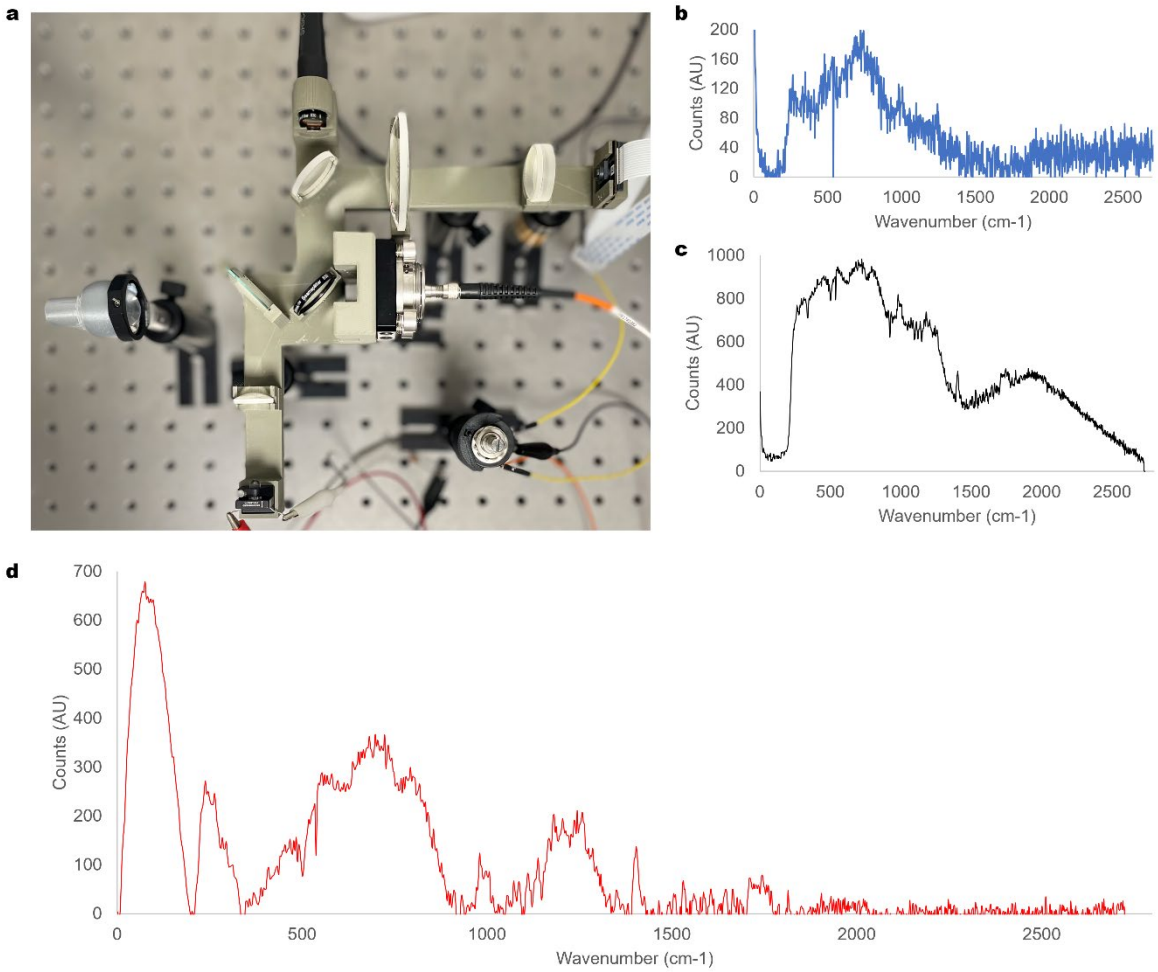

Figure 5.5. ***a*** *Photograph of the final aligned portable Raman system mounted into a 3D printed rig to ensure a consistent and stable set-up.* ***b*** *Single 30 second spectrum obtained using the portable Raman system through the phantom eye model without the sample holder present.* ***c*** *Averaged spectrum of 12 retinal samples, 10 single spectra obtained from each retina of 30 second acquisitions, at 2.4 mW power.* ***d*** *The same averaged spectrum produced in (c) with baseline subtracted. Where AU is Arbitrary Units.*

The Raman spectra of complex retinal tissue collected in this chapter were produced by averaging multiple single measurements, then baseline subtraction, cosmic ray removal and, when relevant, peak picking were carried out within the WiRE 5.2 (Renishaw Plc, Wotton-under-Edge, UK) software of the commercial Raman device, for consistency. Baseline subtraction was completed with a polynomial order of 11. This is a least squares polynomial fit which models a polynomial curve to the lowest points (the baseline) of a raw spectrum, subtracting this curve leaves behind the peaks that sit above any unwanted signal e.g. autofluorescence or noise generated by the detector. The Peak Pick tool is applied to the wavenumbers to select a limited number of best-defined peaks. This scans the x-axis for an increase in intensity above the baseline to determine where peaks can be located based on the threshold settings, which is especially valuable with noisy data that cannot always be visually identified. The slope detection method was utilised with a peak threshold height of 50 counts and width of 25 cm^{-1}, identifying 9 characteristic peaks.

Much like the ink on silicon study, the final averaged spectrum of fresh, *ex vivo* porcine retinae produced by the 830 nm portable Raman system was compared to the Renishaw inVia confocal Raman system, shown in **Fig. 5.6.** The top spectrum produced by the portable Raman system is the same as produced in **Fig. 5.5d**, whilst the bottom spectrum is formed of 28 single spectra of 10 second acquisition time, averaged and baseline subtracted, with the 830 nm laser set to 84 mW. The grey bars represent the position of 9 peaks of interest in the portable Raman retina spectrum, translated down to the Renishaw inVia spectrum which has already been offset by the necessary 43 cm^{-1} error. Overall, there is a clear overlap between the fresh *ex vivo* porcine retinae spectra produced by both 830 nm Raman systems.

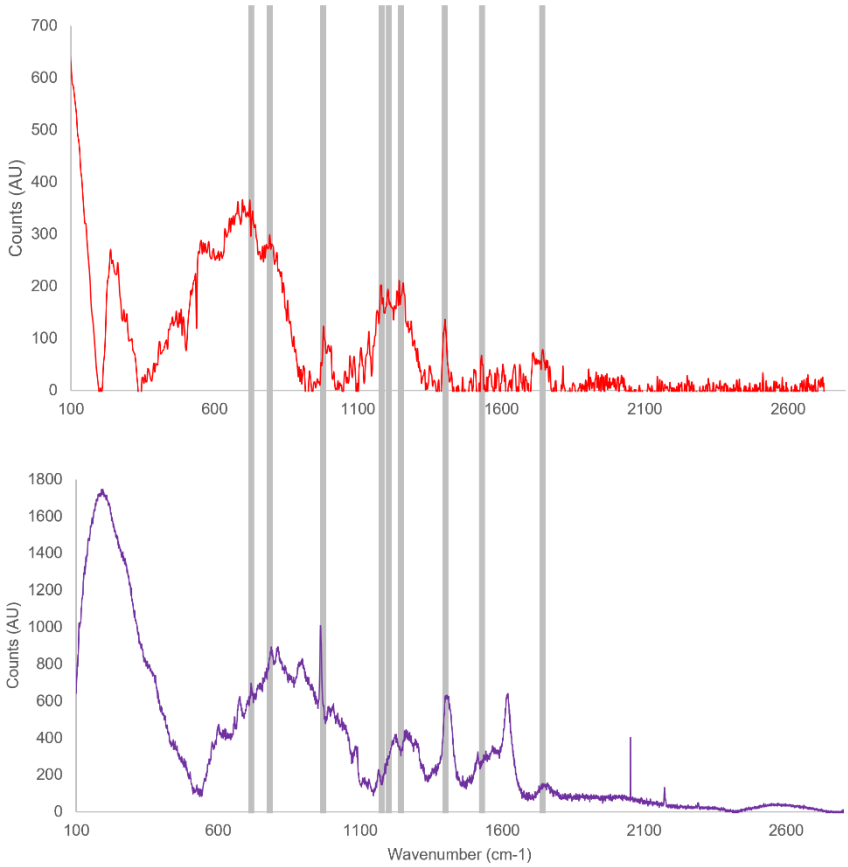

Figure 5.6. ***a*** *Comparison between spectra of fresh porcine retinae obtained by the portable and InVia Raman systems.* ***(top)*** *Averaged spectrum of 12 retinal samples, 10 single spectra obtained from each retina of 30 second acquisitions, at 2.4 mW power.* ***(bottom)*** *830 nm laser set to 84 mW producing 28 single spectra averaged of 10 second acquisitions with baseline subtracted. Where AU is Arbitrary Units. Grey bars highlight the location of peaks of interest that have been assigned in* ***Table 5.2.***

The 9 peaks of interest identified in the fingerprint region have been assigned in **Table 5.2.** In the limited examples of retinal samples investigated using Raman spectroscopy, there is evidence of peaks present near those assigned in this study, using ~ 785 nm excitation wavelengths. Stiebing *et* al. assigned the 1204 cm^{-1} peak in neurodegenerative mouse retina to Rhodopsin, the most abundant protein in rod cells of the retina[66]. Whilst studies looking at the Ganglion Cell Layer GCL identified characteristic peaks at 786 and 1251 cm^{-1}[67], [68]. In a highly comparable study

developing an in-house built Raman system for eye-based measurements, a 1524 cm^{-1} peak was characterised in human retinal samples[43].

Table 5.2. Assigned peaks of interest identified in the spectrum of fresh porcine retinae produced by the 830 nm Raman spectroscopy. Peak wavenumber location was offset by + 43 ± 8 cm-1, as this is what was observed in **Fig. 5.4.** Peaks were assigned and barcoded in grey in **Fig. 5.6,** to highlight their location and map them onto the Renishaw InVia Raman spectrum produced of the same fresh porcine retinae, to determine the extent of agreement. ν = stretching; s = symmetric; a = anti-symmetric.

Peak (cm^{-1})	Assignment	Ref.
723	ν_s(C-S)	[69]
793	δ(C$_3$-O-H)	[70]
980	ν_s(C-H) lipid group	[71]
1182	Amide III protein group	[71]
1205	τ(CH$_2$)	[70]
1244	δ(=CH)	[71]
1403	δ(CH$_2$), τ(CH$_2$)	[72]
1531	ν_s(C=N)	[70]
1756	ν_s(CO$_2$)	[62]

5.5 Creating the 3D Printed Housing

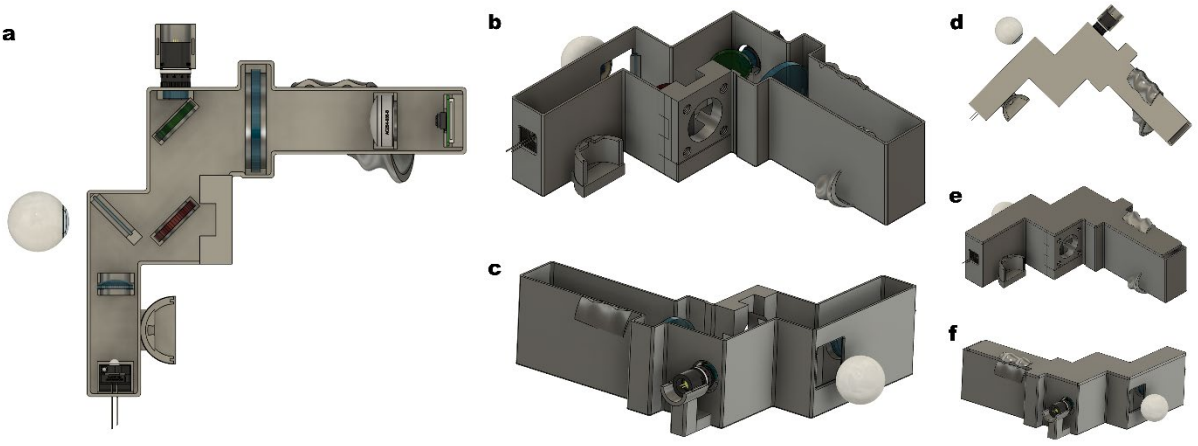

Figure 5.7. Renderings of the 3D printed housing of the 830 nm portable Raman system with integrated fundus camera and an eye model in the patient position. ***a.*** *Top view without the lid to expose the internal components.* ***b.*** *Isometric view without the lid present, highlighting the potentiometer slot and fibre port mount where the Raman scatter is collected.* ***c.*** *Back view without the lid present, showing the patient's eye location and the laser entrance and mount.* ***d.*** *Top view with lid present, showing the ergonomic grips added for hand guidance and comfort.* ***e.*** *Isometric view with lid present, showing the small gap between the lid end and edge of device to allow the NoIR camera ribbon to exit.* ***f.*** *Back view with lid present, showing another view of the ergonomic grips for user comfort.*

Once the dual Raman spectroscopy and fundus imaging systems were functioning in the optimised set-up, the basic 3D mounts could be developed into a first working prototype. We knew the mounts were appropriate for positioning and fixing the components into place, the next considerations were towards blocking out external

light and making the design handheld. Alongside functionality, commercial considerations were important, such as miniaturising the design as much as possible, not only to increase suitability for PoC use but also, to reduce the 3D printing time and amount of material used, to bring down costs and maximise production. 3D renderings of the initial working prototype are shown in **Fig. 5.7,** with the lid removed to expose all necessary components, and the lid in place to demonstrate the closed design.

The 3D-printed working prototype is presented in **Fig. 5.8,** demonstrating the placement of the potentiometer and exit fibre port. This was printed using Fused Filament Fabrication (FFF) of 1.75 mm Green Grey Matt Polylactic Acid (PLA) (183-0245, RS) on a Prusa i3 MK3S+ 3D printer. The entire system requires two printing runs, taking 18 hours and 43 minutes in total, and 143 g of filament. The design was made in consideration of requiring as little support material to be removed as possible. With all components in place, the 830 nm portable Raman system weighs ~ 416 grams and has 187.9 x 183.9 x 67.8 mm dimensions.

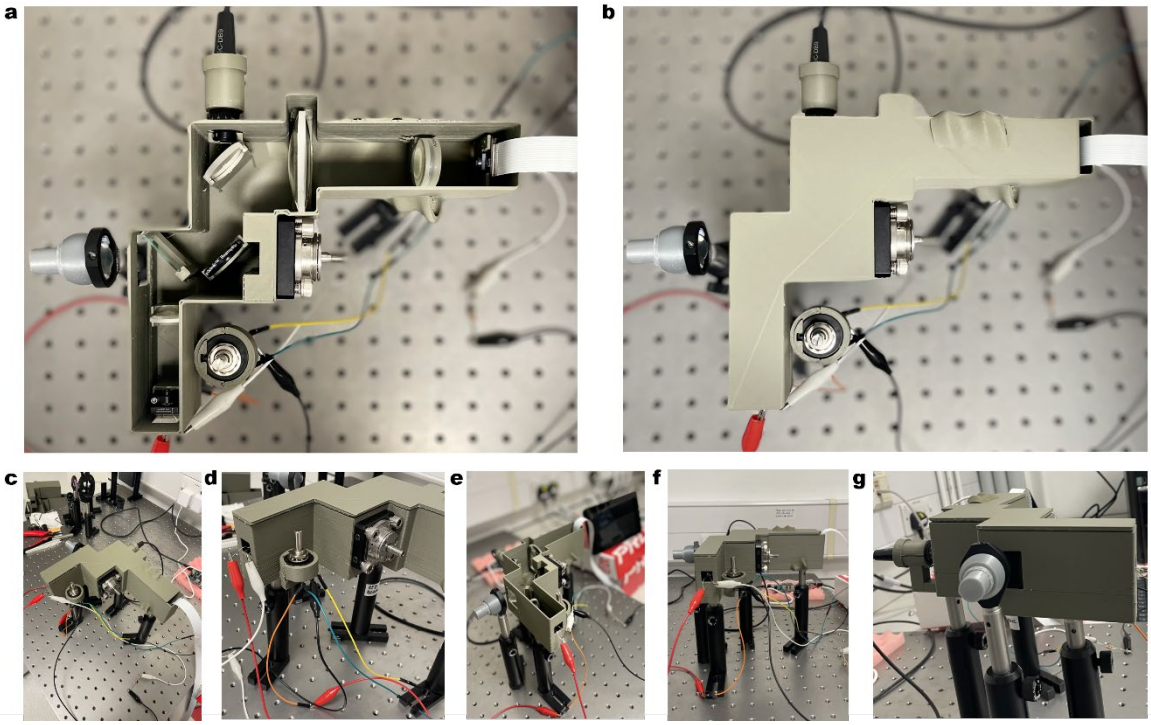

Figure 5.8. Photographs of the final 830 nm Portable Raman device, housing 3D printed using PLA. ***a.*** *Top view without lid to expose all of the internal components.* ***b.*** *Top view with lid present to demonstrate closed housing. This is how the device would be sealed to prevent components being shifted or debris entering the system.* ***c.*** *Isometric view of the system with the lid present.* ***d.*** *Closer isometric view highlighting how the potentiometer is fixed to the system and how the fibre port is attached* ***e.*** *Back isometric view without the lid present.* ***f.*** *Side view of the white LED location and wiring to the Raspberry Pi.* ***g.*** *Back view showing the patient's eye slot and the side of the 830 nm laser.*

Alongside functionality and portability, the user experience is vital when considering medical device commercialisation. Fundus imaging provides not only structural diagnostic information but also a visible target to aid healthcare providers in aiming and focusing the portable system. Design-wise, the external 3D housing had ergonomic hand grips added to guide where to hold the device and improve comfort, as demonstrated in **Fig. 5.9.**

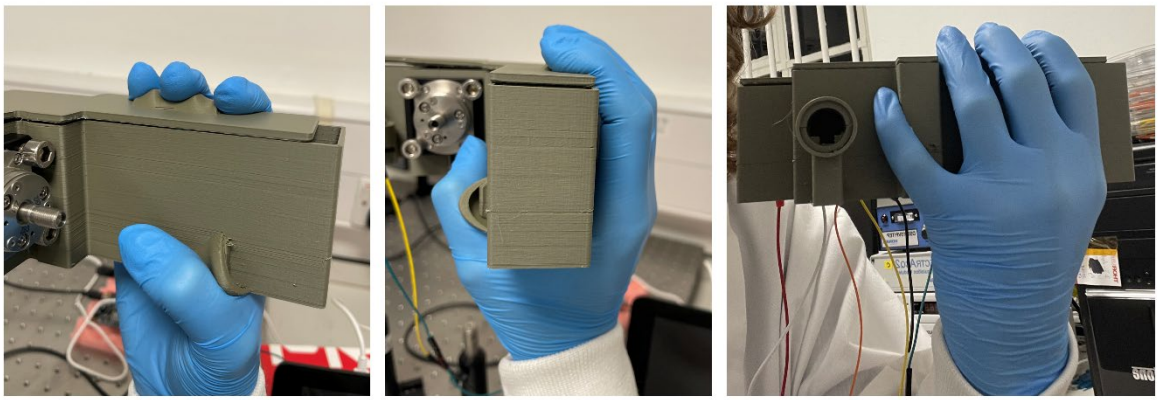

Figure 5.9. Photographs demonstrating how the 830 nm portable Raman system is handheld, with ergonomic grips to guide the hand position and provide user comfort. ***(left)*** *The side view of a hand utilising the grips.* ***(middle)*** *The end view of the hand holding the grips.* ***(right)*** *The back side view of the hand holding the grips, the circular aperture is where the 830 nm laser is mounted.*

The external additions to the 830 nm Portable Raman system include the portable spectrometer, the 7” touchscreen module and the laptop for data processing. There is an optional keyboard and mouse connected to the Raspberry Pi touchscreen to aid with development but is not necessary for use of the current final system. The entire set-up is shown in **Fig. 5.10.** Suggestions for the next steps that could be taken to improve the entire set-up, by making all components handheld and removing the need for a laptop are outlined in **Section 7.2.**

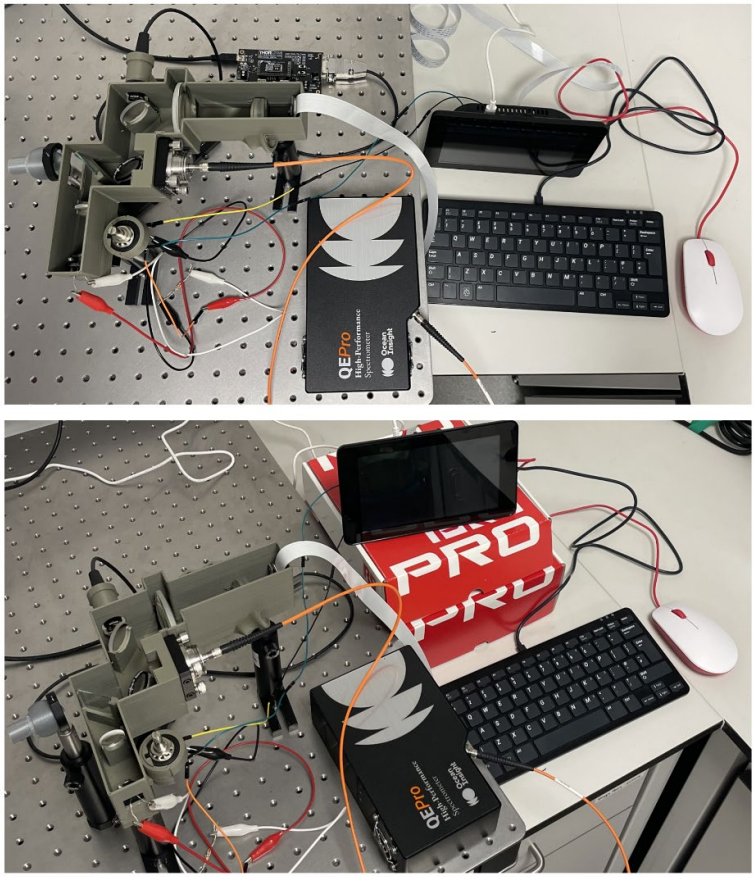

Figure 5.10. Birdseye view photographs of the 830 nm portable Raman system, with the 3D printed housing of the internal components, along with the spectrometer (QEPro), 7” touchscreen module with Raspberry Pi 4 attached and optional keyboard and mouse.

5.6 Conclusion

In this chapter, a working prototype of the 830 nm portable Raman system was achieved with integrated handheld fundus imaging, built upon a Raspberry Pi module for complete telemedicine applications. Fine-tuned alignment was achieved both on the optical table and within 3D printed mounts to obtain spectra from fresh, *ex vivo* porcine retinae for which characteristic peaks were assigned.

A 3D printed housing was CAD designed for secure mounting of all the internal and external optical components, along with the reduction of stray light and an optimal user experience both for the patient and healthcare provider. Looking towards commercialisation, it would be appropriate to discuss needs and desirables with ophthalmologists, to determine how accessible the current device design is and how to best assess patients, whether this be with a chinrest or a non-contact method of alignment such as a focal point for patients to position themselves with.

In collaboration with Dstl and PBL, the first concrete stages have been completed towards the development of an improved eye model for which the portable Raman devices can be tested, with the potential to spike the blood used within the perfusion system with TBI biomarkers or source from TBI patients, for a complete translational platform. The continued success of this project, alongside continued progress with the cell damage study established in **Section 4.7,** would allow for informed modifications to be made to the laser system to ensure the device adheres to laser safety regulations, whilst producing sufficient spectral information and providing a comfortable patient experience.

The groundwork laid in this chapter will not only aid the millions of people affected by TBI around the world, either suffering themselves, supporting a loved one with the condition or through being a healthcare provider, but also change the way neurodegenerative diseases and disorders are accessed. This will increase knowledge of disease development to improve how patients are diagnosed, treated, and rehabilitated, allowing for better patient autonomy and work environments for healthcare professionals.

5.7 References

[1] M. D. Wiles, “Management of traumatic brain injury: a narrative review of current evidence,” *Anaesthesia*, vol. 77 Suppl 1, no. S1, pp. 102–112, Jan. 2022, doi: 10.1111/ANAE.15608.

[2] C. Oris, S. Kahouadji, J. Durif, D. Bouvier, and V. Sapin, “S100B, Actor and Biomarker of Mild Traumatic Brain Injury,” *Int. J. Mol. Sci.*, vol. 24, no. 7, Apr. 2023, doi: 10.3390/IJMS24076602.

[3] A. I. R. Maas and D. K. Menon, “Traumatic brain injury: integrated approaches to improve prevention, clinical care, and research,” *Lancet Neurol.*, vol. 16, no. 12, pp. 987–1048, Dec. 2017, doi: 10.1016/S1474-4422(17)30371-X.

[4] D. Pavlovic, S. Pekic, M. Stojanovic, and V. Popovic, “Traumatic brain injury: neuropathological, neurocognitive and neurobehavioral sequelae,” *Pituitary*, vol. 22, no. 3, 2019, doi: 10.1007/S11102-019-00957-9.

[5] D. Najem *et al.*, “Traumatic brain injury: Classification, models, and markers,” *Biochem. Cell Biol.*, vol. 96, no. 4, pp. 391–406, 2018, doi: 10.1139/bcb-2016-0160.

[6] A. J. Fox, H. L. Filmer, and P. E. Dux, “The influence of self-reported history of mild traumatic brain injury on cognitive performance,” *Sci. Rep.*, vol. 12, no. 1, pp. 1–12, Oct. 2022, doi: 10.1038/s41598-022-21067-w.

[7] Z. Habli, F. Kobeissy, and M. L. Khraiche, “Advances in point-of-care platforms for traumatic brain injury: recent developments in diagnostics,” *Rev. Neurosci.*, vol. 33, no. 3, pp. 327–345, Apr. 2022, doi: 10.1515/REVNEURO-2021-0103/ASSET/GRAPHIC/J_REVNEURO-2021-0103_FIG_006.JPG.
[8] E. Hillman, “Optical brain imaging in vivo: techniques and applications from animal to man,” *J. Biomed. Opt.*, vol. 12, no. 5, p. 051402, 2007, doi: 10.1117/1.2789693.
[9] A. Ercole *et al.*, “Current and emerging technologies for probing molecular signatures of traumatic brain injury,” *Front. Neurol.*, vol. 8, Aug. 2017, doi: 10.3389/fneur.2017.00450.
[10] H. S. Ghaith *et al.*, “A Literature Review of Traumatic Brain Injury Biomarkers,” *Mol. Neurobiol.*, vol. 59, no. 7, pp. 4141–4158, Apr. 2022, doi: 10.1007/S12035-022-02822-6.
[11] Y. Khristoforova, L. Bratchenko, and I. Bratchenko, “Raman-Based Techniques in Medical Applications for Diagnostic Tasks: A Review,” *Int. J. Mol. Sci.*, vol. 24, no. 21, Nov. 2023, doi: 10.3390/IJMS242115605.
[12] M. Edalatfar *et al.*, “Biofluid Biomarkers in Traumatic Brain Injury: A Systematic Scoping Review,” *Neurocrit. Care*, vol. 35, no. 2, pp. 559–572, Oct. 2021, doi: 10.1007/S12028-020-01173-1.
[13] K. K. Wang *et al.*, “An update on diagnostic and prognostic biomarkers for traumatic brain injury,” *Expert Rev. Mol. Diagn.*, vol. 18, no. 2, pp. 165–180, Feb. 2018, doi: 10.1080/14737159.2018.1428089.
[14] A. Jeromin and R. Bowser, “Biomarkers in Neurodegenerative Diseases,” in *Advances in Neurobiology*, vol. 15, Springer New York LLC, 2017, pp. 491–528.
[15] O. Hansson, “Biomarkers for neurodegenerative diseases,” *Nat. Med. 2021 276*, vol. 27, no. 6, pp. 954–963, Jun. 2021, doi: 10.1038/s41591-021-01382-x.
[16] N. H. Johnson *et al.*, “Inflammatory Biomarkers of Traumatic Brain Injury,” *Pharmaceuticals (Basel).*, vol. 15, no. 6, p. 660, May 2022, doi: 10.3390/PH15060660.
[17] L. P. Evans *et al.*, “Acute vitreoretinal trauma and inflammation after traumatic brain injury in mice,” *Ann. Clin. Transl. Neurol.*, vol. 5, no. 3, pp. 240–251, Mar. 2018, doi: 10.1002/acn3.523.
[18] N. Marchesi, F. Fahmideh, F. Boschi, A. Pascale, and A. Barbieri, “Ocular Neurodegenerative Diseases: Interconnection between Retina and Cortical Areas,” *Cells*, vol. 10, no. 9, Sep. 2021, doi: 10.3390/CELLS10092394.
[19] P. Colligris, M. Jesus Perez De Lara, B. Colligris, and J. Pintor, “Ocular Manifestations of Alzheimer’s and Other Neurodegenerative Diseases: The Prospect of the Eye as a Tool for the Early Diagnosis of Alzheimer’s Disease,” *J. Ophthalmol.*, vol. 2018, pp. 1–12, 2018, doi: 10.1155/2018/8538573.
[20] G. Guidoboni *et al.*, “Neurodegenerative Disorders of the Eye and of the Brain: A Perspective on Their Fluid-Dynamical Connections and the Potential of Mechanism-Driven Modeling,” *Front. Neurosci.*, vol. 14, p. 1173, Nov. 2020, doi: 10.3389/FNINS.2020.566428/BIBTEX.
[21] F. Z. Javaid, J. Brenton, L. Guo, and M. F. Cordeiro, “Visual and Ocular Manifestations of Alzheimer’s Disease and Their Use as Biomarkers for Diagnosis and Progression,” *Front. Neurol.*, vol. 7, p. 55, 2016, doi: 10.3389/fneur.2016.00055.
[22] H. M. Kersten, R. H. Roxburgh, and H. V. Danesh-Meyer, “Ophthalmic manifestations of inherited neurodegenerative disorders,” *Nat. Rev. Neurol. 2014 106*, vol. 10, no. 6, pp. 349–362, May 2014, doi: 10.1038/nrneurol.2014.79.
[23] D. Romaus-Sanjurjo *et al.*, “Alzheimer’s Disease Seen through the Eye: Ocular Alterations and Neurodegeneration,” *Int. J. Mol. Sci. 2022, Vol. 23, Page 2486*, vol. 23, no. 5, p. 2486, Feb. 2022, doi: 10.3390/IJMS23052486.
[24] R. Mani, L. Asper, and S. K. Khuu, “Deficits in saccades and smooth-pursuit eye movements in adults with traumatic brain injury: a systematic review and meta-analysis,” *Brain Inj.*, vol. 32, no. 11, pp. 1315–1336, Sep. 2018, doi: 10.1080/02699052.2018.1483030.
[25] M. Hunfalvay, N. P. Murray, C. M. Roberts, A. Tyagi, K. W. Barclay, and F. R. Carrick, “Oculomotor Behavior as a Biomarker for Differentiating Pediatric Patients With Mild Traumatic Brain Injury and Age Matched Controls,” *Front. Behav. Neurosci.*, vol. 14, no. 581819, Nov. 2020, doi: 10.3389/fnbeh.2020.581819.
[26] A. Shteyman and B. M. DeBroff, “Ophthalmic Manifestations, Evaluation, and Guidelines for Testing of Concussion,” *Open Ophthalmol. J.*, vol. 17, no. 1, Jan. 2023, doi: 10.2174/18743641-V17-E230111-2022-43.
[27] Y. Wang, X. Gu, and Y. Chen, “Advances in multi-modal non-invasive imaging techniques in the diagnosis and treatment of polypoidal choroidal vasculopathy,” *Front. Med.*, vol. 10, 2023, doi: 10.3389/FMED.2023.1221846.
[28] C. Delrue, R. Speeckaert, M. Oyaert, S. De Bruyne, and M. M. Speeckaert, “From Vibrations to Visions: Raman Spectroscopy’s Impact on Skin Cancer Diagnostics,” *J. Clin. Med.*, vol. 12, no. 23, Dec. 2023, doi: 10.3390/JCM12237428.
[29] Q. U. A. Virani, H. Fatima Aziz, and S. Shamim, “Raman Spectroscopy: Can It Change The Future Of Brain Tumour Surgery?s,” *J. Pak. Med. Assoc.*, vol. 73, no. 11, pp. 2291–2292, 2023, doi: 10.47391/JPMA.23-96.
[30] K. Kong, C. Kendall, N. Stone, and I. Notingher, “Raman spectroscopy for medical diagnostics - From in-vitro biofluid assays to in-vivo cancer detection,” *Adv. Drug Deliv. Rev.*, vol. 89, pp. 121–134, Jul. 2015, doi: 10.1016/j.addr.2015.03.009.
[31] S. Aitekenov *et al.*, “Raman, Infrared and Brillouin Spectroscopies of Biofluids for Medical Diagnostics and for Detection of Biomarkers,” *Crit. Rev. Anal. Chem.*, vol. 53, no. 7, pp. 1561–1590, 2023, doi: 10.1080/10408347.2022.2036941.

[32] P. Giamougiannis *et al.*, “A comparative analysis of different biofluids towards ovarian cancer diagnosis using Raman microspectroscopy,” *Anal. Bioanal. Chem.*, vol. 413, no. 3, pp. 911–922, Jan. 2021, doi: 10.1007/S00216-020-03045-1/FIGURES/4.
[33] H. J. Koster, A. Guillen-Perez, J. S. Gomez-Diaz, M. Navas-Moreno, A. C. Birkeland, and R. P. Carney, “Fused Raman spectroscopic analysis of blood and saliva delivers high accuracy for head and neck cancer diagnostics,” *Sci. Reports 2022 121*, vol. 12, no. 1, pp. 1–13, Nov. 2022, doi: 10.1038/s41598-022-22197-x.
[34] Y. V. Kistenev, A. V. Borisov, A. A. Samarinova, S. Colón-Rodríguez, and I. K. Lednev, “A novel Raman spectroscopic method for detecting traces of blood on an interfering substrate,” *Sci. Reports 2023 131*, vol. 13, no. 1, pp. 1–15, Apr. 2023, doi: 10.1038/s41598-023-31918-9.
[35] X. Zhang *et al.*, “Robust and Universal SERS Sensing Platform for Multiplexed Detection of Alzheimer’s Disease Core Biomarkers Using PAapt-AuNPs Conjugates,” *ACS Sensors*, vol. 4, no. 8, pp. 2140–2149, 2019, doi: 10.1021/acssensors.9b00974.
[36] F. Dell’olio, “Multiplexed Liquid Biopsy and Tumor Imaging Using Surface-Enhanced Raman Scattering,” *Biosens. 2021, Vol. 11, Page 449*, vol. 11, no. 11, p. 449, Nov. 2021, doi: 10.3390/BIOS11110449.
[37] H. Noothalapati, K. Iwasaki, and T. Yamamoto, “Non-invasive diagnosis of colorectal cancer by Raman spectroscopy: Recent developments in liquid biopsy and endoscopy approaches,” *Spectrochim. Acta Part A Mol. Biomol. Spectrosc.*, vol. 258, p. 119818, Sep. 2021, doi: 10.1016/J.SAA.2021.119818.
[38] J. Li *et al.*, “Harnessing the power of Raman spectroscopic imaging for ophthalmology,” *Front. Chem.*, vol. 11, p. 1211121, May 2023, doi: 10.3389/FCHEM.2023.1211121/BIBTEX.
[39] S. Alba-Arbalat *et al.*, “In Vivo Molecular Changes in the Retina of Patients With Multiple Sclerosis,” *Invest. Ophthalmol. Vis. Sci.*, vol. 62, no. 6, pp. 11–11, May 2021, doi: 10.1167/IOVS.62.6.11.
[40] R. J. Erckens, F. H. M. Jongsma, J. P. Wicksted, F. Hendrikse, W. F. March, and M. Motamedi, “Raman spectroscopy in ophthalmology: From experimental tool to applications in vivo,” *Lasers in Medical Science*, vol. 16, no. 4. Springer London, pp. 236–252, 2001, doi: 10.1007/PL00011360.
[41] R. J. Erckens *et al.*, “Noninvasive Raman spectroscopic identification of intraocular lens material in the living human eye,” *J. Cataract Refract. Surg.*, vol. 27, no. 7, pp. 1065–1070, Jul. 2001, doi: 10.1016/S0886-3350(00)00828-2.
[42] C. C. Lin, M. T. Kuo, and H. C. Chang, “Review: Raman spectroscopy - A novel tool for noninvasive analysis of ocular surface fluid,” *J. Med. Biol. Eng.*, vol. 30, no. 6, pp. 343–354, 2010, doi: 10.5405/JMBE.846.
[43] C. Stiebing *et al.*, “Nonresonant Raman spectroscopy of isolated human retina samples complying with laser safety regulations for in vivo measurements,” *Neurophotonics*, vol. 6, no. 04, p. 1, Sep. 2019, doi: 10.1117/1.nph.6.4.041106.
[44] B. Li *et al.*, “Imaging lutein and zeaxanthin in the human retina with confocal resonance Raman microscopy,” *Proc. Natl. Acad. Sci.*, vol. 117, no. 22, pp. 12352–12358, Jun. 2020, doi: 10.1073/PNAS.1922793117.
[45] W. Gellermann, I. V. Ermakov, M. R. Ermakova, R. W. McClane, D.-Y. Zhao, and P. S. Bernstein, “In vivo resonant Raman measurement of macular carotenoid pigments in the young and the aging human retina,” *J. Opt. Soc. Am. A*, vol. 19, no. 6, p. 1172, Jun. 2002, doi: 10.1364/josaa.19.001172.
[46] I. V. Ermakov, M. R. Ermakova, and W. Gellermann, “Simple raman instrument for in vivo detection of macular pigments,” *Appl. Spectrosc.*, vol. 59, no. 7, pp. 861–867, Jul. 2005, doi: 10.1366/0003702054411616.
[47] R. Sentosa *et al.*, “Towards in vivo molecular imaging of the retina: OCT-guided Raman spectroscopy,” *Invest. Ophthalmol. Vis. Sci.*, vol. 64, no. 8, pp. 2918–2918, Jun. 2023.
[48] P. S. Bernstein, M. D. Yoshida, N. B. Katz, R. W. McClane, and W. Gellermann, “Raman detection of macular carotenoid pigments in intact human retina,” *Investig. Ophthalmol. Vis. Sci.*, vol. 39, no. 11, pp. 2003–2011, 1998, Accessed: Jan. 29, 2021. [Online]. Available: https://iovs.arvojournals.org/article.aspx?articleid=2161540.
[49] J. W. Zhang, D. Chan, and J. M. Sivak, “A Novel ex-vivo Model for Studying Early Pressure-Induced Retinal and Optic Nerve Head Responses in The Human Eye,” *Invest. Ophthalmol. Vis. Sci.*, vol. 63, no. 7, pp. 923-A0392-923 – A0392, Jun. 2022.
[50] J. Kralik, M. van Wyk, B. Leonardon, G. Schilardi, S. Schneider, and S. Kleinlogel, “The Bovine Ex Vivo Retina: A Versatile Model for Retinal Neuroscience,” *Invest. Ophthalmol. Vis. Sci.*, vol. 64, no. 11, Aug. 2023, doi: 10.1167/IOVS.64.11.29.
[51] P. Wright, J. Sanderson, J. Kelsall, and G. Healing, “Development of an Ex Vivo Human Retina Model for Assessment of Retinotoxicity,” *Invest. Ophthalmol. Vis. Sci.*, vol. 56, no. 7, pp. 2475–2475, Jun. 2015.
[52] S. Schnichels *et al.*, “Retinal Organ Cultures as Alternative Research Models,” *ATLA Altern. to Lab. Anim.*, vol. 47, no. 1, pp. 19–29, Mar. 2019, doi: 10.1177/0261192919840092/ASSET/IMAGES/LARGE/10.1177_0261192919840092-FIG3.JPEG.
[53] J. Schaeffer, C. Delpech, F. Albert, S. Belin, and H. Nawabi, “Adult Mouse Retina Explants: From ex vivo to in vivo Model of Central Nervous System Injuries,” *Front. Mol. Neurosci.*, vol. 13, p. 599948, Nov. 2020, doi: 10.3389/FNMOL.2020.599948/BIBTEX.
[54] H. O. Orlans, T. L. Edwards, S. R. De Silva, M. I. Patrício, and R. E. MacLaren, “Human Retinal Explant Culture for Ex Vivo Validation of AAV Gene Therapy,” *Methods Mol. Biol.*, vol. 1715, pp. 289–303, 2018, doi: 10.1007/978-1-4939-7522-8_21.
[55] M. Peng, S. M. Curry, Y. Liu, H. Lohawala, G. Sharma, and T. P. Sharma, “The ex vivo human

translaminar autonomous system to study spaceflight associated neuro-ocular syndrome pathogenesis," *Microgravity*, vol. 8, no. 1, pp. 1–14, Oct. 2022, doi: 10.1038/s41526-022-00232-5.
[56] A. Murali *et al.*, "Retinal explant culture: A platform to investigate human neuro-retina," *Clin. Experiment. Ophthalmol.*, vol. 47, no. 2, pp. 274–285, Mar. 2019, doi: 10.1111/CEO.13434.
[57] J. Ye *et al.*, "Dual-wavelength excitation combined Raman spectroscopy for detection of highly fluorescent samples," *Appl. Opt.*, vol. 60, no. 23, pp. 6918–6927, Aug. 2021, doi: 10.1364/AO.431564.
[58] W. tong Pan, P. miao Liu, D. Ma, and J. jun Yang, "Advances in photobiomodulation for cognitive improvement by near-infrared derived multiple strategies," *J. Transl. Med.*, vol. 21, no. 1, p. 135, Dec. 2023, doi: 10.1186/S12967-023-03988-W.
[59] J. McCarthy, S. Bhattacharya, T. S. Perova, R. A. Moore, H. Gamble, and B. M. Armstrong, "Composition and stress analysis in Si structures using micro-Raman spectroscopy," *Scanning*, vol. 26, no. 5, pp. 235–239, 2004, doi: 10.1002/SCA.4950260504.
[60] J. T. Kloprogge and R. L. Frost, "Raman microscopy study of basic aluminium nitrate," *Spectrochim. Acta Part A Mol. Biomol. Spectrosc.*, vol. 55, no. 1, pp. 163–169, Dec. 1998, doi: 10.1016/S1386-1425(98)00178-4.
[61] D. Shin, Y. S. Choi, and B. H. Hong, "Graphene-Enhanced Raman Spectroscopy Reveals the Controlled Photoreduction of Nitroaromatic Compound on Oxidized Graphene Surface," *ACS Omega*, vol. 3, no. 9, pp. 11084–11087, Sep. 2018, doi: 10.1021/ACSOMEGA.8B01285.
[62] K. I. Hadjiivanov *et al.*, "Power of Infrared and Raman Spectroscopies to Characterize Metal-Organic Frameworks and Investigate Their Interaction with Guest Molecules," *Chem. Rev.*, vol. 121, no. 3, pp. 1286–1424, Feb. 2021, doi: 10.1021/ACS.CHEMREV.0C00487.
[63] L. E. Eijsink *et al.*, "In Situ EPR and Raman Spectroscopy in the Curing of Bis-Methacrylate-Styrene resins Supporting information," 2022.
[64] G. Niaura, R. Mažeikiene, and A. Malinauskas, "Structural changes in conducting form of polyaniline upon ring sulfonation as deduced by near infrared resonance Raman spectroscopy," *Synth. Met.*, vol. 145, no. 2–3, pp. 105–112, Sep. 2004, doi: 10.1016/J.SYNTHMET.2004.04.010.
[65] M. Chauhan, C. Maddi, A. Jha, V. Subramanian, and P. Valdastri, "Characterization of Urease enzyme using Raman and FTIR Spectroscopy," *Biophotonics Congr. Opt. Life Sci. Congr. 2019 (2019), Pap. JT4A.46*, vol. Part F168-BODA 2019, p. JT4A.46, Apr. 2019, doi: 10.1364/BODA.2019.JT4A.46.
[66] C. Stiebing *et al.*, "Biochemical Characterization of Mouse Retina of an Alzheimer's Disease Model by Raman Spectroscopy," *ACS Chem. Neurosci.*, vol. 11, no. 20, pp. 3301–3308, Oct. 2020, doi: 10.1021/acschemneuro.0c00420.
[67] M. Marro *et al.*, "Dynamic molecular monitoring of retina inflammation by in vivo Raman spectroscopy coupled with multivariate analysis," *J. Biophotonics*, vol. 7, no. 9, pp. 724–734, 2014, doi: 10.1002/jbio.201300101.
[68] Q. Wang *et al.*, "Exploring Raman spectroscopy for the evaluation of glaucomatous retinal changes," *https://doi.org/10.1117/1.3642010*, vol. 16, no. 10, p. 107006, Oct. 2011, doi: 10.1117/1.3642010.
[69] G. Pezzotti *et al.*, "Raman Probes for In Situ Molecular Analyses of Peripheral Nerve Myelination," *ACS Chem. Neurosci.*, vol. 11, no. 15, pp. 2327–2339, Aug. 2020, doi: 10.1021/ACSCHEMNEURO.0C00284.
[70] G. Pezzotti, "Raman spectroscopy in cell biology and microbiology," *J. Raman Spectrosc.*, vol. 52, no. 12, pp. 2348–2443, Dec. 2021, doi: 10.1002/JRS.6204.
[71] S. Ding, "Effects of tissue fixation on Raman spectroscopic characterization of retina," Iowa State University, 2015.
[72] C. Farber *et al.*, "Complementarity of Raman and Infrared Spectroscopy for Structural Characterization of Plant Epicuticular Waxes," *ACS Omega*, vol. 4, no. 2, pp. 3700–3707, Feb. 2019, doi: 10.1021/ACSOMEGA.8B03675/ASSET/IMAGES/LARGE/AO-2018-03675F_0006.JPEG.

Chapter 6

Producing a Spectral Library of the Prospective Biomarkers of Traumatic Brain Injury

In this chapter, an extensive Raman spectral library is produced to provide a reference for researchers in this field. At this stage, the portable eye-based Raman devices are not yet suitable for animal or human testing, therefore cannot confirm the peaks present in spectra obtained from control or trauma *in vivo* retinal samples. As established, the direct links between the retina and brain *via* the optical tract, allow for grounds that TBI biomarkers established in biofluid will undergo a detectable change in the retinae biochemistry. Therefore, it is of interest to characterise prospective TBI biomarkers identified in biofluid using Raman spectroscopy (RS) to aid future injury profiling and to provide spectral information as RS is increasingly implemented in clinical settings.

RS-based detection is used to profile a panel of 18 TBI-indicative biomarkers (human, animal, and synthetically derived) in raw form and in aqueous solution to mimic the structure found in biofluid. The subsequently derived unique spectral reference library, exploiting four excitation lasers of 514, 633, 785, and 830 nm, will aid the development of rapid, non-destructive, and label-free spectroscopy-based neurodiagnostics.

These biomarkers, released during cellular damage, provide additional means of diagnosing TBI and assessing the severity of injury. The spectroscopic profiles of each marker are classed according to their acute, sub-acute, and chronic temporal injury phases and are accompanied by detailed peak assignment tables. The intensity ratios of significant peaks are compared, to assess variance between lasers, with the smallest variance found for UCHL1 ($\sigma^2 = 0.000164$) and the highest for sulfatide ($\sigma^2 = 0.158$). Prospective biomarker spectra are overlayed and traced, modelling the strongest peaks present when obtaining Raman spectra from future TBI samples, which are implemented in spectra from fresh, *ex vivo* porcine retinal samples obtained with the 635 and 830 nm portable, eye-based Raman devices.

Overall, this work paves the way for defining and setting the most appropriate diagnostic time window for detection following brain injury. Further rapid and specific detection of these biomarkers, from easily accessible biofluids, would not only enable the triage of TBI, predict outcomes, indicate the progress of recovery, and save healthcare providers costs, but also cement the potential of Raman-based spectroscopy as a powerful tool for neurodiagnostics.

Acknowledgement of contributing material and authors
Content within this chapter has been published in the following journal paper:

- Harris G, Stickland CA, Lim M, Goldberg Oppenheimer P. Raman Spectroscopy Spectral Fingerprints of Biomarkers of Traumatic Brain Injury. Cells. 2023 Nov 8;12(22):2589. doi: 10.3390/cells12222589. PMID: 37998324; PMCID: PMC10670390.

6.1 Introduction

As established in **Chapter 1**, TBI is a major burden on healthcare services worldwide[1], ranging in severity from mild/moderate concussion to severe and chronic loss of cognitive and motor function [2]. Recent research [3 – 8] has been focusing on establishing the temporal profile of TBIs and the associated biomarkers including their emergence (i.e., acute phase), crucial for early-stage diagnostics, persistence, and decline (sub-acute and chronic phases)—indicative of the longer-term effects and prognosis as well as development of new therapeutics. TBI biomarkers have been shown to have a characteristic timeframe of acute (<24 h), sub-acute (1 day–3 weeks) and chronic (3 weeks–6 months), as the initial insult causes acute damage to the brain, and is typically followed by a biochemical cascade leading to secondary injuries over the following month(s) [9–11]. This indicates that identifying TBI in the acute phase and intervening before further damage occurs is vital for long-term neurological recovery. However, the development of point-of-care (PoC), timely TBI diagnostic technologies remains an unmet need and there is no definite triaging and therapeutic patient pathway [12].

The GCS uses the patient's eye, verbal, and motor responses to enumerate the injury and categorise it as either severe (3–8), moderate (9–12), or mild (13–15) [13], placing pressure on the healthcare provider in making a subjective decision. Neuroimaging will identify skull fractures, hematoma, and haemorrhage to determine if neurosurgery is necessary [2], however, the main challenge lies in the fact that pre-hospital and emergency department (ED) assessment is predominantly based on insensitive GCS and history acquisition with guidance on CT being often vague and costly.

Mild TBI (mTBI), specifically, is often underdiagnosed if not identified rapidly at the point of injury, with 90% of acute cases undetected and not admitted to ED [2,14,15]. Therefore, the development of successful TBI biomarker diagnostics from blood [16], or other biofluids, i.e., cerebrospinal fluid (CSF) [8], saliva [17], urine [18], and tears [19], would lead to improved triage of severe and high-risk injuries and improve outcomes, whilst appropriate classification of low-risk, mTBI patients would support the decision-making of pre-hospital healthcare providers to reduce referral to hospital care, decrease the number of ED visits and allow for the focusing of resources on those who need it the most.

Concurrently, Raman spectroscopy, a rapid, label-free technique has been increasingly used in medical and diagnostic applications for producing non-destructive chemical information [20]. This sensitive vibrational spectroscopy excites molecular bonds within a sample, providing a unique biomolecular spectral fingerprint of target biomarkers in a rapid analytical response [21, 22]. These spectroscopic barcodes have been shown to identify the various diseases from which the biofluid has been collected, such as blood [23,24], CSF [25, 26], urine [27,28], saliva [24,29], and tears [30,31]. In contrast to the in vitro bioassays, the availability of inexpensive, portable Raman devices makes this technique particularly attractive for PoC testing, analysis, and screening of biofluids. There is limited yet growing research in the development of Raman spectroscopy for biofluid-based neurodiagnostics [32–36].

In this study, we investigate a broad panel of 18 biomarkers *via* Raman spectroscopy profiling and establish a spectral reference library for the interpretation of the Raman fingerprints of prospective TBI-indicative biomarkers in biofluid. The carefully selected

cohort of TBI-indicative biomarkers, classed as either acute, sub-acute or chronic phase, are profiled in both the raw and reconstituted state forms (providing the purest form and mimicking the biomarker in biofluid) acquired *via* a range of Raman laser excitation wavelengths: 514, 633, 785, and 830 nm.

Subsequently, for each post-TBI phase, Raman spectroscopy temporal-phase biomarker profiling establishes an important baseline library in the form of a "multi-biochemical barcode", yielding a characteristic tool for ongoing and future spectroscopic studies for diagnostic applications. The derived Raman fingerprints, combined with the identified and assigned biochemical peaks, provide us with knowledge of the molecule's physiological role. This barcoding and assignment are applied to spectra obtained in **Chapter 2** and **Chapter 5** of fresh *ex vivo* porcine retinal samples using 635 and 830 nm excitation wavelengths respectively, with the two portable, eye-based Raman devices, identifying prospective TBI biomarker peaks in trauma samples.

Whilst research continues to unravel new rapid PoC technologies for TBI diagnostics from biofluids and tissue, it is imperative to establish fingerprints of the inherent characteristics of TBI biomarkers in various injury phases, where the detected changes via Raman spectroscopy could, in the long-term, be attributed to underpinning the variations in TBIs with various severity and as a function of temporal evolution. This could not only improve the treatment of TBI through specific targeting of the damage in contrast to current methods, which mostly rely on symptomatic relief [37], but could also provide a further panel of candidate first-line screening TBI-indicative biomarkers. This lays the platform for defining their functionality in the complex TBI pathology and, in the longer term, cements Raman spectroscopy as a powerful technique for future biomarker discovery in both neurodiagnostics as well as for other detrimental diseases with many ramifications.

6.2 Material and Methods

6.2.1 TBI Biomarker Preparation

The selected raw biomarkers were purchased without purification and tested in both solid and solution states. These were divided into three main groups of acute, sub-acute, and chronic phases (**Fig. 6.1**). The TBI cohort selection was based on an extensive literature overview of recent research on TBI biomarkers (animal and human) and temporal courses studied in a range of biofluids including blood, plasma, CSF, urine, and the key biomarkers of neuroinflammation [3], [38]–[45]. Biomarkers included in the panel were obtained in the purest form without any active additives, to avoid impacting spectral signatures. This yielded a cohort of 18 biomarkers including the N-Acetyl-L-aspartic acid (NAA), ganglioside, Glutathione (GSH), Neuron-Specific Enolase (NSE), Glial fibrillary acidic protein (GFAP), Ubiquitin carboxyl-terminal hydrolase isozyme L1 (UCHL1), cholesterol, D-serine, sphingomyelin, sulfatide, cardiolipin, Interleukin-6 (IL-6), S100B, galactocerebroside, glucose, myo-inositol, Interleukin-18 (IL-18), and Neurofilament light chain (NFL).

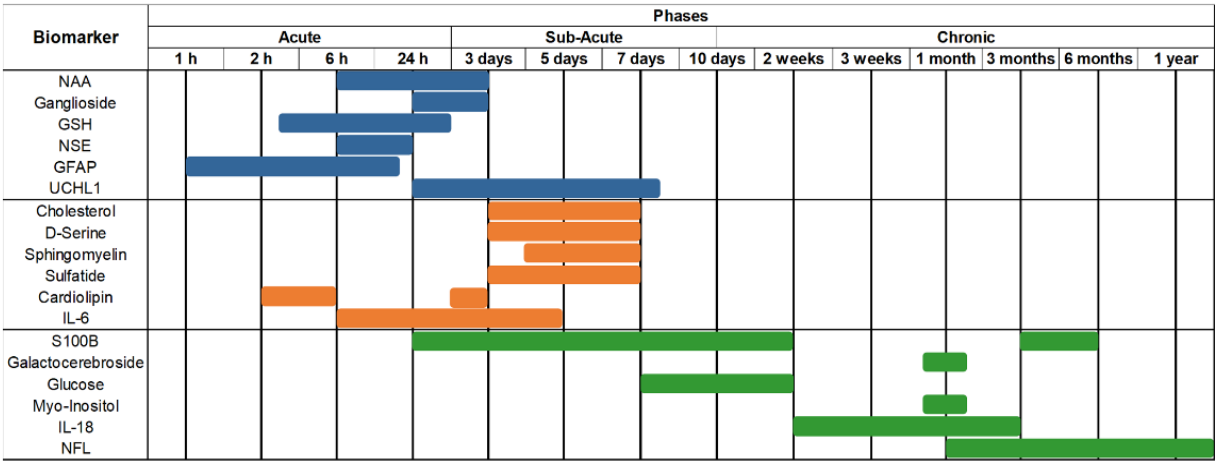

Figure 6.1. Schematic timeline overview of the TBI biomarkers and their phases, during which each biomarker has been reported to either increase, persist or decline post-injury. Biomarkers: N-Acetyl-L-aspartic acid (NAA) [48], Ganglioside [105], [44], Glutathione (GSH) [50], Neuron-Specific Enolase (NSE) [140], Glial fibrillary acidic protein (GFAP) [4], Ubiquitin carboxyl-terminal hydrolase isozyme L1 (UCHL1) [136], Cholesterol [60], D-Serine [153], Sphingomyelin [69], Sulfatide [71], Cardiolipin [74, 209], Interleukin-6 (IL-6) [78], [79] , S100B [159], [40], Galactocerebroside [85], Glucose [160], Myo-Inositol [93], Interleukin-18 (IL-18) [96], Neurofilament light chain (NFL) [9].

Subsequently, reconstituted biomarker samples were prepared following the technical details provided in the individual data sheets. Typically, this included centrifugation at 8 G for 2 min prior to adding the solvent of distilled H_2O (18.2 MΩ) or chloroform/ethanol, yielding 1:1 *v*/*v* solutions. After 20 min, to allow full dissolvement, 3 µL samples of each biomarker were deposited onto an aluminium slide and dried in an ambient environment for Raman measurement.

6.2.2 Reference Chemicals

Human-derived biomarkers included the S100B (HY-P70659, Cambridge Bioscience), Cambridge, United Kingdom, IL-6 (H7416-10UG, Merck, Darmstadt, Germany), NSE (13219-H08E-SIB-50 ug, Stratech, Ely, United Kingdom), GFAP (C227-10 ug, Generon, Slough, United Kingdom), IL-18 (CSB-YP614514HU, Antibodies.com, Cambridge, United Kingdom), NFL (pro-2584-10 ug, Generon), and UCHL1 (UC1-H5140-50 ug, Generon). Animal-derived biomarkers included the galactocerebroside (C4905-10MG, Merck), sphingomyelin (1051-25 mg, Cambridge Bioscience), ganglioside (860053P-10MG, Scientific Laboratory Supplies, Nottingham, United Kingdom), sulfatide (56-1085-7-LAO-25 mg, Stratech), and cardiolipin (C0563-10MG, Merck). Synthetically produced biomarkers included the NAA (00920-5G, Merck), cholesterol (C8667-1G, Generon), glucose (CAY23733-50, Cambridge Bioscience), D-serine (A11353.06, VWR International, Lutterworth, United Kingdom), myo-inositol (A13586.22, VWR International), and GSH (G4251-300MG, Merck).

6.2.3 Raman Spectroscopy Protocol

Raman measurements were carried out using the InVia Qontor confocal Raman system (Renishaw) equipped with four excitation lasers, which were adjusted for optimal throughput, fluorescence control, and sensitivity. Optical measurements were carried out with a specially adapted research-grade microscope (Leica [Wetzlar, Germany] DM 2700M) equipped with an incoherent white light source, allowing confocal measurements with a 2.0 µm depth resolution. Four excitation wavelengths

of 514, 633, 785, and 830 nm were employed in this study to enable a breadth of spectral profiles. To avoid photochemical effects in the spectra, sample damage or degradation, extended spectral Raman scans were acquired over a range of 200–3200 cm^{-1}, 50× objective lens, and an acquisition time of 10 s with 5 accumulations. All Raman spectra were collected at the ambient temperature.

6.2.4 Data Processing

The acquired Raman spectra were collected using Renishaw WiRE 5.2 (Renishaw Plc, Wotton-under-Edge, United Kingdom) and cosmic rays were removed during baseline subtraction with a polynomial order of 11 and a 1.5 noise tolerance. Extended spectra were subsequently averaged per biomarker, taking into account the laser excitation wavelength as well as the raw and reconstituted states. The Peak Pick tool (WiRE 5.2) was utilised across the x-axis range to select the six characteristic bands for each assignment, while the slope detection method was utilised with 15 smooth points and a peak threshold height of 500 counts.

6.3 Results and Discussion

6.3.1 Prospective TBI Biomarker Physiology

The biomarkers studied, based on references to TBIs in the literature, were classified within three main injury phases as acute, sub-acute, and chronic (**Fig. 6.1**), the corresponding detailed information for each biomarker, including the accessible biofluid source, physiological function, post-TBI response, and the role they play in head injuries along with the associated phase behaviour are summarised in **Table 6.1**.

Table 4.1. Overview of the studied TBI biomarkers cohort with the corresponding physiological significance. Source refers to the biofluid in which the biomarker has been analyzed in the literature. N-Acetyl-L-aspartic acid (NAA); Glutathione (GSH); Neuron-Specific Enolase (NSE); Glial fibrillary acidic protein (GFAP); Ubiquitin carboxyl-terminal hydrolase isozyme L1 (UCHL1); Inter-leukin-6 (IL-6); Interleukin-18 (IL-18); Neurofilament light chain (NFL).

Biomarker	Source	Physiological Function	TBI Role	TBI Response	Refs
NAA	Blood CSF	Synthesised in neurons, specific to the nervous system. Has roles in maintaining myelin lipid synthesis and in promoting neuronal mitochondria ATP production.	Marks injury type. Depletion in grey matter and white matter represent neuronal loss and axonal damage, respectively. Rate of replenishment is inversely proportional to injury severity.	↓	[33], [46]–[48]
Ganglioside	Serum CSF Brain	Cellular signalling, protein, and ion channel modulator. Main carrier of sialic acid in the nervous system, improving intercellular communications.	Functional disruption causes neurodegeneration, cellular dysfunctions and promotes disease pathogenesis.	↑	[49]
GSH	Blood CSF	Essential antioxidant, converted from its reduced state (GSH) to its oxidised form to	GSH depletion coupled with neuroinflammation leads to build-up of free radicals, further damaging the brain and neurons.	↓	[50], [51]

		regulate free radicals from the brain.			
NSE	CSF	Tissue-specific cytosol-based enzymes, upon stimulation, translocate to the cell surface to act as a plasminogen receptor.	The degree of damage is directly correlated to the amount of NSE expressed.	↑	[52]
GFAP	Blood CSF	Intermediate filament III protein. Maintains glial cytoskeleton structure, neighbouring neurons, and blood-brain barrier (BBB).	Post-trauma, astroglial cells undergo astrogliosis, causing cellular hypertrophy and increased GFAP expression. Excess GFAP can cause glial scars in brain tissue which delays axon regeneration.	↑	[53]–[55]
UCHL1	Blood CSF	A brain-specific enzyme features in the ubiquitin-proteasome pathway to maintain axonal protein integrity. Regulates axonal transport, structure, and synapsis.	Selectively increases upon axonal damage, utilised to remove damaged and defective proteins from axons.	↑	[56], [57]
Cholesterol	CSF Brain Serum	Key component of the cellular membrane, maintaining structure and fluidity. Cholesterol and phospholipids are transported to nerve cells for repair, upkeep and to promote neurite proliferation.	Increased cholesterol is in proportion to cellular damage. Removing excess cholesterol has an anti-inflammatory effect. Dysregulation of brain cholesterol negatively affects neuronal and glial function. Cholesterol builds up from dysregulation and causes cellular toxicity.	↑	[58]–[62]
D-Serine	Brain CSF Blood	*α*-amino acid, abundant in the brain. Binds to N-methyl-d-aspartate (NMDA) and δ_2 glutamate receptors to contribute to learning and memory function.	Reactive glial cells become D-Serine synthesisers under inflammatory conditions, causing NMDA receptor hyperactivation, and leading to hippocampal synaptic damage.	↑	[63]
Sphingomyelin	CSF Blood	Vital in regulation of cellular growth rate, differentiation, and death in the central nervous system. Supports myelination in the brain, and aids in cognitive maturation and regulation of inflammatory responses.	Increased levels are reported in the hippocampus over 12 months after TBI, contributing to neurological disease pathogenesis. Breakdown products regulate the sphingomyelin cycle which inhibits protein kinase c, regulating	↑	[64]–[69]

			neuronal signal transduction and function.		
Sulfatides	Brain CSF Serum	Abundant in myelin sheath and myelinating cells. Negatively regulates and improves oligodendrocyte differentiation and survival. Maintains myelin and axonal-glial signalling.	Effects functional properties of the membrane, and dysregulation of sulfatides can lead to seizures.	↓	[70], [71]
Cardiolipin	Inner Mitochondrial Membrane	Involved in regulating mitochondrial metabolism. The structural component of mitochondrial membranes regulates protein and enzyme activity central to mitochondrial function.	Damaged mitochondria trigger neuronal death when oxidised. Cardiolipin acts as an elimination signal for damaged mitochondria, thus limiting neuronal damage and preserving cognitive functions.	↑	[72]–[74]
IL-6	CSF Serum Blood	Pleiotropic cytokine with operations in immunity regulation, regeneration processes, neural functions, and cardiovascular protective mechanisms.	Usually undetectable in healthy brain parenchyma but present within an hour following TBI. Upregulated production following trauma from inflammatory cascades to salvage neurons. Sustained inflammation is ultimately damaging.	↑	[75]–[79]
S100B	Blood CSF Brain	Calcium-binding protein involved in long-term synaptic plasticity modulation, cellular growth and structure, calcium concentration maintenance and energy metabolism. Mitigates mitochondrial failure through calcium modulation.	Overexpression leads to disrupted calcium homeostasis. Increased levels indicate structural damage and cellular death.	↑	[80], [81]
Galactocerebroside	CSF Brain	Major lipid component in the brain, which maintains myelin sheath structure and stability. Important for development of normal myelin in the central nervous system.	Galactosylcerimidase dysfunction prevents Galactocerebroside from degrading, instead, it accumulates in globoid cells in the brain, leading to white matter diseases.	↑	[82]–[85]
Glucose	Blood	Main energy source to the brain, used for action potential and	Early low glucose levels and low lactate/glucose ratio post-TBI are associated with poor outcomes.	↓	[86]–[88]

		postsynaptic potential generation. Synthesises BBB-regulated neuroactive compounds and sustains brain homeostasis.	Not associated with ischemia.		
Myo-Inositol	CSF Blood	Regulates glial and neuronal activity and participates in intracellular signalling pathways. Regulates intracellular [Ca_2^+] and membrane permeability.	Increased levels are correlated to glial proliferation, increased rate of membrane turnover and myelin sheath damage. Correlated to astrogliosis and dysregulation of cellular osmotic functions.	↑	[89]–[93]
IL-18	CSF	Inducer of inflammatory cytokines; synthesised as an inactive precursor in microglia and activated by caspase-1 in a forward loop.	Has roles in neuroinflammation and neurodegeneration. Induces respiratory burst and degranulation of polymorphonuclear leukocytes resulting in a release of neurotoxic enzymes.	↑	[94]–[96]
NFL	CSF Blood	Integral in maintaining axonal cytoskeleton through radial growth. Larger myelinated axons result in more NFL, leading to faster conduction speed.	NFL levels rapidly increase following trauma to account for damaged axons and is released into the interstitial space and integrated into CSF. Indicates significant axonal damage and progression rate of disease.	↑	[97]–[99]

6.3.2 Prospective TBI Biomarker Spectra and Peak Assignment

The Raman spectrum is commonly referred to in terms of discrete regions, the low wavenumber region (100–200 cm^{-1}), the fingerprint region (500–2000 cm^{-1}), and the high wavenumber region (2000–4000 cm^{-1}) [46, 47]. In this study, Raman spectra were collected in the extended spectral regions of 200–3200 cm^{-1}, however, only the fingerprint region from 200 to 1800 cm^{-1} was used where the main bands of interest were identified.

Spectral profiles for each biomarker were acquired for both solids as well as of the solute forms, with the former inherently yielding better resolved, sharper Raman peaks. It is well-established that Raman band frequencies are more complex and shifted in the liquid phase, relative to the solid, due to the higher variability of the intermolecular forces and molecular collisions in the liquid phase, which shifts the frequencies of intra-molecular vibrations and broaden the bands, relative to the highly regular and stable solid structures.

6.3.2.1 Acute Phase

Acute TBI biomarkers have been shown to be applicable in triaging, diagnosing, and eliminating the presence of TBI at the earliest stages (i.e., golden-hour biomarkers)

and are thus particularly important for the development of diagnostic PoC modalities as well as intervention for TBI[102], [103]. Therefore, biochemical changes and concentration variations in biomarkers are reflected through the spectral information when comparing healthy control cohorts to acute, sub-acute, and chronic phases, which are vital for PoC diagnostics and injury monitoring.

Figure 6.2. Spectra of raw and reconstituted Acute TBI biomarkers using all four laser excitation wavelengths 514 (green), 633 (red), 785 (blue) and 830 nm (yellow). Counts are in Arbitrary Units as this is a relative value and therefore not comparable between spectra on different axes. Reconstituted biomarkers better mimic how each may be found in biofluid thus differences between this and the raw form is necessary for diagnostic applications of Raman Spectroscopy

The differences in biomolecule state are illustrated in **Fig. 6.2**, allowing for comparison between, not only raw and reconstituted biomarker states but also, excitation wavelength lasers: 514, 633, 785 and 830 nm. A clear agreement can be observed between the raw spectra (black) acquired by all four lasers within each biomarker, whilst there is more variation and notably less spectral information in the reconstituted form. This is especially true in spectra obtained from NAA, GSH, NSE, and UCHL1, but not the case for ganglioside and GFAP which is comparable in both raw and reconstituted states. Noting the differences in both states and having both available is

essential for future researchers profiling for TBI in different environments as the field continues to progress.

Representative average spectra of acute TBI biomarkers are presented in **Fig. 6.3,** alongside peak assignment provided in **Table 6.2**. Each biomarker produced unique and distinctive spectral features, and differences between utilising the four laser wavelengths can be identified. Strong characteristic peaks of NAA are found in the 949–957 cm^{-1} and 987–992 cm^{-1} regions for the four-excitation laser used (**Fig. 6.3a**), with the main peaks being associated with the C-N stretching as well as CH_2-CH wagging[104]. NAA is an amino acid derivative located in neurons where the decreasing levels are proportional to neuronal loss and axonal damage[47] and, thus, a decrease in characteristic Raman peak intensity can be an important indicator following brain trauma.

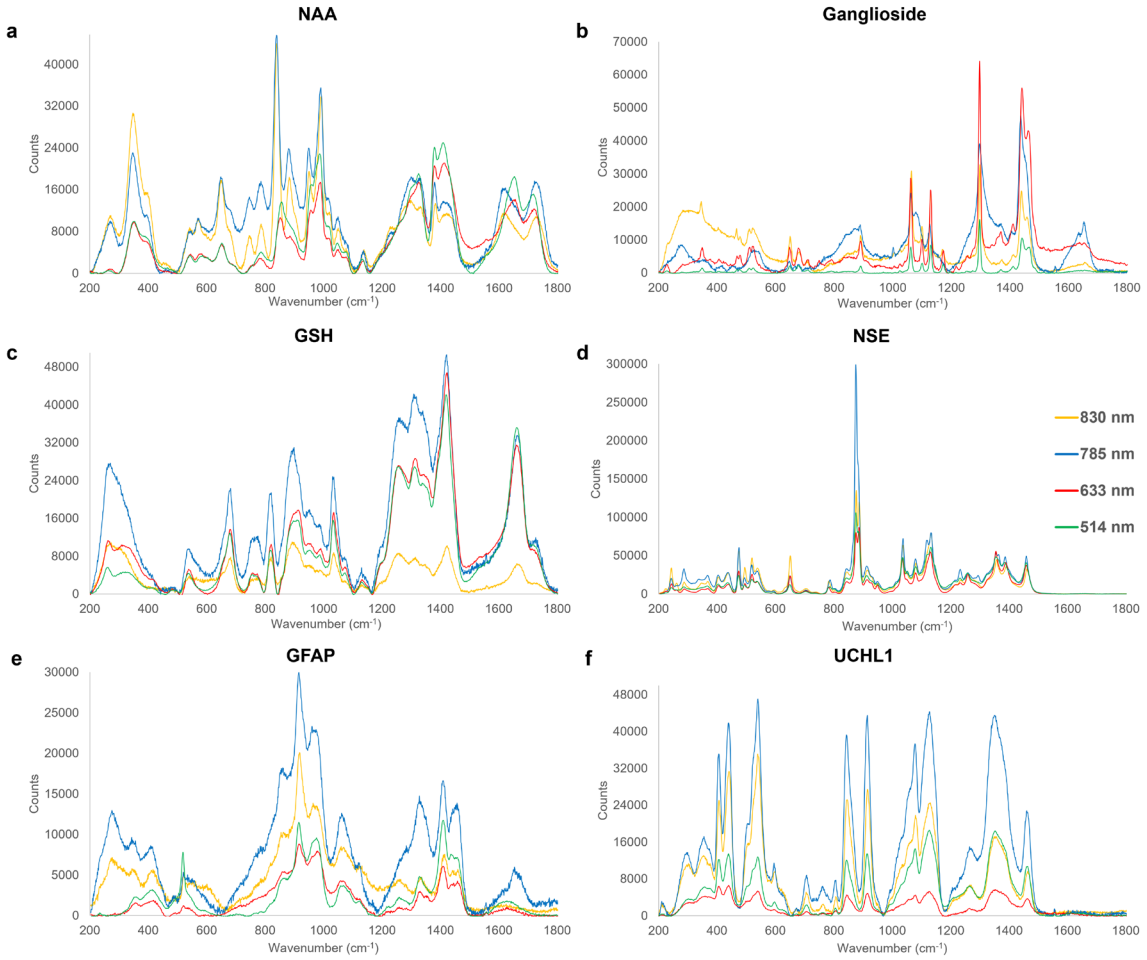

*Figure 6.3. Characteristic Raman spectra fingerprints of acute phase reconstituted TBI biomarkers, acquired at excitation wavelengths of 514nm (green), 633nm (red), 785nm (blue) and 830nm (yellow). Significant Raman peak assignments for each are summarized in **Table 6.2**.*

The most intense peaks of ganglioside, a sialic acid-bearing glycosphingolipid[105], are detected at 1297–1298 cm^{-1} and 1437–1442 cm^{-1} (**Fig. 6.3b**). The bands at 1297 and 1440 cm^{-1} are assigned to bending and twisting of CH_2 bonds[106], which optimally could be employed relative to other characteristic peaks of ganglioside post-TBI[107]. These peak intensities have been reported to decrease in counts in tandem with cell loss[107], in contrast to the other characteristic peaks of ganglioside (**Table**

6.2), which are typically shown to increase in response to neurodegeneration and cellular dysfunction (**Table 6.1**)[49].

Table 6.2. Peak assignment of significant peaks present in the acute TBI biomarker cohort. ν = stretching; δ = bending; τ = twisting ; ρ = rocking; ω = wagging; s = symmetric; a = anti-symmetric; arom = aromatic; skel = skeletal.

Wavenumber (cm^{-1})	Assignment	Origin	Ref
347-353	ν_{skel}(C- C)	NAA	[104]
473-475	ν(S-S)	NSE	[112]
518-521	C(OH), *Ring deformation*	GFAP	[104], [113]
647-651	ν(C-S), τ(C-C), *Ring breathing mode*	NAA, NSE, Ganglioside	[113]–[115]
679-682	ν(C-S)	GSH	[113]
705-708	*Ring deformation*	UCHL1	[113]
806	ν_s(C-N-C)	UCHL1	[104]
819-821	CH *deformation*	GSH	[104]
843-845	δ(H(C-O-H)), ρ(H(C-O-H))	UCHL1	[113]
875-877	ν(C-C), ν_a(C-N)	NSE	[82], [113]
889-891	ν_{arom}(C-O), ν(C-C), $\omega(CH_2)$	Ganglioside	[116]–[118]
914-918	ν(C-N), *Pyranose ring asymmetric vibration*	GFAP, UCHL1	[104], [113]
949-957	ν(C-N)	NAA	[104]
974-980	ν_a(C-C), $\rho(CH_2)$	GFAP	[113], [119]
987-992	ν(C-N), $\omega(CH_2$- CH)	NAA	[120]
1031-1037	δ(C-H), ν(C-C), $\nu_a(C\text{-}C\text{-}N^+)$	GSH, NSE	[121], [122]
1060-1068	ν(C-O), ν_{skel}(C-C), $\tau(NH_2)$	Ganglioside, GFAP	[113], [123], [124]
1077-1082	ν(C-O), ν(C-C), $\tau(CH_2)$	NSE, UCHL1	[125], [126]
1127- 1130	ν(C-N), ν(C-C)	Ganglioside, UCHL1	[127], [128]
1131-1138	ν(C-C)	NAA	[129]
1297-1298	$\tau(CH_2)$	Ganglioside	[130]
1311-1315	δ(C-H)	GSH	[131]
1328-1336	$\omega(CH_2)$, $\tau(CH_2)$	GFAP	[113]
1352-1354	$\tau(CH_2)$	UCHL1	[126]
1378-1383	$\nu_s(COO^-)$	NAA	[132]

1408-1410	δ(C-H), v_s(COO^-)	GFAP	[113], [133]
1420-1424	δ(CH_2), v_s(COO^-), v_s(CO_2)	GSH	[109], [110], [131]
1437-1442	δ(CH_2), τ(CH_2)	Ganglioside	[134]
1458-1460	δ(CH_2)	NSE	[135]
1660-1662	v(C-N(H)-C=O), v(C=C)	GSH	[104]

GSH, a non-enzymatic antioxidant tripeptide present in cells to protect membranes from oxidative damage[108], exhibits the most intense peaks located at 1420–1424 cm^{-1} and 1660–1662 cm^{-1} (**Fig. 6.3c**), attributed to the -CH_2 bending mode of proteins[109], and symmetrical stretching of the carboxylic acid COO^- [110], and the Amide I region, indicative of amino acids[111], respectively. Post-TBI apoptosis could lead to GSH depletion and thus a reduction in characteristic peak intensity which, when coupled with neuroinflammation, results in TBI secondary injury due to free radicals build-up further damaging neurons and the brain (**Table 6.1**)[51].

NSE is a glycolytic tissue-specific enzyme associated with neuronal damage and post-traumatic inflammation[136], [137], increasing in expression with injury severity[52]. The strongest peak for NSE (**Fig. 6.3d**) at 875–877 cm^{-1} at all four employed excitation wavelengths is assigned to the stretching of C-C bonds and the asymmetric stretching of C-N bonds[113], [138] associated with phenylalanine. A secondary peak of interest at 1077–1082 cm^{-1} is attributed to the stretching of C-O and C-C bonds[125] along with the twisting of CH_2 bonds[126]. NSE is plausible for monitoring post-TBI changes since it is only expressed in a direct correlation to the degree of damage and translocated from the cytosol to the cell surface upon stimulation, acting as a plasminogen receptor[52], [139], [140].

GFAP is a structural filament protein of astrocytes[15], with its levels known to increase in response to astrogliosis post-trauma, as discussed in **Table 6.1.** The most intense detected spectral bands are found in the region of 914–918 cm^{-1} (**Fig. 6.3e**), assigned to C-N stretching[113], and asymmetric vibration of the pyranose ring[104], also present in the UCHL1 spectrum (**Fig. 3f**), increasing in response to TBI, and thus might collectively be an important candidate peak of interest for TBI Raman-based diagnostics.

A further sharp peak present in the 1408–1410 cm^{-1} region is assigned to the bending of C-H bonds and symmetrical stretching of COO^- bonds[113], [133], along with a wider band at 1060–1068 cm^{-1}, assigned to the skeletal stretching of C-C bonds and indicative of changes in protein levels[124]. GFAP has been shown to increase after brain trauma because of reactive astrogliosis. Its overexpression, causing scarring of the brain, can be used to distinguish between the healthy and damaged tissue, giving an indication of the amount of damage, and delaying the axonal regeneration[54].

UCHL1, a cytoplasmic enzyme found in neurons, is selectively increased following axonal trauma to remove damaged and defective proteins from axons[56], [141]. Unfortunately, the glycerol-environment buffer of this protein dominates the spectral

fingerprint with aliphatic chains[126], [142] and, therefore, only smaller peaks in the 600–800 cm^{-1} region are identified to be unique to the UCHL1 marker (**Fig. 6.3f**) with the 705–708 cm^{-1} band assigned to ring deformation[113], and the 806 cm^{-1} peak assigned to the symmetrical stretching of C-N-C bonds present in amino acids[104].

6.3.2.2 Sub-Acute Phase

Detection of sub-acute TBI biomarkers is vital for multiple-level diagnostics when the patient is admitted to hospital and a complementary rapid diagnostic technique is required alongside structural neuroimaging. This lays the platform for not only enabling timely TBI management at ED, A&E, etc. for early neuroprotective measures but also for the correct transfer to the most appropriate neurological facility. Rapid diagnosis in the early clinical phase will lay a platform for a range of improvements in personalised medicine and management, reduce strain on the healthcare system, and enable better-quality post-neurotraumatic care. Similarly, in the military context, where neurosurgical support is not routinely deployed and TBI management often requires evacuation, the ability to diagnose and assess TBI severity pre-hospital would avoid unnecessary strategic evacuation and maintain operational effectiveness.

The spectra obtained from the full panel of sub-acute TBI biomarkers using all four lasers in the raw and reconstituted state are presented in **Fig. 6.4.** There is clear agreement between the raw and reconstituted peaks in the spectra of cholesterol and cardiolipin, as opposed to the spectra from IL-6 which have many differences in peak location. A split between the 514 and 633 nm with the 785 and 830 nm laser wavelengths is observed in spectra produced from sulfatide and IL-6, these differences are noticed not only in the complex reconstituted state of the biomarkers but also in the raw form too. D-Serine proves difficult to characterise between laser wavelength, as raw spectra obtained using the 633, 785 and 830 nm lasers are consistent but low counts and spectral information are produced in solute form. Whilst spectrum produced from the reconstituted D-Serine using the 514 nm laser wavelength has little agreement with the raw form and the other laser wavelengths. This type of discrepancy highlights the difference in the performance of each laser wavelength depending on the application and is very useful when providing grounds for which excitation wavelength is best suited for Raman-based TBI diagnostics in biofluids.

Average spectra of sub-acute TBI solute-form biomarkers using all four laser wavelengths are shown in **Fig. 6.5** with the corresponding peak assignments summarised in **Table 6.3**. Cholesterol's sterol-centred structure presents a unique and large number of intense peaks (**Fig. 6.5a**), including the 700 cm^{-1} band of the in-plane deformation of its B ring[143], as well as a sharp peak at 1673 cm^{-1}, assigned to the B ring C=C stretching[144]. Cholesterol is structurally important in the cellular membrane with its increases following TBI proportionally related to the cellular damage[145]. As a response to neuro-inflammation, apolipoprotein E transports cholesterol and phospholipids by forming a protein–lipid complex to damaged nerve cells to assist the cellular damage as well as to increase neurite proliferation[58], [59]; whilst cholesterol removal is associated with the anti-inflammatory response[60], [61]. If left unchecked, the dysregulation of cholesterol in the brain can negatively affect neuronal and glial functions and in due course, leading to cellular toxicity[62].

Figure 6.4. Spectra of raw and reconstituted sub-acute TBI biomarkers using all four laser excitation wavelengths 514 (green), 633 (red), 785 (blue) and 830 nm (yellow). Counts are in Arbitrary Units as this is a relative value and therefore not comparable between spectra on different axes.

Table 6.3. Peak assignment of significant peaks present in the sub-acute TBI biomarker cohort. v = stretching; δ = bending; τ = twisting ; ρ = rocking; ω = wagging; s = symmetric; a = anti-symmetric; arom = aromatic; skel = skeletal

Wavenumber (cm^{-1})	Assignment	Origin	Ref
512-516	$\rho(COO^-)$	D-Serine	[135]
520-525	δ(N-C=O)	IL-6	[104]
549	δ(N-C-S)	IL-6	[104]
561	-OH *out of plane deformation*	IL-6	[104]
700-702	*In-plane deformation of B ring*	Cholesterol	[146]
717-720	v_s(C-N)	Sphingomyelin	[113]
809-815	v(C-C)	D-Serine	[104]
850-854	$\rho(CH_2)$	D-Serine	[135]

888-893	$v_{arom}(C\text{-}O)_4$, $v(C\text{-}C)$, $\omega(CH_2)$	Sulfatide	[116]–[118]
917-923	$v(C\text{-}C)$	D-Serine	[135]
959-964	PO_4 *vibration*, $v_s(C\text{-}N\text{-}C)$, $\delta(C\text{-}H)$	Cholesterol, IL-6	[104], [147]
970-974	$v(C\text{-}N)$	D-Serine, Cardiolipin	[113], [135]
1062-1067	$v(C\text{-}O)$, $v(C\text{-}C)$, $\tau(NH_2)$	Sphingomyelin, Sulfatide, IL-6	[113], [123], [124]
1107-1111	$v_a(SO_4)$, $v(C\text{-}N)$, $v(C\text{-}C)$, $v(C\text{-}OH)$,	Sulfatide, Cardiolipin	[23], [148]
1127-1130	$v(C\text{-}N)$, $v(C\text{-}C)$, $v_{skel}(C\text{-}C)$	Sphingomyelin, Sulfatide, IL-6	[127], [128]
1176-1179	$v_{skel}(C\text{-}C)$	Cholesterol	[144]
1266-1268	$v(C\text{–}O)$	Cardiolipin	[149]
1295-1299	$\tau(CH_2)$	Sphingomyelin, Sulfatide	[130]
1302-1304	$\tau(CH_2)$	Cardiolipin	[146]
1327-1336	$\omega(CH_2)$, $\tau(CH_2)$	Cholesterol, D-Serine	[113]
1436-1441	$\delta(CH_2)$, $\tau(CH_2)$, $v(CH_2/CH_3)$	Cholesterol, Sphingomyelin, Sulfatide, Cardiolipin	[134], [150]
1656-1660	$v(C{=}O)$, $v(C{=}C)$	Sphingomyelin, Cardiolipin	[111], [151]
1672-1674	$v(C{=}C)$	Cholesterol	[144]

D-Serine is a non-essential polar amino acid, which serves as a precursor to purines and pyrimidines, and is an important neurotransmitter[152]. The characteristic fingerprint of D-Serine (**Fig. 6.5b**) exhibits strong peaks in the range of 917–923 cm^{-1}, attributed to its C-C backbone stretching[135], as well as at 1327–1336 cm^{-1} from the twisting of its CH_2 groups[113]. Serine is a co-ligand activator of NMDA receptors and of δ_2 glutamate receptors, which have regulatory roles in synaptic plasticity and long-term potentiation[63]. Increases in serine following TBI is caused by reactive glial cells, which under inflammatory conditions turn into D-serine synthesisers. An increase in D-serine leads to hyperactivation of NMDA receptors, which damages hippocampal synapsis and is known to disrupt learning and memory formation[86] [87]. Blocking D-serine production under inflammatory conditions has been related to improved outcomes following brain trauma[63].

Sphingomyelin can be spectrally identified by a characteristic set of peaks in the range of 717–720 cm^{-1} and 1295–1299 cm^{-1}, due to the symmetric stretching of C-N and the twisting of CH_2, respectively[107], [113] (**Fig. 6.5c**). Sphingomyelin is a prominent sphingolipid, found in the plasma membrane with a distribution ratio correlating specifically with cholesterol for suitable membrane function[154]. This lipid plays a vital role within the CNS in terms of cellular growth, differentiation, and death[64]. In the brain, sphingomyelin is also associated with improved cognitive maturation, brain myelination, and regulation of inflammatory responses[65], [155]. Levels of sphingomyelin have been shown to increase following TBIs for over 12 months,

rendering it a neuro-marker for both sub-acute as well as chronic phases[66]. Disruption of sphingomyelin metabolism is known to dysregulate the mitochondrial energy pathways, slowing the healing process and increasing the risk of secondary injuries, contributing to the overall TBI pathogenesis[156].

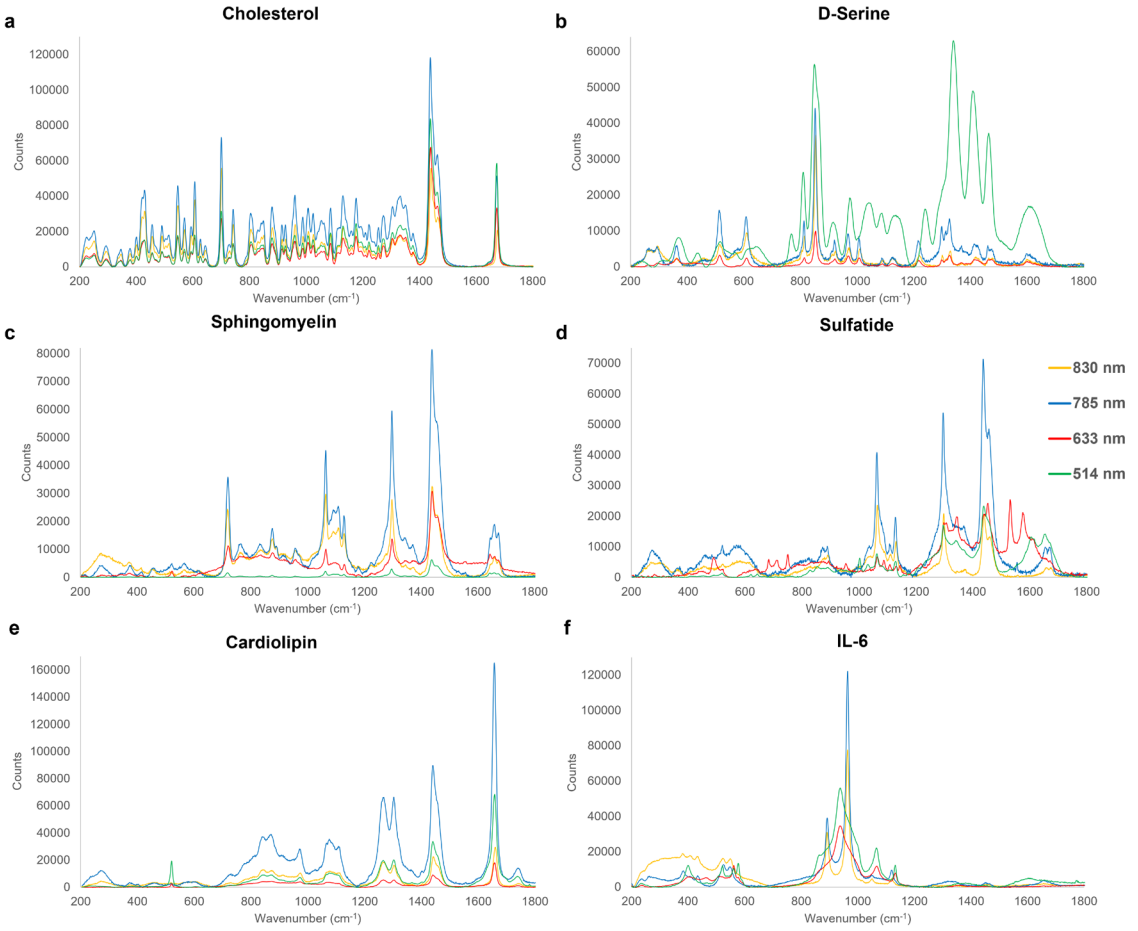

Figure 6.5. Spectra of sub-acute TBI biomarkers, laser excitation wavelengths 514 (green), 633 (red), 785 (blue) and 830 nm (yellow) are overlayed. Significant peaks are picked and assigned in Table 3.

Sulfatides are a class of sulfo-lipids, abundantly present in brain tissue and are a main feature in myelin sheath and within myelinating cells[70]. Spectral characteristic fingerprints of sulfatides are shown in **Fig. 6.5d**. These representative peaks include the stretching of the C-OH from the sulphated pyranose ring and C-C backbone along with the CH_2 wagging in the range of 888–893 cm^{-1}[116]–[118], with the anti-symmetric stretching of the SO_4 group identified at 1107–1111 cm^{-1}[148]. Sulfatides, directly derived from galactocerebrosides, constitute promising candidate TBI biomarkers due to their roles in protein trafficking, neuronal transduction, and negative regulation in oligodendrocyte differentiation[157]. Following TBI, sulfatide levels decrease in the brain subsequently, allowing oligodendrocyte production to occur at a higher rate, thus providing axonal myelin wrapping with improved action potential and transmission. However, due to the functional role of sulfatides within the membrane, the dysregulation can lead to physiological responses such as seizures[70].

Cardiolipin, a mitochondrial-specific phospholipid, which signals damaged mitochondria[72] (**Fig. 6.5e**), is found to exhibit dominant PO_4 vibrations at 959–964

cm^{-1} and C-O stretching from the linoleic acid groups in the range of 1266–1268 cm^{-1}[147], [149]. Cardiolipin is known to be central to mitochondrial function, with roles in both regulation of metabolism and membrane structure maintenance[72], with damaged and dysregulated mitochondria triggering neuronal death[73], [158]. Cardiolipin is externalised from the inner mitochondrial membrane to signal damaged mitochondria and promote mitophagy, ultimately limiting further neuronal damage and retaining cognitive functions[158], resulting in increases in its concentration linked to the extent of mitochondrial damage[73], [158].

IL-6, an inflammatory cytokine, yields a distinctive spectral signature (**Fig. 6.4f**) with peptide bonds bending within the protein detected in the 520–525 cm^{-1} region[104], and a sharp peak at 959–964 cm^{-1}, associated with the symmetric stretching of the C-N-C bonds of proteins [[104]]. The pleiotropic IL-6 is involved in immunity, regeneration, and neural functions [75]. Whilst in healthy brain tissue it is not typically detectable, it has been found to be present within an hour of brain injury, making it a reliable marker of TBI-induced damage[76], [77]. IL-6 is further upregulated during inflammatory cascades to help healing including the salvation of neurons; however, a prolonged detection of this biomarker is indicative of sustained inflammation, resulting in more damage over healing [158].

6.3.2.3 Chronic Phase

Chronic TBI biomarkers span a larger timeframe and are particularly important in cases of undiagnosed mTBI, frequently causing patients long-term effects. Certain chronic biomarkers are expressed in the early phase, during the acute phase, and continue to be expressed in the longer term [40], [159], [160]. The chosen representative chronic biomarkers (**Fig. 6.1**) provide important underpinning spectral fingerprints, contributing towards ongoing investigations on chronic biomarkers and their post-TBI mechanisms and, once confirmed, the emerging findings would enable the detected biomarker levels at late time points to be used to identify TBI survivors who are at high risk of progressive neurological damage, triggered by their initial TBI. Rapid detection and an in-depth understanding of chronic TBI biomarkers would aid the development of TBI therapeutics and enable *in situ* tracking of TBI pathology and injury evolution at hospital. Real-time spectroscopy for TBI monitoring would further improve target management and understanding of injury heterogeneity, evolution, and penetrance of pharmacological agents, identify novel targets for intervention, and could lead to the development of modalities for tactful therapeutic modifying therapies in TBIs.

The comparisons between the biomolecular solid and solute states of the chronic TBI biomarker panel are presented in **Fig. 6.6**. There is very good agreement in peak location between the raw spectra (black) acquired by all four lasers within each biomarker, as well as most in the reconstituted state. The largest differences in the solute state are present in the galactocerebroside spectra, where large fluorescence can be seen from the 633 nm laser (red) and unusual short, sharp peaks present when using the 830 nm laser (yellow). Unfortunately, spectra produced from IL-18 shares peak location and spectral shape with that of UCHL1 in the acute panel, suggesting that the glycerol-environment buffer of this protein dominates the spectral fingerprint. However, some small peaks will be present despite the overpowering glycerol contamination, providing peaks unique to IL-18 as a chronic TBI biomarker for biofluid-based diagnostics.

Figure 6.6. Spectra of raw and reconstituted chronic TBI biomarkers using all four laser excitation wavelengths 514 (green), 633 (red), 785 (blue) and 830 nm (yellow). Counts are in Arbitrary Units as this is a relative value and therefore not comparable between spectra on different axes.

Laser excitation wavelengths can be directly compared per chronic biomarker in the reconstituted form in **Fig. 6.7**, and the extensive agreement in spectral information is illustrated, highlighting only the fluorescence from galactocerebroside when utilising the 633 nm laser, and the corresponding peak assignments are summarised in **Table 6.4**. S100B is a calcium-binding protein expressed in astrocytes and is the first brain biomarker to be recognised and utilised within clinical practice guidelines[15], [161]. S100B, known to be neuroprotective and neurotrophic, is regarded as a suitable marker due to its involvement in the modulation of long-term synaptic plasticity and energy metabolism by maintaining calcium concentration and ensuring correct mitochondrial function[80], [81]. Characteristic dominant spectral peaks are identified for S100B throughout the entire 200–1800 cm^{-1} region (**Fig. 6.7a and Table 6.4**). The most intense bands are at 936–937 cm^{-1}, assigned to stretching of the C-C bond of proline and valine[162], and at 1002–1004 cm^{-1}, due to aromatic phenyl breathing of the C-C bond of the phenylalanine[113], [163]. Post-TBI, increased S100B levels accompany structural damage and cellular death[81]. This would result in higher intensity of identified Raman peaks, posing it as a promising marker for Raman-based neuro-diagnostics. Physiologically, the implication of increased S100B levels disrupts

the correct calcium homeostasis, leading to mitochondrial failures and damaging long-term hippocampal potentiation[80], [81].

Table 6.4. Peak assignment of significant peaks present in the chronic TBI biomarker cohort. v = stretching; δ = bending; τ = twisting ; ρ = rocking; ω = wagging; s = symmetric; a = anti-symmetric; arom = aromatic; skel = skeletal; Δ = ring breathing vibration,

Wavenumber (cm^{-1})	Assignment	Origin	Ref
422-424	*In-plane* δ_{arom}(C-OH)	Glucose	[104], [164]
504-506	OH *out-of-plane deformation*	Myo-Inositol	
517-520	C-OH *deformation*	Glucose	[104]
559-560	OH *out-of-plane deformation*	S100B	[104]
606-607	CCC *in-plane deformation*	NFL	[165]
804-807	v_s (C-N-C)	IL-18	[120]
842-844	*Out-of-plane* δ_{arom}(CH), ρ (H(C-O-H))	IL-18	[113], [142]
891-893	$v_s(COO^-)$, v(C-C)	NFL (glycine)	[166], [167]
896-899	$v_{\text{aliphatic}}$(C-H)	Myo-Inositol	[104]
912-914	v(C-CH_3)	IL-18	[168]
936-937	v(C-C)	S100B	[162], [169]
1002-1004	Δ_{arom}(C-C)	S100B	[170]
1008-1010	Δ_{arom}(C-C)	Myo-Inositol	[171]
1040-1041	v(C-CH_3), v(C-C), δ(CH)	NFL	[163], [172]
1058-1066	v(C-O), v_{skel}(C-C), $\tau(NH_2)$	S100B, Galactocerebroside, Glucose	[123], [124]
1077-1080	v(C-C), v(C-O)	IL-18	[113], [173]
1116-1121	δ(CH), v(C-C),	Myo-Inositol	[174], [175]
1124-1127	v(C-C)	Glucose	[127]
1128-1133	v_{skel}(C-C), v(C-N)	S100B, Galactocerebroside, IL-18	[113], [127], [128]
1143-1146	v(C-N), δ(CH)	NFL	[131], [176], [177]
1217-1218	v(C-C)	Myo-Inositol	[178], [179]
1259-1261	Amide III (v(CN) δ(NH)	IL-18	[180], [181]
1295-1298	$\tau(CH_2)$	Galactocerebroside	[130]
1321-1323	δ(CH), $\tau(CH_2)$,	NFL (glycine)	[182], [183]

1357-1359	$\nu_{\text{aliphatic}}(\text{CH})$	Myo-Inositol	[104]
1368-1371	$\delta(\text{CH}_2)$	Glucose	[184]
1409-1411	ν(C-C), δ(C-H)	NFL	[113]
1439-1441	$\nu(\text{CH}_2/\text{CH}_3)$	Galactocerebroside	[150]
1458-1464	ω(C-H), $\delta(\text{CH}_3)$, ν(C=O), ν_{arom}(C=C)	Galactocerebroside, Glucose, IL-18	[185]–[187]
1603-1608	$\nu_a(\text{COO}^-)$, ν(C=C), ν(C=O)	S100B	[113], [131], [188]
1672-1676	ν(C=C)	Galactocerebroside	[144]

Galactocerebrosides are a major glycolipid of the myelin within the CNS and the most abundant glycolipid component of myelin[189], [190]. **Fig. 6.7b** exhibits dominant spectral peaks in the fingerprint spectrum, particularly, above the 1000 cm^{-1} region. A characteristic peak in the 1128–1133 cm^{-1} range is assigned to the C-N stretching of the amine bond in the acyl chain[113], and the C-C bond skeletal stretching of the acyl backbone common to lipids[128], and further in the 1295–1298 cm^{-1} region, assigned to the twisting of CH_2 bonds of lipids[107]. This biomarker accumulates in the brain in globoid cells when there is galactosylcerimidase dysfunction, preventing galactocerebroside from degrading, potentially leading to a long-term white matter disease (**Table 6.1**). Overall, peaks in the range of 1295–1299 cm^{-1} are also present in the spectra of sphingomyelin, sulfatide and ganglioside, creating a potential band of interest for the detection of chronic TBI biomarkers via Raman spectroscopy as well as to assess post-TBI recovery and response to interventions.

Glucose is the predominant and preferred energy source of the mammalian brain, with levels present indicating metabolism in astrocytes[88], [160]. Overall, biomarkers in the chronic phase had a larger number of characteristic peaks identified in the lower wavenumber and fingerprint regions 200–800 cm^{-1} than the earlier phases with two intense bands determined from the glucose spectrum (**Fig. 6.7c**) in the 422–424 and 517–520 cm^{-1} regions, with the former attributed to the in-plane aromatic bending of the C-OH bond[104] and the latter assigned to C-OH bond deformation (**Table 6.4**)[104]. Decreases in glucose levels post-TBI have been shown to be associated with poor outcomes due to the indication of an increased need for energy for tissue repair. Glucose metabolism post-trauma has also been shown to lead to an increase in anaerobic glycolysis; however, this has been specifically proven to be a result of ischemia. Furthermore, glucose levels can be compared to other metabolites downstream in the glycolytic pathway such as the ratio of pyruvate (aerobic product) to lactate (anaerobic product). A larger ratio typically correlates to more glycolytic than mitochondrial activity and is associated with worse outcomes, due to an indication that neurons might be too damaged to take up lactate[88].

Myo-inositol, a sugar derivative, has been reported to increase in proportion with TBI severity[191], and in correlation with glial proliferation, membrane turnover, and myelin sheath damage (**Table 6.1**). Spectral peaks of myo-inositol are highly consistent across the four excitation wavelengths used (**Fig. 6.7d**) with the most intense bands at 504–506 cm^{-1}, assigned to out-of-plane deformation of -OH bonds and further in 1116–1121 cm^{-1} and 1217–1218 cm^{-1} regions, attributed to stretching of the C-C

bonds[175], [178], [192]. Further intense peaks at 896–899 cm^{-1} and 1357–1359 cm^{-1} arise from CH bending within the aliphatic structure of myo-inositol[104]. Increases in myo-inositol levels post-TBI provide a good marker of the proliferation of glial cells, membrane turnover, myelin sheath damage as well as astrogliosis and cellular osmotic dysregulation[89]–[91], [193].

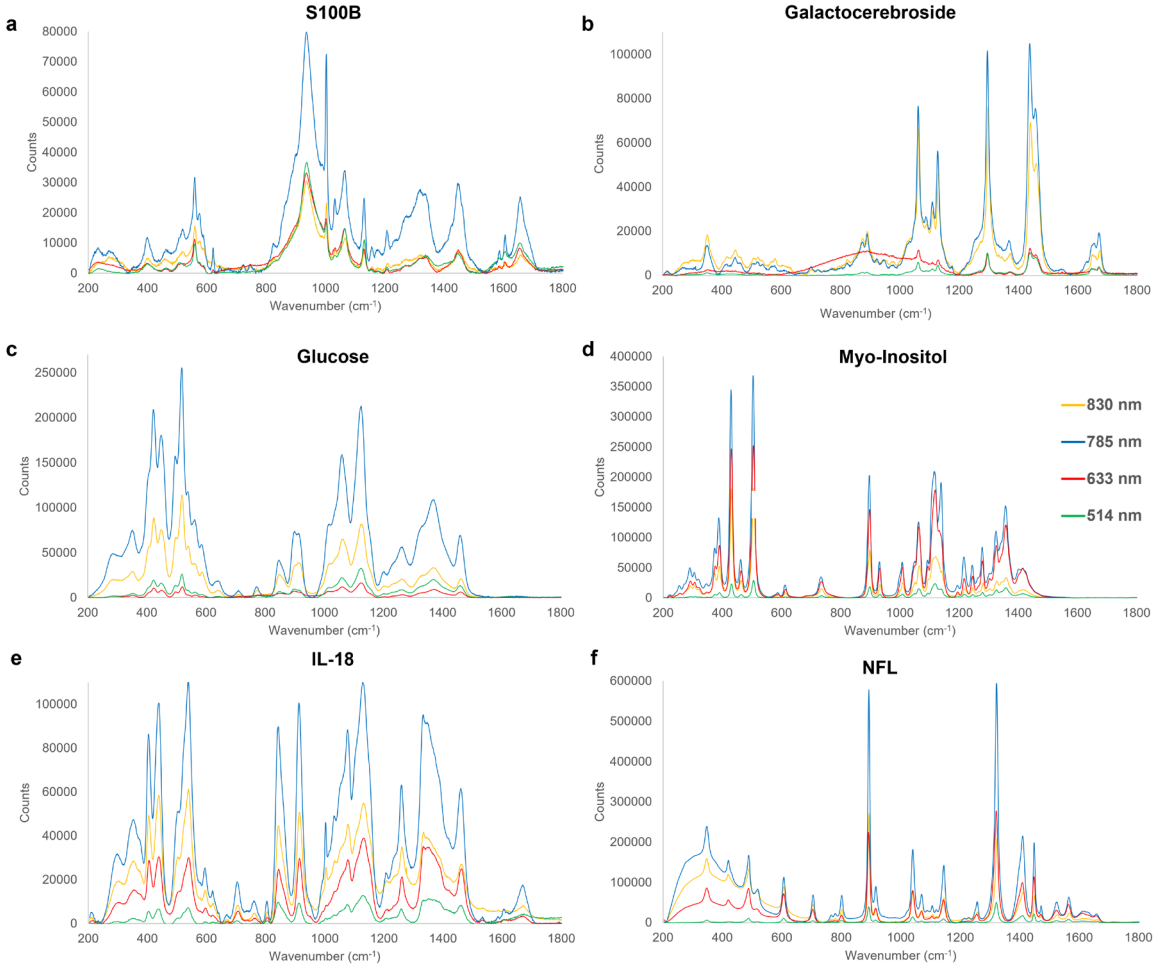

Figure 6.7. Spectra of Chronic TBI biomarkers, laser excitation wavelengths 514 (green), 633 (red), 785 (blue) and 830 nm (yellow) are overlayed. Significant peaks are picked and assigned in Table 4.

IL-18 is a pro-inflammatory cytokine, produced by microglia and stored in the cytosol as an inactive precursor (**Fig. 6.7e**)[94]. The most representative fingerprint peaks of IL-18 are identified at 1259–1261 cm^{-1}, from the amide III stretching of C-N and bending of N-H, specific to proteins[194], [195], and a sharp peak at 806 cm^{-1}, assigned to the protein-specific symmetrical stretch of C-N-C bonds[104]. Following TBI, IL-18 is known to externalise and bind to the plasma membrane. Uncontrolled or dysregulated IL-18 can lead to releases of neurotoxic enzymes as well as cause chronic inflammatory diseases, whilst IL-18 inhibition has been shown to prevent further damage[95], [196].

Finally, the NFL marker has been shown to play a role in maintaining the axonal cytoskeleton[97], and although not necessarily specific to TBI, its rapid increase in CSF is indicative of a considerable axonal injury with change in its concentration correlating the severity of damage[98]. It has been therefore suggested that monitoring the NFL levels is useful for determining the extent of trauma as well as the response

to any therapeutic interventions[99]. This marker exhibits a characteristic spectral fingerprint consisting of sharp peaks (**Fig. 6.7f**), with the most prominent at 891–893 cm^{-1}, due to symmetrical stretching of carboxylic acids and C-C bonds[166], [167], and the 1321–1323 cm^{-1}, attributed to CH bending and CH_2 twisting modes[182], [183].

Further to the spectral assignments of brain-specific molecular species, it is of importance to consider the identified and selected group of correlative changes in Raman peak ratios with key features of these representing quantifiable biochemical changes. The use of characteristic Raman peak ratios allows for the important information to be easily extracted from spectra (particularly, for multiplex mixtures in complex biological environments such as the body fluid or brain tissue) to gain more information and in conjunction with multivariate analysis methods, the ratio-metric inspection and assignment of Raman spectra can be used to identify spectral changes informed by chemical and spectroscopic knowledge, showing clear systematic trends with identifiable features of biomolecules. With these key Raman peak ratios correlating with structural and quantitative biomarker information, analysis of fingerprint spectra could be performed more accurately than the individual peak changes, which could be often masked in complex biofluids. We have thus utilised dominant peak ratios of the solute state TBI biomarkers, which also allows comparison of their variation across the four excitation wavelength lasers (**Fig. 6.8**).

Characteristic peaks were selected without bias from the six assigned bands identified via the peak pick method for each studied biomarker in acute, sub-acute and chronic phases, generating the unique intensity ratios barcode in the fingerprint region. The use of the relative peak ratio intensity provides more accurate and reproducible information over the absolute Raman intensity, which differs among different Raman devices and changing conditions, and is of further importance for multivariate analysis methods often employed in conjunction with Raman spectroscopy detection and analysis [197], [198]. These peak ratios yield the combined unique spectroscopic barcode for each brain-injury marker, which could be used as a reference for rapid and accurate diagnostics of TBI in easily accessible biofluids as well as allow to easier quantify the performance of emerging spectroscopic techniques via the standard variation of the ratios between the amplitudes of two Raman bands from a given biomarker over repeated measurements (**Fig. 6.8**). For the majority of the biomarkers, within the experimental error, there was no significant difference in the identified peak ratios when varying the excitation laser except for GFAP, sulfatide and glucose (p *** < 0.0001, one-way ANOVA), which had the largest variance per phase group, with sulfatide having the highest variance of the entire cohort ($\sigma^2 = 0.158$). This suggests that greater consideration should be given to the choice of the Raman excitation laser to detect this biomarker since the molecular bonds of interest are excited at varied intensity strengths depending on the laser wavelength. Conversely, UCHL1, cardiolipin, and IL-18 exhibited the lowest variance within their corresponding phase group, with the lowest overall cohort variance found to be for UCHL1 ($\sigma^2 = 0.000164$) with the highest peak agreement amongst the four excitation lasers.

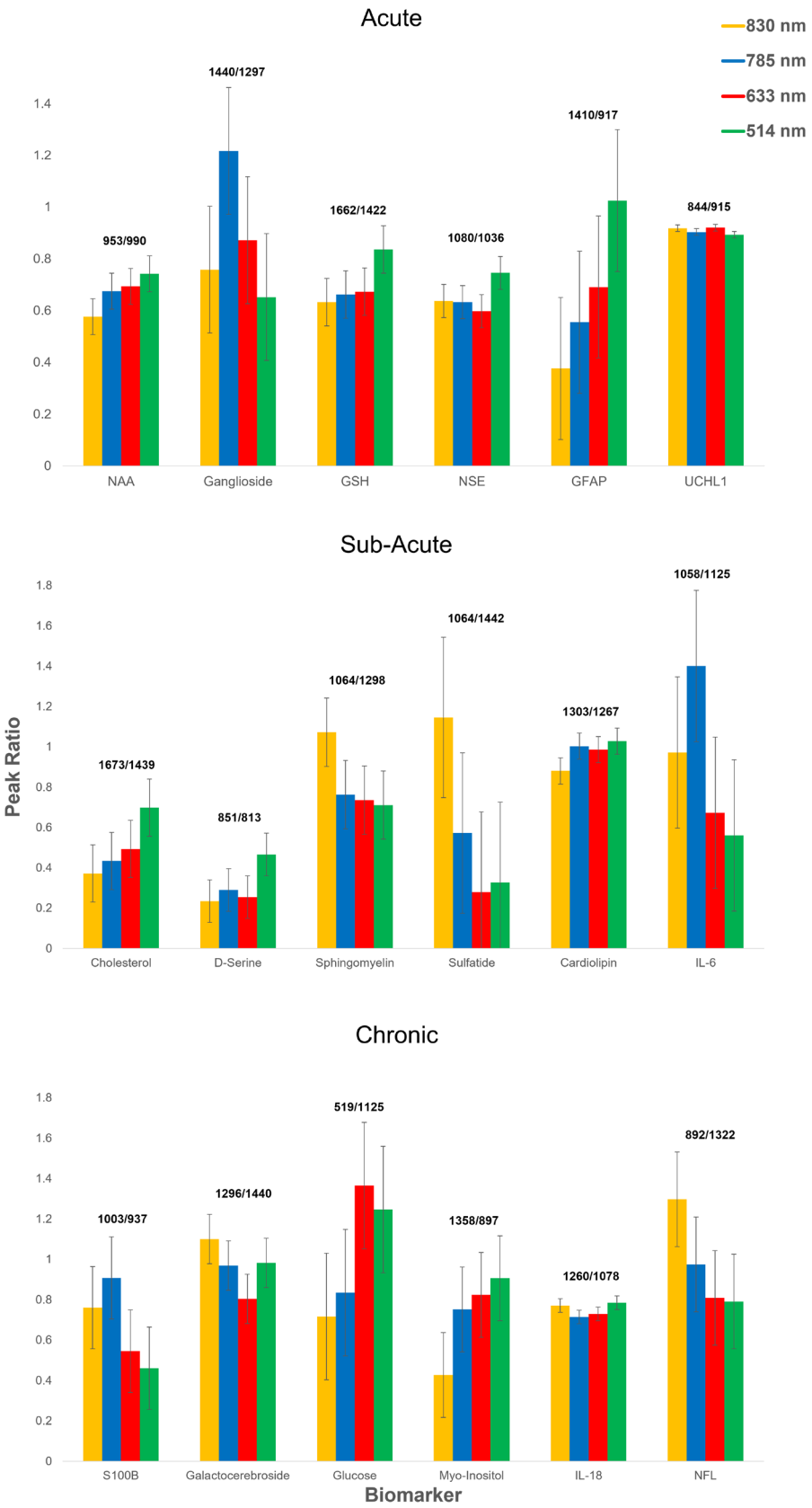

*Figure 6.8. Characteristic peak ratios identified from spectral fingerprints per each studied TBI-indicative biomarker at four excitation wavelengths of 514nm (green), 633nm (red), 785nm (blue) and 830nm (yellow). (p***<0.0001, one-way ANOVA).*

6.3.3 Injury Profiling in Fresh *ex vivo* Porcine Retinae

The motivation of this study was to provide a library of spectra and peak assignments to aid future TBI and Raman spectroscopy research, not only as a reference but also, to create prospective biomarker panels for injury profiling. During the optimisation and first use of the 635 nm and 830 nm portable Raman devices, fresh *ex vivo* porcine retinae, for which the pigs were stunned and rendered unconscious for slaughter, modelling mild – to – -moderate TBI. This biomarker library can now be utilised for injury profiling of the portable spectral data of porcine retinae.

For PoC diagnostics, the acute phase is essential, and therefore the acute panel of potential TBI biomarkers is of interest. **Fig. 6.9a** overlays the 6 prospective acute TBI biomarker panel using a 633 nm laser wavelength, in the 2000 – 3200 cm^{-1} high wavenumber region which was investigated in **Section 2.4** in **Chapter 2** with the EyeD device. In this region, there are only contributing peaks from ganglioside (green), GSH (pink) and NSE (red), whilst the remaining three biomarkers NAA (light blue), GFAP (yellow) and UCHL1 (dark blue) sit underneath the more dominant peaks. Although this is now a small panel, looking at the trace (yellow) of the acute biomarker panel (**Fig. 6.9b(i)**) there is clear agreement with the shape of the porcine spectrum produced by the SKiNET SOMDI of the trauma retinal model using the 635 nm portable Raman system featured in the left panel of **Fig. 6.9b(ii).** The grey bars in **Fig. 6.9b(i)** illustrate the location of the characteristic peaks at 2851 and 2922 cm^{-1} from ganglioside and NSE, respectively. These match the locations of the peaks of interest 2850 and 2930 cm^{-1} in the right panel of **Fig. 6.9b (ii).**

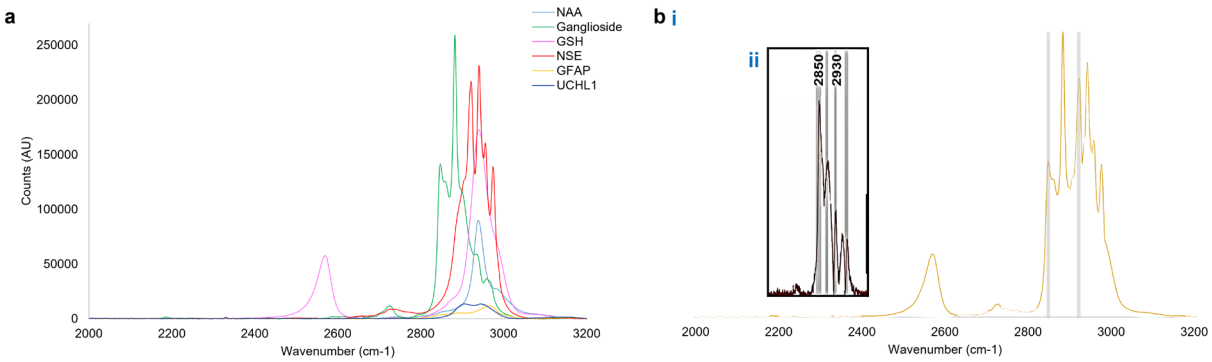

Figure 6.9. ***a*** *Overlayed spectra of the 633 nm panel of acute TBI biomarkers, cropped in the high wavenumber region (2000-3200 cm^{-1}). The combined spectra were collected with comparable Raman parameters in laser power, objective lens and acquisition time. There are no contributing peaks from NAA (light blue), GFAP (yellow) and UCHL1 (dark blue).* ***b (i)*** *Trace of the overlayed 633 nm panel of acute TBI biomarkers, with contributing peaks from ganglioside, GSH, NSE. Two grey bars illustrate the location of two characteristic peaks at 2851 and 2922 cm^{-1} from ganglioside and NSE, respectively.* ***(ii)*** *Insert from Chapter 2 showing the high wavenumber region of:* ***(ii) Fig. 2.10b:*** *A TBI porcine retinal sample spectrum produced by the 635 nm portable Raman system (EyeD), illustrating two peaks of interest at 2850 and 2930 cm^{-1}, in agreement with peaks present in spectra of the three-contributing acute TBI biomarkers in* ***(i).***

The development of the 830 nm portable Raman system is in the early prototype stage and built with components that are more modifiable than that of the 635 nm EyeD device, therefore there are more opportunities to customise the 830 nm system for uses other than PoC diagnostics. For example, the application of near-infra-red wavelengths for low-level light therapy (LLLT) is a growing field of literature, harnessing the deep tissue penetration depth and phototherapeutic properties of wound healing and reduction of apoptosis[199]–[201]. It is therefore of interest to look at all three TBI phases when creating traces for hypothetical models for prospective biomarker panels. The overlayed spectra of each TBI phase are provided in the left-hand side column of **Fig. 6.10,** for which all powers are matched**.** These overlays suggest that GSH (pink) and GFAP (yellow) in the acute phase group, alongside sulfatide (red) in the sub-acute group, could be excluded from our group of prospective biomarkers as they do not contribute peaks to their respective panel of stronger spectra; whilst all chronic phase biomarkers contribute.

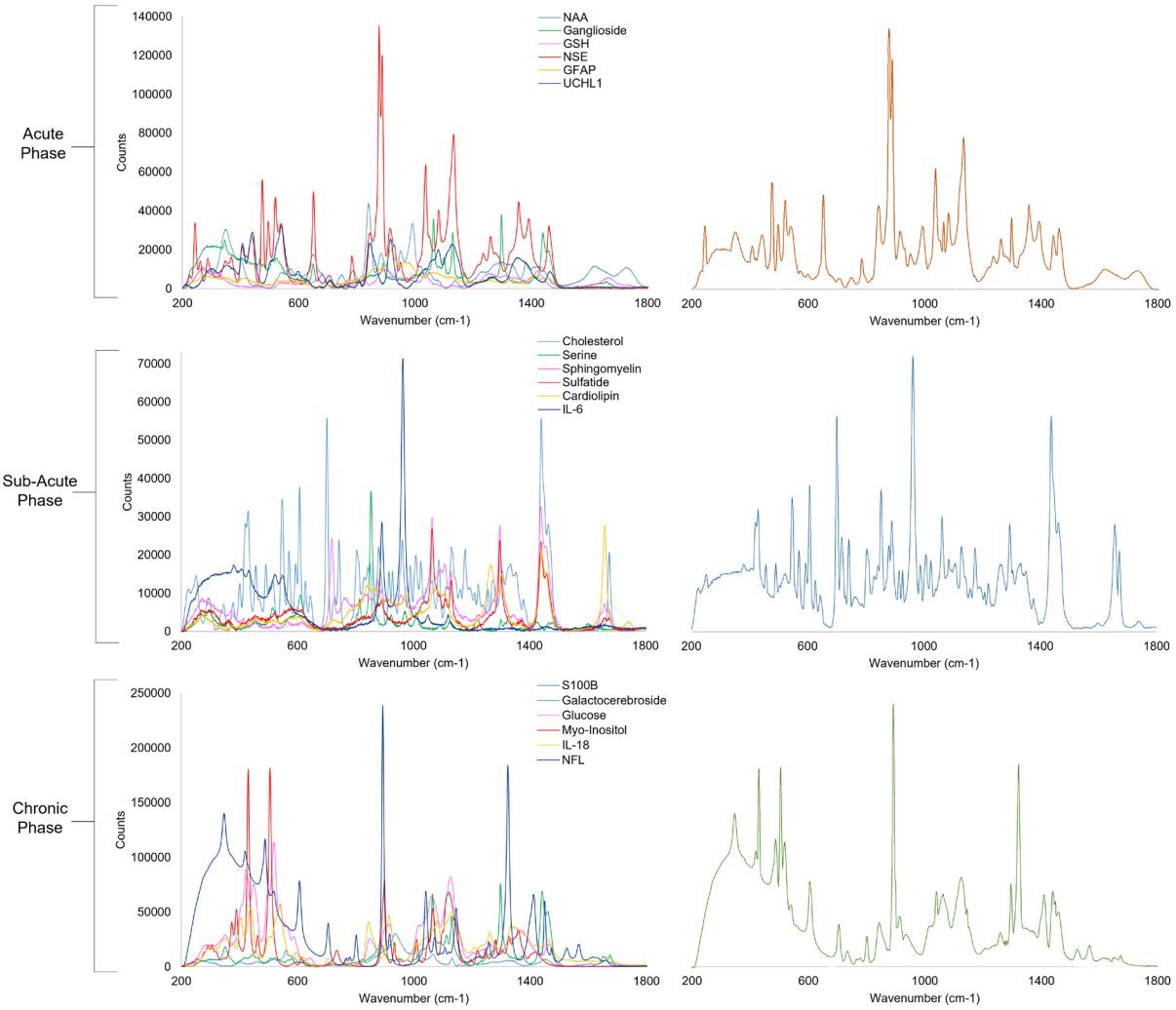

Figure 6.10. Overlayed spectra of the biomarkers within each phase group using an 830 nm excitation wavelength. The combined spectra were collected with comparable Raman parameters in laser power, objective lens and acquisition time. ***(left)*** *In the acute phase, all biomarkers contribute peaks to the overlay except for GSH (pink) and GFAP (yellow) which sit underneath the stronger spectra. In the sub-acute phase, only sulfatide (red) does not contribute peaks to the overlay, whereas in the chronic phase all biomarkers contribute peaks.* ***(right)*** *The traces produced of the uppermost line of the combined spectra per TBI phase, this produces three hypothetical spectral panels that could model what peaks may be present if all prospective biomarkers are profiled when diagnosing in each phase group.*

In the right-hand side column of **Fig. 6.10** are traces produced of the uppermost line of the combined spectra per TBI phase, this produces three hypothetical spectral panels that could model what peaks may be present if all prospective biomarkers are profiled when diagnosing in each phase group. Whilst this is a method to hypothesise the three multiplex biomarker panels for TBI diagnostics and monitoring over 1 hour to 6 months, actual biomarker elevation/depletion may differ *in vitro* and *in vivo* TBI samples.

In the **Chapter 1** literature review, I combined current article findings from research surrounding both TBI and ocular manifestations of neurodegeneration to produce a table of prospective TBI biomarkers that may be changeable and detectable in the retina or optic nerve (**Table 1.2**)**.** This table was used as a foundation for the prospective TBI biomarker cohort chosen for this study, though not all were able to be sourced in the correct state, in pure form or within budget, resulting in a shortlist of NAA, GSH, NSE, GFAP, UCHL1 and S100B. Ganglioside and cardiolipin were added to the eye-based cohort once being investigated in **Chapter 2.** The now eight, eye-based TBI biomarkers were overlayed using the 830 nm excitation wavlength, and it can be observed in **Fig. 6.11a,** that only the GSH (grey) and GFAP (red) spectra cannot be seen above the stronger peaks. This results in six biomarkers contributing spectral information to the trace in **Fig. 6.11b,** producing a hypothetical model of biomarkers indicating neuro-injury in the retina.

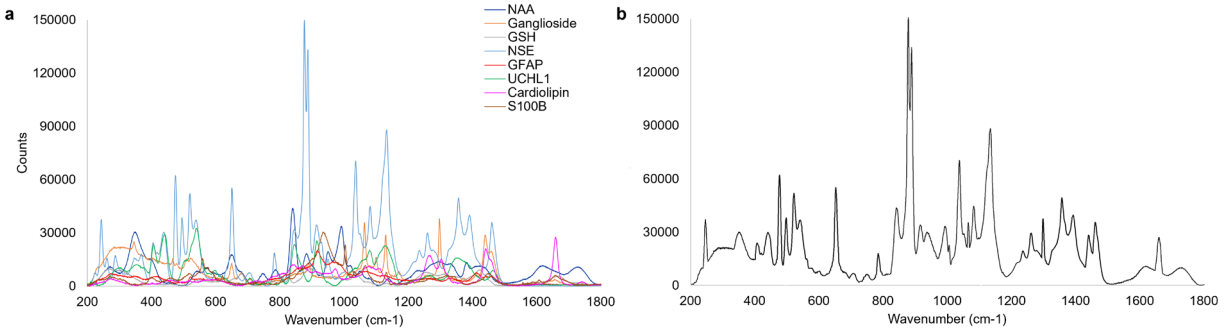

Figure 6.11. ***(left)*** *Overlayed spectra of eight TBI biomarkers that are prospective indicators of neuro-injury in the retina using an 830 nm excitation wavelength. The combined spectra were collected with comparable Raman parameters in laser power, objective lens and acquisition time. All biomarkers have visible characteristic peaks except for GSH (grey) and GFAP (red), which remain underneath the uppermost line of the combined spectrum.* ***(right)*** *Trace of the uppermost line of the combined spectrum, to produce a hypothetical spectrum of the panel of eye-based TBI biomarkers*

The 830 nm spectrum trace of eye-based TBI biomarker panel can then be utilised for injury profiling of the fresh, *ex vivo* porcine retinal trauma samples for which spectra were obtained using the 830 nm portable Raman system in **Chapter 5.** A direct comparison between the two spectra is given in **Fig. 6.12a,** with the eye-based TBI biomarker panel trace (black) above the retina spectrum (red), where the grey bars illustrate the characteristic peaks identified in **Fig. 5.6** of **Chapter 5,** five of which are shared between the two spectra. To demonstrate this closely, **Fig. 6.12b** features a cropped view of the overlayed eye-based biomarker spectra with five grey bars representing characteristic peaks in the porcine retina spectrum, matching with NSE (light blue) and NAA (dark blue) peaks. Underneath the uppermost spectrum, the five characteristic peaks can be seen to be present in other biomarker spectra such as

UCHL1 (green) and cardiolipin (pink), but with lower counts; these will be of importance when we consider that TBI biomarkers are subject to increase or decrease following injury, as described in **Table 6.1.** A shortened version of the assignment table (**Table 5.2**) from **Chapter 5** is provided in **Fig. 6.12c,** featuring only the peaks present in both the eye-based TBI biomarker panel trace and the retina spectrum produced by the 830 nm portable Raman system.

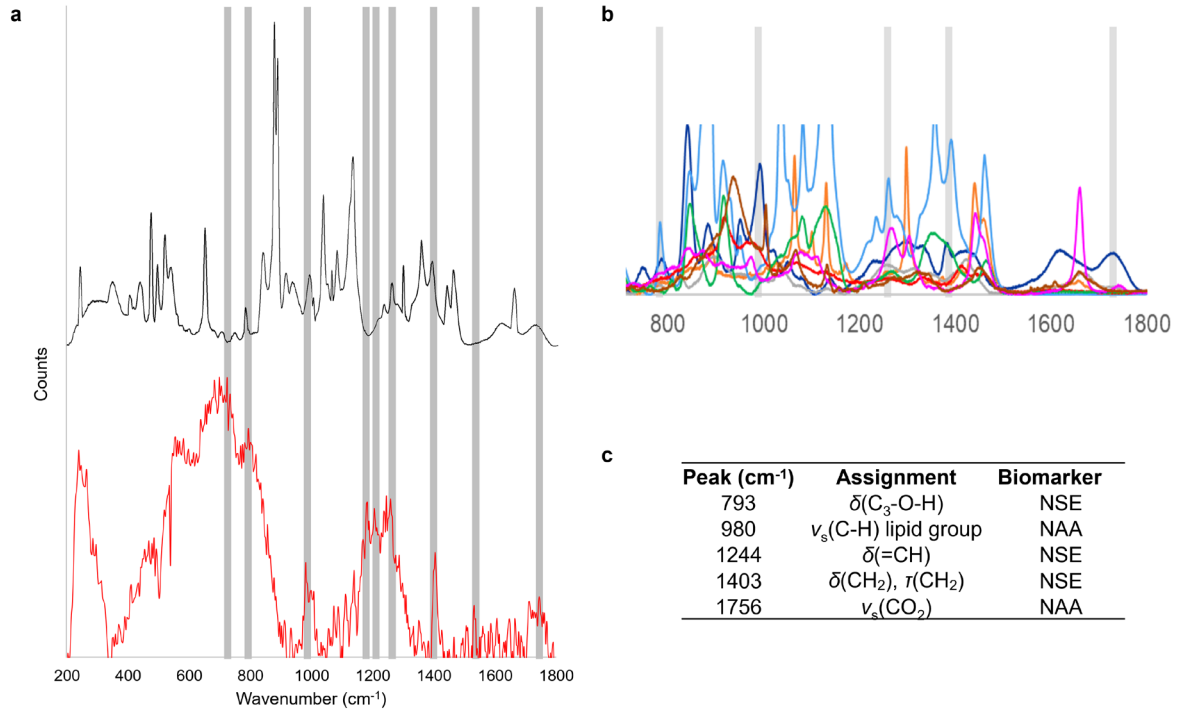

Peak (cm^{-1})	Assignment	Biomarker
793	$\delta(C_3\text{-O-H})$	NSE
980	ν_s(C-H) lipid group	NAA
1244	δ(=CH)	NSE
1403	$\delta(CH_2)$, $\tau(CH_2)$	NSE
1756	$\nu_s(CO_2)$	NAA

Figure 6.12. Injury profiling and barcoding of the characteristic peaks previously identified in fresh ex vivo *porcine retina in* ***Figure 5.6*** *translated to the overlayed spectral trace of prospective eye-based TBI biomarkers using an 830 nm excitation wavelength.* ***a*** *Comparison of the overlayed eye-based TBI biomarker panel spectrum trace (black) and averaged spectrum of fresh porcine retinae obtained by the portable Raman system (red). The red spectrum produced by the portable Raman system, with the nine grey bars highlighting the location of peaks of interest and originally features in* ***Figure 5.6*** *and* ***Table 5.2 in Chapter 5.*** *Porcine retinae spectrum of 12 retinal samples, 10 single spectra obtained from each retina of 30 second acquisitions, at 2.4 mW power, biomarker panel spectrum was acquired with a 50× objective lens, a 10 s acquisition with 5 accumulations, and approximate 75 mW laser power.* ***b*** *A cropped view of the characteristic peaks from the porcine retinae spectrum (indicated by the grey bars) present in the eye-based TBI biomarker spectrum. The eye-based TBI biomarker spectrum shares five of the nine peaks of interest, contributed from the NAA (dark blue) and NSE (light blue) peaks.* ***c*** *The five peaks of interest that overlap in the porcine and eye-based biomarker spectra, as assigned in* ***Table 5.2,*** *and the attributing biomarker to each peak.*

This analysis suggests the presence of NSE and NAA in the porcine retinal tissue in the acute phase of TBI at the time of slaughter, at this stage, it is only possible to conclude that NSE and NAA peaks could be detectable using the 830 nm portable device, further work would need to be done to confirm whether the presence of these peaks could indicate TBI or instead their elevation/depression needs to be monitored as a ratio could dictate TBI presence.

6.4 Current Challenges and Outlook

Overall, Raman-based diagnosis of TBI pathologies via biofluid detection is emerging as a promising tool for rapid PoC diagnostics, and with the addition of the identified molecular profiles, a simple process of a *'*spectroscopic barcode*'* will ensure variation due to the presence and/or change in the level of a particular TBI-indicative biomarker

and, further, treatments and various underlying conditions will be taken into account and reduce the error in the data interpretation of the associated changes, leading towards improved diagnostic accuracy.

It is worth noting, however, that whilst important progress has been accomplished herein via Raman spectroscopy spectral fingerprints of biomarkers of TBI, several limitations and challenges remain. Firstly, in terms of study design, biomarkers were sourced to avoid Raman-active additives such as buffers, which would impact the accuracy of the characters' fingerprint. This has, therefore, removed several candidate biomarkers identified in the literature since pure forms were not available. Furthermore, we used a varied source of human/animal TBI biomarkers, with five out of the overall eighteen investigated biomarkers derived from animals, due to limitations in availability. Whilst animal model systems frequently share similarities of specific aspects of TBIs, providing the opportunity to target specific biomarkers, animal neuromarker models, however, can occasionally recapitulate only parts of the pathology observed in human TBI [202]–[207].

Recognising the opportunities and limitations of translational biomarkers is therefore critical to advancing human TBI therapies. Importantly, this study aims to bridge the gap between preclinical and clinical research as well as to better demonstrate interactions between central expression of TBI pathological markers and peripheral examinations, which could subsequently be used for diagnosis and evaluation of treatment efficacy. Nevertheless, it is important to note, that we did not carry out spectroscopic detection and classification of TBI vs. healthy biomarkers but rather established the characteristic fingerprints for each chosen biomarker, which is a standalone spectroscopic barcode for either human- or animal-derived neuromarkers. In each case, there is a value and significance to having the 'baseline' fingerprint data, as in the case of a rapidly evolving and multifaceted pathology such as TBI, they may provide integrative and complementary clinically useful information or may be useful for different investigations, time points, or settings. For instance, animal biomarker models provide a major advantage for investigating preclinical measures of therapeutic efficacy [202], [203]. Faster and less expensive results can be garnered from these allowing only the most promising candidates to advance to more costly clinical trials (e.g., Sabbagh et al. [208]) and represent an important approach to exploring the translational utility of a novel compound.

In preclinical systems, animal biomarkers could also be effective for valuing the translational worth of a compound before costly human trials are initiated. Animal model biomarker assessments can verify proof of concept for a candidate treatment. Furthermore, the identification of consistent biomarkers may shed light on core mechanisms responsible for the disorder, as well as interactions between several of the identified pathologies. Notably, the subsequent use of both human and animal biomarkers can form a bridge between animal and human studies to facilitate translational research. By using the same biomarkers in animals and humans, observations in the preclinical stage can be more easily extended to clinical trials. This forward translation can be complemented by a backward one, where observations in humans can be studied via animals.

An additional challenge is that the spectral bands associated with some biomarkers are also present in several other proteins, and so these changes cannot always solely

be attributed to a particular molecule. Therefore, a broad panel of biomarkers should be used in such cases, essential to delivering a diagnosis with high accuracy and specificity. This, with further emerging novel hybrid Raman-AI techniques [209], [210], will in turn enable supporting large-scale triaging and screening for early signs of brain injury, particularly useful for identifying high-risk patients and implementing intervention measures, given both the increased incidence and the prevalence of TBIs. Indeed, considerable research in recent years has focused on potential biomarkers to improve diagnosis and patient phenotyping to enable timely and targeted management. For instance, S100B has been implemented in Scandinavian countries and the ALERT-TBI study showed high sensitivity for the combination of GFAP and neuronal UCHL1 measured within 12 h of injury, forming the basis of the first FDA-approved TBI test for triaging the need for CT scanning [211].

One further issue that needs to be addressed for real-world adoption is a lack of standardisation in methods used within the current literature, from matters pertaining to biofluid collection, storage and pre-processing, to those concerning Raman measurement protocols and chemometric analyses and classification. Standardisation of protocols and conducting larger-scale clinical studies are vital for advancing the clinical translation of Raman spectroscopy biomarker profiling in TBI diagnostic and prognostic applications. Finally, there has been an increase in the literature surrounding the development of Raman spectroscopy-based technologies for TBI detection, utilising surface-enhanced Raman spectroscopy (SERS), microfluidics, and Raman probes [33], [35], [36], [212], [213]. As such new spectroscopic technologies are being engineered and prototyped, it is essential to improve the understanding of brain injury biomarkers and their mechanism in various post-TBI phases, which will continue to grow alongside these, particularly when utilising human biofluids and TBI models.

6.5 Conclusions

A Raman spectroscopy fingerprint library has been generated for a large cohort of TBI-indicative biomarkers. The spectral fingerprint of each studied biomarker generates a unique signature, and comparisons of certain values for determined frequencies and their raw and aqueous solution states are determined. These spectra provide the fundamental information necessary to track the biochemical changes induced by the neurological markers categorised according to the different stages of post-brain injury, i.e., the acute, sub-acute and chronic phases. These can not only assist in understanding the TBI mechanism and check the presence, persistence or fading of characteristic biomolecules in brain tissue or biofluids following injuries, but also establish Raman spectroscopy-aided diagnosis of TBI as a complementary point-of-need technique. The longer-term goal would be to identify biomarkers or distinctive patterns, which would help to rapidly detect, triage, and monitor TBIs by analysing the differences in Raman spectral signatures.

The most dominant peak ratios for each biomarker have been further identified, highlighting the various advantages amongst which by using the ratio-metric approach over the absolute Raman intensity of individual bands, eliminates the need to measure the amplitude of each peak, often necessary for ensuring consistency and reproducibility of the intensity and/or wavenumber position, which can be challenging between each measurement, especially when performed by a non-expert at the PoC.

Traces of overlayed spectra within each TBI phase produce hypothetical models of the unique spectral fingerprint that may be obtained when all biomarkers are present in a sample. These traces from the spectral library have been applied to fresh, *ex vivo,* porcine retinal trauma samples to profile for TBI by identifying biomarker peaks of interest in the retina spectra obtained using our in-house-built portable Raman devices. This analysis suggests the presence of acute TBI biomarkers present in trauma retina using 633 / 635 nm excitation wavelengths in the high wavenumber region, as well as eye-based TBI biomarkers present when using 830 nm excitation wavelengths in the fingerprint region.

Reliable PoC diagnostic tools, such as Raman spectroscopy, could improve the specificity of diagnosis and triage of TBI and would greatly aid resource availability in healthcare by reducing the number of unnecessary ED visits for mild TBI and increasing the proportion of patients with moderate/severe TBIs appropriately triaged to attend trauma facilities. With millions of ED visits every year and the high cost per visit without treatment or investigation, even a small reduction will result in massive cost savings. Furthermore, the pathophysiology of injury evolution is multi-faceted, and not understood well enough to provide effective pharmacological targeting to reduce burden or progression. An in-depth understanding of the biochemical injury evolution will allow interventions to be used more effectively and identify novel therapeutic targets to guide tactful treatments. The generated spectral library would further assist in the emerging developments of Raman spectroscopy-based technologies, for rapid acquisition of molecular fingerprints of TBI biochemistry to safely measure proxies for cerebral injury via the body fluids, which will soon provide a tangible path towards non-invasive PoC diagnostics for TBI.

6.6 References

[1] A. Khellaf, D. Z. Khan, and A. Helmy, “Recent advances in traumatic brain injury,” *J. Neurol.*, vol. 266, no. 11, pp. 2878–2889, Nov. 2019, doi: 10.1007/s00415-019-09541-4.

[2] A. Capizzi, J. Woo, and M. Verduzco-Gutierrez, “Traumatic Brain Injury: An Overview of Epidemiology, Pathophysiology, and Medical Management,” *Med. Clin. North Am.*, vol. 104, no. 2, pp. 213–238, Mar. 2020, doi: 10.1016/j.mcna.2019.11.001.

[3] K. K. Wang *et al.*, “An update on diagnostic and prognostic biomarkers for traumatic brain injury,” *Expert Rev. Mol. Diagn.*, vol. 18, no. 2, pp. 165–180, Feb. 2018, doi: 10.1080/14737159.2018.1428089.

[4] H. Adrian, K. Mårten, N. Salla, and V. Lasse, “Biomarkers of traumatic brain injury: Temporal changes in body fluids,” *eNeuro*, vol. 3, no. 6, pp. 1–13, Dec. 2016, doi: 10.1523/ENEURO.0294-16.2016.

[5] A. Ercole, E. P. Thelin, A. Holst, B. M. Bellander, and D. W. Nelson, “Kinetic modelling of serum S100b after traumatic brain injury,” *BMC Neurol.*, vol. 16, no. 1, p. 93, Jun. 2016, doi: 10.1186/s12883-016-0614-3.

[6] S. M. Lippa, J. K. Werner, M. C. Miller, J. M. Gill, R. Diaz-Arrastia, and K. Kenney, “Recent Advances in Blood-Based Biomarkers of Remote Combat-Related Traumatic Brain Injury,” *Curr. Neurol. Neurosci. Rep.*, vol. 20, no. 12, Dec. 2020, doi: 10.1007/s11910-020-01076-w.

[7] F. H. Kobeissy *et al.*, “Neuroproteomics and systems biology-based discovery of protein biomarkers for traumatic brain injury and clinical validation,” *Proteomics - Clin. Appl.*, vol. 2, no. 10–11, pp. 1467–1483, 2008, doi: 10.1002/prca.200800011.

[8] D. V. Agoston, A. Shutes-David, and E. R. Peskind, “Biofluid biomarkers of traumatic brain injury,” *Brain Inj.*, vol. 31, no. 9, pp. 1195–1203, Jul. 2017, doi: 10.1080/02699052.2017.1357836.

[9] P. Shahim *et al.*, “Time course and diagnostic utility of NfL, tau, GFAP, and UCH-L1 in subacute and chronic TBI,” *Neurology*, vol. 95, no. 6, pp. e623–e636, Aug. 2020, doi: 10.1212/WNL.0000000000009985.

[10] R. Rubenstein *et al.*, “Comparing plasma phospho tau, total tau, and phospho tau–total tau ratio as acute and chronic traumatic brain injury biomarkers,” *JAMA Neurol.*, vol. 74, no. 9, pp. 1063–1072, Sep. 2017, doi: 10.1001/jamaneurol.2017.0655.

[11] J. Chitturi, Y. Li, V. Santhakumar, and S. S. Kannurpatti, “Consolidated biochemical profile of subacute

stage traumatic brain injury in early development," *Front. Neurosci.*, vol. 13, no. MAY, p. 431, May 2019, doi: 10.3389/FNINS.2019.00431/BIBTEX.
[12] M. C. Dewan *et al.*, "Estimating the global incidence of traumatic brain injury," *J. Neurosurg.*, vol. 130, no. 4, pp. 1080–1097, Apr. 2019, doi: 10.3171/2017.10.JNS17352.
[13] G. Teasdale, A. Maas, F. Lecky, G. Manley, N. Stocchetti, and G. Murray, "The Glasgow Coma Scale at 40 years: Standing the test of time," *Lancet Neurol.*, vol. 13, no. 8, pp. 844–854, 2014, doi: 10.1016/S1474-4422(14)70120-6.
[14] J. J. Bazarian, P. Veazie, S. Mookerjee, and E. B. Lerner, "Accuracy of mild traumatic brain injury case ascertainment using ICD-9 codes," *Acad. Emerg. Med.*, vol. 13, no. 1, pp. 31–38, Jan. 2006, doi: 10.1197/j.aem.2005.07.038.
[15] J. R. Huie, S. Mondello, C. J. Lindsell, and L. Antiga, "Biomarkers for Traumatic Brain Injury: Data Standards and Statistical Considerations," *J. Neurotrauma*, vol. 38, no. 18, pp. 2514–2529, Apr. 2021, doi: 10.1089/neu.2019.6762.
[16] W. R. McBride, N. R. Eltman, and R. L. Swanson, "Blood-Based Biomarkers in Traumatic Brain Injury: A Narrative Review With Implications for the Legal System," *Cureus*, vol. 15, no. 6, Jun. 2023, doi: 10.7759/CUREUS.40417.
[17] I. Mavroudis, F. Petridis, I. M. Balmus, A. Ciobica, D. L. Gorgan, and A. C. Luca, "Review on the Role of Salivary Biomarkers in the Diagnosis of Mild Traumatic Brain Injury and Post-Concussion Syndrome," *Diagnostics (Basel, Switzerland)*, vol. 13, no. 8, Apr. 2023, doi: 10.3390/DIAGNOSTICS13081367.
[18] J. Mozafari, M. A. Fahimi, K. Mohammadi, H. Barzegari, M. G. Hanafi, and A. Saki-Malehi, "The diagnostic accuracy of serum and urinary S100B protein in children and adolescents with mild traumatic brain injury."
[19] H. Zetterberg and K. Blennow, "Fluid markers of traumatic brain injury," *Mol. Cell. Neurosci.*, vol. 66, no. PB, pp. 99–102, May 2015, doi: 10.1016/J.MCN.2015.02.003.
[20] E. Cordero, I. Latka, C. Matthäus, I. Schie, and J. Popp, "In-vivo Raman spectroscopy: from basics to applications.," *J. Biomed. Opt.*, vol. 23, no. 7, pp. 1–23, 2018, doi: 10.1117/1.JBO.23.7.071210.
[21] E. B. Hanlon *et al.*, "Prospects for in vivo Raman spectroscopy," *Physics in Medicine and Biology*, vol. 45, no. 2. pp. R1-59, Feb. 2000, doi: 10.1088/0031-9155/45/2/201.
[22] S. Guo, T. Bocklitz, and J. Popp, "Optimization of Raman-spectrum baseline correction in biological application," *Analyst*, vol. 141, no. 8, pp. 2396–2404, Apr. 2016, doi: 10.1039/C6AN00041J.
[23] Z. Birech, P. W. Mwangi, F. Bukachi, and K. M. Mandela, "Application of Raman spectroscopy in type 2 diabetes screening in blood using leucine and isoleucine amino-acids as biomarkers and in comparative anti-diabetic drugs efficacy studies," *PLoS One*, vol. 12, no. 9, p. e0185130, Sep. 2017, doi: 10.1371/JOURNAL.PONE.0185130.
[24] H. J. Koster, A. Guillen-Perez, J. S. Gomez-Diaz, M. Navas-Moreno, A. C. Birkeland, and R. P. Carney, "Fused Raman spectroscopic analysis of blood and saliva delivers high accuracy for head and neck cancer diagnostics," *Sci. Rep.*, vol. 12, no. 1, pp. 1–13, Nov. 2022, doi: 10.1038/s41598-022-22197-x.
[25] E. Ryzhikova *et al.*, "Raman spectroscopy and machine learning for biomedical applications: Alzheimer's disease diagnosis based on the analysis of cerebrospinal fluid," *Spectrochim. Acta. A. Mol. Biomol. Spectrosc.*, vol. 248, Mar. 2021, doi: 10.1016/J.SAA.2020.119188.
[26] R. Sathyavathi *et al.*, "Raman spectroscopy provides a powerful, rapid diagnostic tool for the detection of tuberculous meningitis in ex vivo cerebrospinal fluid samples," *J. Biophotonics*, vol. 6, no. 8, p. 567, Aug. 2013, doi: 10.1002/JBIO.201200110.
[27] C. Chen *et al.*, "Urine Raman spectroscopy for rapid and inexpensive diagnosis of chronic renal failure (CRF) using multiple classification algorithms," *Optik (Stuttg).*, vol. 203, p. 164043, Feb. 2020, doi: 10.1016/J.IJLEO.2019.164043.
[28] V. Kavuru, R. S. Senger, J. L. Robertson, and D. Choudhury, "Analysis of urine Raman spectra differences from patients with diabetes mellitus and renal pathologies," *PeerJ*, vol. 11, Feb. 2023, doi: 10.7717/PEERJ.14879/SUPP-1.
[29] E. Buchan, M. Hardy, P. de C. Gomes, L. Kelleher, H. O. M. Chu, and P. G. Oppenheimer, "Emerging Raman spectroscopy and saliva-based diagnostics: from challenges to applications," *Appl. Spectrosc. Rev.*, 2022, doi: 10.1080/05704928.2022.2130351.
[30] S. Kim *et al.*, "Label-Free Surface-Enhanced Raman Spectroscopy Biosensor for On-Site Breast Cancer Detection Using Human Tears," *ACS Appl. Mater. Interfaces*, vol. 12, no. 7, pp. 7897–7904, 2020, doi: 10.1021/acsami.9b19421.
[31] C. Camerlingo *et al.*, "Characterization of human tear fluid by means of surface-enhanced raman spectroscopy," *Sensors*, vol. 19, no. 5, pp. 1–9, 2019, doi: 10.3390/s19051177.
[32] G. Cennamo *et al.*, "Surface-enhanced Raman spectroscopy of tears: toward a diagnostic tool for neurodegenerative disease identification," *J. Biomed. Opt.*, vol. 25, no. 08, p. 1, 2020, doi: 10.1117/1.jbo.25.8.087002.
[33] J. J. S. Rickard, V. Di-Pietro, D. J. Smith, D. J. Davies, A. Belli, and P. G. Oppenheimer, "Rapid optofluidic detection of biomarkers for traumatic brain injury via surface-enhanced Raman spectroscopy," *Nat. Biomed. Eng.*, vol. 4, no. 6, pp. 610–623, Feb. 2020, doi: 10.1038/s41551-019-0510-4.
[34] C. Li, K. A. Shah, and R. K. Narayan, "Rapid detection of traumatic brain injury," *Nat. Biomed. Eng.*, vol. 4, no. 6, pp. 579–580, Jun. 2020, doi: 10.1038/s41551-020-0574-1.
[35] M. Mowbray, C. Banbury, J. J. S. Rickard, D. J. Davies, and P. Goldberg Oppenheimer, "Development and Characterization of a Probe Device toward Intracranial Spectroscopy of Traumatic Brain Injury," *ACS*

Biomater. Sci. Eng., vol. 7, pp. 1252–1262, Mar. 2021, doi: 10.1021/acsbiomaterials.0c01156.
[36] A. R. Stevens *et al.*, “Raman Spectroscopy as a Neuromonitoring Tool in Traumatic Brain Injury: A Systematic Review and Clinical Perspectives,” *Cells*, vol. 11, no. 7, pp. 1–22, Apr. 2022, doi: 10.3390/CELLS11071227.
[37] C. Feinberg *et al.*, “Association of Pharmacological Interventions With Symptom Burden Reduction in Patients With Mild Traumatic Brain Injury: A Systematic Review,” *JAMA Neurol.*, vol. 78, no. 5, pp. 596–608, May 2021, doi: 10.1001/JAMANEUROL.2020.5079.
[38] M. Marro *et al.*, “Dynamic molecular monitoring of retina inflammation by in vivo Raman spectroscopy coupled with multivariate analysis,” *J. Biophotonics*, vol. 7, no. 9, pp. 724–734, 2014, doi: 10.1002/jbio.201300101.
[39] G. Harris *et al.*, “Review: Emerging Eye-Based Diagnostic Technologies for Traumatic Brain Injury,” *IEEE Rev. Biomed. Eng.*, vol. 16, pp. 530–559, 2023, doi: 10.1109/RBME.2022.3161352.
[40] A. E. Böhmer *et al.*, “Neuron-specific enolase, S100B, and glial fibrillary acidic protein levels as outcome predictors in patients with severe traumatic brain injury,” *Neurosurgery*, vol. 1. Böhmer, no. 6, pp. 1624–1630, Jun. 2011, doi: 10.1227/NEU.0b013e318214a81f.
[41] M. U. Gutierre, J. P. M. Telles, L. C. Welling, N. N. Rabelo, M. J. Teixeira, and E. G. Figueiredo, “Biomarkers for traumatic brain injury: a short review,” *Neurosurg. Rev.*, vol. 44, no. 4, pp. 2091–2097, Aug. 2021, doi: 10.1007/S10143-020-01421-0.
[42] H. Zetterberg, D. H. Smith, and K. Blennow, “Biomarkers of mild traumatic brain injury in cerebrospinal fluid and blood,” *Nat. Rev. Neurol.*, vol. 9, no. 4, p. 201, Apr. 2013, doi: 10.1038/NRNEUROL.2013.9.
[43] B. Damien, O. Charlotte, B. Marina, D. Julie, and S. Vincent, “Interest of blood biomarkers to predict lesions in medical imaging in the context of mild traumatic brain injury,” *Clin. Biochem.*, Aug. 2020, doi: 10.1016/j.clinbiochem.2020.08.001.
[44] A. S. Woods *et al.*, “Gangliosides and CeramidesChange in a Mouse Model of Blast Induced Traumatic Brain Injury,” *ACS Chem. Neurosci.*, vol. 4, no. 4, p. 594, Apr. 2013, doi: 10.1021/CN300216H.
[45] H. J. Kim, J. W. Tsao, and A. G. Stanfill, “The current state of biomarkers of mild traumatic brain injury,” *JCI insight*, vol. 3, no. 1, Jan. 2018, doi: 10.1172/jci.insight.97105.
[46] J. R. Moffett, P. Arun, P. S. Ariyannur, and A. M. A. Namboodiri, “N-Acetylaspartate reductions in brain injury: Impact on post-injury neuroenergetics, lipid synthesis, and protein acetylation,” *Front. Neuroenergetics*, vol. 5, no. DEC, p. 69505, Dec. 2013, doi: 10.3389/FNENE.2013.00011/BIBTEX.
[47] R. J. Shannon *et al.*, “Extracellular N -Acetylaspartate in Human Traumatic Brain Injury,” *J. Neurotrauma*, vol. 33, no. 4, pp. 319–329, Feb. 2016, doi: 10.1089/neu.2015.3950.
[48] A. Belli *et al.*, “Extracellular N-acetylaspartate depletion in traumatic brain injury,” *J. Neurochem.*, vol. 96, no. 3, pp. 861–869, 2006, doi: 10.1111/j.1471-4159.2005.03602.x.
[49] S. Sipione, J. Monyror, D. Galleguillos, N. Steinberg, and V. Kadam, “Gangliosides in the Brain: Physiology, Pathophysiology and Therapeutic Applications,” *Front. Neurosci.*, vol. 14, p. 1004, Oct. 2020, doi: 10.3389/FNINS.2020.572965/BIBTEX.
[50] L. Koza and D. Linseman, “Glutathione precursors shield the brain from trauma,” *Neural Regen. Res.*, vol. 14, no. 10, p. 1701, Oct. 2019, doi: 10.4103/1673-5374.257520.
[51] N. Khatri, M. Thakur, V. Pareek, S. Kumar, S. Sharma, and A. K. Datusalia, “Oxidative Stress: Major Threat in Traumatic Brain Injury,” *CNS Neurol. Disord. Drug Targets*, vol. 17, no. 9, pp. 689–695, Jun. 2018, doi: 10.2174/1871527317666180627120501.
[52] A. Haque, S. K. Ray, A. Cox, and N. L. Banik, “Neuron specific enolase: a promising therapeutic target in acute spinal cord injury,” *Metab. Brain Dis.*, vol. 31, no. 3, pp. 487–495, Jun. 2016, doi: 10.1007/S11011-016-9801-6/FIGURES/3.
[53] Z. Yang and K. K. W. Wang, “Glial fibrillary acidic protein: from intermediate filament assembly and gliosis to neurobiomarker,” *Trends Neurosci.*, vol. 38, no. 6, pp. 364–374, 2015, doi: 10.1016/J.TINS.2015.04.003.
[54] M. V. Sofroniew, “Molecular dissection of reactive astrogliosis and glial scar formation,” *Trends Neurosci.*, vol. 32, no. 12, pp. 638–647, Dec. 2009, doi: 10.1016/J.TINS.2009.08.002.
[55] S. F. Tzeng, H. Y. Hsiao, and O. T. Mak, “Prostaglandins and cyclooxygenases in glial cells during brain inflammation,” *Curr. Drug Targets. Inflamm. Allergy*, vol. 4, no. 3, pp. 335–340, Jun. 2005, doi: 10.2174/1568010054022051.
[56] H. Liu *et al.*, “Role of UCHL1 in axonal injury and functional recovery after cerebral ischemia,” *Proc. Natl. Acad. Sci. U. S. A.*, vol. 116, no. 10, pp. 4643–4650, Mar. 2019, doi: 10.1073/PNAS.1821282116/SUPPL_FILE/PNAS.1821282116.SAPP.PDF.
[57] S. Shahjouei *et al.*, “The diagnostic values of UCH-L1 in traumatic brain injury: A meta-analysis,” *https://doi.org/10.1080/02699052.2017.1382717*, vol. 32, no. 1, pp. 1–17, Jan. 2017, doi: 10.1080/02699052.2017.1382717.
[58] N. Nathoo, R. Chetty, J. R. Van Dellen, and G. H. Barnett, “Genetic vulnerability following traumatic brain injury: the role of apolipoprotein E,” *Mol. Pathol.*, vol. 56, no. 3, pp. 132–136, 2003, doi: 10.1136/MP.56.3.132.
[59] J. M. Surmacki, L. Ansel-Bollepalli, F. Pischiutta, E. R. Zanier, A. Ercole, and S. E. Bohndiek, “Label-free monitoring of tissue biochemistry following traumatic brain injury using Raman spectroscopy,” *Analyst*, vol. 142, no. 1, pp. 132–139, Jan. 2017, doi: 10.1039/c6an02238c.
[60] C. M. Cartagena *et al.*, “Cortical Injury Increases Cholesterol 24S Hydroxylase (Cyp46) Levels in the Rat Brain,” *J. Neurotrauma*, vol. 25, no. 9, p. 1087, Sep. 2008, doi: 10.1089/NEU.2007.0444.

[61] A. D. Kay, S. P. Day, M. Kerr, J. A. R. Nicoll, C. J. Packard, and M. J. Caslake, “Remodeling of Cerebrospinal Fluid Lipoprotein Particles after Human Traumatic Brain Injury,” *https://home.liebertpub.com/neu*, vol. 20, no. 8, pp. 717–723, Jul. 2004, doi: 10.1089/089771503767869953.
[62] H. Xu *et al.*, “Brain-specific loss of Abcg1 disturbs cholesterol metabolism and aggravates pyroptosis and neurological deficits after traumatic brain injury,” *Brain Pathol.*, vol. 33, no. 3, p. e13126, May 2023, doi: 10.1111/BPA.13126.
[63] S. A. Tapanes *et al.*, “Inhibition of glial D-serine release rescues synaptic damage after brain injury,” *Glia*, vol. 70, no. 6, p. 1133, Jun. 2022, doi: 10.1002/GLIA.24161.
[64] A. V. Alessenko and E. Albi, “Exploring Sphingolipid Implications in Neurodegeneration,” *Front. Neurol.*, vol. 11, p. 513554, May 2020, doi: 10.3389/FNEUR.2020.00437/BIBTEX.
[65] N. Schneider *et al.*, “Sphingomyelin in Brain and Cognitive Development: Preliminary Data,” *eNeuro*, vol. 6, no. 4, Jul. 2019, doi: 10.1523/ENEURO.0421-18.2019.
[66] J. O. Ojo *et al.*, “Converging and differential brain phospholipid dysregulation in the pathogenesis of repetitive mild traumatic brain injury and Alzheimer’s disease,” *Front. Neurosci.*, vol. 13, no. FEB, p. 416109, Feb. 2019, doi: 10.3389/FNINS.2019.00103/BIBTEX.
[67] G. Wang and E. Bieberich, “Sphingolipids in neurodegeneration (with focus on ceramide and S1P),” *Adv. Biol. Regul.*, vol. 70, pp. 51–64, Dec. 2018, doi: 10.1016/J.JBIOR.2018.09.013.
[68] K. Yang, W. C. Taft, C. E. Dixon, C. A. Todaro, R. K. yu, and R. L. Hayes, “Alterations of protein kinase C in rat hippocampus following traumatic brain injury,” *J. Neurotrauma*, vol. 10, no. 3, pp. 287–295, 1993, doi: 10.1089/NEU.1993.10.287.
[69] S. H. Lee *et al.*, “Acid Sphingomyelinase Inhibitor, Imipramine, Reduces Hippocampal Neuronal Death after Traumatic Brain Injury,” *Int. J. Mol. Sci. 2022, Vol. 23, Page 14749*, vol. 23, no. 23, p. 14749, Nov. 2022, doi: 10.3390/IJMS232314749.
[70] T. Takahashi and T. Suzuki, “Role of sulfatide in normal and pathological cells and tissues,” *J. Lipid Res.*, vol. 53, no. 8, pp. 1437–1450, Aug. 2012, doi: 10.1194/JLR.R026682.
[71] L. J. Sparvero *et al.*, “Imaging mass spectrometry reveals loss of polyunsaturated cardiolipins in the cortical contusion, hippocampus, and thalamus after traumatic brain injury,” *J. Neurochem.*, vol. 139, no. 4, pp. 659–675, Nov. 2016, doi: 10.1111/JNC.13840.
[72] G. Paradies, V. Paradies, F. M. Ruggiero, and G. Petrosillo, “Role of Cardiolipin in Mitochondrial Function and Dynamics in Health and Disease: Molecular and Pharmacological Aspects,” *Cells*, vol. 8, no. 7, Jul. 2019, doi: 10.3390/CELLS8070728.
[73] C. T. Chu, J. Ji, and R. K. Dagda, “Cardiolipin externalization to the outer mitochondrial membrane acts as an elimination signal for mitophagy in neuronal cells,” *Nat. Cell Biol. 2013 1510*, vol. 15, no. 10, pp. 1197–1205, Sep. 2013, doi: 10.1038/ncb2837.
[74] H. Chao *et al.*, “Cardiolipin-Dependent Mitophagy Guides Outcome after Traumatic Brain Injury,” *J. Neurosci.*, vol. 39, no. 10, pp. 1930–1943, Mar. 2019, doi: 10.1523/JNEUROSCI.3415-17.2018.
[75] G. Schett, “Physiological effects of modulating the interleukin-6 axis,” *Rheumatology*, vol. 57, no. suppl_2, pp. ii43–ii50, Feb. 2018, doi: 10.1093/RHEUMATOLOGY/KEX513.
[76] A. J. Williams, H. H. Wei, J. R. Dave, and F. C. Tortella, “Acute and delayed neuroinflammatory response following experimental penetrating ballistic brain injury in the rat,” *J. Neuroinflammation*, vol. 4, no. 1, pp. 1–12, Jul. 2007, doi: 10.1186/1742-2094-4-17/FIGURES/6.
[77] S. Z. Y. Ooi *et al.*, “Interleukin-6 as a prognostic biomarker of clinical outcomes after traumatic brain injury: a systematic review,” *Neurosurg. Rev.*, vol. 45, no. 5, pp. 3035–3054, Oct. 2022, doi: 10.1007/S10143-022-01827-Y.
[78] R. G. Kumar *et al.*, “Acute CSF interleukin-6 trajectories after TBI: Associations with neuroinflammation, polytrauma, and outcome,” *Brain. Behav. Immun.*, vol. 45, pp. 253–262, Mar. 2015, doi: 10.1016/J.BBI.2014.12.021.
[79] A. A. Antunes, V. S. Sotomaior, K. S. Sakamoto, C. P. de C. Neto, C. Martins, and L. R. Aguiar, “Interleukin-6 Plasmatic Levels in Patients with Head Trauma and Intracerebral Hemorrhage,” *Asian J. Neurosurg.*, vol. 5, no. 1, p. 68, Jan. 2010, Accessed: Apr. 17, 2023. [Online]. Available: /pmc/articles/PMC3198669/.
[80] H. Nishiyama, T. Knöpfel, S. Endo, and S. Itohara, “Glial protein S100B modulates long-term neuronal synaptic plasticity,” *Proc. Natl. Acad. Sci. U. S. A.*, vol. 99, no. 6, pp. 4037–4042, Mar. 2002, doi: 10.1073/PNAS.052020999/ASSET/46135AAC-0DC2-4BF9-B7E8-E51C2525A0D5/ASSETS/GRAPHIC/PQ0520209006.JPEG.
[81] A. Goyal *et al.*, “S100b as a Prognostic Biomarker in Outcome Prediction for Patients with Severe Traumatic Brain Injury,” *J. Neurotrauma*, vol. 30, no. 11, p. 946, Jun. 2013, doi: 10.1089/NEU.2012.2579.
[82] C. Krafft, L. Neudert, T. Simat, and R. Salzer, “Near infrared Raman spectra of human brain lipids,” *Spectrochim. Acta Part A Mol. Biomol. Spectrosc.*, vol. 61, no. 7, pp. 1529–1535, May 2005, doi: 10.1016/J.SAA.2004.11.017.
[83] R. M. N. Boustany, “Lysosomal storage diseases—the horizon expands,” *Nat. Rev. Neurol. 2013 910*, vol. 9, no. 10, pp. 583–598, Aug. 2013, doi: 10.1038/nrneurol.2013.163.
[84] J. Marcus and B. Popko, “Galactolipids are molecular determinants of myelin development and axo–glial organization,” *Biochim. Biophys. Acta - Gen. Subj.*, vol. 1573, no. 3, pp. 406–413, Dec. 2002, doi: 10.1016/S0304-4165(02)00410-5.
[85] J. Guan *et al.*, “Transplantation of human mesenchymal stem cells loaded on collagen scaffolds for the

treatment of traumatic brain injury in rats," *Biomaterials*, vol. 34, no. 24, pp. 5937–5946, Aug. 2013, doi: 10.1016/J.BIOMATERIALS.2013.04.047.
[86] P. Mergenthaler, U. Lindauer, G. A. Dienel, and A. Meisel, "Sugar for the brain: the role of glucose in physiological and pathological brain function," *Trends Neurosci.*, vol. 36, no. 10, p. 587, Oct. 2013, doi: 10.1016/J.TINS.2013.07.001.
[87] P. M. Vespa *et al.*, "Persistently low extracellular glucose correlates with poor outcome 6 months after human traumatic brain injury despite a lack of increased lactate: a microdialysis study," *J. Cereb. Blood Flow Metab.*, vol. 23, no. 7, pp. 865–877, Jul. 2003, doi: 10.1097/01.WCB.0000076701.45782.EF.
[88] I. Jalloh, K. L. H. Carpenter, A. Helmy, T. A. Carpenter, D. K. Menon, and P. J. Hutchinson, "Glucose metabolism following human traumatic brain injury: methods of assessment and pathophysiological findings," *Metab. Brain Dis.*, vol. 30, no. 3, pp. 615–632, Jun. 2015, doi: 10.1007/S11011-014-9628-Y/FIGURES/1.
[89] A. J. López-Gambero, C. Sanjuan, P. J. Serrano-Castro, J. Suárez, and F. R. De Fonseca, "The Biomedical Uses of Inositols: A Nutraceutical Approach to Metabolic Dysfunction in Aging and Neurodegenerative Diseases," *Biomed. 2020, Vol. 8, Page 295*, vol. 8, no. 9, p. 295, Aug. 2020, doi: 10.3390/BIOMEDICINES8090295.
[90] A. Brand, C. Richter-Landsberg, and D. Leibfritz, "Multinuclear NMR studies on the energy metabolism of glial and neuronal cells," *Dev. Neurosci.*, vol. 15, no. 3–5, pp. 289–298, 1993, doi: 10.1159/000111347.
[91] M. Haris, K. Cai, A. Singh, H. Hariharan, and R. Reddy, "In vivo mapping of brain myo-inositol," *Neuroimage*, vol. 54, no. 3, pp. 2079–2085, Feb. 2011, doi: 10.1016/J.NEUROIMAGE.2010.10.017.
[92] S. Ashwal *et al.*, "Proton Spectroscopy Detected Myoinositol in Children with Traumatic Brain Injury," *Pediatr. Res. 2004 564*, vol. 56, no. 4, pp. 630–638, Oct. 2004, doi: 10.1203/01.pdr.0000139928.60530.7d.
[93] A. S. Kierans *et al.*, "Myoinositol and glutamate complex neurometabolite abnormality after mild traumatic brain injury," *Neurology*, vol. 82, no. 6, p. 521, Feb. 2014, doi: 10.1212/WNL.0000000000000105.
[94] S. Alboni, D. Cervia, S. Sugama, and B. Conti, "Interleukin 18 in the CNS," *J. Neuroinflammation*, vol. 7, no. 1, pp. 1–12, Jan. 2010, doi: 10.1186/1742-2094-7-9/FIGURES/1.
[95] U. Felderhoff-Mueser, O. I. Schmidt, A. Oberholzer, C. Bührer, and P. F. Stahel, "IL-18: a key player in neuroinflammation and neurodegeneration?," *Trends Neurosci.*, vol. 28, no. 9, pp. 487–493, Sep. 2005, doi: 10.1016/J.TINS.2005.06.008.
[96] A. Ciaramella *et al.*, "Increased Levels of Serum IL-18 Are Associated with the Long-Term Outcome of Severe Traumatic Brain Injury," *Neuroimmunomodulation*, vol. 21, no. 1, pp. 8–12, Dec. 2014, doi: 10.1159/000354764.
[97] S. Narayanan, A. Shanker, T. Khera, and B. Subramaniam, "Neurofilament light: a narrative review on biomarker utility," *Fac. Rev.*, vol. 10, May 2021, doi: 10.12703/R/10-46.
[98] M. Khalil *et al.*, "Neurofilaments as biomarkers in neurological disorders," *Nat. Rev. Neurol. 2018 1410*, vol. 14, no. 10, pp. 577–589, Aug. 2018, doi: 10.1038/s41582-018-0058-z.
[99] L. Gaetani, K. Blennow, P. Calabresi, M. Di Filippo, L. Parnetti, and H. Zetterberg, "Neurofilament light chain as a biomarker in neurological disorders," *J. Neurol. Neurosurg. Psychiatry*, vol. 90, no. 8, pp. 870–881, Aug. 2019, doi: 10.1136/JNNP-2018-320106.
[100] M. S. Bergholt, A. Serio, and M. B. Albro, "Raman Spectroscopy: Guiding Light for the Extracellular Matrix," *Front. Bioeng. Biotechnol.*, vol. 7, p. 491962, Nov. 2019, doi: 10.3389/FBIOE.2019.00303/BIBTEX.
[101] A. H. Chau, J. T. Motz, J. A. Gardecki, S. Waxman, B. E. Bouma, and G. J. Tearney, "Fingerprint and high-wavenumber Raman spectroscopy in a human-swine coronary xenograft in vivo," *J. Biomed. Opt.*, vol. 13, no. 4, p. 040501, 2008, doi: 10.1117/1.2960015.
[102] A. I. R. Maas and D. K. Menon, "Traumatic brain injury: integrated approaches to improve prevention, clinical care, and research," *Lancet Neurol.*, vol. 16, no. 12, pp. 987–1048, Dec. 2017, doi: 10.1016/S1474-4422(17)30371-X.
[103] J. Zhang, V. Puvenna, and D. Janigro, "Biomarkers of Traumatic Brain Injury and Their Relationship to Pathology," in *Translational Research in Traumatic Brain Injury*, CRC Press/Taylor and Francis Group, 2016, pp. 263–276.
[104] G. Socrates, *Infrared and Raman Characteristic Group Frequencies: Tables and Charts. 3rd ed.* John Wiley & Sons, Ltd, 2004.
[105] V. Rubovitch, Y. Zilberstein, J. Chapman, S. Schreiber, and C. G. Pick, "Restoring GM1 ganglioside expression ameliorates axonal outgrowth inhibition and cognitive impairments induced by blast traumatic brain injury," *Sci. Rep.*, vol. 7, no. 1, pp. 1–12, Jan. 2017, doi: 10.1038/srep41269.
[106] E. Staniszewska-Slezak, K. Malek, and M. Baranska, "Complementary analysis of tissue homogenates composition obtained by Vis and NIR laser excitations and Raman spectroscopy," *Spectrochim. Acta - Part A Mol. Biomol. Spectrosc.*, vol. 147, pp. 245–256, Aug. 2015, doi: 10.1016/j.saa.2015.03.086.
[107] S. Qiu *et al.*, "Raman profile alterations of irradiated human nasopharyngeal cancer cells detected with laser tweezer Raman spectroscopy," *RSC Adv.*, vol. 10, no. 24, pp. 14368–14373, Apr. 2020, doi: 10.1039/D0RA01173H.
[108] A. Pastore, G. Federici, E. Bertini, and F. Piemonte, "Analysis of glutathione: Implication in redox and detoxification," *Clin. Chim. Acta*, vol. 333, no. 1–2, pp. 19–39, Jul. 2003, doi: 10.1016/S0009-8981(03)00200-6.
[109] H. J. Shin, J. H. Lee, Y. D. Kim, I. Shin, T. Sim, and D. K. Lim, "Raman-Based in Situ Monitoring of

Changes in Molecular Signatures during Mitochondrially Mediated Apoptosis," *ACS Omega*, vol. 4, no. 5, pp. 8188–8195, May 2019, doi: 10.1021/ACSOMEGA.9B00629/ASSET/IMAGES/LARGE/AO-2019-006293_0006.JPEG.
[110] S. M. Rolfe, M. R. Patel, I. Gilmour, K. Olsson-Francis, and T. J. Ringrose, "Defining Multiple Characteristic Raman Bands of α-Amino Acids as Biomarkers for Planetary Missions Using a Statistical Method," *Orig. Life Evol. Biosph.*, vol. 46, no. 2–3, pp. 323–346, Jun. 2016, doi: 10.1007/S11084-015-9477-7/FIGURES/3.
[111] R. Galli *et al.*, "Rapid Label-Free Analysis of Brain Tumor Biopsies by Near Infrared Raman and Fluorescence Spectroscopy—A Study of 209 Patients," *Front. Oncol.*, vol. 9, p. 1165, Nov. 2019, doi: 10.3389/fonc.2019.01165.
[112] C. Nims, B. Cron, M. Wetherington, J. Macalady, and J. Cosmidis, "Low frequency Raman Spectroscopy for micron-scale and in vivo characterization of elemental sulfur in microbial samples," *Sci. Rep.*, vol. 9, no. 1, pp. 1–12, May 2019, doi: 10.1038/s41598-019-44353-6.
[113] G. Pezzotti, "Raman spectroscopy in cell biology and microbiology," *J. Raman Spectrosc.*, vol. 52, no. 12, pp. 2348–2443, Dec. 2021, doi: 10.1002/JRS.6204.
[114] N. Kourkoumelis, G. Gaitanis, A. Velegraki, and I. D. Bassukas, "Nail Raman spectroscopy: A promising method for the diagnosis of onychomycosis. An ex vivo pilot study," *Med. Mycol.*, vol. 56, no. 5, pp. 551–558, Jul. 2018, doi: 10.1093/MMY/MYX078.
[115] E. Koglin, J. M. Séquaris, and P. Valenta, "Surface enhanced raman spectroscopy of nucleic acid bases on Ag electrodes," *J. Mol. Struct.*, vol. 79, no. C, pp. 185–189, Jan. 1982, doi: 10.1016/0022-2860(82)85050-3.
[116] Z. Luan *et al.*, "Identification of lesional tissues and nonlesional tissues in early gastric cancer endoscopic submucosal dissection specimens using a fiber optic raman system," *Gastroenterol. Res. Pract.*, vol. 2020, 2020, doi: 10.1155/2020/8015024.
[117] J. Depciuch *et al.*, "Spectroscopic evaluation of carcinogenesis in endometrial cancer," *Sci. Rep.*, vol. 11, no. 1, pp. 1–12, Apr. 2021, doi: 10.1038/s41598-021-88640-7.
[118] C. Farber *et al.*, "Complementarity of Raman and Infrared Spectroscopy for Structural Characterization of Plant Epicuticular Waxes," *ACS Omega*, vol. 4, no. 2, pp. 3700–3707, Feb. 2019, doi: 10.1021/ACSOMEGA.8B03675/ASSET/IMAGES/LARGE/AO-2018-03675F_0006.JPEG.
[119] Y. Zhou *et al.*, "Human brain cancer studied by resonance Raman spectroscopy," *https://doi.org/10.1117/1.JBO.17.11.116021*, vol. 17, no. 11, p. 116021, Nov. 2012, doi: 10.1117/1.JBO.17.11.116021.
[120] X. Zhang, Q. Zhou, Y. Huang, Z. Li, and Z. Zhang, "Contrastive Analysis of the Raman Spectra of Polychlorinated Benzene: Hexachlorobenzene and Benzene," *Sensors 2011, Vol. 11, Pages 11510-11515*, vol. 11, no. 12, pp. 11510–11515, Dec. 2011, doi: 10.3390/S111211510.
[121] J. Sacharz *et al.*, "Epileptic rat brain tissue analyzed by 2D correlation Raman spectroscopy," *Spectrochim. Acta - Part A Mol. Biomol. Spectrosc.*, vol. 188, pp. 581–588, Jan. 2018, doi: 10.1016/j.saa.2017.07.046.
[122] J. Zhu *et al.*, "Surface-enhanced Raman spectroscopy investigation on human breast cancer cells," *Chem. Cent. J.*, vol. 7, no. 1, pp. 1–5, Feb. 2013, doi: 10.1186/1752-153X-7-37/FIGURES/4.
[123] M. Y. Jahmani, M. E. Hammadeh, M. A. Al Smadi, and M. K. Baller, "Label-Free Evaluation of Chromatin Condensation in Human Normal Morphology Sperm Using Raman Spectroscopy," *Reprod. Sci.*, vol. 28, no. 9, pp. 2527–2539, Sep. 2021, doi: 10.1007/S43032-021-00494-6/FIGURES/5.
[124] S. Tfaili, C. Gobinet, G. Josse, J. F. Angiboust, M. Manfait, and O. Piot, "Confocal Raman microspectroscopy for skin characterization: a comparative study between human skin and pig skin," *Analyst*, vol. 137, no. 16, pp. 3673–3682, Jul. 2012, doi: 10.1039/C2AN16292J.
[125] Z. Huang, A. McWilliams, H. Lui, D. I. McLean, S. Lam, and H. Zeng, "Near-infrared Raman spectroscopy for optical diagnosis of lung cancer," *Int. J. Cancer*, vol. 107, no. 6, pp. 1047–1052, Dec. 2003, doi: 10.1002/IJC.11500.
[126] A. Mudalige and J. E. Pemberton, "Raman spectroscopy of glycerol/D2O solutions," *Vib. Spectrosc.*, vol. 45, no. 1, pp. 27–35, Oct. 2007, doi: 10.1016/J.VIBSPEC.2007.04.002.
[127] A. Synytsya, M. Judexova, D. Hoskovec, M. Miskovicova, and L. Petruzelka, "Raman spectroscopy at different excitation wavelengths (1064, 785 and 532 nm) as a tool for diagnosis of colon cancer," *J. Raman Spectrosc.*, vol. 45, no. 10, pp. 903–911, Oct. 2014, doi: 10.1002/JRS.4581.
[128] K. Katsara, K. Psatha, G. Kenanakis, M. Aivaliotis, and V. M. Papadakis, "Subtyping on Live Lymphoma Cell Lines by Raman Spectroscopy," *Materials (Basel).*, vol. 15, no. 2, p. 546, Jan. 2022, doi: 10.3390/MA15020546/S1.
[129] L. L. Tay, R. G. Tremblay, J. Hulse, B. Zurakowski, M. Thompson, and M. Bani-Yaghoub, "Detection of acute brain injury by Raman spectral signature," *Analyst*, vol. 136, no. 8, pp. 1620–1626, Mar. 2011, doi: 10.1039/C0AN00897D.
[130] S. Qiu *et al.*, "Raman profile alterations of irradiated human nasopharyngeal cancer cells detected with laser tweezer Raman spectroscopy," *RSC Adv.*, vol. 10, no. 24, pp. 14368–14373, Apr. 2020, doi: 10.1039/D0RA01173H.
[131] K. I. Hadjiivanov *et al.*, "Power of Infrared and Raman Spectroscopies to Characterize Metal-Organic Frameworks and Investigate Their Interaction with Guest Molecules," *Chem. Rev.*, vol. 121, no. 3, pp. 1286–1424, Feb. 2021, doi: 10.1021/ACS.CHEMREV.0C00487.
[132] B. A. Marekha *et al.*, "Intermolecular interactions in mixtures of 1-n-butyl-3-methylimidazolium acetate

and water: Insights from IR, Raman, NMR spectroscopy and quantum chemistry calculations," *J. Mol. Liq.*, vol. 210, pp. 227–237, Oct. 2015, doi: 10.1016/J.MOLLIQ.2015.05.015.
[133] Z. Movasaghi, S. Rehman, and I. U. Rehman, "Raman Spectroscopy of Biological Tissues," *http://dx.doi.org/10.1080/05704920701551530*, vol. 42, no. 5, pp. 493–541, Sep. 2007, doi: 10.1080/05704920701551530.
[134] E. Staniszewska-Slezak, K. Malek, and M. Baranska, "Complementary analysis of tissue homogenates composition obtained by Vis and NIR laser excitations and Raman spectroscopy," *Spectrochim. Acta - Part A Mol. Biomol. Spectrosc.*, vol. 147, pp. 245–256, Aug. 2015, doi: 10.1016/j.saa.2015.03.086.
[135] P. T. C. Freire *et al.*, "Raman Spectroscopy of Amino Acid Crystals," *Raman Spectrosc. Appl.*, Feb. 2017, doi: 10.5772/65480.
[136] T. Mehta *et al.*, "Current Trends in Biomarkers for Traumatic Brain Injury," *Open Access J Neurol Neurosurg*, vol. 12, no. 4, pp. 86–94, 2020, doi: 10.19080/OAJNN.2020.12.555842.
[137] M. U. Gutierre, J. P. M. Telles, L. C. Welling, N. N. Rabelo, M. J. Teixeira, and E. G. Figueiredo, "Biomarkers for traumatic brain injury: a short review," *Neurosurg. Rev.*, vol. 44, no. 4, pp. 2091–2097, 2021, doi: 10.1007/s10143-020-01421-0.
[138] C. Krafft, L. Neudert, T. Simat, and R. Salzer, "Near infrared Raman spectra of human brain lipids," *Spectrochim. Acta - Part A Mol. Biomol. Spectrosc.*, vol. 61, no. 7, pp. 1529–1535, May 2005, doi: 10.1016/j.saa.2004.11.017.
[139] E. P. Thelin *et al.*, "Utility of neuron-specific enolase in traumatic brain injury; relations to S100B levels, outcome, and extracranial injury severity," *Crit. Care*, vol. 20, no. 1, pp. 1–15, Sep. 2016, doi: 10.1186/S13054-016-1450-Y/TABLES/4.
[140] R. Smith, M. Chepisheva, T. Cronin, and B. M. Seemungal, "Diagnostic Approaches Techniques in Concussion/Mild Traumatic Brain Injury: Where are we?," *Neurosensory Disord. Mild Trauma. Brain Inj.*, pp. 247–277, Jan. 2019, doi: 10.1016/B978-0-12-812344-7.00016-9.
[141] L. Papa *et al.*, "Serum levels of ubiquitin C-terminal hydrolase distinguish mild traumatic brain injury from trauma controls and are elevated in mild and moderate traumatic brain injury patients with intracranial lesions and neurosurgical intervention," *J. Trauma Acute Care Surg.*, vol. 72, no. 5, pp. 1335–1344, May 2012, doi: 10.1097/TA.0b013e3182491e3d.
[142] E. Bik, A. Dorosz, L. Mateuszuk, M. Baranska, and K. Majzner, "Fixed versus live endothelial cells: The effect of glutaraldehyde fixation manifested by characteristic bands on the Raman spectra of cells," *Spectrochim. Acta Part A Mol. Biomol. Spectrosc.*, vol. 240, p. 118460, Oct. 2020, doi: 10.1016/J.SAA.2020.118460.
[143] A. Ricciardi *et al.*, "Raman spectroscopy characterization of the major classes of plasma lipoproteins," *Vib. Spectrosc.*, vol. 109, Jul. 2020, doi: 10.1016/J.VIBSPEC.2020.103073.
[144] K. Czamara, K. Majzner, M. Z. Pacia, K. Kochan, A. Kaczor, and M. Baranska, "Raman spectroscopy of lipids: a review," *J. Raman Spectrosc.*, vol. 46, no. 1, pp. 4–20, Jan. 2015, doi: 10.1002/JRS.4607.
[145] T. Huff, B. Boyd, and I. Jialal, "Physiology, Cholesterol," *StatPearls*, Dec. 2017, Accessed: Aug. 09, 2023. [Online]. Available: http://europepmc.org/books/NBK470561.
[146] A. Ricciardi *et al.*, "Raman spectroscopy characterization of the major classes of plasma lipoproteins," *Vib. Spectrosc.*, vol. 109, p. 103073, Jul. 2020, doi: 10.1016/J.VIBSPEC.2020.103073.
[147] J. J. Freeman, B. Wopenka, M. J. Silva, and J. D. Pasteris, "Raman spectroscopic detection of changes in bioapatite in mouse femora as a function of age and in vitro fluoride treatment," *Calcif. Tissue Int.*, vol. 68, no. 3, pp. 156–162, 2001, doi: 10.1007/S002230001206.
[148] N. Buzgar, A. Buzatu, and I. Sanislav, "The Raman study on certain sulfates," 2009.
[149] Y. Cao, D. Shen, Y. Lu, and Y. Huang, "A Raman-scattering Study on the Net Orientation of Biomacromolecules in the Outer Epidermal Walls of Mature Wheat Stems (Triticum aestivum)," *Ann. Bot.*, vol. 97, no. 6, pp. 1091–1094, Jun. 2006, doi: 10.1093/AOB/MCL059.
[150] C. Farber, M. Shires, K. Ong, D. Byrne, and D. Kurouski, "Raman spectroscopy as an early detection tool for rose rosette infection," *Planta*, vol. 250, no. 4, pp. 1247–1254, Oct. 2019, doi: 10.1007/S00425-019-03216-0/FIGURES/4.
[151] E. V. Timchenko, L. A. Zherdeva, P. E. Timchenko, L. T. Volova, and U. V. Ponomareva, "Detailed Analysis of the Structural Changes of Bone Matrix During the Demineralization Process Using Raman Spectroscopy," *Phys. Procedia*, vol. 73, pp. 221–227, Jan. 2015, doi: 10.1016/J.PHPRO.2015.09.161.
[152] T. Ito *et al.*, "D-serine metabolism and its importance in development of Dictyostelium discoideum," *Front. Microbiol.*, vol. 9, no. APR, p. 334767, Apr. 2018, doi: 10.3389/FMICB.2018.00784/BIBTEX.
[153] E. J. Perez *et al.*, "Enhanced astrocytic d-serine underlies synaptic damage after traumatic brain injury," *J. Clin. Invest.*, vol. 127, no. 8, pp. 3114–3125, Aug. 2017, doi: 10.1172/JCI92300.
[154] J. P. Slotte, "Biological functions of sphingomyelins," *Prog. Lipid Res.*, vol. 52, no. 4, pp. 424–437, 2013, doi: 10.1016/J.PLIPRES.2013.05.001.
[155] K. Kurek, B. Łukaszuk, D. M. Piotrowska, P. Wiesiołek, A. M. Chabowska, and M. Zendzian-Piotrowska, "Metabolism, physiological role, and clinical implications of sphingolipids in gastrointestinal tract," *Biomed Res. Int.*, vol. 2013, 2013, doi: 10.1155/2013/908907.
[156] S. A. Novgorodov *et al.*, "Essential roles of neutral ceramidase and sphingosine in mitochondrial dysfunction due to traumatic brain injury," *J. Biol. Chem.*, vol. 289, no. 19, pp. 13142–13154, 2014, doi: 10.1074/JBC.M113.530311.
[157] A. Uphoff, M. Hermansson, P. Haimi, and P. Somerharju, "Analysis of complex lipidomes," *Med. Appl. Mass Spectrom.*, pp. 223–249, Jan. 2008, doi: 10.1016/B978-044451980-1.50013-6.

[158] H. Chao *et al.*, “Cardiolipin-Dependent Mitophagy Guides Outcome after Traumatic Brain Injury,” *J. Neurosci.*, vol. 39, no. 10, pp. 1930–1943, Mar. 2019, doi: 10.1523/JNEUROSCI.3415-17.2018.
[159] K. K. W. Wang, F. H. Kobeissy, Z. Shakkour, and J. A. Tyndall, “Thorough overview of ubiquitin C-terminal hydrolase-L1 and glial fibrillary acidic protein as tandem biomarkers recently cleared by US Food and Drug Administration for the evaluation of intracranial injuries among patients with traumatic brain injury,” *Acute Med. Surg.*, vol. 8, no. 1, p. e622, Jan. 2021, doi: 10.1002/AMS2.622.
[160] J. Shi *et al.*, “Review: Traumatic brain injury and hyperglycemia, a potentially modifiable risk factor,” *Oncotarget*, vol. 7, no. 43, p. 71052, Oct. 2016, doi: 10.18632/ONCOTARGET.11958.
[161] O. Calcagnile, A. Anell, and J. Undén, “The addition of S100B to guidelines for management of mild head injury is potentially cost saving,” *BMC Neurol.*, vol. 16, Oct. 2016, doi: 10.1186/s12883-016-0723-z.
[162] Y. Li *et al.*, “Micro-Raman spectroscopy study of cancerous and normal nasopharyngeal tissues,” *J. Biomedial Opt.*, vol. 18, no. 2, pp. 1–6, Feb. 2013, doi: 10.1117/1.JBO.18.2.027003.
[163] A. Girard *et al.*, “Raman spectroscopic analysis of skin as a diagnostic tool for Human African Trypanosomiasis,” *PLOS Pathog.*, vol. 17, no. 11, p. e1010060, Nov. 2021, doi: 10.1371/JOURNAL.PPAT.1010060.
[164] F. E. Malherbe and H. J. Bernstein, “The Infrared and Raman Spectra of p-Dioxane,” *J. Am. Chem. Soc.*, vol. 74, no. 17, pp. 4408–4410, Sep. 1952, doi: 10.1021/JA01137A051/ASSET/JA01137A051.FP.PNG_V03.
[165] F. Liu, H. Gu, X. Yuan, Y. Lin, and X. Dong, “Chloride ion-dependent surface-enhanced Raman scattering study of biotin on the silver surface,” *J. Phys. Conf. Ser.*, vol. 277, no. 1, p. 012025, Jan. 2011, doi: 10.1088/1742-6596/277/1/012025.
[166] K. A. Khnykina, V. V. Kireev, N. V. Krunina, N. D. Kundikova, and E. V. Verina, “Influence of Environment on Raman Spectra of Glycine and Prospect of Their Use for Functional Diagnostics of Human Beings,” *Proc. - 2018 Glob. Smart Ind. Conf. GloSIC 2018*, Dec. 2018, doi: 10.1109/GLOSIC.2018.8570138.
[167] F. Quilès and A. Burneau, “Infrared and Raman spectra of alkaline-earth and copper(II) acetates in aqueous solutions,” *Vib. Spectrosc.*, vol. 16, no. 2, pp. 105–117, May 1998, doi: 10.1016/S0924-2031(98)00004-6.
[168] I. M. Asher, K. J. Rothschild, E. Anastassakis, and H. E. Stanley, “Raman Spectroscopy of Uncomplexed Valinomycin. 1. The Solid State,” *J. Am. Chem. Soc.*, vol. 99, no. 7, pp. 2024–2032, 1977, doi: 10.1021/JA00449A002/ASSET/JA00449A002.FP.PNG_V03.
[169] S. Duraipandian, D. Traynor, P. Kearney, C. Martin, J. J. O’Leary, and F. M. Lyng, “Raman spectroscopic detection of high-grade cervical cytology: Using morphologically normal appearing cells,” *Sci. Rep.*, vol. 8, no. 1, pp. 1–8, Oct. 2018, doi: 10.1038/s41598-018-33417-8.
[170] A. E. Guimarães *et al.*, “Near Infrared Raman Spectroscopy (NIRS): A technique for doping control,” *J. Spectrosc.*, vol. 20, no. 4, pp. 185–194, 2006, doi: 10.1155/2006/328210.
[171] H.-H. Liu, S.-H. Lin, and N.-T. Yu, “Resonance Raman enhancement of phenyl ring vibrational modes in phenyl iron complex of myoglobin,” *Biophys. J.*, vol. 57, 1990, doi: 10.1016/S0006-3495(90)82604-7.
[172] V. Nava, M. L. Frezzotti, and B. Leoni, “Raman Spectroscopy for the Analysis of Microplastics in Aquatic Systems,” *Appl. Spectrosc.*, vol. 75, no. 11, pp. 1341–1357, Nov. 2021, doi: 10.1177/00037028211043119/ASSET/IMAGES/LARGE/10.1177_00037028211043119-FIG5.JPEG.
[173] Z. Huang *et al.*, “Effect of formalin fixation on the near-infrared Raman spectroscopy of normal and cancerous human bronchial tissues,” *Int. J. Oncol.*, vol. 23, no. 3, pp. 649–655, Sep. 2003, doi: 10.3892/ijo.23.3.649.
[174] P. Bock and N. Gierlinger, “Infrared and Raman spectra of lignin substructures: Coniferyl alcohol, abietin, and coniferyl aldehyde,” *J. Raman Spectrosc.*, vol. 50, no. 6, pp. 778–792, Jun. 2019, doi: 10.1002/JRS.5588.
[175] O. D. Ayala *et al.*, “Raman microspectroscopy differentiates perinatal pathogens on ex vivo infected human fetal membrane tissues,” *J. Biophotonics*, vol. 12, no. 9, p. e201800449, Sep. 2019, doi: 10.1002/JBIO.201800449.
[176] J. C. Ramirez-Perez and D. Durigo, “Surface-Enhanced Raman Spectroscopy (SERS) for characterization SARS-CoV-2,” *J. Saudi Chem. Soc.*, vol. 26, no. 5, p. 101531, Sep. 2022, doi: 10.1016/J.JSCS.2022.101531.
[177] L. F. Maia, R. F. Fernandes, M. R. Almeida, and L. F. C. de Oliveira, “Rapid assessment of chemical compounds from Phyllogorgia dilatata using Raman spectroscopy,” *Rev. Bras. Farmacogn.*, vol. 25, no. 6, pp. 619–626, Nov. 2015, doi: 10.1016/J.BJP.2015.09.002.
[178] I. Palings, E. Van den Berg, R. A. Mathies, J. A. Pardoen, C. Winkel, and J. Lugtenburg, “Assignment of Fingerprint Vibrations in the Resonance Raman Spectra of Rhodopsin, Isorhodopsin, and Bathorhodopsin: Implications for Chromophore Structure and Environment,” *Biochemistry*, vol. 26, no. 9, pp. 2544–2556, 1987, doi: 10.1021/BI00383A021/SUPPL_FILE/BI00383A021_SI_001.PDF.
[179] R. P. Paradkar, R. M. Patel, E. Knickerbocker, and A. Doufas, “Raman spectroscopy for spinline crystallinity measurements. I. Experimental studies,” *J. Appl. Polym. Sci.*, vol. 109, no. 5, pp. 3413–3420, Sep. 2008, doi: 10.1002/APP.28388.
[180] P. Kukura, D. W. McCamant, P. H. Davis, and R. A. Mathies, “Vibrational structure of the S2 (1Bu) excited state of diphenyloctatetraene observed by femtosecond stimulated Raman spectroscopy,” *Chem. Phys. Lett.*, vol. 382, no. 1–2, pp. 81–86, Nov. 2003, doi: 10.1016/J.CPLETT.2003.10.051.
[181] A. K. Yadav and P. Singh, “A review of the structures of oxide glasses by Raman spectroscopy,” *RSC Adv.*, vol. 5, no. 83, pp. 67583–67609, Aug. 2015, doi: 10.1039/C5RA13043C.

[182] A. Bankapur, E. Zachariah, S. Chidangil, M. Valiathan, and D. Mathur, “Raman Tweezers Spectroscopy of Live, Single Red and White Blood Cells,” *PLoS One*, vol. 5, no. 4, p. e10427, 2010, doi: 10.1371/JOURNAL.PONE.0010427.
[183] M. V. Cañamares, F. Pozzi, and J. R. Lombardi, “Raman, SERS, and DFT Analysis of the Main Alkaloids Contained in Syrian Rue,” *J. Phys. Chem. C*, vol. 123, no. 14, pp. 9262–9271, Apr. 2019, doi: 10.1021/ACS.JPCC.9B01355/ASSET/IMAGES/LARGE/JP-2019-013556_0007.JPEG.
[184] O. Anjos, R. P. F. Guiné, A. J. A. Santos, V. B. Paula, H. Pereira, and L. M. Estevinho, “Evaluation of FT-Raman and FTIR-ATR spectroscopy for the quality evaluation of Lavandula spp. Honey,” *Open Agric.*, vol. 6, no. 1, pp. 47–56, Jan. 2021, doi: 10.1515/OPAG-2020-0210/MACHINEREADABLECITATION/RIS.
[185] S. M. Moosavinejad *et al.*, “Evaluation of degradation in chemical compounds of wood in historical buildings using FT-IR and FT-Raman vibrational spectroscopy,” *Maderas. Cienc. y Tecnol.*, vol. 21, no. 3, pp. 381–392, 2019, doi: 10.4067/S0718-221X2019005000310.
[186] A. Fiedler, M. Baranska, and H. Schulz, “FT-Raman spectroscopy—a rapid and reliable quantification protocol for the determination of natural indigo dye in Polygonum tinctorium,” *J. Raman Spectrosc.*, vol. 42, no. 3, pp. 551–557, Mar. 2011, doi: 10.1002/JRS.2726.
[187] J. Gao, H. Gu, X. Dong, and F. Liu, “The determination of captopril in Solution by Raman spectroscopy,” *J. Phys. Conf. Ser.*, vol. 277, no. 1, p. 012009, Jan. 2011, doi: 10.1088/1742-6596/277/1/012009.
[188] L. Q. Zheng, M. Servalli, A. D. Schlüter, and R. Zenobi, “Tip-enhanced Raman spectroscopy for structural analysis of two-dimensional covalent monolayers synthesized on water and on Au (111),” *Chem. Sci.*, vol. 10, no. 42, pp. 9673–9678, Oct. 2019, doi: 10.1039/C9SC03296G.
[189] T. Menge, P. H. Lalive, H. C. Von Büdingen, B. Cree, S. L. Hauser, and C. P. Genain, “Antibody responses against galactocerebroside are potential stage-specific biomarkers in multiple sclerosis,” *J. Allergy Clin. Immunol.*, vol. 116, no. 2, pp. 453–459, 2005, doi: 10.1016/J.JACI.2005.03.023.
[190] M. Podbielska, S. B. Levery, and E. L. Hogan, “The structural and functional role of myelin fast-migrating cerebrosides: pathological importance in multiple sclerosis,” *Clin. Lipidol.*, vol. 6, no. 2, p. 159, Apr. 2011, doi: 10.2217/CLP.11.8.
[191] I. Thomas, A. M. Dickens, and J. P. Posti, “Serum metabolome associated with severity of acute traumatic brain injury,” *Nat. Commun. 2022 131*, vol. 13, no. 1, pp. 1–15, May 2022, doi: 10.1038/s41467-022-30227-5.
[192] T. Dhanani, T. Dou, K. Biradar, J. Jifon, D. Kurouski, and B. S. Patil, “Raman Spectroscopy Detects Changes in Carotenoids on the Surface of Watermelon Fruits During Maturation,” *Front. Plant Sci.*, vol. 13, p. 832522, May 2022, doi: 10.3389/FPLS.2022.832522/FULL.
[193] S. Ashwal *et al.*, “Proton Spectroscopy Detected Myoinositol in Children with Traumatic Brain Injury,” *Pediatr. Res. 2004 564*, vol. 56, no. 4, pp. 630–638, Oct. 2004, doi: 10.1203/01.pdr.0000139928.60530.7d.
[194] D. Tong *et al.*, “Application of Raman spectroscopy in the detection of hepatitis B virus infection,” *Photodiagnosis Photodyn. Ther.*, vol. 28, pp. 248–252, Dec. 2019, doi: 10.1016/J.PDPDT.2019.08.006.
[195] A. Rygula, K. Majzner, K. M. Marzec, A. Kaczor, M. Pilarczyk, and M. Baranska, “Raman spectroscopy of proteins: a review,” *J. Raman Spectrosc.*, vol. 44, no. 8, pp. 1061–1076, Aug. 2013, doi: 10.1002/JRS.4335.
[196] N. Tsutsumi *et al.*, “The structural basis for receptor recognition of human interleukin-18,” *Nat. Commun.*, vol. 5, 2014, doi: 10.1038/NCOMMS6340.
[197] S. J. Choquette, E. S. Etz, W. S. Hurst, D. H. Blackburn, and S. D. Leigh, “Relative Intensity Correction of Raman Spectrometers: NIST SRMs 2241 Through 2243 for 785 nm, 532 nm, and 488 nm,” *Appl. Spectrosc.*, vol. 61, no. 2, pp. 117–129, 2007.
[198] R. R. Jones, D. C. Hooper, L. Zhang, D. Wolverson, and V. K. Valev, “Raman Techniques: Fundamentals and Frontiers,” *Nanoscale Res. Lett. 2019 141*, vol. 14, no. 1, pp. 1–34, Jul. 2019, doi: 10.1186/S11671-019-3039-2.
[199] R. G. Calderhead, W. S. Kim, T. Ohshiro, M. A. Trelles, and D. B. Vasily, “Adjunctive 830 nm light-emitting diode therapy can improve the results following aesthetic procedures,” *Laser Ther.*, vol. 24, no. 4, pp. 277–289, Dec. 2015, doi: 10.5978/islsm.15-OR-17.
[200] P. K. Min and B. L. Goo, “830 nm light-emitting diode low level light therapy (LED-LLLT) enhances wound healing: a preliminary study,” *Laser Ther.*, vol. 22, no. 1, pp. 43–49, 2013, doi: 10.5978/ISLSM.13-OR-06.
[201] P. Avci *et al.*, “Low-level laser (light) therapy (LLLT) in skin: stimulating, healing, restoring,” *Semin. Cutan. Med. Surg.*, vol. 32, no. 1, p. 41, Mar. 2013, Accessed: Jan. 25, 2024. [Online]. Available: /pmc/articles/PMC4126803/.
[202] P. M. Iannaccone and H. J. Jacob, “Rats!,” *Dis. Model. Mech.*, vol. 2, no. 5–6, pp. 206–210, Apr. 2009, doi: 10.1242/DMM.002733.
[203] B. Weber *et al.*, “Modeling trauma in rats: similarities to humans and potential pitfalls to consider,” *J. Transl. Med. 2019 171*, vol. 17, no. 1, pp. 1–19, Sep. 2019, doi: 10.1186/S12967-019-2052-7.
[204] S. Basu, A. M. Schtjltz, B. Manju, and S. Roseman, “Enzymatic Synthesis of Galactocerebroside by a Galactosyltransferase from Embryonic Chicken Brain*,” *J. Biol. Chem.*, vol. 246, no. 13, pp. 4272–4279, 1971, doi: 10.1016/S0021-9258(18)62081-2.
[205] Z. Kaabia *et al.*, “Plasma lipidomic analysis reveals strong similarities between lipid fingerprints in human, hamster and mouse compared to other animal species,” *Sci. Rep.*, vol. 8, no. 1, pp. 1–9, Oct. 2018, doi: 10.1038/s41598-018-34329-3.
[206] F. Huang *et al.*, “Analysis and Comparison of Mouse and Human Brain Gangliosides via Two-Stage

Matching of MS/MS Spectra," *ACS Omega*, vol. 7, no. 7, pp. 6403–6411, Feb. 2022, doi: 10.1021/ACSOMEGA.1C07070/ASSET/IMAGES/LARGE/AO1C07070_0003.JPEG.
[207] Z. Jiang, T. Shen, H. Huynh, X. Fang, Z. Han, and K. Ouyang, "Cardiolipin Regulates Mitochondrial Ultrastructure and Function in Mammalian Cells," *Genes (Basel).*, vol. 13, no. 10, p. 1889, Oct. 2022, doi: 10.3390/GENES13101889.
[208] J. J. Sabbagh, J. W. Kinney, and J. L. Cummings, "Alzheimer's disease biomarkers in animal models: closing the translational gap," *Am. J. Neurodegener. Dis.*, vol. 2, no. 2, p. 108, Jul. 2013, Accessed: Oct. 31, 2023. [Online]. Available: /pmc/articles/PMC3703123/.
[209] C. Banbury *et al.*, "Development of the Self Optimising Kohonen Index Network (SKiNET) for Raman Spectroscopy Based Detection of Anatomical Eye Tissue," *Sci. Rep.*, vol. 9, no. 1, pp. 1–9, Dec. 2019, doi: 10.1038/s41598-019-47205-5.
[210] F. Lussier, V. Thibault, B. Charron, G. Q. Wallace, and J. F. Masson, "Deep learning and artificial intelligence methods for Raman and surface-enhanced Raman scattering," *TrAC Trends Anal. Chem.*, vol. 124, p. 115796, Mar. 2020, doi: 10.1016/J.TRAC.2019.115796.
[211] M. D. Ward, A. Weber, V. D. Merrill, R. D. Welch, J. J. Bazarian, and R. H. Christenson, "Predictive Performance of Traumatic Brain Injury Biomarkers in High-Risk Elderly Patients," *J. Appl. Lab. Med.*, vol. 5, no. 1, pp. 91–100, Jan. 2020, doi: 10.1093/jalm.2019.031393.
[212] O. Terrones, J. Olazar-Intxausti, I. Anso, M. Lorizate, J. A. Nieto-Garai, and F. X. Contreras, "Raman Spectroscopy as a Tool to Study the Pathophysiology of Brain Diseases," *Int. J. Mol. Sci.*, vol. 24, no. 3, p. 2384, Jan. 2023, doi: 10.3390/IJMS24032384.
[213] M. Ge *et al.*, "Serum-based Raman spectroscopic diagnosis of blast-induced brain injury in a rat model," *Biomed. Opt. Express*, vol. 14, no. 7, pp. 3622–3634, Jul. 2023, doi: 10.1364/BOE.495285.

Chapter 7 – Summary and Future Work

7.1 Work in Progress – Establishing an Ocular LIVING-ORGAN System

A running theme in this work, as well as in previous chapters, is the limitations presented when testing portable lasers, cameras and Raman systems on healthy eye samples, let alone TBI models. Questions surrounding laser safety, spectral information and biomarkers cannot be answered in completion without better eye tissue and optical systems to test upon. This creates a backwards project for which the technology cannot be proven to produce useful diagnostic results without going through all necessary steps to make a functioning prototype, which will inevitably cross new limitations when utilised *ex vivo* versus when utilising the phantom eye and *dead* porcine eye models.

There are two types of eye models of interest, one that mimics the anatomy and function of an *in vitro* eye called Opto-Mechanical models, matching both biomechanical and optical properties[1], [2]. The second type of eye model utilises cells or tissue from eye donors either as *ex vivo* or *in vitro* models, to provide a biochemical copy. These models are less established than Opto-Mechanical ones, with most literature only citing one eye segment being cultured, grown or preserved such as the retina or cornea[3], [4].

Opto-mechanical computational models can be separated as either advancing the understanding of mechanical behaviours of the eye or aiding analysis and prediction of how changes in eye biometrics affect the eye's optical system[1]. Common applications for opto-mechanical models are towards evaluating vision correction, calibrating ophthalmic instruments, or demonstrating eye movement[5]. Many researchers developing these models do not manufacture them[6]–[9], however, there are examples of computational models being built as life-sized, fluid-filled physical systems to best emulate physiological conditions[10]–[13]. These allow ophthalmologists to accurately predict the *in vivo* performance of artificial devices such as contact lenses and intraocular lenses[2], [14].

Cell and tissue-based eye models include 2D cell cultures, 3D organoids, organotypic retinal cultures and animal models[15]–[18]. Retinal cultures can include one or all three main retinal cellular layers: the ganglion cell layer, inner nuclear layer, and outer nuclear layer[15]. Such models are highly physiologically relevant, but typically to one pathology or tissue type, and at this stage incompatible with the optical function of the eye. However, some studies have developed *ex vivo* retinal models for which animal retinae are removed, dissected, and preserved in solution to achieve viability for up to

a few hours[19], [20], suitable for obtaining electrophysiological responses and observing molecular mechanisms, for example[21], [22].

Whilst animal models are popular as they best mimic *in situ* responses, there are several anatomical, physiological, and functional differences between animal and human tissue[15], therefore utilising human cells is sometimes preferred. Mutali *et* al. state that the only true way to emulate the cell characteristics, inter-cell interactions and architecture of the human retina is by using explants, however, the limitations in ethics and viability are detrimental to experimental studies[15].

To test the portable, eye-based Raman systems, a suitable eye model would need to be both optically functional and physiologically accurate. Alongside this, the ideal model would be intact rather than dissected and capable of modification to achieve both healthy and trauma states. When considering first-stage testing, the system could utilise animal eyes with close parameters to that of a human eye, but translation to human eye samples is essential. To explore a potential model, a collaboration with the Defence Science and Technology Laboratory (Dstl) and Pebble Biotechnology Laboratories (PBL) was established.

PBL are specialists in machine perfusion, which is a technique commonly used to aid organ donation [23]–[26]. During the perfusion process, a continuous supply of metabolic substrates are provided, whilst taking frequent blood samples to analyse biochemistry and temperature to ensure organ quality[24], [27].

PBL create their LIVING-ORGAN systems as ethical alternatives to using live laboratory animals in research. Perfusion is used to recreate the physiological environment necessary to keep *ex vivo* organs. Utilising perfusion for organ testing in drug development and medical research massively reduces costs in animal testing, increases translatability by using human-relevant organs and removes the need for regulatory approval.

There are examples of *ex vivo* ocular systems in literature[28], such as the OcuScience Ex Vivo ERG Adapter, utilised for functional testing of viable retina tissue[29], however, this technique requires retinal dissection. The high precision and extensive stages required within the protocols of an *ex vivo* cornea infection model[30], or *ex vivo* confocal microscopy of the choroid[31], for example, present limited reproducibility, which is a vital facet when creating models for drug or device testing[32].

Though relatively simple, there are many challenges to perfusing a small organ such as the eye, there is a high risk of vascular injury due to miscalculated pressure, ischaemic injury if the perfusion rate is inconsistent and infection introduced by both the blood used and from the tissue itself[23]. To address the limitations of existing models, PBL set out to develop a physiological approach to eye perfusion. The first task for eye perfusion was the identification and cannulation of the ophthalmic artery (**Fig. 7.1b**), requiring intricate dissection to enucleate the eye, a micro-cannula and a microscope to achieve perfect placement and avoid piercing the tissue. Once a cannulation method was established, it was vital to optimise the technique of the team to avoid mistakes and reduce the time between animal death, dissection, and cannulation.

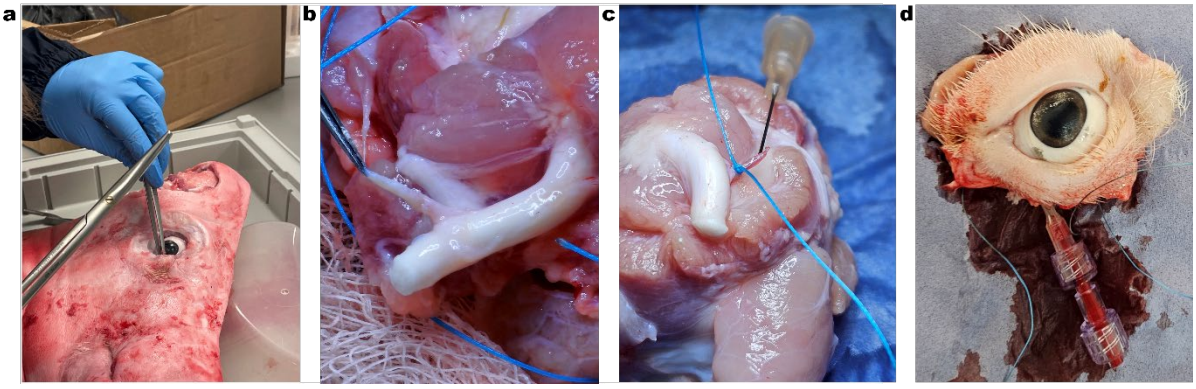

Figure 7.1. Photographs of the enucleated eye with ophthalmic artery located and successful cannulation. ***(a)*** *Shows the halved pig head having ocular tissue removed from the orbital socket.* ***(b)*** *Example of the ophthalmic artery, located next to the optic nerve.* ***(c)*** *The microcannula in place ready for perfusion.* ***(d)*** *The LIVING EYE model in progress with blood flow taking place.*

Following cannulation, shown in **Fig. 7.1c**, arterial flow had to be determined, requiring a flow rate 0.001% lower than that of typical perfusion systems. It was therefore a necessity to create a miniature circuit incorporating life-support technology used for neonatal critical care, to restore physiological blood flow (an illustration of the perfused eye connected to this system is shown in **Fig. 7.1d**).

An important difference between the eye perfusion and the perfusion PBL achieved in previous organs and limbs, is that the oxygen levels of venous blood outflow is higher than that of the arterial blood. Alongside this, there are many assumptions made and inaccuracies about porcine eye vasculature, resulting in 18 months of trial and error for the PBL team to learn from the physical model as opposed to literature and textbooks.

Pig heads are obtained from a local abattoir slaughtered following UK FSA health guidelines or electrical stunning and an incision to the neck. The head is placed in a cold store within 10 minutes from death, the eye is then cannulated and perfused within 90 minutes from death. The aim is to mobilise the LIVING EYE perfusion set-up to cannulate the eye at the abattoir, reducing the time between death and cannulation even further, however, the current method for canulating the miniature artery requires a stereo microscope which limits portability.

The LIVING-EYE model at present is capable of perfusing *ex vivo* porcine eyes for 24 hours, with low levels of apoptosis and no corneal clouding. The next goal of PBL is to explore validation methods of full ocular function. Imaging techniques such as OCT can be implemented to ensure retinal structure is comparable to that of a healthy *in vivo* porcine eye. Along with this, there is the opportunity to implant electrodes into the ophthalmic nerve to record responses to visual stimuli to verify visual function. This project will result in an *ex vivo* model that mimics both the physiological and optical environment of the eye for device testing over a timeframe completely unattainable with the current *ex vivo* porcine eye samples I currently have access to.

7.2 Future Work

The first action that could be taken towards the commercialisation of the 830 nm portable Raman and fundus device from **Chapter 5,** involves modification and optimisation of the external components. Whilst all of the optical components are completely handheld and portable, the addition of the spectrometer, laptop and Raspberry Pi render the system suitable for tabletop use. There is opportunity to build the 3D housing upon the spectrometer, as the surface area of the two systems are comparable, however, this would increase the mass of the system and limit the amount of time a clinician could continuously hold the device. Therefore, a miniaturised spectrometer could be sourced or an in-house built spectrometer to allow for complete modification.

A project is currently underway within the ANMSA group towards python-based spectroscopic analysis and machine-learning classification, integrated onto the Raspberry Pi module, to remove the need for the laptop. The remaining Raspberry Pi with touchscreen could then be mounted onto the side of the portable Raman and fundus imaging system for a completely handheld device. This is applicable to the continued commercialisation of the EyeD from **Chapter 2**, for which funding has been secured with Dstl and Ploughshare Innovations, which could fund the first rounds of animal testing for the Class 1 device.

In vivo testing for the 830 nm device is not as simple to organise due to the higher-class laser system. Therefore, the continuation of the cell damage study with Dstl from **Chapter 4** would prove insightful in establishing limits in exposure time, laser power and spot size. Once obtaining the best values, the laser diode system could be modified to meet safety requirements whilst still obtaining good signal-to-noise ratio of retinal spectra.

Parallel to final laser settings, the classification and extraction produced by SKiNET tested in **Chapter 2** must be improved for higher reliability in identifying control and trauma samples. This will not only require the optimisation of parameters such as test data but also higher quality test samples. Whilst the PBL LIVING EYE model would be ideal, a supplier must be located to provide control pigs that are slaughtered through euthanasia where the animal does not undergo any head trauma.

TBI biofluid or tissue samples are essential for the application of the reference spectral library developed in **Chapter 6.** The study produced traces of hypothetical models of the prospective TBI biomarkers present in trauma samples in the acute, sub-acute and chronic phases, however, legitimate samples are needed for comparison. The lack of information about TBI biomarker concentration in different biofluids throughout the injury profile is a big limitation in translating TBI diagnostics towards biochemical methods. When considering temporal profiles, the literature surrounding TBI biomarkers must be standardised in protocol for better data cohesion. Therefore, applying the reference library to new control and trauma biofluid samples will aid in determining the specificity and sensitivity of Raman Spectroscopy as a TBI diagnostic technique.

It is also necessary to return to the fundus camera element developed in **Chapter 3,** to reduce glare obstructing the camera-view. As discussed previously, glare masking could be removed through image processing, however, this may cause lagging when utilising a live view of the patient. Therefore, it may be necessary to return to the LED illumination set-up, using multiple off-axis lights to avoid corneal glare. Further still, the narrative around patient experience should be explored further, with the addition of a focal point to align the patient and guidance, along with a potential chinrest for comfort.

The interdisciplinary and multifaceted nature of this project requires small iterations across all of the sub-sections to ensure complete compatibility. Once a spectral signal is obtained from a human retina with a portable, low-power Raman Spectroscopy and fundus imaging system, many questions formed regarding peaks, counts, limits of detection (to name a few) during the creation of this thesis will be answered, however, this cannot be realised without the technology being tweaked, tested and optimised.

Therefore, although there are a number of avenues that still need to be explored, stemming from the work carried out in this thesis, I believe there are important contributions to the field of eye-based TBI Raman spectroscopy and handheld fundus imaging hidden in each wrong turn, roadblock, and crossed-out idea. It has been a privilege to make revelations and mistakes towards a field dedicated to improving the patient journey of TBI sufferers and healthcare professionals, and I hope that the work within this thesis will one day be translated into a triaging system that reduces suffering and increases neurological recovery in TBI diagnostics.

7.3 Summary

This thesis explores the many side-by-side avenues that must be taken to achieve a diagnostic device capable of obtaining biochemically and structurally relevant information from the eye using a laser and fundus camera. The contrasting themes addressed within this body of work require compromises to be made in terms of laser power, acquisition times and working distances, in order to meet safety regulations and be useful for both patients and healthcare providers. With this in consideration, I come to the end of my project with a working, handheld prototype that can produce *ex*

vivo fundus images of whole porcine eyes, low-power Raman spectra of *ex vivo* retinae within a phantom eye model, alongside a reference library of 18 prospective TBI biomarkers for future injury profiling across the three temporal phases: acute, sub-acute and chronic.

The collaborations, discussions and mini-projects branching from this thesis subject has lead to a number of innovative experimental designs and ideas including the retinal cell damage study with Dstl, the LIVING EYE model with PBL and even an exploration of the therapeutic properties of 633 nm laser wavelengths for low-level light therapy on murine brain samples with Davies *et* al. (**Appendix H**), leading to a clinical review on Raman spectroscopy as a neuromonitoring tool with Stevens *et* al. (**Appendix G**). Whether it be at conferences or networking events, I've found interest in the use of Raman spectroscopy in clinical settings from eye researchers, neuroscientists and defence surgeons. The value in a rapid, non-destructive biochemical technique that can be implemented outside of a laboratory environment is recognised across disciplines and I am excited to see the growth in research towards Raman-based diagnostics and eye-based Raman spectroscopy over the upcoming years.

7.4 References

[1] M. Shahiri, A. Jóźwik, and M. Asejczyk, "Opto-mechanical self-adjustment model of the human eye," *Biomed. Opt. Express*, vol. 14, no. 5, p. 1923, May 2023, doi: 10.1364/BOE.484824.

[2] A. R. Amorim, B. Bret, and J. M. González-Méijome, "Opto-Mechanical Eye Models, a Review on Human Vision Applications and Perspectives for Use in Industry," *Sensors (Basel).*, vol. 22, no. 19, Oct. 2022, doi: 10.3390/S22197686.

[3] S. Schnichels *et al.*, "Retina in a dish: Cell cultures, retinal explants and animal models for common diseases of the retina," *Prog. Retin. Eye Res.*, p. 100880, Jul. 2020, doi: 10.1016/j.preteyeres.2020.100880.

[4] T. M. Shiju, R. Carlos de Oliveira, and S. E. Wilson, "3D in vitro corneal models: a review of current technologies," *Exp. Eye Res.*, vol. 200, p. 108213, Nov. 2020, doi: 10.1016/J.EXER.2020.108213.

[5] Y. Zhao and F. Fang, "Dynamic opto-mechanical eye model with peripheral refractions," *Opt. Express*, vol. 31, no. 8, p. 12097, Apr. 2023, doi: 10.1364/OE.485252.

[6] K. Wang, D. T. Venetsanos, M. Hoshino, K. Uesugi, N. Yagi, and B. K. Pierscionek, "A Modeling Approach for Investigating Opto-Mechanical Relationships in the Human Eye Lens," *IEEE Trans. Biomed. Eng.*, vol. 67, no. 4, pp. 999–1006, Apr. 2020, doi: 10.1109/TBME.2019.2927390.

[7] W. Śródka and D. R. Iskander, "Optically inspired biomechanical model of the human eyeball," *J. Biomed. Opt.*, vol. 13, no. 4, p. 044034, 2008, doi: 10.1117/1.2952189.

[8] J. J. Esteve-Taboada, A. J. Del Águila-Carrasco, I. Marín-Franch, P. Bernal-Molina, R. Montés-Micó, and N. López-Gil, "Opto-mechanical artificial eye with accommodative ability," *Opt. Express*, vol. 23, no. 15, p. 19396, Jul. 2015, doi: 10.1364/OE.23.019396.

[9] S. Regal, D. O'Connor, P. Brige, R. Delattre, T. Djenizian, and M. Ramuz, "Determination of optical parameters of the porcine eye and development of a simulated model," *J. Biophotonics*, vol. 12, no. 11, p. e201800398, Nov. 2019, doi: 10.1002/JBIO.201800398.

[10] A. Bonfiglio, A. Lagazzo, R. Repetto, and A. Stocchino, "An experimental model of vitreous motion induced by eye rotations," *Eye Vis. (London, England)*, vol. 2, no. 1, Dec. 2015, doi: 10.1186/S40662-015-0020-8.

[11] A. Arianpour, E. J. Tremblay, I. Stamenov, J. E. Ford, D. J. Schanzlin, and Y. Lo, "An optomechanical model eye for ophthalmological refractive studies," *J. Refract. Surg.*, vol. 29, no. 2, pp. 126–132, Feb. 2013, doi: 10.3928/1081597X-20130117-08.

[12] K. R. Denninghoff and M. H. Smith, "Optical model of the blood in large retinal vessels," *J. Biomed. Opt.*, vol. 5, no. 4, p. 371, 2000, doi: 10.1117/1.1289144.

[13] M. F. Coughlan, T. Mihashi, and A. V. Goncharov, "Opto-mechanical design of a dispersive artificial eye," *Appl. Opt.*, vol. 56, no. 15, p. 4338, May 2017, doi: 10.1364/AO.56.004338.

[14] T. Eppig, M. Gillner, K. Zoric, J. Jäger, A. Löffler, and A. Langenbucher, "Biomechanical eye model and measurement setup for investigating accommodating intraocular lenses," *Z. Med. Phys.*, vol. 23, no. 2, pp. 144–152, 2013, doi: 10.1016/J.ZEMEDI.2013.02.003.

[15] A. Murali *et al.*, “Retinal explant culture: A platform to investigate human neuro-retina,” *Clin. Experiment. Ophthalmol.*, vol. 47, no. 2, pp. 274–285, Mar. 2019, doi: 10.1111/CEO.13434.
[16] H. O. Orlans, T. L. Edwards, S. R. De Silva, M. I. Patrício, and R. E. MacLaren, “Human Retinal Explant Culture for Ex Vivo Validation of AAV Gene Therapy,” *Methods Mol. Biol.*, vol. 1715, pp. 289–303, 2018, doi: 10.1007/978-1-4939-7522-8_21.
[17] M. Peng, S. M. Curry, Y. Liu, H. Lohawala, G. Sharma, and T. P. Sharma, “The ex vivo human translaminar autonomous system to study spaceflight associated neuro-ocular syndrome pathogenesis,” *Microgravity*, vol. 8, no. 1, pp. 1–14, Oct. 2022, doi: 10.1038/s41526-022-00232-5.
[18] P. Wright, J. Sanderson, J. Kelsall, and G. Healing, “Development of an Ex Vivo Human Retina Model for Assessment of Retinotoxicity,” *Invest. Ophthalmol. Vis. Sci.*, vol. 56, no. 7, pp. 2475–2475, Jun. 2015.
[19] S. Schnichels *et al.*, “Retinal Organ Cultures as Alternative Research Models,” *ATLA Altern. to Lab. Anim.*, vol. 47, no. 1, pp. 19–29, Mar. 2019, doi: 10.1177/0261192919840092/ASSET/IMAGES/LARGE/10.1177_0261192919840092-FIG3.JPEG.
[20] F. Vinberg, A. V. Kolesnikov, and V. J. Kefalov, “Ex Vivo ERG analysis of photoreceptors using an In Vivo ERG system,” *Vision Res.*, vol. 101, p. 108, 2014, doi: 10.1016/J.VISRES.2014.06.003.
[21] J. Kralik, M. van Wyk, B. Leonardon, G. Schilardi, S. Schneider, and S. Kleinlogel, “The Bovine Ex Vivo Retina: A Versatile Model for Retinal Neuroscience,” *Invest. Ophthalmol. Vis. Sci.*, vol. 64, no. 11, Aug. 2023, doi: 10.1167/IOVS.64.11.29.
[22] J. Schaeffer, C. Delpech, F. Albert, S. Belin, and H. Nawabi, “Adult Mouse Retina Explants: From ex vivo to in vivo Model of Central Nervous System Injuries,” *Front. Mol. Neurosci.*, vol. 13, p. 599948, Nov. 2020, doi: 10.3389/FNMOL.2020.599948/BIBTEX.
[23] C. J. E. Watson, R. Gaurav, and A. J. Butler, “Current Techniques and Indications for Machine Perfusion and Regional Perfusion in Deceased Donor Liver Transplantation,” *J. Clin. Exp. Hepatol.*, vol. 14, no. 2, p. 101309, Mar. 2024, doi: 10.1016/J.JCEH.2023.101309.
[24] P. Ramos *et al.*, “Abdominal Organ Preservation Solutions in the Age of Machine Perfusion,” *Transplantation*, vol. 107, no. 2, pp. 326–340, Feb. 2023, doi: 10.1097/TP.0000000000004269.
[25] M. I. Bellini, M. Nozdrin, J. Yiu, and V. Papalois, “Machine Perfusion for Abdominal Organ Preservation: A Systematic Review of Kidney and Liver Human Grafts,” *J. Clin. Med.*, vol. 8, no. 8, Aug. 2019, doi: 10.3390/JCM8081221.
[26] S. Salehi, K. Tran, and W. L. Grayson, “Focus: Medical Technology: Advances in Perfusion Systems for Solid Organ Preservation,” *Yale J. Biol. Med.*, vol. 91, no. 3, p. 301, Sep. 2018, Accessed: Feb. 19, 2024. [Online]. Available: /pmc/articles/PMC6153619/.
[27] O. S. Ozgur *et al.*, “Current practice and novel approaches in organ preservation,” *Front. Transplant.*, vol. 2, p. 1156845, Jun. 2023, doi: 10.3389/FRTRA.2023.1156845.
[28] G. N. Barbalho *et al.*, “Dynamic Ex Vivo Porcine Eye Model to Measure Ophthalmic Drug Penetration under Simulated Lacrimal Flow,” *Pharmaceutics*, vol. 15, no. 9, p. 2325, Sep. 2023, doi: 10.3390/PHARMACEUTICS15092325/S1.
[29] “Ex VIVO ERG — OcuScience,” *OcuScience*. https://ocuscience.us/pages/ex-vivo-erg-lab-system (accessed Feb. 19, 2024).
[30] U. Ubani-Ukoma, A. Chauhan, G. Schultz, and D. J. Gibson, “An ex vivo cornea infection model,” *MethodsX*, vol. 7, p. 100876, Jan. 2020, doi: 10.1016/J.MEX.2020.100876.
[31] A. M. Eltanahy, C. Franco, P. Jeyaraj, S. Goswami, E. Hughes, and A. L. Gonzales, “Ex vivo ocular perfusion model to study vascular physiology in the mouse eye,” *Exp. Eye Res.*, vol. 233, p. 109543, Aug. 2023, doi: 10.1016/J.EXER.2023.109543.
[32] C. Rousou, P. Hoogenboom, K. A. van Overdam, G. Storm, J. Dorrestijn, and E. Mastrobattista, “A technical protocol for an experimental ex vivo model using arterially perfused porcine eyes,” *Exp. Eye Res.*, vol. 181, pp. 171–177, Apr. 2019, doi: 10.1016/J.EXER.2019.02.003.

Appendix A

Supporting Material for Chapter 2

Table A1. Measurements of RNFL and GCL thickness from trauma and healthy retina, extracted from ImageJ. Averages used to calculate the ratio increase.

	RNFL	
	Trauma Post-Mortem	Control Alive
	432.62	369.16
	423.60	261.83
	130.14	321.08
	111.09	287.62
	149.96	227.49
	114.69	135.81
	185.01	247.34
	126.90	202.97
	186.46	114.58
	198.63	152.21
	192.03	122.99
	128.85	133.92
	230.51	255.81
	176.92	182.89
	384.12	171.00
	213.79	158.89
	234.07	187.79
	252.07	128.47
	219.20	221.88
	112.05	177.1
	112.35	132.43
	128.26	105.15
	267.08	179.89
	180.90	119.00
Average	**203.80**	**191.55**
Ratio of Thickness (Post-Mortem/Alive)		**1.064**

	GCL	
	Trauma Post-Mortem	Control Alive
	91.55	49.06
	74.92	55.88
	53.84	79.28
	42.67	72.92
	41.29	55.88
	47.4	49.51
	71.26	52.00
	67.46	42.75
	96.2	52.13
	61.4	54.33
	44.5	45.83
	79.67	49.00
	79.06	73.27
	68.25	68.25
	75.07	45.10
	75.58	55.88
	49.41	31.25
	50.85	54.17
	71.25	39.09
	52.63	33.33
	55.83	64.85
	97.58	52.30
	62.96	47.93
	47.3	57.32
Average	**64.91**	**53.39**
Ratio of Thickness (Post-Mortem/Alive)		1.216

Table A2. Standard error of mean (SEM) calculated from the retinal layer thicknesses in Table A1, utilised as error bars in Figure 2.9c. Where STD = Standard Deviation; n = number of measurements per sub-group.

	RNFL		GCL	
	Alive	Post-Mortem	Alive	Post-Mortem
Average	191.6	203.8	53.4	64.9
STD	93.8	70.0	16.8	11.9
n	24	24	24	24
SEM	14.3	19.2	2.4	3.4

Appendix B

Supporting Material for Chapter 4

Table B1. ImageJ measurements of cell fluorescence in control inserts and cells exposed to 40 mW 830 nm laser light for 30 seconds.

	40 mW Laser Exposure for 30 seconds		
	Stain	**Area**	**Area Percentage (%)**
Control	Red	2867.64	0.23
	Blue	84344.64	6.83
	Green	431591.27	34.99
Exposed	Red	60371.76	4.87
	Blue	185108.59	14.79
	Green	186151.09	15.12

Table B2. ImageJ measurements of cell fluorescence in control inserts, cells exposed to 50 mW 830 nm laser light for 10 minutes using the phantom eye lens and a sham model (underwent starvation and heat).

		50 mW Laser Exposure for 10 Minutes		
		Stain	**Area**	**Area Percentage (%)**
Control	T0	Red	2867.64	0.23
		Blue	84344.64	6.83
		Green	431591.27	34.99
	T24	Red	147783.83	2.00
		Blue	76920.78	1.03
		Green	591404.78	8.08
Exposed	T0	Red	4554.49	0.58
		Blue	35423.84	4.55
		Green	147755.05	18.96
	T24	Red	60474.25	0.82
		Blue	385045.41	5.22
		Green	1398248.46	18.99
SHAM	T0	Red	10233.55	1.31
		Blue	40581.71	5.21
		Green	147675.03	18.95
	T24	Red	232046.30	3.17
		Blue	493181.82	6.65
		Green	1789324.11	24.41

Appendix C

Supporting Material for Chapter 6

*Table C1. Ratios of the chosen two characteristic peaks indicated in **Figure 6.8.** p-values produced using an ANOVA test of all the 4 excitation wavelength ratios.*

Acute		
NAA	**Wavelength (nm)**	**Ratio**
	830	0.58
	785	0.68
	633	0.69
	514	0.74
p-value		0.0000761

Sub-Acute		
Cholesterol	**Wavelength (nm)**	**Ratio**
	830	0.37
	785	0.43
	633	0.49
	514	0.70
p-value		0.0000760

Chronic		
S100B	**Wavelength (nm)**	**Ratio**
	830	0.76
	785	0.91
	633	0.54
	514	0.46
p-value		0.0000761

Ganglioside		
	830	0.76
	785	1.22
	633	0.87
	514	0.65
p-value		0.0000762

D-serine		
	830	0.23
	785	0.29
	633	0.25
	514	0.47
p-value		0.0000759

Galactocerebroside		
	830	1.10
	785	0.97
	633	0.80
	514	0.98
p-value		0.0000763

GSH		
	830	0.63
	785	0.66
	633	0.67
	514	0.84
p-value		0.0000761

Sphingomyelin		
	830	1.07
	785	0.76
	633	0.74
	514	0.71
p-value		0.0000762

Glucose		
	830	0.72
	785	0.83
	633	1.36
	514	1.25
p-value		0.0000763

NSE		
	830	0.64
	785	0.63
	633	0.60
	514	0.75
p-value		0.0000761

Sulfatide		
	830	1.15
	785	0.57
	633	0.28
	514	0.33
p-value		0.0000760

Myo-Inositol		
	830	0.43
	785	0.75
	633	0.82
	514	0.91
p-value		0.0000761

GFAP		
	830	0.38
	785	0.56
	633	0.69
	514	1.03
p-value		0.0000761

Cardiolipin		
	830	0.88
	785	1.00
	633	0.99
	514	1.03
p-value		0.0000763

IL-18		
	830	0.77
	785	0.71
	633	0.73
	514	0.79
p-value		0.0000761

UCHL1		
	830	0.92
	785	0.90
	633	0.92
	514	0.89
p-value		0.0000762

IL-6		
	830	0.97
	785	1.40
	633	0.67
	514	0.56
p-value		0.0000762

NFL		
	830	1.30
	785	0.97
	633	0.81
	514	0.79
p-value		0.0000763

Table C2. Intensity values and calculated ratios of the characteristic peaks of each biomarker at all four excitation wavelengths (514, 633, 785 and 830 nm).

Acute

Wavelength (nm)	NAA		
	Peak Intensity at:		Ratio
	953 cm-1	990 cm-1	
830	19460.70426	33757.60417	0.5765
785	23935.67383	35440.70898	0.6754
633	12082.42269	17432.39811	0.6931
514	16928.93457	22814.46908	0.7420
	Stdev		0.0695
	Variance		0.0048

Wavelength (nm)	Ganglioside		
	Peak Intensity at:		Ratio
	1297 cm-1	**1440 cm-1**	
830	32771.62956	24847.88216	0.758213201
785	39083.44271	47566.08464	1.217039271
633	64115.07292	55915.48307	0.872111354
514	16187.70182	10559.49447	0.652315849
	Stdev		0.245103086
	Variance		0.060075523

Wavelength (nm)	GSH		
	Peak Intensity at:		Ratio
	1422 cm-1	**1662 cm-1**	
830	10182.3029	6441.03125	0.632571169
785	50574.31836	33498.83236	0.66236844
633	46761.88281	31471.72917	0.673021001
514	42086.2474	35178.84766	0.835875133
	Stdev		0.091558764
	Variance		0.008383007

Wavelength (nm)	NSE		
	Peak Intensity at:		Ratio
	1036 cm-1	**1080 cm-1**	
830	63454.91927	40418.86914	0.63696983
785	72117.9375	45640.56966	0.632860163
633	45870.89193	27431.82617	0.598022515
514	47594.57031	35480.63346	0.745476495
	Stdev		0.063865911
	Variance		0.004078855

Wavelength (nm)	GFAP		
	Peak Intensity at:		Ratio
	917 cm-1	**1410 cm-1**	
830	20090.15527	7561.375651	0.376372186
785	29949.21289	16627.00147	0.555173237
633	8810.918945	6085.527181	0.690680191
514	11450.93994	11737.42025	1.02501806
	Stdev		0.274226019
	Variance		0.075199909

Wavelength (nm)	UCHL1		
	Peak Intensity at:		Ratio
	844	**915**	
830	25175.63932	27420.85938	0.918119997
785	39267.82422	43462.05339	0.903496755
633	4488.970134	4877.522217	0.920338224
514	12041.04858	13481.69893	0.893140297
	Stdev		0.012823688
	Variance		0.000164447

Sub-Acute

Wavelength (nm)	Cholesterol		
	Peak Intensity at:		Ratio
	1439 cm-1	**1673 cm-1**	
830	55721.84017	20720.07227	0.371848313
785	118215.8229	51275.59766	0.433745639
633	67525.59115	33319.03516	0.493428263
514	83626.99479	58429.54557	0.698692399
	Stdev		0.141813312
	Variance		0.020111015

Wavelength (nm)	Serine		
	Peak Intensity at:		Ratio
	813 cm-1	**851 cm-1**	
830	8576.838867	36665.98991	0.233918105
785	12781.6377	44100.36914	0.289830628
633	2522.830078	9924.986491	0.254189774
514	26259.4401	56370.72266	0.465834725
	Stdev		0.105815786
	Variance		0.011196981

Wavelength (nm)	Sphingomyelin		
	Peak Intensity at:		Ratio
	1064 cm-1	**1298 cm-1**	
830	29750.02018	27747.07813	1.072185693
785	45314.47331	59438.24219	0.762379095
633	10015.77169	13621.71143	0.735279979
514	2107.047078	2963.698812	0.710951825
	Stdev		0.169299163
	Variance		0.028662207

Wavelength (nm)	Sulfatide		
	Peak Intensity at:		Ratio
	1064 cm-1	**1442 cm-1**	
830	23540.0625	20542.51758	1.145919063
785	40813.66895	71290.10677	0.572501162
633	6747.790202	24171.95866	0.279157775
514	7633.669759	23260.55729	0.328180863
	Stdev		0.397589088
	Variance		0.158077083

Wavelength (nm)	Cardiolipin		
	Peak Intensity at:		Ratio
	1267 cm-1	**1303 cm-1**	
830	18419.21094	16215.23177	0.880343454
785	66129.14844	66320.22656	1.002889469
633	5364.459473	5288.473958	0.985835383
514	19569.43083	20114.5542	1.027855862
	Stdev		0.064926797
	Variance		0.004215489

Wavelength (nm)	IL-6		
	Peak Intensity at:		Ratio
	1058 cm-1	**1125 cm-1**	
830	4663.757161	4801.566081	0.971299173
785	6770.091146	9481.074382	1.400435264
633	11698.02881	7870.414063	0.672798314
514	22010.16602	12343.01884	0.560787176
	Stdev		0.375143482
	Variance		0.140732632

Chronic

Wavelength (nm)	S100B		
	Peak Intensity at:		Ratio
	937 cm-1	**1003 cm-1**	
830	30538.5293	23227.625	0.760600642
785	79786.63021	72417.33333	0.907637447
633	33108.57422	18040.28581	0.544882594
514	36679.29492	16865.20622	0.459801811
	Stdev		0.203719704
	Variance		0.041501718

Wavelength (nm)	Galactocerebroside		
	Peak Intensity		Ratio
	1296 cm-1	**1440 cm-1**	
830	76019.40365	69105.80729	1.100043638
785	101608.0547	104866.3047	0.968929486
633	9863.101237	12272.54785	0.80367185
514	10111.28687	10298.62337	0.981809558
	Stdev		0.121865869
	Variance		0.01485129

Wavelength (nm)	Glucose		
	Peak Intensity at:		Ratio
	519 cm-1	**1125 cm-1**	
830	114083.2917	81742.10156	0.716512474
785	255382.5625	213039.0078	0.834195592
633	12078.06771	16479.49154	1.364414568
514	26045.30176	32465.36068	1.246495855
	Stdev		0.313519978
	Variance		0.098294776

Wavelength (nm)	Myo-Inositol		
	Peak Intensity at:		Ratio
	897 cm-1	**1358 cm-1**	
830	79405.54362	33887.69401	0.426767357
785	202567.0938	152287.8802	0.751789826
633	146123.1042	120364.6068	0.823720571
514	18304.3418	16586.3278	0.906141722
	Stdev		0.209921221
	Variance		0.044066919

Wavelength (nm)	IL-18		
	Peak Intensity at:		Ratio
	1078 cm-1	**1260 cm-1**	
830	45232.0459	34869.37435	0.770899783
785	88374.61654	63082.60286	0.71380907
633	29031.51693	21185.46875	0.72974033
514	8600.350423	6752.108073	0.785096855
	Stdev		0.033609405
	Variance		0.001129592

Wavelength (nm)	NFL		
	Peak Intensity at:		Ratio
	892 cm-1	**1322 cm-1**	
830	271582.2161	209369.9531	1.297140359
785	578361.7083	593670.5729	0.9742132
633	224219.737	277269.1354	0.808671822
514	39581.2181	50041.26693	0.790971543
	Stdev		0.234589195
	Variance		0.05503209

Appendix D

REVIEW: EMERGING EYE-BASED DIAGNOSTIC TECHNOLOGIES FOR TRAUMATIC BRAIN INJURY

The review article “Review: Emerging Eye-Based Diagnostic Technologies for Traumatic Brain Injury” can be found by clicking this link: https://pubmed.ncbi.nlm.nih.gov/35320105/

Appendix E

WINDOW INTO THE MIND: ADVANCED HANDHELD SPECTROSCOPIC EYE-SAFE TECHNOLOGY FOR POINT-OF-CARE NEURODIAGNOSTIC

The journal article “Window into the mind: Advanced handheld spectroscopic eye-safe technology for point-of-care neurodiagnostic” can be found by clicking this link: https://pubmed.ncbi.nlm.nih.gov/37967190/

Appendix F

SPECTROSCOPY SPECTRAL FINGERPRINTS OF BIOMARKERS OF TRAUMATIC BRAIN INJURY

The journal article “Raman Spectroscopy Spectral Fingerprints of Biomarkers of Traumatic Brain Injury” can be found by clicking this link: https://pubmed.ncbi.nlm.nih.gov/37998324/

Appendix G

RAMAN SPECTROSCOPY AS A NEUROMONITORING TOOL IN TRAUMATIC BRAIN INJURY: A SYSTEMATIC REVIEW AND CLINICAL PERSPECTIVES

The review article “Raman Spectroscopy as a Neuromonitoring Tool in Traumatic Brain Injury: A Systematic Review and Clinical Perspectives” can be found by clicking this link:
https://pubmed.ncbi.nlm.nih.gov/35406790/

Appendix H

RAMAN PHOTOBIOMODULATION REDUCES HIPPOCAMPAL APOPTOTIC CELL DEATH AND PRODUCES A RAMAN SPECTROSCOPIC “SIGNATURE”

The journal article “Photobiomodulation reduces hippocampal apoptotic cell death and produces a Raman spectroscopic "signature"” can be found by clicking this link: https://pubmed.ncbi.nlm.nih.gov/35239693/